



HAL
open science

Investigation of Local and Global Hydrodynamics of a Dynamic Filtration Module (RVF Technology) for Intensification of Industrial Bioprocess

Xiaomin Xie

► **To cite this version:**

Xiaomin Xie. Investigation of Local and Global Hydrodynamics of a Dynamic Filtration Module (RVF Technology) for Intensification of Industrial Bioprocess. Fluids mechanics [physics.class-ph]. INSA de Toulouse, 2017. English. NNT : 2017ISAT0020 . tel-01718041

HAL Id: tel-01718041

<https://theses.hal.science/tel-01718041>

Submitted on 27 Feb 2018

HAL is a multi-disciplinary open access archive for the deposit and dissemination of scientific research documents, whether they are published or not. The documents may come from teaching and research institutions in France or abroad, or from public or private research centers.

L'archive ouverte pluridisciplinaire **HAL**, est destinée au dépôt et à la diffusion de documents scientifiques de niveau recherche, publiés ou non, émanant des établissements d'enseignement et de recherche français ou étrangers, des laboratoires publics ou privés.

Université Fédérale



Toulouse Midi-Pyrénées

THÈSE

En vue de l'obtention du

DOCTORAT DE L'UNIVERSITÉ DE TOULOUSE

Délivré par
Institut National des Sciences Appliquées de Toulouse (INSA de Toulouse)

Discipline ou spécialité :
Ingénieries microbienne et enzymatique

Présentée et soutenue par

Xiaomin XIE

Le 22 mai 2017

Investigation of Local and Global Hydrodynamics of a Dynamic Filtration
Module (RVF Technology) for Intensification of Industrial Bioprocess

Etude de l'hydrodynamique d'un module de Filtration Dynamique (RVF
Technologie) pour intensifier les bioprocédés industriels

JURY

Christine MORESOLI (Professeure)	Université de Waterloo, Canada	Rapporteur
Luhui DING (Professeur)	Université de Technologie de Compiègne, France	Rapporteur
Fethi ALOUI (Professeur)	Université de Valenciennes, France	Rapporteur
Nicolas JITARIOUK (Dr.)	RVF Filtration Co., France	Examineur
Audrey DEVATINE (MDC)	ENSIACET, France	Examineur
Alain LINE (Professeur)	INSA de Toulouse, France	Membre invité
Henri BOISSON (DR CNRS)	IMFT, France	Membre invité

Ecole doctorale : ED SEVAB

Unité de recherche : LISBP (INRA UMR792, CNRS UMR5504, INSA de Toulouse)

Directeur(s) de Thèse :

Dr. Luc FILLAUDEAU (Directeur de recherche INRA, Directeur de thèse)

Prof. Philippe SCHMITZ (Professeur INSA de Toulouse, Co-Directeur de thèse)

Dr. Nicolas DIETRICH (Maitre de Conférences INSA de Toulouse, Co-Directeur de thèse)

πάντα ῥεῖ (Panta rhei).

Ἡράκλειτος

Everything flows.

Heraclitus

万物皆流，无物常住。

赫拉克利特

Acknowledgement

I would like to express my gratitude to my supervisors Luc FILLAUDEAU, Philippe SCHMITZ and Nicolas DIETRICH, who opened my world to a breakthrough research topic. A special and big thanks to Alain LINÉ, who's always generous to help me and teach me about the knowledge of fluid mechanics. Thanks to Claude Le Men and Christophe ANDRÉ for their help on my image and data processing. Thanks to all of them for the useful comments, remarks through the learning process of this thesis. I am very grateful for their kindness, concerning not only my daily work but also my daily life.

My sincere gratitude also goes out to all the jury members Christine Moresoli, Luhui Ding, Fethi Aloui, Nicolas Jitariouk, Audrey Devatine, Henri Boisson, thank you for evaluating my PhD manuscript and the helpful advices to improve and optimize this thesis.

I would like to thank also José MOREAU and Bernard REBOUL for their mechanical contribution and Pascal DEBREYNE (PIHM, Lille) for data acquisition and electrical control for experimental setup. Those valuable data were from a smart and beautiful experimental platform which was carefully setup by them.

Thanks to all the participants in my thesis defense on 22nd May 2017, who have willingly shared their precious time during the process of my presentation and interviewing.

Thanks to Dr. Yang LIU for his talent and contribution on my literature review.

Thanks to Dr. Harminder SINGH for introducing and showing me the PIV setup.

My fellow PhD students need to be acknowledged. Thanks Carlos ROBLES, Jian LIU, Cuong NGUYEN, Tuan LE, Naila BOUAYED, Weichao HUANG, Haiyang WU, Yanfeng GAO, Qiuming MA, Lixia YANG, Feishi XU, Lan LAN, Pablo LÓPEZ, Cristina PÉREZ, Paul JACOB, Allan HAYATO SHIMAKO, Maria FATARORVA and Rana SAGNAK, who encouraged and pushed me to move on, and told me to never give up.

Thanks to my best Chinese friend Linqing WANG, Juan XIAO, Wenxiang ZHANG, Qianhong JIANG and Zhe LI, who always listen to me and stand by my side.

Thank Florence LERAY, who's sitting next to me for more than 2 years and always nice to me. I own you a beer, or two.

Thank Manon MONTANER, who has a very warm smile and always asked me to be brave.

Thank dear Chao LI and Peter HARRIS, who always thought about me when I was alone. You guys never forgot about me every important day.

Thanks Elsa FREDERIC, Claude Le Men, Krichart WONGWAILIKHIT and Vincent QUEDEVILLE who always fed me with chocolates, specially Claude who always told me: I am the best!

I appreciate the helps from my dear colleagues in LISBP, especially colleagues in team 7 and 8, you helped me to grow up a lot. I hereby express my biggest thanks to you all!

I would like to thank JP P. D., it was always great to talk with you about life.

Besides, thank Julien P. for sharing happiness and sadness with me.

Last but not at least, greatest thanks to my dear family, especially Mom and Dad, for the continuous and endless support, love, comfort and guidance they have given me during all my 29 years. Thank to my brothers for loving me and helping me putting pieces together when I fall.

To all the people who believed in me, thank you for shaping my life...

Abstract

This thesis focuses on the understanding and the control of dynamic interactions between physical and biological mechanisms considering an alternative membrane separation into industrial bioprocess. It aims to carry scientific knowledge related to the control of bioreaction considering complex hydrodynamics and retention-permeation locks specific to membrane separation.

A dynamic filtration technology, called Rotating and Vibrating Filtration (RVF), was investigated. It consists of filtration cells in series including two flat disc membranes fixed onto porous substrates in the vicinity of a three-blade impeller attached to a central shaft. This simple mechanical device runs continuously and generates a high shear stress as well as a hydrodynamic perturbation in the narrow membrane-blade gap.

Several scientific and technical locks motivating this work are to characterize and to quantify (i) the velocity fields locally and instantaneously, (2) the shear stresses at membrane surface and (3) the mechanical impact on microbial cells.

To this end, experiments and numerical simulations have been performed to investigate the hydrodynamics at global and local scales under laminar and turbulent regimes with Newtonian fluids under biotic and abiotic environment.

For global approach, investigation of Residence Time Distribution (RTD) and thermal balance was carried out and compared to the previous global study (power consumption and friction curves). Analytical study of distribution functions was conducted and statistical moments were calculated and discussed. A systemic analysis was used to describe the hydrodynamic behaviors of the RVF module. Combining Computational Fluid Dynamics (CFD) and RTD observations, it leads to demonstrate dysfunctioning conditions and area.

For the local approach, Particle Image Velocimetry (PIV) was carried out in both horizontal and vertical planes and compared to CFD simulation. PIV preliminary study was conducted with a trigger strategy to access through angle-resolved measurements to an averaged velocity field. PIV further study were performed with a non-trigger strategy and applied to Proper Orthogonal Decomposition (POD) analysis in order to identify the coherent structure of the flow by decomposing the organized and turbulent fluctuations.

For the bioprocess application, an exploratory work characterized the effect of Dynamic Filtration on prokaryote cell population (*Escherichia coli*) by quantifying cell integrity or damage as a function of time and rotation speed during filtration process in turbulent regime.

Keywords: Membrane bioreactor, bioprocess engineering, dynamic filtration, fluid mechanics, hydrodynamics, Particle Image Velocimetry, Residence Time Distribution (RTD), Computational Fluid Dynamic (CFD), Proper Orthogonal Decomposition (POD), microbial suspension.

Résumé

Cette thèse porte sur la compréhension et le contrôle des interactions dynamiques entre les mécanismes physiques et biologiques en considérant un procédé alternatif de séparation membranaire pour les bioprocédés industriels. L'objectif premier est un apport de connaissances scientifiques liées à la maîtrise de la bioréaction en considérant l'hydrodynamique complexe et les verrous rétention-perméation.

Une technologie de filtration dynamique, appelée Rotating and Vibrating Filtration (RVF), a été spécifiquement étudiée. Elle se compose de cellules de filtration en série comprenant deux membranes circulaires planes fixées sur des supports poreux au voisinage d'un agitateur à trois pales planes attachées à un arbre central. Ce dispositif mécanique simple fonctionne en continu et génère une contrainte de cisaillement élevée ainsi qu'une perturbation hydrodynamique dans un entrefer étroit (pale-membrane).

Les verrous scientifiques et techniques qui motivent ce travail, sont la caractérisation et la quantification (1) des champs de vitesse locaux et instantanés, (2) des contraintes pariétales de cisaillement à la surface de la membrane et (3) l'impact mécanique sur les cellules microbiennes.

Dans ce but, des expériences et des simulations numériques ont été réalisées pour étudier l'hydrodynamique à des échelles globales et locales, en régimes laminaire et turbulent avec des fluides newtoniens dans des environnements biotique et abiotique.

Pour l'approche globale, la distribution des temps de séjour (RTD) et le bilan thermique ont été réalisés et comparés aux précédentes études globales (courbes de consommation de puissance et de frottement). Une étude analytique des fonctions de distribution a été effectuée et les moments statistiques ont été calculés et discutés. Une analyse systémique a été utilisée pour décrire les comportements hydrodynamiques du module RVF. En combinant la simulation des écoulements (CFD) et les observations (RTD), les conditions et les zones de dysfonctionnement des cellules de filtration sont éclairées.

Pour l'approche locale, la vélocimétrie laser (PIV) a été réalisée dans les plans horizontaux et verticaux et comparée à la simulation numérique (CFD). Une étude préliminaire basée sur une synchronisation entre la prise d'image et la position de l'agitateur (résolution angulaire) a permis d'accéder aux champs de vitesse moyens. Une campagne de mesure PIV a été réalisée sans

synchronisation afin d'appliquer une décomposition orthogonale aux valeurs propres (POD) pour identifier les composantes moyennes, organisées et turbulentes des champs de vitesse (énergie cinétique).

Pour l'application aux bioprocédés, un travail exploratoire a caractérisé l'effet de la filtration dynamique sur des cellules procaryotes (*E. coli*) en quantifiant l'intégrité cellulaire ou leur dégradation en fonction du temps et de la vitesse de rotation.

Mots clés: Bioréacteur à membranaire, bioprocédé, filtration dynamique, mécanique des fluides, hydrodynamique, vélocimétrie laser (PIV), distribution de temps de séjour (RTD), analyse dynamique et computationnelle des fluides (CFD), décomposition orthogonale aux valeurs propres(POD), suspension microbienne.

List of scientific communications and publications

Journal papers

- **1 paper accepted by *Separation and Purification Technology* (selected from WFC12 / special issue)**

Xiaomin XIE, Claude LE MEN, Nicolas DIETRICH, Philippe SCHMITZ, Luc FILLAUDEAU, Local Hydrodynamic Investigation by PIV and CFD within a Dynamic Filtration Unit under Laminar Flow. *Journal Separation and Purification Technology (special issue of WFC12th, 2016.)* -in press

- **1 paper submitted to *Chemical Engineering Research and Design* on 28/10/2017 (selected from ISMIP2017)**

X. Xie, N. Dietrich, L. Fillaudeau, C. Le Men, P. Schmitz, A. Liné, Local Hydrodynamic Investigation within a Dynamic Filtration Unit under Laminar Flow, *Chemical Engineering Research and Design* - under review with minor corrections

- **1 paper under work, regarding on RTD**

Xiaomin XIE, Nicolas DIETRICH, Philippe SCHMITZ, Christophe ANDRE, Luc FILLAUDEAU, Residence time distribution in a dynamic filtration module. *Chemical Engineering Journal* – to be submitted

- **1 review under work, regarding on Dynamic Filtration module**

Xiaomin XIE, Nicolas DIETRICH, Philippe SCHMITZ, Luc FILLAUDEAU, A review of Dynamic Filtration Module - under work.

National conferences

- SFGP (2017) – poster communication and extended paper

Xiaomin XIE, Christophe ANDRE, Nicolas DIETRICH, Philippe SCHMITZ, Luc FILLAUDEAU, Residence time distribution in a dynamic filtration module, 16ème SFGP, poster session THEME 4 : Le génie des procédés au service de l'innovation pour les bio-productions, 11 - 13 July 2017, Nancy, France

Reference of extended paper : Récents Progrès en Génie des Procédés, Numéro 110 - 2017 ISSN: 1775-335X ; ISBN: 978-2-910239-85-5, Ed. SFGP, Paris, France, pp 4.6-1, 4.6-11

International conferences

- ECCE10 (2015)

XIE Xiaomin, LE MEN Claude, DIETRICH Nicolas, SCHMITZ Philippe, FILLAUDEAU Luc, Investigation of Velocity Field by Particle Image Velocimetry in a Dynamic Filtration Module, European Congress of Chemical Engineering, 27th September – 1st October 2015, Nice, France, session: Fluid separations processes and technologies. (Oral presentation + proceeding).

- International Workshop on MBR/Quorum Quenching-MBR (2015)

Nicolas Dietrich, Mélanie Jimenez, Xiaomin Xie, and Gilles Hébrard, Optical Techniques to Evaluate Hydrodynamics and Mass Transfer in Bioreactors, International Workshop on MBR/Quorum Quenching-MBR, 19th November, 2015, Seoul National University, Korea.

- WFC12 (2016)

Xiaomin XIE, Nicolas DIETRICH, Philippe SCHMITZ, Luc FILLAUDEAU, Laminar Flow in a RVF Dynamic Filtration Unit: Local Hydrodynamic Approach, 12th World Filtration Congress, April 11-15th, 2016, Taipei, China, session L10: Vibration, Hydrodynamics, Thermal & Hybrid-Process Enhanced Filtration (Oral presentation + proceeding).

- WFC12 (2016)

Xiaomin XIE, Youssef EL RAYESS, Yannick MANON, Nicolas JITARIOUK, Claire ALBASI, Martine MIETTON-PEUCHOT, Audrey DEVATINE, Philippe SCHMITZ, Nicolas DIETRICH and Luc FILLAUDEAU, Wine clarification with Rotating and Vibrating Filtration (RVF) from wine-membrane interactions up to critical frequency identification, 12th World Filtration Congress, April 11-15th, 2016, Taipei, China, poster session PM: membrane filtration (Poster presentation PM-48 + abstract).

- ISMIP9 (2017) - oral presentation + abstract accepted

X. Xie, N. Dietrich, L. Fillaudeau, P. Schmitz, A. Liné, Local Hydrodynamic Investigation by PIV within a Dynamic Filtration Unit under Laminar Flow, International Symposium on Mixing in Industrial Processes IX, 25th-28th June 2017, Hyatt Regency Birmingham, UK, session 7: single phase laminar and turbulent minxing (Oral presentation + abstract).

Table of Contents

Acknowledgement	V
Abstract	VII
Résumé	IX
List of scientific communications and publications	XI
Table of Contents	XIII
List of figures	XVIII
List of tables	XXVII
Nomenclature	XXVIII
Chapter I: Introduction	2
Chapter II: Literature review on Dynamic Filtration modules	8
1 Introduction of membrane filtration process	9
1.1 Aim and context	9
1.2 Scientific production related to DF.....	13
2 Specification and Application of Industrial and Commercial Dynamic Filtration Module	20
2.1 DF module with mobile membrane	26
2.1.1 Cylindrical membrane modules.....	26
2.1.2 Rotating flat membrane modules.....	27
2.1.3 Vibrating flat membrane modules	30
2.1.4 Vibrating hollow fiber	31
2.2 DF modules with stationary membrane	32
2.2.1 Rotating flat disk modules	32
3 Theory: criteria to characterize internal fluid dynamics	35
3.1 Global approach.....	35
3.1.1 Dimensionless analysis in dynamic filtration.....	35
3.1.1.1 Reynolds number in tube	37
3.1.1.2 Reynolds number in mixing and rotating system.....	37
3.1.1.3 Reynolds number for vibrating systems.....	38
3.1.2 Friction curve and power consumption curve	38

3.2 Semi-local approaches	40
3.2.1 Radial pressure and core velocity coefficient induced by mixing	41
3.2.1.1 Radial pressure	41
3.2.1.1 Discussion of core velocity coefficient	42
3.2.2 Shear rate and shear stress calculation.....	46
3.2.2.1 Rotating systems.....	46
3.2.2.2 Vibrating systems	48
3.3 Local approaches	50
3.3.1 PIV/PTV	50
3.3.2 Molecular tagging velocimetry (MTV)/Planar laser-induced fluorescence imaging (PLIF). 50	
3.3.3 Doppler velocimetry (LDV).....	51
3.3.4 Electrochemical method	51
3.3.5 Computational Fluid Dynamics (CFD).....	51
Chapter III: Materials and methods.....	56
1 RVF module and experimental set-up.....	57
1.1 Specification of RVF module.....	57
1.2 Specification of membrane.....	58
1.3 General experimental set-up.....	58
2 Experiment fluids	62
2.1 Abiotic approach	62
2.1.1 Water	62
2.1.2 BREOX solution	62
2.1.3 Tracer solutions.....	63
2.1.3.1 Salt solutions (RTD)	63
2.1.3.2 Rhodamine suspensions (PIV).....	64
2.2 Escherichia coli (<i>E. coli</i> WK6) cell suspension (partnership with Hazar KRAIEM, PhD IPT/LISBP)	64
3 Global investigations: Residence Time Distribution (RTD) and thermal balance	65
3.1 Theory of RTD	65

3.2	RTD set-up.....	67
3.3	Methodology	69
3.3.1	RTD: data treatment and analysis.....	69
3.3.2	Power consumption and thermal balance.....	71
3.3.2.1	Power consumption	71
3.3.2.2	Thermal balance	71
3.3.3	Experiment strategy and operating procedure.....	72
3.3.4	Method of modeling: systematic analysis	73
4	Local investigations: Particle Image Velocimetry (PIV).....	75
4.1	Principle of PIV.....	75
4.2	PIV set-up	76
4.2.2	Horizontal field configuration.....	77
4.2.3	Vertical field configuration.....	79
4.3	Experimental strategy and operating conditions.....	79
4.4	Data treatments	80
4.4.1	From images to velocity fields.....	80
4.4.2	Interpolation.....	81
4.4.3	Statistical analysis: convergence	82
4.4.4	POD analysis.....	85
4.4.4.1	Principle of POD analysis	85
4.4.4.2	POD data treatment.....	86
4.4.4.3	Reconstruction of instantaneous velocity field from POD	88
5	Local investigation: CFD simulation in laminar flow.....	89
5.1	Governing equations and boundary conditions	89
5.2	Numerical method and calculation mesh	91
5.3	Operating conditions.....	91
6	Application of RVF module with <i>E.coli</i> suspension.....	92
6.1	Experiment strategy	93
6.2	Operating procedures	93

Chapter IV: Results and Discussion	96
1 Global approach: Thermal balance and RTD	97
1.1 Thermal balance	97
1.2 Residence Time Distribution (RTD).....	98
1.2.1. Analytical studies	99
1.2.1.1 Distribution and cumulative distribution functions.....	99
1.2.1.2 Discussion of moments	102
1.2.1.3 Reduced signal of outlet distribution function.....	107
1.2.2 Systemic analysis and modeling of RTD	109
1.2.2.1 Proposal of reactor models	109
1.2.2.2 Model adjustment and comparison	112
1.3 Simulation of fluid streamlines by CFD under laminar flow regime.....	114
2 Local approach with Particle Image Velocimetry (PIV).....	119
2.1 Preliminary study-PIV with trigger strategy	120
2.1.1 Laminar regime	120
2.1.1.1 Velocity field.....	120
2.1.1.2. Velocity profiles	123
2.1.1.3 Comparison with CFD simulation	126
2.1.2 Turbulent regime.....	132
2.1.2.1 Velocity field analyses.....	132
2.1.2.2. Velocity profiles	134
2.2 POD analysis (with non-trigger strategy).....	138
2.2.1 Laminar regime	139
2.2.1.1 Mean laminar flow.....	139
2.2.1.2 Fluctuations in laminar flow (at N = 2 Hz)	145
2.2.2 Turbulent regime.....	159
2.2.2.1. Mean turbulent flow.....	159
2.2.2.2 Organized flow versus turbulence	165
3 Application to cell suspensions	180

3.1 Observation of integrate and disrupted cells by microscopy.....	180
3.2 Particle size distribution (PSD) by DLS, impact of time and mixing rate	181
Chapter V: Conclusions.....	186
Reference.....	193
Annexes.....	209
Extended Abstract	227
Résumé Étendu.....	233

List of figures

Chapter II: Literature review on Dynamic Filtration modules

Fig.II. 1 Comparison between Dead-end (DEF), Cross-flow (CF) and dynamic (DF) filtration.....	12
Fig.II. 2 Evolution of the number of publication per year	14
Fig.II. 3 Cooperation network among top 20 most productive countries (source: Web of Science category of journals)	17
Fig.II. 4 Cooperation network among top 10 most productive institutions (source: Web of Science category of journals).....	18
Fig.II. 5 Small overview of application field and filtration type in Dynamic Filtration	19
Fig.II. 6 Classification of DF modules according to the membrane motion	20
Fig.II. 7 Friction curve established with RVF lab-scale module [5].....	40
Fig.II. 8 Power consumption curve established with RVF lab-scale module [5]	40
Fig.II. 9 Determination of hydrodynamic performances, evolution of the radial pressure distribution versus the radius and the rotational speed[4,5].....	42
Fig.II. 10 Evolution of core velocity coefficient, $K\theta$ as a function of gap-to-radius ratio, z/R_m . Values are reported from literature for DF modules using confined rotating impeller close to membrane and established under laminar or turbulent regimes	44

Chapter III: Materials and Methods

Fig.III. 1 Scheme and illustration of filtration cell and of RVF module.....	58
Fig.III. 2 All equipment used in this study	59
Fig.III. 3 Experimental set-up and injection device (a) C1, C2: Electrical conductivity measurement; T1, T2: Temperature measurement; Q _r : Feeding flow rate, (b) Injection device.....	68
Fig.III. 4 Conductivity measurements at the inlet and outlet	69
Fig.III. 5 Principle of Particle Image Velocimetry (PIV), figure modified from Nicolas DIETRICH's PhD thesis[192]	76
Fig.III. 6 Schematic diagram and apparatus used in the experiment (a) horizontal PIV schematic diagram (b) PIV system synchronized with a CCD camera, double pulsed laser and the RVF module with the transparent cell; (c) the transparent filtration cell installed with a black painted impeller; (d) the transparent filtration cell with laser beam (e) An optical trigger synchronized with the PIV system.	77
Fig.III. 7 Schematic diagram and apparatus used in the experiment (a) vertical PIV schematic diagram; (b) The PIV system synchronized with a CCD camera, double pulsed laser and the RVF module with the transparent cell; (c) the transparent filtration cell installed with a black painted impeller.....	79
Fig.III. 8 Velocity calculation at the specific point by Inverse Distance Weighting Interpolation (IDW).....	82

Fig.III. 9 Convergence of mean IDW velocity U_{ml} (a, b and c) and the associated standard deviation σI (d, e and f) as a function of the number of image pairs I . Observations in this example are reported for 3 radius ($R=30, 45$ and 65 mm) for 6 different slices within the gap (z_1 to z_6) at $\theta=-50^\circ$, in horizontal measurement. Operating conditions: $N=2$ Hz, $Q_f=50$ L/h BREOX solution $\mu=0.80$ Pa·s, with optical trigger..... 83

Fig.III. 10 Convergence of (a) velocity u (x direction) and v (y direction) and (b) the associated standard deviation σI as a function of the number of image pairs I . Observations in this example are reported for a random point in within the gap ($z=1.5$ mm) in horizontal measurement. Operating conditions: $N=2$ Hz, $Q_f=50$ L/h, BREOX solution $\mu=0.80$ Pa·s, without optical trigger. 84

Fig.III. 11 Geometry of the RVF filtration cell (a) and calculation mesh (b) used in CFD software COMSOL 4.3a. 1 and 2: Fluid cross-sections (vertical periodic); 4 and 5: fluid cross-section for inlet (bottom) and outlet (top); 6: surface of the rotating solid impeller. 3: the upper and lower walls where the membrane are mounted; 7: surrounding wall of the filtration cell 90

Fig.III. 12 Wall shear stress acting on adherent cells in a flow chamber with parallel plates. (modified from [208,209]) 92

The streamlines are the lines tangential to velocity vectors at a given time.. Simulation of Fig.IV. 12 was conducted with $Q_f=45$ L/h, $N=2$ Hz, corresponding to vertical mean pressure gradients ($\partial P/\partial z$) 1.17 Pa/m. Fig.IV. 13a introduces the streamline start from cross-section1 within the whole filtration cell, while Fig.IV. 12b presents part of the streamlines that follow the impeller movement. These streamlines seem to be almost parallel to each other, indicating a well-organized flow motion. However, by comparing these two figures, it seems streamlines are more organized following the impeller rotation (in the same fluid layer with the impeller) than the streamlines close to the wall. It may be explained by the effect of the low mixing efficiency close to the wall, especially close to the central shaft. In Fig.IV. 12c, as expected, streamlines velocity is found almost equal to zero close to the surrounding wall and it remained rotating in the same radial annular; it highly refers to a low mixing dead-zone without exchange flow to the rest of the fluid. Nevertheless, a large magnitude of velocity between the streamlines is noticeable..... 114

Chapter IV: Results and Discussions

Fig.IV. 1 Temperature variation of the test fluid with different mixing rate..... 97

Fig.IV. 2 Heat dissipation and estimated power consumption as a function of mixing rate 98

Fig.IV. 3 Inlet and outlet distribution function $x(t)$ and $y(t)$ in (a) laminar flow regime, operating condition: 35% BREOX solution, $\mu=0.35$ Pa·s, $Q_f=100$ L/h, $N=0$ ($T_{in}=22.7 \pm 0.01^\circ\text{C}$, $T_{out}=23.0 \pm 0.02^\circ\text{C}$) and 25 Hz ($T_{in}=22.2 \pm 0.14^\circ\text{C}$, $T_{out}=26.3 \pm 0.13^\circ\text{C}$); and in (b) turbulent flow regime, operating condition: water, $\mu=1$ mPa·s, $Q_f=100$ L/h, $N=0$ ($T_{in}=13.0 \pm 0.12^\circ\text{C}$, $T_{out}=13.1 \pm 0.11^\circ\text{C}$) and 50 Hz ($T_{in}=14.8 \pm 0.02^\circ\text{C}$, $T_{out}=19.3 \pm 0.02^\circ\text{C}$). 100

Fig.IV. 4 Outlet distribution function $y(t)$ for (a) laminar flow regime, operating condition: 35% BREOX solution, $\mu=0.35$ Pa·s, $Q_f=100$ L/h, $N=0, 2, 10, 25$ Hz; and for (b) turbulent flow regime, operating condition: water, $\mu=1$ mPa·s, $Q_f=100$ L/h, $N=0, 2, 10, 25, 50$ Hz. 101

Fig.IV. 5 Cumulative function $Y(t)$ at the outlet for (a) laminar flow regime, operating condition: 35% BREOX solution $\mu=0.35$ Pa·s, $Q_f=25, 100$ L/h, $N= 2, 10, 25$ Hz; and for (b) turbulent flow regime, operating condition: water, $\mu=1$ mPa·s, $Q_f=50, 150, 300$ L/h, $N=2, 10, 25, 50$ Hz 102

Fig.IV. 6 Mean residence time t_s as a function of rotation speed N for (a) laminar flow regime, operating condition: BREOX solution $\mu=0.35$ Pa·s, $Q_f=25, 50, 100$ L/h, $N=0, 2, 10, 25$ Hz; and for (b) turbulent flow regime, operating condition: water, $Q_f=50, 100, 150, 300$ L/h, $N=0, 2, 10, 25, 50$ Hz 104

Fig.IV. 7 Used volume V_1 as a function of mixing Reynolds number. Laminar flow regime $Re_{mixing}<1200$,; operating condition: BREOX solution $\mu=0.35$ Pa·s, $Q_f=25, 50, 100$ L/h, $N=0, 2, 10, 25$ Hz; Turbulent flow $Re_{mixing}>3\times 10^4$ operating condition: water, $Q_f=50, 100, 150, 300$ L/h, $N=0, 2, 10, 25, 50$ Hz 105

Fig.IV. 8 Reduced variance β^2 as a function of mixing Reynolds number. Laminar flow regime: $Re_{mixing}<1200$, operating condition: BREOX solution $\mu=0.35$ Pa·s, $Q_f=25, 50, 100$ L/h, $N=0, 2, 10, 25$ Hz; Turbulent flow regime: $Re_{mixing}>3\times 10^4$ operating condition: water, $Q_f=50, 100, 150, 300$ L/h, $N=0, 2, 10, 25, 50$ Hz 106

Fig.IV. 9 Reduced $yt/ts \cdot ts$ as a function of reduced time t'/ts , for (a) laminar flow regime, operating conditions for a1: BREOX solution $\mu=0.35$ Pa·s, $Q_f=100$ L/h, $N=0, 2, 10, 25$ Hz, operating conditions for a2: BREOX solution $\mu=0.35$ Pa·s, $Q_f=25, 50, 100$ L/h, $N=25$ Hz; for (b) Turbulent flow regime, operating conditions: water, $Q_f=50, 300$ L/h, $N=0, 50$ Hz 108

Fig.IV. 10 Proposed models equivalent to RVF model, with the ideal plug flow reactor equivalent to the real tubes 110

Fig.IV. 11 Comparison of curves fitting from Model 1, Model 2 and Model 3. (a) in laminar regime (b) in turbulent regime..... 113

Fig.IV. 12 Illustration of streamlines start from cross-section 1 issued from CFD simulation (a) within the whole filtration cell; (b) streamlines follow the impeller rotation; and (c) close to the surrounding wall $R=69$ mm; Direction of the streamline: from cross-section 1 to 2; Operating conditions: $Q_f= 45$ L/h, $N=2$ Hz; $\mu=0.85$ Pa·s and $T=20^\circ\text{C}$ 115

Fig.IV. 13 Illustration of streamlines in the filtration cell issued from CFD simulation in 3D (a, b, c, d) and 2D (e, f, g, h) view with rotation frequency $N=0$ Hz (a, e), $N=2$ Hz (b, f), $N=5$ Hz (c, g), $N=10$ Hz (d, h). Direction of the streamline: from cross-section 4 to 5; Operating conditions: $Q_f= 45$ L/h; $\mu=0.85$ Pa·s and $T=20^\circ\text{C}$. * Notice each figure has 500 streamlines 116

Fig.IV. 14 Brief schematic of horizontal measurement 119

Fig.IV. 15 Brief schematic of vertical measurement 119

Fig.IV. 16 Illustration of PIV raw images in horizontal measurement (a, d), instantaneous velocity fields (b, e, issued from single image pair) and time-averaged velocity fields (c, f, averaged of 1000 image pairs) in the RVF module. Slice positions: z_1 close to the wall (a, b and c) and z_6 close to the impeller (d, e and f); Operating conditions: $Q_f= 45$ L/h, $N=2$ Hz; $\mu=0.85$ Pa·s and $T=20^\circ\text{C}$. Symbols: \circ , leading edge and \triangle , trailing edge of blade 121

Fig.IV. 17 Vertical measurement in laminar flow. Illustration of PIV raw images (a, b, c), instantaneous velocity fields (d, e, f, issued from single image pair) and time-averaged velocity fields (g, h, i, averaged of 300 image pairs).

Vertical positions: R=30 mm (a, d, g), R=45 mm (b, e, h), R=65 mm (c, f, i); Operating conditions: $Q_f= 50$ L/h, N=2 Hz; $\mu=0.85$ Pa·s and $T=20^\circ\text{C}$	123
Fig.IV. 18 Evolution of mean velocity profiles U_m and their radial and angular components U_θ U_r as a function of angular position for 6 horizontal planes (z_1 to z_6) within the membrane-impeller gap. (a): IDW mean velocity at R=30, 45 and 65 mm; (b): mean, radial and angular velocity profiles, U_m, U_θ and U_r , at R=45 mm. Operating conditions: $Q_f= 45$ L/h, N=2 Hz; $\mu=0.85$ Pa·s and $T=20^\circ\text{C}$. Symbols: \circ , leading edge and \triangle , trailing edge of blade	124
Fig.IV. 19 Vertical velocity profile at z direction at R=30 mm, R=45 mm and R=65 mm (between two blades) and compare to the CFD simulation. Operating conditions: $Q_f= 50$ L/h, N=2 Hz; $\mu=0.85$ Pa·s and $T=20^\circ\text{C}$	126
Fig.IV. 20 Velocity fields in CFD simulation with 6 slices, from z_1 (a) to z_6 (f). Operating conditions: $Q_f= 45$ L/h, N=2 Hz; BREOX solution, $\mu=0.85$ Pa·s and $T=20^\circ\text{C}$	127
Fig.IV. 21 Field of wall shear stress ($z=0$ and 14 mm) calculated from CFD simulations. Operating conditions: $Q_f= 45$ L/h, N=2 Hz; $\mu=0.85$ Pa·s and $T=20^\circ\text{C}$ (Notice: $z=0$ and 14 mm is at the surface of the walls where membranes are mounted).....	128
Fig.IV. 22 Evolution of mean velocity U_m issued from PIV horizontal measurement and CFD simulations as a function of z for 3 points, at radius R=45 mm (point 1: leading edge, point 2: between two blades, point 3: trailing edge). Operating conditions: $Q_f= 45$ L/h, N=2 Hz; $\mu=0.85$ Pa·s and $T=20^\circ\text{C}$. (Notice: $z=0$ and 14 mm is at the surface of the walls where membranes are mounted, this 14 mm gap is including upper gap $0 < z < 3$ impeller thickness $3 < z < 11$, and lower gap $11 < z < 14$)	130
Fig.IV. 23 Illustration of PIV raw images in horizontal measurement (a, d), instantaneous velocity fields (b, e, issued from single image pair) and time-averaged velocity fields (c, f, averaged of 1000 image pairs) in the RVF module. Slice positions: z_1 close to the wall (a, b and c) and z_6 close to the impeller (d, e and f); Operating conditions: $Q_f= 100$ L/h, N=10 Hz; water, $\mu=1$ mPa·s and $T=20^\circ\text{C}$. Symbols: \circ , leading edge and \triangle , trailing edge of blade	133
Fig.IV. 24 Vertical measurement in turbulent flow. Illustration of PIV raw images (a, b, c), instantaneous velocity fields (d, e, f, issued from single image pair). Vertical positions: R=30 mm (a, d), R=45 mm (b, e), R=65 mm (c, f); Operating conditions: $Q_f= 100$ L/h, N=10 Hz; water, $\mu=01$ mPa·s and $T=20^\circ\text{C}$	134
Fig.IV. 25 Evolution of mean velocity profiles U_m and their radial and angular components U_θ U_r as a function of angular position for 6 horizontal planes (z_1 to z_6) within the membrane-impeller gap. (a) IDW mean velocity at R=30, 45 and 65 mm; (b): mean, radial and angular velocity profiles, U_m, U_θ and U_r , at R=65 mm. Operating conditions: $Q_f= 100$ L/h, N=10 Hz; water, $\mu=1$ mPa·s and $T=20^\circ\text{C}$. Symbols: \circ , leading edge and \triangle , trailing edge of blade	135
Fig.IV. 26 Vertical velocity profile at z direction at R=30 mm, R=45 mm and R=65 mm. Operating conditions: $Q_f= 100$ L/h, N=10 Hz; water, $\mu=1$ mPa·s and $T=20^\circ\text{C}$	136
Fig.IV. 27 Radial profiles of tangential mean velocities at 3 planes, $z=0.25, 1.5$ and 2.75 mm (distance from the upper wall). Operating conditions: horizontal measurements at $Q_f= 50$ L/h, N=2 Hz; BREOX solution, $\mu=0.85$ Pa·s, $Re_{mixing}=42$, and $T=20^\circ\text{C}$	140

Fig.IV. 28 Radial profiles of viscous mean shear at 3 planes, $z=0.25, 1.5, \text{ and } 2.75$ mm (distance from the upper wall). Operating conditions: horizontal measurements at $Q_f= 50$ L/h, $N=2$ Hz; BREOX solution, $\mu=0.85$ Pa·s, $Re_{mixing}=42$, and $T=20^\circ\text{C}$	141
Fig.IV. 29 Vertical profiles of tangential mean velocities at 3 radius, $R=30, 45$ and 65 mm. Operating conditions: vertical measurements at $Q_f= 50$ L/h, $N=2$ Hz; BREOX solution, $\mu=0.85$ Pa·s, $Re_{mixing}=42$, and $T=20^\circ\text{C}$	142
Fig.IV. 30 Vertical profiles of dimensionless velocity $k\theta$ (local velocity coefficient) at 3 radius $R=30, 45$ and 65 mm with $N=2$ and 10 Hz. Operating conditions: vertical measurements at $Q_f= 50$ L/h; BREOX solution, $\mu=0.85$ Pa·s, $Re_{mixing}=42$ and 210 , and $T=20^\circ\text{C}$	143
Fig.IV. 31 Vertical profiles of viscous mean shear stress at 3 radius $R=30, 45$ and 65 mm with $N=2$ and 10 Hz. Operating conditions: vertical measurements at $Q_f= 50$ L/h; BREOX solution, $\mu=0.85$ Pa·s, $Re_{mixing}=42$ and 210 , and $T=20^\circ\text{C}$	144
Fig.IV. 32 Radial profiles of wall shear stress compare to CFD, at 3 radius $R=30, 45$ and 65 mm with $N=2$ and 10 Hz. Operating conditions: vertical measurements at $Q_f= 50$ L/h; BREOX solution, $\mu=0.85$ Pa·s, $Re_{mixing}=42$ and 210 , and $T=20^\circ\text{C}$	144
Fig.IV. 33 Eigenvalue spectrum. Operating conditions: horizontal measurement at plane $z_2=1.5$ mm, $Q_f= 50$ L/h, $N=2$ Hz, $Re_{mixing}=42$; BREOX solution, $\mu=0.85$ Pa·s and $T=20^\circ\text{C}$, data acquisition rate 7 Hz, 1000 pairs of images	147
Fig.IV. 34 First mode (a) eigen function, and (b) pdf of normalized POD coefficient. Operating conditions: horizontal measurement at plane $z_2=1.5$ mm, $Q_f= 50$ L/h, $N=2$ Hz, $Re_{mixing}=42$; BREOX solution, $\mu=0.85$ Pa·s and $T=20^\circ\text{C}$, data acquisition rate 7 Hz, 1000 pairs of images.....	148
Fig.IV. 35 Reconstructed velocity with the first mode (POD reconstructed) compared to the statistical average of the velocity (Reynolds averaged). Operating conditions: horizontal measurement at plane $z_2=1.5$ mm, $Q_f= 50$ L/h, $N=2$ Hz, $Re_{mixing}=42$; BREOX solution, $\mu=0.85$ Pa·s and $T=20^\circ\text{C}$, data acquisition rate 7 Hz, 1000 pairs of images.....	148
Fig.IV. 36 Second and third mode (a, c) eigen function, and (b, d) pdf of normalized POD coefficient. Operating conditions: horizontal measurement at plane $z_2=1.5$ mm, $Q_f= 50$ L/h, $N=2$ Hz, $Re_{mixing}=42$; BREOX solution, $\mu=0.85$ Pa·s and $T=20^\circ\text{C}$, data acquisition rate 7 Hz, 1000 pairs of images	150
Fig.IV. 37 Portrait of phase between coefficients of mode 2 and 3. Operating conditions: horizontal measurement at plane $z_2=1.5$ mm, $Q_f= 50$ L/h, $N=2$ Hz, $Re_{mixing}=42$; BREOX solution, $\mu=0.85$ Pa·s and $T=20^\circ\text{C}$, data acquisition rate 7 Hz, 1000 pairs of images.....	151
Fig.IV. 38 Fourth and fifth mode (a, c) eigen function, and (b, d) pdf of normalized POD coefficient. Operating conditions: horizontal measurement at plane $z_2=1.5$ mm, $Q_f= 50$ L/h, $N=2$ Hz, $Re_{mixing}=42$; BREOX solution, $\mu=0.85$ Pa·s and $T=20^\circ\text{C}$, data acquisition rate 7 Hz, 1000 pairs of images	152
Fig.IV. 39 Portrait of phase between coefficients of mode 4 and 5. Operating conditions: horizontal measurement at plane $z_2=1.5$ mm, $Q_f= 50$ L/h, $N=2$ Hz, $Re_{mixing}=42$; BREOX solution, $\mu=0.85$ Pa·s and $T=20^\circ\text{C}$, data acquisition rate 7 Hz, 1000 pairs of images.....	153

Fig.IV. 40 Sixth and seventh mode (a, c) eigen function, and (b, d) pdf of normalized POD coefficient. Operating conditions: horizontal measurement at plane $z_2=1.5$ mm, $Q_f= 50$ L/h, $N=2$ Hz, $Re_{mixing}=42$; BREOX solution, $\mu=0.85$ Pa·s and $T=20^\circ\text{C}$, data acquisition rate 7 Hz, 1000 pairs of images	154
Fig.IV. 41 Instantaneous reconstructed velocity field based on mode 2 to 5. Operating conditions of the raw data: horizontal measurement at plane $z_2=1.5$ mm, $Q_f= 50$ L/h, $N=2$ Hz, $Re_{mixing}=42$; BREOX solution, $\mu=0.85$ Pa·s and $T=20^\circ\text{C}$, data acquisition rate 7 Hz, 1000 pairs of images.....	155
Fig.IV. 42 Vertical profiles of Root Mean Square (RMS) shear at 3 radius $R=30, 45$ and 65 mm with $N=2$ and 10 Hz. Operating conditions: vertical measurements at $Q_f= 50$ L/h; BREOX solution, $\mu=0.85$ Pa·s, $Re_{mixing}=42$ and 210 , and $T=20^\circ\text{C}$	156
Fig.IV. 43 Radial profiles of viscous mean shear stress at $N=2$ and 10 Hz. Operating conditions: vertical measurements at $Q_f= 50$ L/h; BREOX solution, $\mu=0.85$ Pa·s, $Re_{mixing}=42$ and 210 , and $T=20^\circ\text{C}$	156
Fig.IV. 44 Radial profiles of the weight of RMS shear (out of viscous mean shear stress) at $N=2$ and 10 Hz. Operating conditions: vertical measurements at $Q_f= 50$ L/h; BREOX solution, $\mu=0.85$ Pa·s, $Re_{mixing}=42$ and 210 , and $T=20^\circ\text{C}$	157
Fig.IV. 45 Vertical profiles of mean tangential velocity ($U\theta$) and mean vertical velocity (Uz). Operating conditions: vertical measurements at $R= 65(a), 45(b)$ and $30(c)$ mm with $Q_f= 100$ L/h; water, $\mu=1$ mPa·s, $N=10$ Hz, $Re_{mixing}=182,250$, and $T=20^\circ\text{C}$	160
Fig.IV. 46 Vertical profiles of mean Reynolds shear stress at $R=65$ mm. Operating conditions: vertical measurements at $Q_f= 100$ L/h; water, $\mu=1$ mPa·s, $N=10$ Hz, $Re_{mixing}=182,250$, and $T=20^\circ\text{C}$	160
Fig.IV. 47 Radial profile of tangential mean velocity (a) and its normalized profile (b) close to the upper wall ($z_1= 0.25$ mm). Operating conditions: horizontal measurements at $Q_f= 100$ L/h; water, $\mu=1$ mPa·s, $N=10$ Hz, $Re_{mixing}=182,250$, and $T=20^\circ\text{C}$	162
Fig.IV. 48 Radial profile of turbulent shear close to the upper wall ($z_1= 0.25$ mm). Operating conditions: horizontal measurements at $Q_f= 100$ L/h; water, $\mu=1$ mPa·s, $N=10$ Hz, $Re_{mixing}=182,250$, and $T=20^\circ\text{C}$	163
Fig.IV. 49 Radial profile of tangential mean velocity (a) and its normalized profile (b) close to the upper wall ($z_2= 1.5$ mm). Operating conditions: horizontal measurements at $Q_f= 100$ L/h; water, $\mu=1$ mPa·s, $N=10$ Hz, $Re_{mixing}=182,250$, and $T=20^\circ\text{C}$	163
Fig.IV. 50 Radial profile of turbulent shear close to the upper wall ($z_2= 1.5$ mm). Operating conditions: horizontal measurements at $Q_f= 100$ L/h; water, $\mu= 1$ mPa·s, $N=10$ Hz, $Re_{mixing}=182,250$, and $T=20^\circ\text{C}$	164
Fig.IV. 51 Eigenvalue spectrum. Operating conditions: horizontal measurement plane $z_2=1.5$ mm, $Q_f= 100$ L/h, $N=10$ Hz; water, $\mu=1$ mPa·s and $T=20^\circ\text{C}$, data acquisition rate 7 Hz, 3778 pairs of images.....	166
Fig.IV. 52 First mode (a) eigenvector, and (b) pdf of normalized POD coefficient. Operating conditions: horizontal measurement plane $z_2=1.5$ mm, $Q_f= 100$ L/h, $N=10$ Hz; water, $\mu=1$ mPa·s and $T=20^\circ\text{C}$, data acquisition rate 7 Hz, 3778 pairs of images	167

Fig.IV. 53 Reconstructed velocity with the first mode (POD reconstructed) compared to the statistical average of the velocity (Reynolds averaged). Operating conditions: horizontal measurement plane $z_2=1.5$ mm, $Q_f= 100$ L/h, $N=10$ Hz; water, $\mu=1$ mPa·s and $T=20^\circ\text{C}$, data acquisition rate 7 Hz, 3778 pairs of images.....	168
Fig.IV. 54 Eigenvectors related to mode 2-9. Same operating conditions with the previous figure.....	169
Fig.IV. 55 Portrait of phase between coefficients of mode 2&3, 4&5, 6&7 and 8&9. Operating conditions: horizontal measurement plane $z_2=1.5$ mm, $Q_f= 100$ L/h, $N=10$ Hz; water, $\mu=1$ mPa·s and $T=20^\circ\text{C}$, data acquisition rate 7 Hz, 3778 pairs of images.....	171
Fig.IV. 56 Portrait of phase between coefficients of mode 2&4, 2&5, 2&6 , 2&7, 2&8 and 2&9. Operating conditions: horizontal measurement plane $z_2=1.5$ mm, $Q_f= 100$ L/h, $N=10$ Hz; water, $\mu=1$ mPa·s and $T=20^\circ\text{C}$, data acquisition rate 7 Hz, 3778 pairs of images	172
Fig.IV. 57 pdf of normalized POD coefficient from mode 2 to 9. Same operating conditions with the previous figure	174
Fig.IV. 58 Instantaneous reconstructed velocity field based on mode 2 to 9. Raw data operating conditions: horizontal measurement plane $z_2=1.5$ mm, $Q_f= 100$ L/h, $N=10$ Hz; water, $\mu=1$ mPa·s and $T=20^\circ\text{C}$, data acquisition rate 7 Hz, 3778 pairs of images.....	175
Fig.IV. 59 Turbulent Reynolds and organized shear stress components (based on mode 2-9). Operating conditions: horizontal measurement plane $z_2=1.5$ mm, $Q_f= 100$ L/h, $N=10$ Hz; water, $\mu=1$ mPa·s and $T=20^\circ\text{C}$, data acquisition rate 7 Hz, 3778 pairs of images.....	176
Fig.IV. 60 Sample of cells which from '0h, 0 Hz'. Operating condition:sampling time beginning of the experiment, $N=0$ Hz, $Q_f=100$ L/h, $T=20^\circ\text{C}$. (Microscopic view $\times 100$, contrast phase, oil) Image has been rescaled.....	180
Fig.IV. 61 Sample of cells which from '5h, 50 Hz'. Operating condition:sampling time the 5 th hour of the experiment, $N=50$ Hz, $Q_f=100$ L/h, $T=20^\circ\text{C}$. (Microscopic view: $\times 100$, contrast phase, oil) image has been rescaled	181
Fig.IV. 62 PSD as a function of time for two extrem operating conditions: (a) $N=0$ Hz, $Q_f=100$ L/h, $T=20^\circ\text{C}$; (b) (a) $N=50$ Hz, $Q_f=100$ L/h, $T=20^\circ\text{C}$	182
Fig.IV. 63 Cumulative volume of particle with $dp>3.80$ μm as a function of time and mixing rate	183

Annexes

Fig.A 1 Configuration of the filtration cell.....	212
Fig.A 2 Technical design of the RVF module.....	212
Fig.A 3 Technical design of the filtration cell (Unit: mm)	213
Fig.A 4 Heat capacity, density and viscosity of BREOX solution as a function of temperature (15 to 45°C) and max concentration (0 to 100% w/w).....	213
Fig.A 5 Comparison of velocity components with two flowrates Operating conditions: $Q_f= 25$ and 45 L/h, $N=2$ Hz; $\mu=0.81$ Pa·s and $T=20^\circ\text{C}$. Measurement position: $R=45$ mm, $z=2.25$ mm	214

Fig.A 6 Evolution of mean velocity profiles U_m and their radial and angular components U_θ U_r as a function of angular position for 6 horizontal planes (z_1 to z_6) within the membrane-impeller gap. (a): IDW mean velocity at $R=30, 45$ and 65 mm; (b): mean, radial and angular velocity profiles, U_m, U_θ and U_r , at $R=65$ mm. Operating conditions: $Q_f= 45$ L/h, $N=2$ Hz; $\mu=0.81$ Pa·s and $T=20^\circ\text{C}$. Symbols: \circ , leading edge and \triangle , trailing edge of blade 214

Fig.A 7 Evolution of mean velocity profiles U_m and their radial and angular components U_θ U_r as a function of angular position for 6 horizontal planes (z_1 to z_6) within the membrane-impeller gap at $R=65$ mm. (a) U_m , (b) U_θ and c U_r . Operating conditions: $Q_f= 25$ L/h, $N=10$ Hz; $\mu=0.81$ Pa·s and $T=20^\circ\text{C}$. Symbols: \circ , leading edge and \triangle , trailing edge of blade 215

Fig.A 8 Evolution of mean velocity profiles U_m and their radial and angular components U_θ U_r as a function of angular position for 3 flowrate ($z=2.25$ mm) within the membrane-impeller gap. (a) U_m , (b) U_θ and c U_r . Operating conditions: $Q_f= 50, 100$ and 150 L/h, $N=10$ Hz; water, $\mu=1$ mPa·s and $T=20^\circ\text{C}$. Symbols: \circ , leading edge and \triangle , trailing edge of blade..... 215

Fig.A 9 Evolution of mean velocity profiles U_m and their radial and angular components U_θ U_r as a function of angular position for 3 flowrate (z_1-z_6) within the membrane-impeller gap. (a) U_m , (b) U_θ and c U_r . Operating conditions: $Q_f= 50$, and 150 L/h, $N=10$ Hz; water, $\mu=1$ mPa·s and $T=20^\circ\text{C}$. Symbols: \circ , leading edge and \triangle , trailing edge of blade..... 215

Fig.A 10 Portrait of phase between coefficients of mode 2 and the given modes. Operating conditions: horizontal measurement at plane $z_2=1.5$ mm, $Q_f= 50$ L/h, $N=2$ Hz, $Re_{\text{mixing}}=42$; BREOX solution, $\mu=0.85$ Pa·s and $T=20^\circ\text{C}$, data acquisition rate 7 Hz, 1000 pairs of images..... 216

Fig.A 11 Portrait of phase between coefficients of mode 3 and the given modes. Operating conditions: horizontal measurement at plane $z_2=1.5$ mm, $Q_f= 50$ L/h, $N=2$ Hz, $Re_{\text{mixing}}=42$; BREOX solution, $\mu=0.85$ Pa·s and $T=20^\circ\text{C}$, data acquisition rate 7 Hz, 1000 pairs of images..... 217

Fig.A 12 Portrait of phase between coefficients of mode 4 and the given modes. Operating conditions: horizontal measurement at plane $z_2=1.5$ mm, $Q_f= 50$ L/h, $N=2$ Hz, $Re_{\text{mixing}}=42$; BREOX solution, $\mu=0.85$ Pa·s and $T=20^\circ\text{C}$, data acquisition rate 7 Hz, 1000 pairs of images..... 218

Fig.A 13 Portrait of phase between coefficients of the given modes. Operating conditions: horizontal measurement at plane $z_2=1.5$ mm, $Q_f= 50$ L/h, $N=2$ Hz, $Re_{\text{mixing}}=42$; BREOX solution, $\mu=0.85$ Pa·s and $T=20^\circ\text{C}$, data acquisition rate 7 Hz, 1000 pairs of images..... 219

Fig.A 14 Reconstructed velocity field based on the related organized motions. Operating conditions of the raw data: horizontal measurement at plane $z_2=1.5$ mm, $Q_f= 50$ L/h, $N=2$ Hz, $Re_{\text{mixing}}=42$; BREOX solution, $\mu=0.85$ Pa·s and $T=20^\circ\text{C}$, data acquisition rate 7 Hz, 1000 pairs of images..... 220

Fig.A 15 Portrait of phase between coefficients of given mode. Operating conditions: horizontal measurement plane $z_2=1.5$ mm, $Q_f= 100$ L/h, $N=10$ Hz; water, $\mu=1$ mPa·s and $T=20^\circ\text{C}$, data acquisition rate 7 Hz, 3778 pairs of images 221

Fig.A 16 Portrait of phase between coefficients of given mode. Operating conditions: horizontal measurement plane $z_2=1.5$ mm, $Q_f= 100$ L/h, $N=10$ Hz; water, $\mu=1$ mPa·s and $T=20^\circ\text{C}$, data acquisition rate 7 Hz, 3778 pairs of images 222

Fig.A 17 Portrait of phase between coefficients of given mode. Operating conditions: horizontal measurement plane $z_2=1.5$ mm, $Q_f= 100$ L/h, $N=10$ Hz; water, $\mu=1$ mPa·s and $T=20^\circ\text{C}$, data acquisition rate 7 Hz, 3778 pairs of images 223

Fig.A 18 Portrait of phase between coefficients of given mode. Operating conditions: horizontal measurement plane $z_2=1.5$ mm, $Q_f= 100$ L/h, $N=10$ Hz; water, $\mu=1$ mPa·s and $T=20^\circ\text{C}$, data acquisition rate 7 Hz, 3778 pairs of images 224

Fig.A 19 Reconstructed velocity field based on the related organized motions. Operating conditions of the raw data: horizontal measurement plane $z_2=1.5$ mm, $Q_f= 100$ L/h, $N=10$ Hz; water, $\mu=1$ mPa·s and $T=20^\circ\text{C}$, data acquisition rate 7 Hz, 3778 pairs of images..... 225

List of tables

Chapter II: Literature review on Dynamic Filtration modules

Table II. 1 Top 5 most productive journals considering the number of articles and citations (source: Web of Science category of journals).....	15
Table II. 2 Top 5 most productive authors (source: Web of Science category of journals).....	15
Table II. 3 Top 5 research categories with the most important number of articles (source: Web of Science category of journals).....	16
Table II. 4 Top 5 most productive countries (source: Web of Science category of journals)	16
Table II. 5 Top 10 most productive institutions (source: Web of Science category of journals).....	17
Table II. 6 Classification and specification of DF modules	21
Table II. 7 Dimensionless numbers used to describe hydrodynamic within Dynamic Filtration device (s: gap, r : radius, ω : angular velocity, μ : viscosity, ρ : density, Q_f : flowrate)	36
Table II. 8 Core velocity coefficient of different DF filters	45
Table II. 9 Four different flow regimes in a rotation system.....	47

Chapter III: Materials and Methods

Table III. 1 Devices and materials used in all experiments.....	60
Table III. 2 Operating procedure of RTD experiment	72
Table III. 3 Operating conditions	80
Table III. 4 Acquisition parameters of PIV system (horizontal measurement)	81
Table III. 5 Acquisition parameters of PIV system (vertical measurement)	81

Chapter IV: Results and Discussions

Table IV. 1 Overview of obtained and discussed results in Chapter IV	96
Table IV. 2 Operating conditions and calculated RTD parameters in laminar flow (SD: standard deviation).....	102
Table IV. 3 Operating conditions and calculated RTD parameters in turbulent flow(SD: standard deviation)	103
Table IV. 4 J value in Model 3.....	112
Table IV. 5 Value of the parameters deduced from velocity measurements (N=2 and 10 Hz for example).....	145

Annexes

Table.A 1 Specification of the existing industrial DF filters.....	209
Table.A 2 Operating conditions of PIV (all experiments)	211

Nomenclature

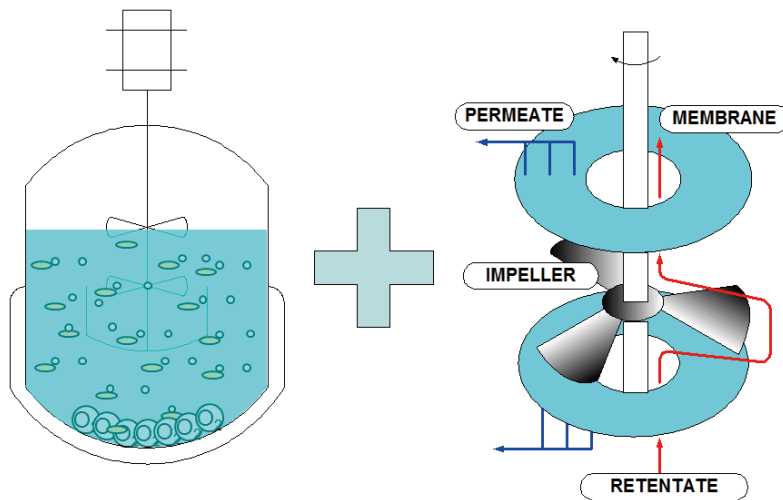
Latin Letter		
$a_k^{(I)}$	Instantaneous (k) scalar (POD coefficient of I^{th} mode), $a_k^{(I)} = \overrightarrow{U}_k \cdot \overrightarrow{\Phi}^{(I)}$	[/]
a, b, c, d	Coefficient of fluid properties calculation	
C	Conductivity	[mS/cm]
C_p	Specific heat capacity	[J/ (kg·°C)]
Da	Darcy number (friction number)	[/]
d_h	$d_h = \frac{4S}{P}$, Equivalent diameter	[m]
d_m	Diameter of the impeller	[m]
Ea	Activation energy	[kJ/mol]
$E(t)$	Residence time distribution with a perfect injection	[1/s]
$F(t)$	Cumulative function based on E(t)	[/]
h_i	Distance from reference points to the interpolation point	[mm]
I	Number of image pair	[/];
IC	Current in power consumption	[A]
K_θ	Core velocity coefficient	[/]
n	Number of the reference points	[/]
N	Rotation frequency of the impeller	[Hz]
Np	Power consumption number	[/]
J	Number of mixing cells	[/]
N	Rotation speed	[Hz]
Np	Power consumption number	[/]
p	Power index	[/]
P_{in}	Inlet pressure	[Pa]
P_{out}	Outlet pressure	[Pa]
PeL	Peclet number	[/]
Q_f	Feeding flowrate	[L/h]
r	Radial coordinate	[mm]
R	Universal gas constant, 8.314 J/(mol °C)	[J/(mol °C)]
Ri	Internal radius of the RF module = radius of the shaft	[mm]
Re	External radius of the RVF module	[mm]
Re_{mixing}	$Re_{mixing} = \frac{\rho N d_m^2}{\mu}$, Reynolds number for a mixing system	[/]
Re_Q	$Re_Q = \frac{\rho u_r d_h}{\mu}$, Reynolds number for a system equivalent to a tube	[/]
S	Skewness	[/]
ts	Mean residence time	[s]
T	Temperature	[°C]
T_{extcyl_upper}	Torque at the external cylinder on the upper wall	[N.m]
T_{extcyl_lower}	Torque at the external cylinder on the lower wall	[N.m]
$T_{extcyl_impeller}$	Torque at the external cylinder on the impeller area	[N.m]

T_{extcyl}	Torque at the entire external cylinder wall	[N.m]
$T_{upper\&lowerwalls}$	Torque on the upper wall and the lower wall	[N.m]
$T_{extcyl_{total}}$	Total torque at the external cylinder wall	[N.m]
TMP	TransMembrane Pressure	[bar]
U	voltage	[V]
$\vec{U}_k^{(i)}$	Instantaneous velocity vector in POD analysis, k here is the number of image pairs	[m/s]
U_i	General expression of instantaneous velocity, $U_i = \bar{U}_i + \tilde{u}_i + u'_i$	[m/s]
\bar{U}_i	Mean velocity	[m/s]
\tilde{u}_i	Organized fluctuation	[m/s]
u'_i	Turbulent fluctuation	[m/s]
\bar{U}_m	Mean velocity magnitude	[m/s]
\bar{U}_θ	Mean angular velocity	[m/s]
\bar{U}_r	Mean radial velocity	[m/s]
\bar{U}_z	Mean vertical velocity	[m/s]
U^*	Friction velocity	[m/s]
$\overline{U_\theta' U_z'}$	Mean Reynolds (fluctuating) shear at vertical plane	[m ² /s ²]
$\overline{U_\theta' U_r'}$	Mean Reynolds (fluctuating) shear at horizontal plane	[m ² /s ²]
u	Velocity vector in x direction	[m/s]
v	Velocity vector in y direction	[m/s]
$V1, V2$	Effective volume and dead-zone volume, $V1+V2=VRVF$	[L]
$VRVF$	Total volume of RVF module, 1.47 L	[L]
w	Velocity vector in z direction	[m/s]
w_j	Weight factor	[/]
x	x coordinate	[mm]
$x(t), y(t)$	Experimental residence time distribution of inlet and outlet	[1/s]
$X(t), Y(t)$	Cumulative function for inlet and outlet	[/]
$X(s), Y(s), G(s)$	Laplace transform function of $x(t)$, $y(t)$ and $E(t)$	[/]
x -y plane	Horizontal plane parallel to the impeller surface	[/]
x -z plane	Vertical plane perpendicular to the impeller surface	[/]
y	y coordinate	[mm]
z	z coordinate	[mm]
Greek symbol		
μ	Viscosity	[Pa.s]
ρ	Density	[kg/m ³]
β	Reduced variance $\beta^2 = \frac{\sigma^2}{t_s^2}$	[/]
τ	Holding time $\tau = \frac{Q_f}{V_{RVF}}$	[s]
Γ	Centered moment of j order	
ω	Angular velocity of the impeller	[rad/s]
θ	Angle, centered at the middle of the rotating shaft	[degree]
σ	Residence time variance	[s ²]

σ_I	Accumulative moving standard deviation of velocity magnitude, I stands for numbers of image pairs	[m/s]
τ_w	Wall shear stress; τ_{w_max} is the maximum wall shear stress	[Pa]
$\tau_{r\theta}$	Local shear stress at horizontal plane	[Pa]
$\tau_{z\theta}, \tau_{z\theta_w}$	Local shear stress at vertical plane, $\tau_{z\theta_w}$ is the shear on the wall	[Pa]
τ_{ecu}	Shear stress at the external cylinder on the upper wall	[pa]
τ_{ecl}	Shear stress at the external cylinder on the lower wall	[pa]
τ_{eci}	Shear stress at the external cylinder on the impeller area	[pa]
τ_{ec}	Shear stress at the entire external cylinder	[pa]
$\varepsilon_u, \varepsilon_l, \varepsilon_m, \varepsilon_{ul}$	Thickness of the upper gap, lower gap, the impeller and the gap between the upper wall to the lower wall	[mm]
Δ_t	Time interval between two image for one image pair	[μ s]
$\lambda^{(I)}$	The eigenvalues associated to I^{th} mode	[/]
$\overline{\Phi^{(I)}}(x, y, z)$	The eigenvector associated to I^{th} mode	[/]
Abbreviation		
CCD	Charge Coupled Device	
CF	Cross-flow	
CFD	Computational Fluid Dynamic	
CSTR	Continuous stirred-tank reactor	
DE	Dead-end (filtration)	
DF	Dynamic Filtration	
DLS	Diffraction Light Scattering	
IA	Interrogation Area	
IDW	Inverse Distance Weighting interpolation	
MF	microfiltration	
MBR	Membrane Bioreactor	
NF	nanofiltration	
OVL	Overlapping coefficient	
PES	polyethersulfone	
PF	Plug flow reactor	
PIV	Particle Image Velocimetry	
POD	Proper Orthogonal Decomposition	
PSD	Particle Size Distribution	
RMS	Root Mean Square	
RTD	Residence Time Distribution	
RVF	Rotating and Vibrating Filtration module	
UF	ultrafiltration	
Other Symbol		
Δ	Trailing edge of the impeller	[/]
O	Leading edge of the impeller	[/]

Chapter I:

Introduction



Bioreactor + RVF module

Chapter I: Introduction

Among three phase reactors, membrane bioreactors (MBR) appeared in the 70s and were largely applied in biotechnology field: pharmaceutical and food industries, white biotechnology. Increasing cell density in bioreactors is useful to improve the overall productivity of fed-batch and continuous processes particularly the biofuel production which has to be competitive according to energetic, economic and environmental criteria. Another determinant factor to optimize the overall performance of biological process is the configuration of the MBR. The performances are strongly influenced by the complex interactions between gas and liquid hydrodynamics as well as the microorganism activities [1]. The specificity of microbial bio-reactions in relation with irreducible couplings between heat, mass transfers and fluid mechanics, led to complex and dynamic systems. In addition, the clarification of fermentation broths (downstream processing) constitutes technical and scientific stakes but also social, economic and environmental challenges (ex. substitution of diatomaceous earth) in order to intensify these bioprocesses.

This PhD thesis focuses on the understanding and the control of dynamic interactions between physical and biological mechanisms considering an alternative membrane separation into bioprocess. It aims to carry scientific knowledge related to the control of bioreaction considering complex hydrodynamics and retention-permeation locks specific to membrane separation. Dynamic filtration is proposed as a technological breakthrough to dead-end and cross-flow filtrations, an alternative technology called RVF (Rotating and Vibrating Filtration) will be specifically scrutinized. Our scientific and technical aims are (1) to highlight the potentialities and constraints of RVF module for bioprocess intensification (dedicated to white and food biotechnologies) and (2) to sustain its industrial transfer. Performances criteria can be declined in terms of intensification and productivity for bioprocess, of safety and quality for liquid food issued from fermentation as well as water management and energetic efficiency in a sustainable development context.

Originality and novelty of this thesis

To this aim, a new and promising device, called Rotating and Vibrating Filtration (RVF) will be investigated. This module enables to improve overall biological and hydrodynamic performances by increasing permeability, by reducing the volume of filtration loop, by uncoupling feed flow rate and local shear rate at membrane surface and by filtering at low TransMembrane pressure (TMP). Its specificity stands in a mechanical device (impeller) close to the membranes (narrow gap) which has been introduced in order to promote turbulences at membrane surface independently of retentate flow-rate. This simple mechanical device runs continuously (up to 50Hz) and maintains a high shear rate as well as unsteady hydrodynamics at the membrane surface. The velocity and static pressure fields close to the membrane exhibit drastic variations associated with pulsating flow due to the shape and rotation of blades. These fluctuations lead to explain filtration performances considering periodic reduction/interruption of transmembrane pressure associated with unsteady generation equivalent to pulsatile flows.

Scientific and technical locks and constrains

From a hydrodynamic point of view, it is important to characterize and to locally and instantaneously quantify the velocity fields, pressure and parietal shear stresses at membrane surface, linked to the operating conditions and the rheological evolution of the fluid. This last one is indeed evolving during the bioprocess and is going to modify the hydrodynamic conditions generated by the dynamic filtration device and thus its efficiency and its performances. Investigation of hydrodynamics allows determining inappropriate conditions (back filtration area due to a negative TMP). Among the identified scientific key points to investigate, the knowledge of the pressure and velocities profiles within filtration cell enable to access to the local velocities and the permeation driving force at membrane surface. These results can be interpreted in terms of radial pressure distribution and core velocity coefficient. Local information can be qualitatively compared to the global hydrodynamic studies (power consumption and pressure drop). The large variations of speed and pressure in RVF module can be highlighted and quantified according to the operating conditions and localization in the filtration cell. Meantime the technological key points, bound either to the existence of dysfunction zones, or to the critical operating conditions can be raised. During the bioprocess, the rheological behavior of the broth may evolve as a function of concentration due to (1)

Chapter I: Introduction

Volume Concentration Factor (VCF) induced by the permeate extraction (eg. food biotechnology: rough beer clarification, wine making, dairy process), (2) the increase of microorganism concentration induced by a growth rate (eg. white biotechnologies, high cell density) or (3) the production of extra-cellular biomolecules. The rheological behavior is modified (change in viscosity, appearance of non-Newtonian behavior up to viscoelastic and viscoelastic behaviors), which affects the flow patterns within the RVF module sometimes drastically.

Scientific questions

This study takes into account these scientific locks, and scientific questions can be formulated considering global and local investigations:

- How global performances (power consumption, friction curve, heat dissipation, Residence Time Distribution) can be characterized and interpreted?
- How long will a cell suffer in such stressful environment?
- What will be the magnitude of this mechanical stress?
- Does it damage microbial cell population?
- What is the local flow pattern in the filtration cell? And how does it organize and structure in the filtration cell?
- Is it possible to identify local and instantaneous velocity and shear stress?
- Are experimental measurements and simulations consistent at global and local scales?

Scientific actions

To answer these scientific questions, it is planned to perform experiments and numerical simulations at global and local scales in laminar and turbulent regimes under biotic and abiotic conditions:

(1) For global approach, investigation of Residence Time Distribution (RTD) and thermal balance will be carried out and compared to the previous global study (power consumption and friction curves).

(2) For the local approach, Particle Image Velocimetry (PIV) will be carried out and compared to CFD simulation. PIV preliminary study will be conducted with a trigger strategy to access through angle-resolved measurements to an averaged velocity field. PIV further study will

Chapter I: Introduction

be performed with a non-trigger strategy and applied to POD analysis in order to identify the coherent structure of the flow by decomposing the organized and turbulent fluctuations.

(3) For the bioprocess application, an exploratory work will characterize the effect of Dynamic Filtration on prokaryote cell population (*Escherichia coli*) by quantifying cell integrity or damage as a function of time and rotation speed during filtration process in turbulent regime.

Thesis structure

This manuscript is based on three main parts: chapters II, III and IV.

Chapter II (Literature review on Dynamic Filtration modules) contains a review of the scientific and technical literature about DF modules from lab to industrial scales. Firstly, the general background of membrane filtration process is introduced, and the worldwide scientific production related to dynamic filtration is quantified and classified. Secondly, an exhaustive inventory of existing DF modules (lab/pilot/industrial scales) is presented and lead to identify the pertinent dimensionless number and geometrical parameters in order to compare these devices and their performances. Thirdly, the materials and methods developed to investigate global and local hydrodynamics are introduced.

Chapter III (Materials and methods) outlines the experimental set-ups and instrumentations as well as the used fluids under laminar and turbulent regimes. The associated methods of data treatment, simulation and modeling will be explained for thermal balance, Residence Time Distribution, Particle Image Velocimetry (with trigger and non-trigger strategies, on horizontal and vertical planes), Computational Fluid Dynamic and application to cell suspension.

Chapter IV (Results and Discussions) is dedicated to answer to the scientific questions, and to compare and to connect the results among different experiments and scales. This chapter includes 3 parts:

(1) Thermal balance & Residence Time Distribution (RTD)

Firstly, thermal effect in laminar and turbulent regimes will be introduced. Then RTD investigation will be presented, resulting analytical studies (including distribution and cumulative functions, moment discussion, reduced signal of outlet distribution function),

Chapter I: Introduction

systemic analysis (modeling by DTS Progepi v4.2), and simulation of streamlines by Computational Fluid Dynamic (CFD) under laminar flow.

(2) Particle Image Velocimetry (PIV)

This part is dedicated to local approach, and it is divided into two main parts: (*Chapter IV 2.1*) conditional averaging (angle-resolved measurements, fixed with trigger strategy) and (*Chapter IV 2.2*) reconstruction of organized motion based on POD processing (non-trigger strategy).

- *Chapter IV 2.1 Preliminary study-PIV with trigger strategy*

As a preliminary study, measurements are conducted in horizontal and vertical planes under both laminar and turbulent regimes. Results will be focused on presenting velocity fields and profiles analysis, and compared with CFD simulation in laminar flow.

- *Chapter IV 2.2 POD analysis (with non-trigger strategy)*

As a further study, instantaneous velocity fields will be applied to POD analysis. Velocity vectors will be decomposed into mean velocity and fluctuations. Thus, mean shear, fluctuating shear, wall shear, torque on the wall, power consumption can be deduced from these local measurements. Results will be partially compared to the global measurements previously conducted.

(3) Application to cell suspension

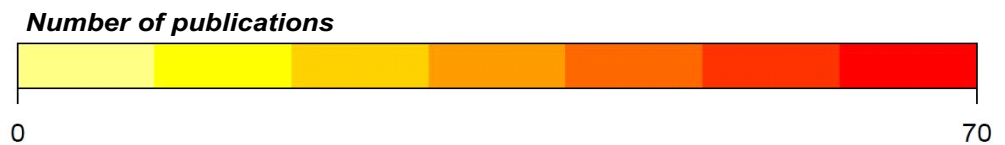
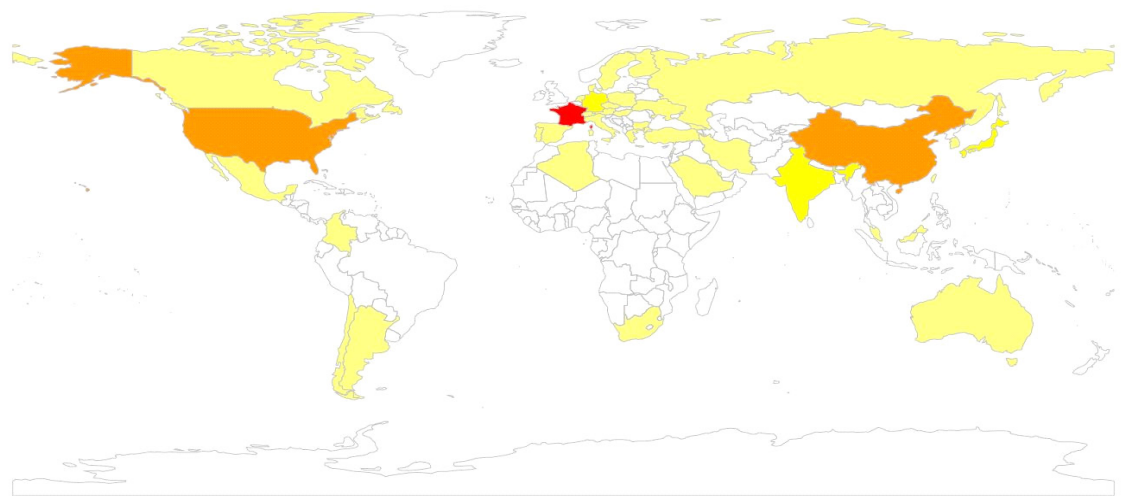
In the last part, RVF module was use to filtrate cell suspension and to characterize the mechanical impact on microbial cells. Integrity or damage of the cells will be observed and quantified.

Finally, overall conclusions of this PhD will be presented in Chapter 5.

Chapter II:

Literature review on

Dynamic Filtration modules



Number of Publications on Dynamic Filtration all over the world

Chapter II: Literature review on Dynamic Filtration modules

Dynamic filtration shows its high efficiency and productivity in separation process in advantage of high shear rate and less accumulation on the membrane surface. This technique has been well documented by numbers of literatures.

In this review, we firstly introduce the general background of membrane filtration process, and the scientific production related to dynamic filtration process.

In the second part, a full inventory and of existing Dynamic Filtration (DF) modules (lab/pilot/industrial scales) is presented, including (1) the definition and classification of DF modules, (2) geometrical complexity of DF modules, and (3) field of applications of DF.

In the third part, the current research on global and local hydrodynamics was introduced concerning on the developed methods.

From 2005 to now, newly devices appeared as the second-generation DF filter by optimizing design and scaling up. Overviewing the existing literature, works regarding on global view were perfectly done, local parameters are necessarily needed to gain insight dynamic filtration. This PhD thesis is thus motivated by the lack of knowledge:

- local and instantaneous hydrodynamics within the filtration cell
- investigation of membrane-fluids interface (local shear stress/rate)
- scale-up of DF module
- objective criteria to design DF modules and to optimize filtration efficiency

In cross-flow filtration, the aim is to reduce the impact of fouling and high fluid velocities are generally necessary to limit the growth of cake on the membrane. A large number of hydrodynamic techniques, based on fluid instabilities, have been investigated such as co-current mode, pulsating flow, periodic stop of the transmembrane pressure, periodic back-flush or a back-shock process, generation of Dean or Taylor vortices, introduction of turbulence promoters (baffled channel, stamped membrane) or the use of a two-phase flow (gas–liquid, liquid–solid). These high velocities require energy and produce large pressure drops along the membrane. Consequently, the transmembrane pressure remains high along most of the membrane, and this may limit solute transmission into the permeate when the cake layer on the membrane is compressible and is packed by pressure.

Dynamic filtration was developed in order to improve filtration performances by increasing wall shear stress at membrane surface. The specificity of dynamic filtration is that a mechanical device has been introduced in order to promote turbulence at membrane surface independently of retentate flow-rate. It consists of creating relative motion between the membrane and its housing since high shear rate produced by the relative motion are independent of the feed flow, which can be kept low. Dynamic filtration stands as a realistic alternative to dead-end and cross-flow filtration. In order to improve performances and to increase shear rate, various systems called dynamic filtration have been studied in bioprocess applications over the last decades. Dynamic filtration modules could use either a vibrating (Schneider et al., 2001) and rotating membrane [2], or the motion of a mechanical device with a rotating [3] and/or vibration disc or impeller [4,5] close to the membrane surface. Several dynamic filtration devices have been reported by manufacturer: Artisan (Artisan Industries), cross-rotational flow (ABB-Flootek), centrifugal membrane filtration (Spintek), cross-rotational membrane filtration (Komline-Sanderson), Hitachi (Hitachi), dynamic membrane filter and vibrating membrane filter (Pall society).

1 Introduction of membrane filtration process

1.1 Aim and context

Membrane separation technology has become widely used in the bioprocess and food processing industry (dairy, juice, wine, water) [6,7]. However, membrane processes are yet to be identified as an industrial alternative by users. The choice of membrane process is a multi-criteria and crucial approach including the diversities of (i) mass transfer processes (from

electro-dialysis up to microfiltration), (ii) the geometry of module (plane, filter-press, tubular, spiral wound, hollow fiber), (iii) the nature and structure of membrane (mean pore diameter and associated distribution / chemical nature: organic, mineral, metal, composite) and (iv) the operating mode (dead-end, cross-flow or dynamic filtration) and technic dedicated to fouling limitation (co-current, back-filtration, back-shock, back-flush,...). The objective aims to improve qualitative and quantitative performances of separation device while reducing fouling mechanism, in other terms the intensification and the efficiency of bioprocess. Retention could be described by mechanical and or physico-chemical retention but the mechanisms of retention result from a complex balance between the nature and structure of membranes, the local hydrodynamic conditions and the product.

Solid-liquid separation is a key operation in membrane bioreactor and in downstream bioprocessing. The efficiency and productivity of separation step will directly affect the overall productivity of the entire bioprocessing and the cost of the product. Due to the type of process (temperature, pressure, degree of automatization, sterility requirements and so on) [8], the cost of separation even covers more than a half of the total costs [9]. Ann-Sofi Jönsson and Ola Wallberg[10] estimated the cost in a kraft lignin recovery process by ultrafiltration, recovered from cooking liquor and black liquor. Operating costs (included electricity cost, membrane replacement cost, maintenance and labor cost) were 950 and 2200 k€/year out of total cost 1810 and 3590 k€/year respectively.

The main differences between the conventional dead-end filtration (perpendicular feed), crossflow filtration (tangential feed) and dynamic filtration (arbitrary feed) are illustrated in Figure 1. In Cross-Flow Micro-Filtration, a dynamic selective layer (particle in suspension, macromolecules, complex) is created and plays an important role in retention mechanism. The propensity of retention, the contribution of the different mechanisms, how mechanisms interplay on soluble and insoluble fractions, the quantification of the fouling layer composition are investigated and are of highly scientific interests [11-15]. In conventional cross-flow filtration, high fluid velocities are generally necessary to limit the growth of cake on the membrane. These high velocities require energy and produce large pressure drops along the membrane. Consequently, the transmembrane pressure remains high along most of the membrane, and this may limit solute transmission into permeate when the cake layer on the membrane is

compressible and is packed by pressure. Dynamic filtration, which consists of creating relative motion between the membrane and its housing, avoids this problem since high shear rate produced by the relative motion are independent of the feed flow, which can be kept low. Among advantages to improve overall biological and hydrodynamic performances, the increase of permeability, the reduction of the filtration loop volume, the uncoupling of feed flow rate and local shear rate at membrane surface and the filtration at low transmembrane pressure can be mentioned. This thesis is designed to highlight the potentialities and constraints of an innovating dynamic filtration device, called Rotating and Vibrating Filtration (RVF technology – patent no. FR-97-14825) will be investigated under hydrodynamic angle for industrial and food biotechnologies in order to intensify separation step while controlling bioreaction.

Realizing the barriers, researchers have devoted great effort to clean and proceed with contaminated membrane, which can sustain high flux and against flux decline. All those way can be typically physical, chemical and biological cleaning both in-situ (online) and ex-situ (offline) [16], including (1) physical cleaning: periodic or continuous backwash [17] or pulsation [18] by the flow ; sweep the membrane surface by different ancillaries, e.g., brush-like or blade-like device, high aeration [19,20], ultrasound [21]; destabilize the cake layer by generating shear stress close to membrane, will be reviewed in detail. (2) chemical cleaning: apply cleaning detergent like surfactant[22]. (3) biological cleaning: enzymatic cleaning agent[23], though less use than the former.

According to the pore size of the membranes, different kinds of membrane filtration can be mainly classified into microfiltration (MF, 0.1-10 μm), ultrafiltration (UF, 1-100 nm), and nanofiltration (NF, 1-10 nm /200-600 Da). Understanding the mechanic movement and fluid behaviors of the flow, membrane filtration also can be categorized into Dead-end Filtration (DEF), Cross-flow Filtration and Dynamic Filtration (DF). Fig.II. 1 illustrates the main difference among the conventional Dead-end Filtration (perpendicular feed), Cross-flow Filtration (tangential feed) and Dynamic Filtration (arbitrary feed). Cross-flow and dynamic filtration (matched with the proper pore size membrane) have been widely developed in lieu of dead-end filtration or centrifugation, mainly because the former allow contamination removal and relatively high efficient separation.

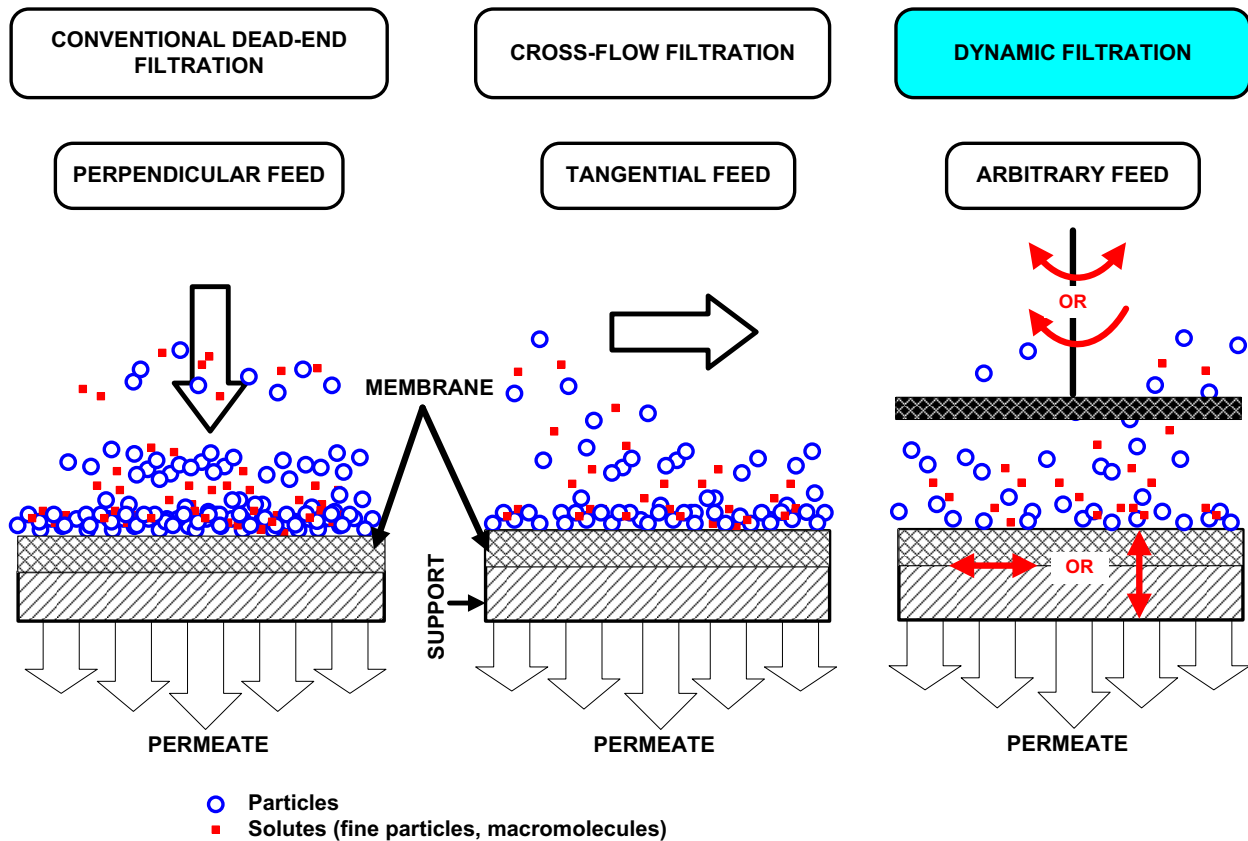


Fig.II. 1 Comparison between Dead-end (DEF), Cross-flow (CF) and dynamic (DF) filtration.

Cross-flow filtration (also known as tangential flow filtration) was typically designed to reduce the impact of fouling by applying a tangential feeding flow passing over the membrane and remove some of deposit from the surface. The contribution of this kind of fouling removal is the shear stresses imposed to the membrane surface and reduce the cake layer, enhance permeability and allow selectivity to be determined by the membrane itself instead of by the layer that forms on the membrane surface. Increasing the feeding flow rate driven by the pump is one of the conventional ways to enhance performance in Cross-flow filtration but consuming rapid increase of pumping power, which is approximately proportional to the cube of flow rate in turbulent flow regime.

However, Dynamic Filtration, also named Shear Enhanced Filtration, appears as a promising and alternative way to those conventional filtrations, which are currently not efficient enough. What makes this system different from the conventional filtration type is that, in the filtration cells, the system consists in creating and promoting the shear rate at the membrane surface by a mechanical part, such as a disk rotating near a fixed membrane, rotating or vibrating

membranes, able to generate high shear rates approximately up to $1-3 \times 10^5 \text{ s}^{-1}$ without large feeding flow rates [24,25]. Taking advantage from this technology, Dynamic Filtration performs its outstanding behaviors in permeability and productivity, leads to a considerably effective and economical process; we highlight its specialty as the following:

- 1- Enhances shear rate on the membrane surface;
- 2- Uncoupled shear rate and TMP from feeding flowrate;
- 3- Relatively low TMP is required;
- 4- Reduce membrane fouling and concentration polarization;
- 5- Less volume of working liquid;
- 6- Considerably energy-saving;

Nevertheless, the drawback is 1) the complex configuration of the filtration device that might lead to higher equipment cost, especially when scaling up. 2) And the limited filtration area that might hold-up the development of productivity.

1.2 Scientific production related to DF

A database interrogation[26] was carried out to review scientific publication and gain insight into research hotspot, information are concerning on (1) number of publications, (2) the most productive journals, (3) the most productive authors, (4) researcher areas, (5) countries and cooperation among them, (6) institutes and cooperation among them, and (7) application fields. This review mainly respects to the publications given by the following methodology:

- Database: Web of Science.
- Advanced search for: TS=(dynamic filtration) and TS=(membrane) and TS=(high shear or shear enhanced or rota* or vibra* or oscilla*)
- Field and time span: Web of Science Core Collection, from 1975 to 2017.
- Updated: Feb.07th 2017.

(1) Number of publications per year

A total of 195 articles on the topic “dynamic filtration” and “shear enhanced filtration” (DF in short thereafter) were found including 4 document types i.e. articles (185, 94.87 %),

proceedings papers (19, 9.7 %), reviews (8, 4.1 %), and book chapter (2, 1.0 %). Fig.II. 2 shows the annual numbers of DF related articles from 1990 to 2015. During the period 1979-1990, average of annual numbers of articles was less than 1. This average number increased rapidly since then, from 4.4 ± 1.6 during 1991-2001 to 12.0 ± 3.0 during 2002-2015, which indicating a development trend of research on DF topic. Among these publications, 99 articles are related to DF module studies.

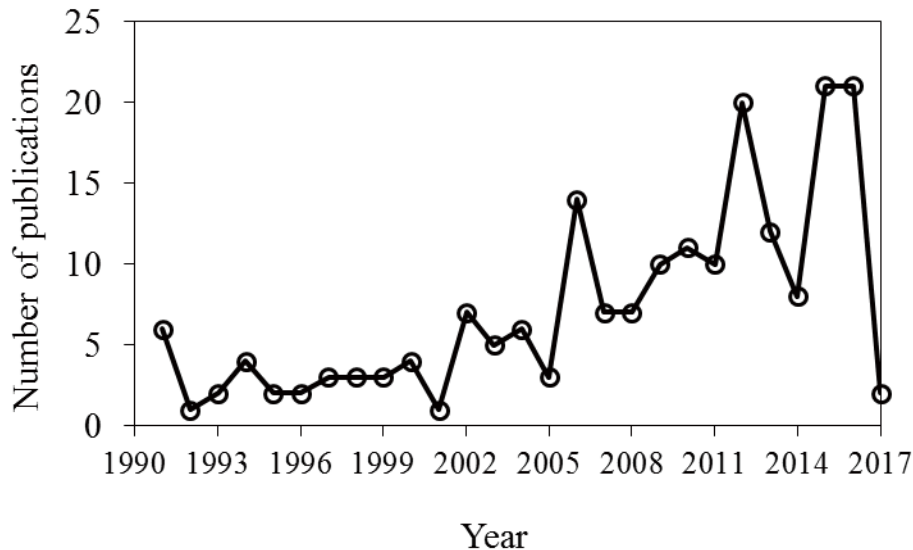


Fig.II. 2 Evolution of the number of publication per year

(2) Most productive journals

According to Journal Citation Reports (JCR) of 2014, the dynamic filtration articles were published by 111 journals among 51 Web of Science subject categories. The 5 most productive journals with the number of articles and categories of journals were shown in Table II. 1. *Journal of Membrane Science* ranked the first place with 23.6 % of total articles published, followed by *Desalination* published 10.8 %.

(3) Most productive authors

Of 195 articles were published by 506 authors including 163 first authors and 133 corresponding authors. Table II. 2 gives the top 7 most productive authors and their ranks as first/corresponding authors. Jaffrin MY from University of Technology of Compiègne (France) contributed the most with 38 articles, and was ranked the first place as corresponding author with

Chapter II: Literature review on Dynamic Filtration modules

25 articles. The second productive corresponding author is Ding LH from University of Technology of Compiègne (France) also, who published 35 articles with 3 of them first-authored.

Table II. 1 Top 5 most productive journals considering the number of articles and citations (source: Web of Science category of journals)

Journal	TA (P)	TC (P)	category
JOURNAL OF MEMBRANE SCIENCE	46 (23.6)	1174 (37.2)	ENGINEERING; POLYMER SCIENCE
DESALINATION SEPARATION AND PURIFICATION TECHNOLOGY	21 (10.8)	282 (8.9)	ENGINEERING; WATER RESOURCES
BIOTECHNOLOGY AND BIOENGINEERING	14 (7.2)	121 (3.8)	ENGINEERING
CHEMICAL ENGINEERING RESEARCH DESIGN	7 (3.6)	132 (4.2)	BIOTECHNOLOGY & APPLIED MICROBIOLOGY
	6 (3.1)	29 (0.9)	ENGINEERING

*TA: Total article; TC: Total citation; P: percentage (%)

Table II. 2 Top 5 most productive authors (source: Web of Science category of journals)

Author	TA(P)
JAFFRIN MY	38 (19.5)
DING LH	35 (18.0)
FRAPPART M	10 (5.1)
BHATTACHARJEE C	9 (4.6)
AKOUM O	7 (3.6)
FANE AG	7 (3.6)
SARKAR D	7 (3.6)

*TA: Total article; P: percentage (%)

(4) Research areas

Table II. 3 shows the top 5 categories with the most articles. Engineering (in general) was ranked 1st with 150 (77.0 %) articles. Polymer Science and Water Resources were ranked 2nd and 3rd with 49 (25.1 %) and 37 (19.0 %) articles respectively. Other categories e.g. Chemistry, Mechanics and Physics, Energy & Fuels, Environmental Science & Ecology were also found in the dynamic filtration topic.

Table II. 3 Top 5 research categories with the most important number of articles (source: Web of Science category of journals)

Category	TA(P)
ENGINEERING	150(77.0)
POLYMER SCIENCE	49(25.0)
WATER RESOURCES	37(19.0)
BIOTECHNOLOGY & APPLIED MICROBIOLOGY	20(10.3)
CHEMISTRY	16(8.2)
ENVIRONMENTAL SCIENCES & ECOLOGY	16(8.2)

*TA: Total article; P: percentage (%)

(5) Most productive countries and cooperation among them

In total, 184 institutions from 40 countries/territories published articles on dynamic filtration topic. Table II. 4 lists the top 5 most productive countries with total number of articles. France was ranked the first place with 52 (26.7 %) articles published, followed distantly by USA and China with 28 (14.4 %) and 23 (11.8 %) articles respectively. The articles from the three countries account for 52.8 % of all articles from the world. In total, the number of internationally cooperative articles was 32 (14.2 %) involved by 27 countries/territories. Fig.II. 3 shows the cooperative network among top 20 most productive countries. The size of node indicates the number of articles participated by the country, while the thickness of line connecting the nodes represents the number of articles cooperated by the two countries. It is shown that both France and USA have the most four partners. Among these intimate relationships, the one between France and China was the most, followed by the ones between France and Algeria, USA and South Korea. Besides, France is the only international partner for China. Denmark, Poland, Spain, Russia and Austria were the countries have no international relationships yet among the top 20 countries.

Table II. 4 Top 5 most productive countries (source: Web of Science category of journals)

Country	TA(P)
FRANCE	52(26.7)
USA	28 (14.4)
PEOPLES R CHINA	23 (11.8)
AUSTRALIA	13 (6.7)
JAPAN	12 (6.2)
INDIA	11 (5.6)
SOUTH KOREA	11 (5.6)

*TA: Total article; P: percentage (%)



Fig.II. 3 Cooperation network among top 20 most productive countries (source: Web of Science category of journals)

Table II. 5 Top 10 most productive institutions (source: Web of Science category of journals)

institution	TA(P)
UNIV TECHNOL COMPIEGNE	41(20.9)
JADAVPUR UNIV	8 (4.1)
DALIAN UNIV TECHNOL	7 (3.6)
UNIV CALCUTTA	7 (3.6)
UNIV NEW S WALES	7 (3.6)
NAGOYA UNIV	6 (3.1)
NANYANG TECHNOL UNIV	5 (2.6)
UNIV ROVIRA VIRGILI	5 (2.6)
NORTHWESTERN UNIV	4 (2.0)
SEOUL NATL UNIV	4 (2.0)

*TA: Total article; P: percentage (%)

(6) Most productive institutes and cooperation among them

Table II. 5 shows the top 10 most productive institutions with the same indicators. The leading institution is University of Technology of Compiègne (France), which published the most articles accounting for 20.9 % of the total and more than half of them were not cooperative articles. Jadavpur University (India) remotely followed with 8 articles published. Table II. 5

Chapter II: Literature review on Dynamic Filtration modules

shows the cooperation among institutes, two close Chinese partners of University of Technology of Compiègne (France) were Chinese Academy of Science and Dalian University of Technology. The strong bilateral cooperation between University of Calcutta (India) and Jadavpur University (India), University of New South Wales (Australia) and Nanyang Technological University (Singapore) were observed.

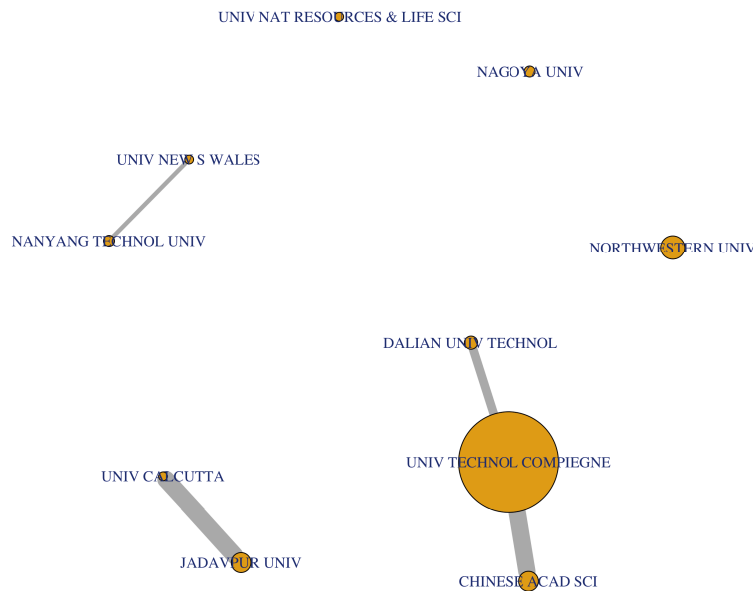


Fig.II. 4 Cooperation network among top 10 most productive institutions (source: Web of Science category of journals)

(7) Overview of application field, methodology and scientific locks

According to the articles which was introduced in the previous section, those 99 related articles indicate that Dynamic filtration are mainly applied in three domain including Water treatment, Food engineering and Biological engineering & Biomedicine. In this bibliographic analysis, 36 out of 99 scientific publications scientific articles (36.5%) are concerning Water treatment. Researchers would like to employ DF membrane technique to treat industrial wastewater, municipal wastewater and drinking water, test fluid are mostly sampling from the related treatment plant, whereas some of them are simulated in laboratory. Besides, 25 scientific articles (25.9%) are applied with DF membrane technique in Food engineering, tested with milk, beer, and juice etc. Presented in Biological engineering & Biomedicine, 25 scientific papers (25.9%) was carried out preferably with DF modules, most of the test fluids are biotic

suspensions such as microalgal suspension, yeast suspension, fermentation broth etc., as well as Bovine serum albumin (BSA) and plasma suspensions.

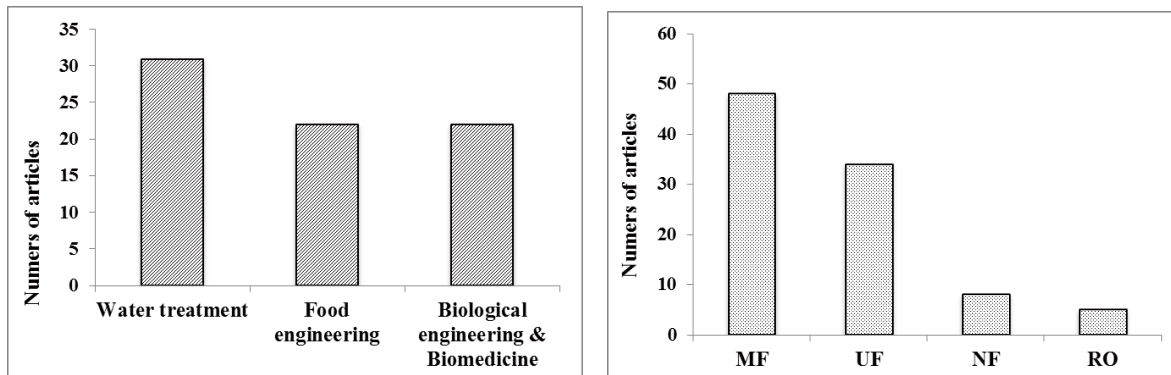


Fig.II. 5 Small overview of application field and filtration type in Dynamic Filtration

Based on those related articles (99 articles are related to DF module), MF was found to be the most popular type among numerous researches, 55 scientific articles (56.5%) are done by employing MF membrane to DF modules, they are mainly concerning on large suspended solids removal such as biotic suspension (cell harvest, yeast suspension, microalgal suspensions), mineral suspension, sludge dewatering etc. And 39 papers (40%) reported UF membrane application in DF modules tested with skim milk, soymilk, juice surfactant solution, BSA suspension, and oily emulsions etc., presented a high efficiency of Chemical Oxygen Demand (COD) and Biological Oxygen Demand (BOD) removal. 8 and 5 papers introduced NF and RO respectively, these two types are mostly used for deeper treatment of separation, such as dissolved metals removal, salts removal, and drinking water purification.

2 Specification and Application of Industrial and Commercial Dynamic Filtration Module

In the recent decades, many efforts and a great number of those studies have been done to develop novel DF module, in lab scale or pilot scale. Reviewing the existing DF modules by our best of knowledge, they can be mainly classified by mobile membrane and stationary membrane in terms of membrane state. And also can be classified by rotation system, which means working fluid is driven by a rotor (disk, disk-like membrane, impeller, arms etc.), and vibration system (some defined as oscillation), which has an external force applied to the system longitudinally, transversely, torsional, or with a mix of these motions.

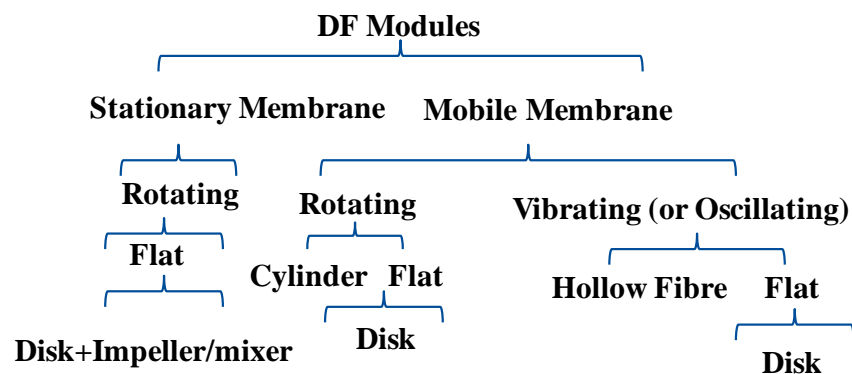


Fig.II. 6 Classification of DF modules according to the membrane motion

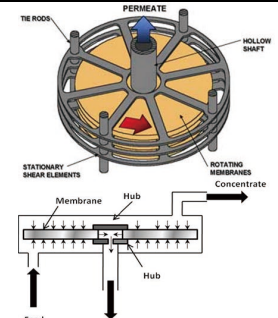
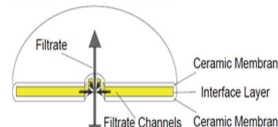
Though the module configuration is of a crucial effect on separation efficiency, membrane material plays a key role and has an inherent impact in the process. Membrane characteristic always refers to pore size, surface charge, roughness and hydrophobicity, etc., which links to its material properties. In terms of material, membrane can be mostly grouped into polymeric, inorganic or composite. Benefit from different advantages of various materials, Dynamic Filtration combined particular membrane shows its great filtration ability to many application field, such as Wastewater Treatment, Food Engineering, Pharmacy and Biological process.

As the most widely used in membrane filtration, organic membrane often refers to polymeric membranes, which are more conventionally used. Among the existing dynamic filtration modules, most of them were applied with organic membranes. They are mostly made from natural polymers include Cellulose, rubber, wool etc., and synthetic polymers include Nitrocellulose, Polytetrafluoroethylene (PTFE), Polyethersulfone (PES), Polyvinylidene Fluoride (PVDF), Polycarbonate Track Etched (PCTE), Polyester Track Etched (PETE), Polypropylene

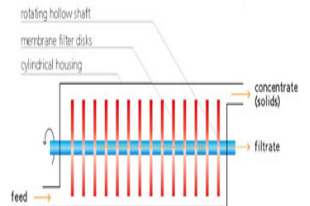
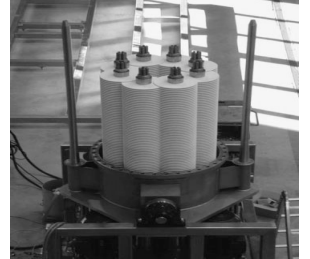
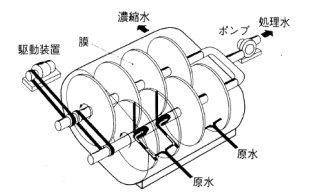
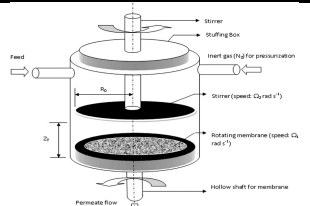
Chapter II: Literature review on Dynamic Filtration modules

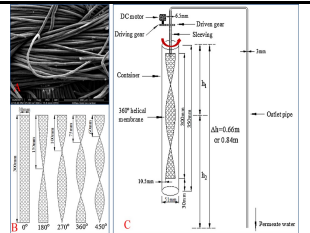
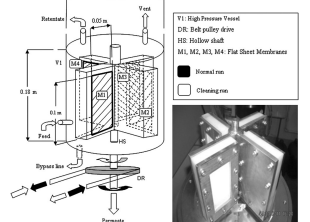
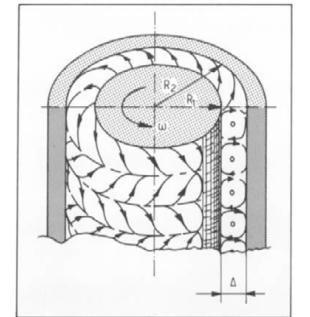
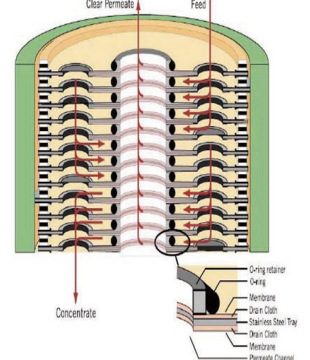
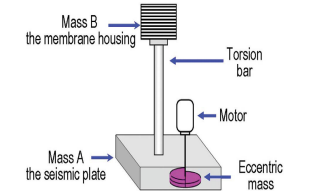
(PP), Nylon, etc., which are lower price and more frequently used. Due to their chemical structure, organic membranes have advantages such as easy forming, higher flexibility, hydrophobic and affinity of fouling[27]. Inorganic membrane is made from ceramic, carbon, silver, silica, zeolite, titania [28] and metals such as palladium, silver and their alloys. In comparison with polymeric membrane, inorganic membrane exhibits a better stability, duration, mechanical strength, regeneration, high tolerance of extreme conditions (heat, high-pressure, acid and basis environment)[27].

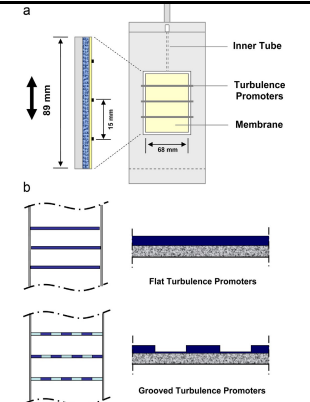
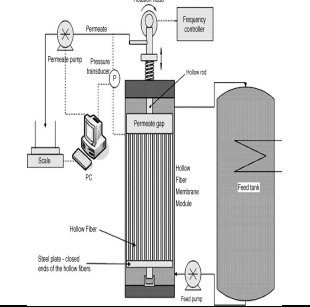
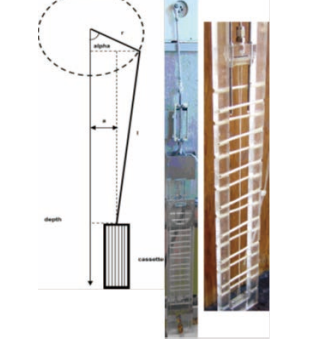
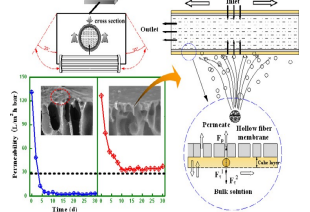
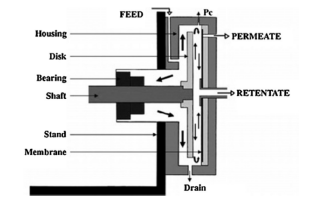
Table II. 6 Classification and specification of DF modules

Technology			Manufacturer	Model	Diagram	Ref
Membrane movement	Mechanical movement	Shape of membrane				
Mobile membrane	Rotating	Disk	Spintek, Huntington Beach, CA, USA	Spintek ST II		[8,29,30]
			SpinTek, Los Alamitos, CA	High shear rotary membrane system (HSR-MS)		[31]
			ANDRITZ KMPT (Vierkirchen, Germany), membrane supplier: KERAFOL	DCF (Dynamic membrane filtration)		[8,32,33]
			Diva Envitec Pvt. Ltd., India	MSDF (modular spin disk filtration)	 	[34]

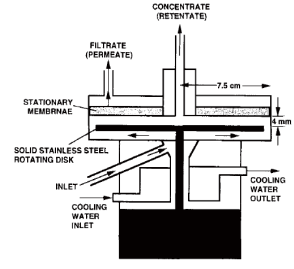
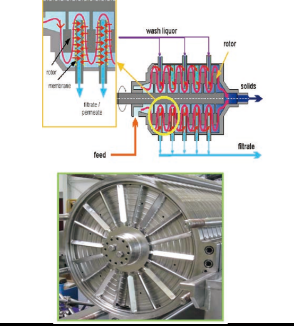
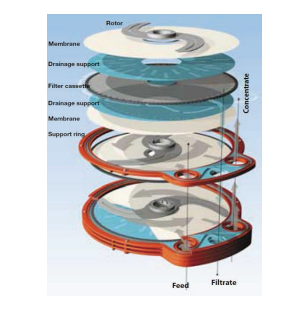
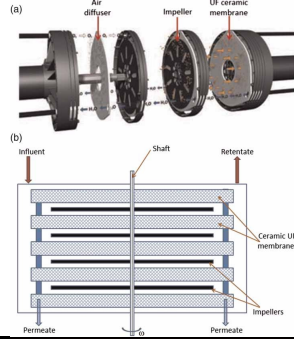
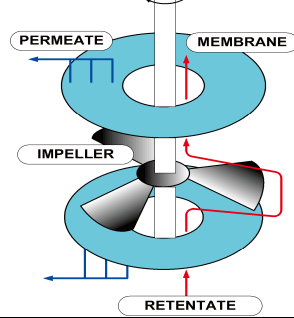
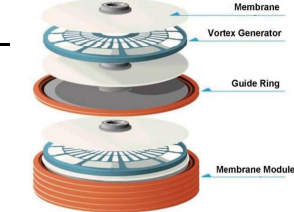
Chapter II: Literature review on Dynamic Filtration modules

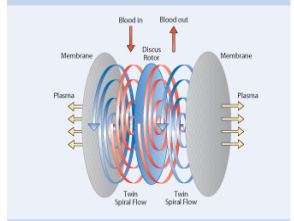
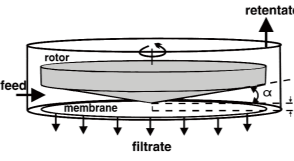
			Fraunhofer IGB, Germany, membrane supplier: KERAFOL	Rotating disk filter		[35]
			Westfalia Separator, Aalen, Germany	MSD (Multi Shafts disks)		[8,33,36]
			Mio Vigneto Products (Automatic Filter System)	Rocket M7 Rocket M7+7		[37]
			Hitachi, Japan	AQUA UFO		[8]
			Novoflow (Oberndorf, Germany)	SSDF (Single Shaft Disk Filter) -1-312 SSDF-2-312 CRD 0.1 lab /0.5 lab (Compact rotating disk filters)		38]
			HUBER (Berching, Germany), Vacuum Rotation Membrane VRM® Bioreactor	VRM 20 VRM 30		[39]
			Gurpreet Engineering Works, Kanpur, UP (India) according to specified design	Rotating disk-membrane (RDM)		[40,41]

		Helical	Dalian University of Technology			[42]
	Flat rectangular sheet	Spinning basket membrane (SBM)	Gurpreet Engineering Works, Kanpur, UP (India)			[43-46]
			Hemascience, Santa Ana, CA, USA	Plasmacell filter		[30]
	Cylinder		Suker AG, Winterthur, Switzerland	Biodruck-filter (BDF-01)		[47]
Vibrating	Disk		New Logic, CA, USA	VSEP series L		[48-50]
			Pall Corp., USA, VMF (Vibrating Membrane Filtration)	VMF-PALLsep PS 50 VMF-PALLsep PS 10 VMF-PALLsep PS 400		[30,51]

		Rectangular sheet	Chemical and Biochemical Engineering Department, Western University, London, Ontario, Canada			[52-57]
		Hollow fiber	CAPEC, Department of Chemical Engineering, Technical University of Denmark	HF membrane filter		[58-60].
			UNESCO Centre for Membrane Science & Technology, The University of New South Wales, Sydney, Australia			[61]
			Zhejiang University of Technology	Pendulum type oscillation (PTO)		[62]
Stationary membrane	Rotating	Disk membrane+ mixer	University of Technology of Compiegne	Rotating disk module (RDM)		[3,24,36,49,63-91]

Chapter II: Literature review on Dynamic Filtration modules

			Pall Corp.,USA, DMF (dynamic membrane filter)	DMF LAB6 system		[92-94]
			Bokela GmbH, Karlsruhe, Germany	DYNO		[8,30,95]
			Metso-Paper, Finland (ex- Raisio- Flootek, Finland ex- ABB Flootek, Sweden)	Optifilter CR (Cross Rotational) Filter, CR 200/1 CR250/2 CR500/5 CR550 / 15 to 30 CR500/100(CROT) CR 1000/ 26 to 60 CR 1000/10 CR 1010/70 to 100		[96-101]
			Grundfos BioBooster (Bjerringbro, Denmark)	Rotating cross-flow (RCF) MBR		[102]
			RVF Filtration, Paris, France	Rotating and Vibrating Filtration System (RVF) RVF5-FD-C RVF5-E-C RVF5-U-C RVF4-L-C RVF-Lab scale in Lisbp		[103] [4]
			FMX (Anti-Fouling Membrane Filtration)	Standard class (FMX- S100)		[104] [105]

			System), BKT water&energy	Economic class (FMX-E)		
			Miltenyi Biotec	Life 18 disk separator		[106]
			Gesellschaft für Biotechnologische Forschung mbH, Biochemical Engineering Division, Germany	Controlled shear filtration (CSF)		[107]

2.1 DF module with mobile membrane

2.1.1 Cylindrical membrane modules

Early in the 1967, Sherwood et al. [108] suggested a rotating cylinder filter in reverse osmosis for salt and water transport, consisted of inner cylinder rotating in a cylindrical stationary housing, first lead our focus on Dynamic Filtration. In ordinary rotating cylinder modules, it is always formed with two cylinders, inner one rotates inside the outer one, that means one of the surfaces moves parallel to the other thus producing shear rates in the annulus.[109]. Taking advantage from Taylor-Couette Flow in the annulus with a relatively low rotation speed, cells and macromolecules can avoid being destroyed. Consequently, rotating cylindrical DF membrane filter was quickly applied to Pharmacy and Biological process.

For example, among the early-commercialized filters, *Biodruck-filter (BDF-01, Sulzer AG, Winterthur, Switzerland)* was dedicated for cell harvesting and cell debris removal[47], with 66 mm diameter and 200 mm length inner cylinder (0.04 m² filtration area) at rotation speed up to 3000 RPM. This membrane was made from Teflon with pore size 0.2 μm and fed with fermentation broth by 5-10 L h⁻¹ within a 4 mm annular gap. Result proved that, by rotation speed at 200 RPM in BDF-01 and 4 m/s flow rate in a tubular membrane (polypropylene, 0.2 μm), the BDF-01 had 3-fold higher flux than the tubular membrane, both with initial cell concentration 3%, pressure range from 105 to 0.8 bar.

With the same concept, a *plasmapheresis filter* was employed in plasma collection. Similarly, a company ‘Mebrex’ developed a Benchmark *Biopurification System* for the steffiod recovery process[110]; *RDF filter (Rotary Dynamic Filtration)* fed with yeast suspension was

studied to realize the fouling mechanism and optimal biological fluid filtration, result was confirmed by microscopic photographs of the membrane surface[111]. Later on, another rotating concentric cylindrical filter, but with a horizontal configuration, was further developed.[112] Other similar modules also have been explored in wastewater treatment [113-115].

2.1.2 Rotating flat membrane modules

Configurations and Specifications

Among the rotary membrane modules, they typically consisted of a membrane mounted onto the porous support driven by one or more central shaft. Such support can be one or more rotary disk, arms or wings, allow a flexible configuration, led to a scale-up of filtration with larger area and capacity.

For instance, *Rotating Membrane Disk Filters (RMDFs)* [2], *Rotating Disk Membrane* [41], *Compact Rotating Disk (CRD filter)* [38], and *High shear rotary membrane system (HSR-MS)* [31] etc. are typical modules. A *stirred rotating disk module* show its innovation by apply a stirrer (rotor) to this rotating-membrane system in reversed direction, generated a high shear rate up to $2 \times 10^5 \text{ s}^{-1}$ at the membrane as well [40,116,117]. Researchers also combined this concept with external cleaning, e.g. *Vacuum Rotation Membrane (VRM, HUBER, Berching, Germany)* filtration unit was consisted with a stack of rotating membrane disk and a powerful aerator in order to clean the contaminated membrane, and also reached a large scale available with diameter approx. 2.3 and 3.2 m, membrane surface approx. 900 m² and 3840 m², design for wastewater treatment plant. Besides, another system equipped with multi-shaft (rotate in the same direction) and overlapping membrane was developed and well-studied, e.g., a two-shaft system, *Dynamic Cross-flow Filter (DCF)* commercialized and made by *KMPT* was tested in biofuel process[32]. Another two shafts filter, a lab scale *MSD (Multi-shaft disk Westfalia Separator, Aalen, Germany) module* studied by Ding et al., permeate flux is one fold higher than that consist of a stationary membrane module in the same disk azimuthal rim velocity. It has also been proved that the overlapping gap was where the maximum shear rate was generated[36]. A larger *MSD system*, commercialized by *Westfalia Separator*, with 8 shafts and fixed a pile of membrane-disk, all shaft and membrane-disk rotate in the same speed. Recently, some newly devices emerged. *Spinning basket membrane (SBM)* was developed by Sarkar.A et al., flat rectangular membrane was fixed to the alternative side of the 4 (could be more) radial hollow

arms, which are driven by a shaft and allow permeate to pass. This system composed a membrane filtration cycle when rotate as a normal run, and a membrane cleaning cycle when rotate in the reverse direction [43-46]. A newly helical lab-scale filter was constructed in a cylinder container, dynamic membranes were twisted in different helical angles (0° , 180° , 270° , 360° and 450°), continuously rotated with 75 and 160 RPM [42,118].

Applications using inorganic membranes

Bendick et al. [31] used a high shear rotary membrane system (HSR-MS, Spin- Tek, Los Alamitos, CA) in microfiltration to treat shipboard wastewater. It is of 0.08 m^2 filtration area and 267 mm diameter of ceramic membrane. An artificial Bilge water containing fuel oil, lubricants, detergents, dust, and lint and black water, which are similar to municipal wastewater, were used with this pilot single-shaft system. They found firstly a high dependency of steady state flux J_{ss} on ω and D in a range of 10 to $433 \text{ L/m}^2\text{h}$. Secondly, they believed that γ and Re were as a function of steady state flux J_{ss} respectively, highly dependent on angular velocity ω and membrane diameter D . and they proved that the relationship of $J_{ss}-Re$ and $J_{ss}-\gamma$ model was indeed existed, J_{ss} relationship was somehow correlated better with γ in both test fluids. And the $J_{ss}-\gamma$ model was extended to large membranes (312 and 374 mm) for prediction, resulting that lager disk can produce similar or somehow greater permeate output when system rotated at lower speed.

Ebrahimi et al. [38] employed the lab scale membrane module CRD 0.1 (Novoflow, Oberndorf, Germany) in MF and UF, it consisted of a ceramic membrane disk driven by a hollow shaft. They assessed the effect on permeability and quality by some operating parameters. Resulting that for both MF and UF ceramic membrane, the permeate flux was dependent on the rotation speed, and they both performed well by high rejection of oil ($>99\%$) and TOC ($>98\%$) in dewatering process water and oily test fluid. Additionally, this rejection was proved to be somehow independent of membrane rotation speed, by testing with 1200, 1500 and 1800 RPM.

Rios et al. [32] used a 152 mm membrane diameter and two-shaft module DCF 152/0.14, a commercial module made by KMPY (Krauss Maffei Process Technology), with filtration area 0.14 m^2 . Two types of MF membranes, PTFE and ceramic, and three microalgal species were tested in this research. The result indicated that, firstly, best result could be achieved after a pre-concentration step, with TMP about 1 bar, pore size of $0.5 \mu\text{m}$ (rather than 0.2), at 100% of the

module capacity (1110 RPM). Secondly, with the optimized process variables, pilot experiments were carried out and able to arrive concentration factor up to 200 and permeability up to $600 \text{ L h}^{-1} \text{ m}^{-2} \text{ bar}^{-1}$. An economic study was also done to prove that, after pre-concentration, which was a sedimentation process, the final overall cost of biomass was reduced by two-fold of magnitude.

Ding et al.[36] investigated the MF of mineral suspension with a Multi-shaft disk (MSD, Westfalia Separator, Aalen, Germany) membrane module, consisted of two stack (12 in total) of 90 mm diameter $0.2 \mu\text{m}$ pore size ceramic membrane mounted with two parallel shafts respectively, available for 0.121 m^2 filtration area, and tested in the CaCO_3 suspension of concentration range from 100 to 280 g/L and mean particle size $3 \mu\text{m}$. They indicated that, this two shafts rotated in same direction and membrane stacks were 15.5% overlap with each other, the maximum shear rate therefor occur within these overlapping because of the differential speed between two adjacent disks has been shown to be uniform and high in those overlapping gap. Concerning its advantage of energy saving, operating at moderate concentration and rotation speed was recommended, by reason of a steady flux and relatively high efficiency also could be achieved by 800 RPM at 40 kPa (in concentration 200 g/L CaCO_3 suspension).

Applications using polymeric membranes

Dal-Cin et al.[29] investigated an UF polymeric membrane module, a rotating Spintek ST-IIL, with diameter 203 mm and filtration area 0.05 m^2 , rotation speed up to 1800 RPM. Maximum operating pressure and temperature of this lab scale module was 310 kPa and 50°C . By testing with 5wt% cutting oil emulsion at 25°C and operating pressure range from 138 kPa to 310 kPa, result indicated that permeate flux increase almost linearly approx. from 100 to 600 RPM, and then reached a plateau and followed by a flux decline with the increasing rotation speed.

Sarkar et al. [43]used a newly UF membrane module, Spinning Basket Membrane (SBM, Gurpreet Engineering Works, Kanpur, UP , India), with 4 rectangular PES membrane, effective filtration area $55 \times 130 \text{ mm}^2$. This system benefit from advantages that firstly by centrifugal forces, shear rate generated on the membrane surface and help to improve the filtration performance; secondly, it had a self-cleaning process to remove membrane contamination by the reversed rotating direction, noted as cleaning run. Researcher tested with PEG solution and

observed that SBM was able to against flux decline about 15% of its initial flux value (recovery by cleaning run), by rotation speed range from 10.47 to 41.9 rad/s.

Overviewing the membrane modules, metallic and ceramic (or the composite of them) membranes are preferred in self-rotating condition. As well as a rotating membrane support, strict membrane condition is needed. It mostly benefits from high mechanical strength, tolerance and duration in terms of consideration of physical process parameters, such as high temperature, solid particle concentration, rotation speed, operating pressure etc. Considering chemical parameters, inorganic membranes also show its good stability and chemical tolerance.

2.1.3 Vibrating flat membrane modules

Configurations and Specifications

Vibration also has been applied in mobile membrane systems. Theoretically, this vibration can be longitudinally, transversely or torsionally in specific amplitude and frequency. For example, commercialized by *New Logic (USA)*, *Vibratory Shear Enhance Processing (VSEP)* represented as the original vibrating filtration device. This filtration body, which consists of alternative overlapping membranes or membrane-coated disks in series, is mounted on a torsion bar driven by a motor. It is able to reach 130 m² filtration area per module and scale up by installing more membrane modules. Researchers has well reported of this device with various applications e.g. yeast suspension [78], dairy[71], microalgal suspension [119] [120], oil-in-water emulsions [121]. Similar principle also introduced in *Vibrating Membrane Filtration module (PallSep-VMF)*, it has been early tested in breweries. Novel configuration has been reported by Goma et al.[54], this system was configured with a flat rectangular membrane immersed vertically in the treatment tank. This membrane was particularly fixed with flat or grooved *Turbulence Promoters (TP)* in series, driven by a motor and moved vertically in yeast suspension investigation [52-57,122].

Applications using polymeric membranes

Akoun et al.[49] investigated a UF PES membrane module, *Vibratory Shear-Enhanced Process (VSEP, New Logic, CA, USA)* series L, equipped with a single annular membrane of 135 mm outer radius and 47 mm inner radius (about 0.05 m²), able to vibrate azimuthally with amplitude 32 mm and frequency up to 60.75 Hz. The experiments were operated with a flow rate

of 120 L h⁻¹ and 45°C. Result indicated that, when test with 9.1% powder milk permeate flux developed with the increasing TMP, 40% permeate flux decline was observed with 86 kPa, however, 8.6% decline with 1500 kPa, likely to maintain at about 80 Lh⁻¹/m², due to its high shear rate on the membrane surface about 3×10⁵ s⁻¹. A membrane module VSEP series i-10 equipped with 610 mm diameter membrane indicated that this kind of membrane device was not only efficient but also energy saving, estimation of total power only consumed 1.83 kWh m⁻³.

2.1.4 Vibrating hollow fiber

Configurations and Specifications

Besides, researchers combined this vibration concept to hollow fiber. In the typical design, a bunch of parallel hollow fiber membranes are immersed in a treatment tank (can be a reactor as well), one side (or both sides) of them is fixed to a vibrating base. Most of the case is applied with longitudinally vibration, e.g. a membrane module, with a total membrane area 256 cm² and 12 cm long hollow fiber membrane, was studied by BEIER et al. [58-60]. This module wears a total membrane area of 488cm² is composed of 54 hollow fibers with a length of 12 cm mounted between two steel plates, one is at the fixed bottom and another is with a rod driven by a transversely rotating head (frequency between 0-30 Hz), presents a vibrating motion. A lower frequency set to 0-15 Hz was presented by Li et al. with a similar design[123], other researcher also explored the membrane module in different motion e.g. transverse vibration [124,125], and pendulum type oscillation[62].

Applications using polymeric membranes

Beier et al.[126]used a hollow fiber membrane module for yeast suspension. This test unit was installed with PES membrane, which is 120 mm long, and 0.0256 m² total membrane area, and tested with different vibration amplitudes (0.2-1.175 mm, peak to peak was twice) and frequency (0-30 Hz), resulting that the critical flux was improved 325% when filtration was carried out at maximum vibration frequency and amplitude, compare to the critical flux measured at minimum condition. Besides, operating below the critical flux was recommended rather than over it, for the reason that the constant permeability and significant fouling removal can be achieved whereas the permeability decline when operate over the critical flux.

2.2 DF modules with stationary membrane

As early as 1978, a specified system consisted of a stationary and a rotating disk was studied. This research conducted mathematical analysis for the viscous flow in the gap between those two disks[127]. Same concept was referenced and further developed in dynamic filtration.

2.2.1 Rotating flat disk modules

Configurations and Specifications

The most common configuration in stationary membrane system consisted of a rotor (can be an impeller, cone, disk or disk welded with promoter) rotating close to the membrane attached on a stationary support. Shear rate on the disk surface is evolved by the gap between the rotor and the membrane and therefore became one of the most important points for researchers.

Many rotating disk modules have been well documented in the literature. *Dynamic Membrane Filter (DMF, Pall Corp., Cortland, NY)* appeared as the first commercial system using this idea, typically consisted with a single solid disk rotating above a stationary membrane and was early tested in Biotechnology [92] [93] [94]. With similar design, *RDM (Rotating Disk Module)* was well studied with various test fluid[67,68,70,79,90,91,128-135], and was often compared to the other system[24,86-88,136-143]. Base on rotating disk concept, novel configuration with two membranes was developed and widely applied. For example, a single-use medical product *LIFE 18-Disk Separator*, which is designed to separate plasma from whole blood, two membranes were configured with a spinning disk rotating between them within a plastic housing, and only reached 50 ml for the volume. Recent decades, applying a useful rotor becomes another general interest. *Cross Rotational Filters (CR-filters, Metso-Paper corp. Finland, ex: Raisio-Flootek, Finland, and ABB Flootek, Sweden)*, was designed with the same principle, but applied a two-blade impeller as a rotor. The company proposes several scales for users, diameter can range from 200 to 1010 mm, e.g. the *OptiFilter CR-1010/100*, with diameter 1010 mm and 100 cassettes, filtration area up to 140 m² [97,98,100,101]. Same concept also has been applied to a filter called *Rotating and Vibrating Filtration module (RVF module, RVF Filtration, Paris, France)*. A lab-scale RVF module has been explored by Fillaudeau et al.[4] and Rayess et al. [144] in beer and wine industry. RVF has two identical filtration cells, each consisted of a three-blade impeller with 135 mm diameter and 8 mm thickness, rotating in a 14 mm gap between two porous substrates, can be operating up to 50 Hz. Other systems, the *DYNO*

Chapter II: Literature review on Dynamic Filtration modules

(Bokela GmbH, Karlsruhe, Germany) and the *FMX* (BKT United, Korea) filter equipped with special rotors. The *DYNO* filter is installed with a blade-like rotor for each filtration cell, able to reach 12 m² of total membrane area [145]. The *FMX* anti-fouling membrane unit, was first proposed to Samsung Fine Chemicals Co., Ltd. in 2005 by applying a high-speed rotating ‘vortex generator’, which are veined discs and has two uneven and asymmetric surface, designed for vortex generation. Standard class *FMX-S100* and economic class *FMX-E* are proposed with filtration area 95 m² and 40 m² [104]. So far, researchers have developed different type of rotors by adding promoters on the disk surface. For example, Bouzerar et al. [3] studied the differences with modified disks equipped with nylon mesh aluminum rods (also called vanes), then Brou et al.[79] continued further study by using different height and number of vanes. As well as the simulation done by Hwang et al.[146], six typed of rotating disk with or without vanes were tested. Similar configuration also can be seen in *Rotating cross-flow (RCF) MBR*[102]. Other systems, a lab-scale *Controlled Shear Filtration (CSF)* [107] module was consisted of a conical rotor rotating above a stationary membrane; a tubular membrane module, which was designed to treat radioactive wastes, was configured with a tubular metallic membrane as a housing and a coaxial inner cylinder as a rotor[147,148].

Applications using ceramic membrane

In our laboratory, Fillaudeau et al. [4]used a pilot scale Rotating and Vibrating Filtration (RVF) module for rough beer clarification. In a single filtration cell (two in total), two ceramic membranes (0.6-4 µm) were fixed parallel onto the stainless steel respectively and formed a 14 mm gap. An impeller with 8 mm thickness and 135 mm diameter was rotated between the membranes, and gave a 3 mm distance between the impeller surface and the membrane surface. In this research, driving force on the membrane surface and the core velocity coefficient were determined with water to understand the fluid mechanic. Afterward, performance of this device was evaluated for two different rough beers and model beers, resulting that ceramic membrane were able to achieve more satisfied quality and flux value than traditional filtrations.

Applications using polymeric membrane

Lee et al. [92]used a DMF LAB 6 (Pall Corp.,USA) system installed with MF Nylon/PVDF membrane (152 mm diameter and 137 cm² filtration area) for yeast suspension. Result showed that in DMF system, flux decline occurred with those three different membranes (PVDF,

0.45 and 1.2 μm pore size for Nylon), no significant different flux was found and both Nylon membranes reached steady flux earlier than the PVDF membrane, at about 40 min. The researcher also found that, 1.2 μm Nylon membrane performed better by 1.4 times higher concentration than the 0.45 μm one, according to their concentration factor profile. Moreover, by comparing to the conventional cross flow system, steady flux and average shear rate of DMF was $100 \text{ L m}^{-2} \text{ h}^{-1}$ and 12000 s^{-1} , 5 and 7.5 fold higher than cross flow system respectively.

With a similar configuration, a Rotating Disk Module (RDM) has already been well studied in the recent years. Performance of this membrane module was further investigated with alfalfa juice filtration MF and UF by Zhang et al.[64]. In this research, RDM module was developed into CRDM and DRDM by modification of loop operation. Wearing the same device configuration, the former one referred to a retentate recycling process (cross flow operation & RDM process), and the latter referred to a retentate non-recycling process (dead end operation & RDM process). With rotation speed of 1000 RPM, TMP of 3 bar for MF and 4 bar for UF, result indicated that CRDM could control concentration polarization and membrane fouling by its open channel and therefore had potential in productivity for leaf protein concentration from alfalfa juice.

Vogel et al. [107] studied the Controlled Shear Filtration module (CSF), which had a conical rotor of 70 mm diameter rotating 0.2 mm above a PVDF membrane (51.5 cm^2 effective filtration area), for MF with animal cell suspension. Result indicated that CSF was able to reach higher shear stress 17.2 N m^{-2} , viability percentage 97%-91%, 290 L h^{-1} , by compare to the traditional cross flow filtration, which is 7 N m^{-2} , 83%, $30 \text{ L h}^{-1} \text{ m}^{-2}$.

Kim et al. [104] investigated a bench scale FMX B-class (BKT Co. Ltd., Korea) for microalgal suspension with MF PVDF membrane (173 mm diameter and 146 cm^2 filtration area). With numerical simulation, result showed that, fluid velocity and average shear stress on the membrane surface was found to be 2 and 7 fold higher than an unperforated disk respectively. However, when compare with experiments result, the real average shear stress was much higher than the simulation, and fouling resistance was found to be 2-3 fold lower than the unperforated one.

3 Theory: criteria to characterize internal fluid dynamics

Under theoretical point of view, dynamic filtration consists of creating relative motion between the membrane and its housing in order to generate high shear rates at membrane surface and oscillating flows (retentate and/or permeate). Among the advantages of DF device, the ability to generate high shear rates independently of the feed flow, which can be kept low, with the increase of permeability, the reduction of the filtration loop volume, the filtration at low transmembrane pressure can be mentioned. The combination of these factors limit fouling propensity and compressibility at membrane surface[3,63,79,87,136,149], which appears as major advantages for ultra and micro-filtration of biological matrices. Film theory stands as the most common theoretical approach to describe permeation flux independently of pressure for mass transfer limited system.

3.1 Global approach

3.1.1 Dimensionless analysis in dynamic filtration

Dimension analysis of mass transfer (by analogy with heat transfer) lead to establish semi-empirical correlation between dimensionless numbers,

$$\text{Sherwood } (Sh), Sh = \frac{k_m \cdot d_h}{D} = \frac{d_h}{\delta}, \text{ Schmidt } (Sc), Sc = \frac{\nu}{D} = \frac{\mu}{\rho D} \text{ and Reynolds } (Re),$$

$Re = \frac{\rho \cdot d_h \cdot U}{\mu}$ such as $f(Sh, Re, Sc) = 0$ in laminar regime, $Sh = A' \cdot Re^\alpha \cdot Sc^\beta \cdot \left(\frac{d_h}{L}\right)^\varepsilon$ and in turbulent regime, $Sh = A'' \cdot Re^\alpha \cdot Sc^\beta$ [Daufin et al. 1998] (D : diffusion coefficient, k_m : transfer coefficient, d_h : hydraulic diameter, δ : thickness of limiting layer, μ : viscosity, U : velocity, ρ : density).

In laminar regime (Graetz-Lévéque's equation): $Sh = 1.62 \cdot \left(Re \cdot Sc \cdot \left(\frac{d_h}{L}\right)\right)^{1/3}$ with

$100 < Re \cdot Sc \cdot \left(\frac{d_h}{L}\right) < 5000$. By rearranging, it becomes $k_m = 1.62 \cdot \left(\frac{U \cdot D^2}{d_h \cdot L}\right)^{1/3}$ and

$$k_m = 0.816 \cdot \left(\frac{\dot{\gamma}}{L} \cdot D\right)^{1/3} \text{ with } \dot{\gamma} = 8 \cdot U / d_h.$$

Chapter II: Literature review on Dynamic Filtration modules

In turbulent regime (Dittus-Boelter's equation): $Sh = 0.023 \cdot Re^{0.80} \cdot Sc^{1/3}$ with $Re > 10000$.

These relations make possible to evaluate mass transfer coefficient, k_m and enable to determine how membrane geometry and operating conditions may be selected to improve flux. These expressions require the identification of diffusion coefficient, D of solutes retained by membrane in water (solvent). These relations highlight that flux may increase if flowrate increases or cross-section reduces. From a general standpoint, all hydrodynamics techniques which increase flow velocity and shear rate at membrane surface enable to increase flux[150]. In microfiltration, various and recent theories take into account hydrodynamics: (1) lateral migration of particles (tubular pinch effect), (2) axial migration of deposit (flowing cake) or hydrodynamic diffusion generated by shear rate (shear-induced diffusion). In the aim to enhance the understanding of transfer mechanism in membrane process, it seems essential to investigate and characterize hydrodynamics (velocity field, shear rate, flow regime) at local and global scales.

Due to complex geometry and flow pattern in dynamic filtration devices (enclosed rotating disc, static membrane), the flow is characterized by an important tri-dimensional nature. This complex flow can be described by various dimensionless numbers Table II. 7 among gap/radius ratio, R , Reynolds number based on flowrate and radius, Re_Q , Mixing Reynolds number, Re_R and Eckman number (inverse of Reynolds number based on gap), E or Re_s^{-1} .

Table II. 7 Dimensionless numbers used to describe hydrodynamic within Dynamic Filtration device (s : gap, r : radius, ω : angular velocity, μ : viscosity, ρ : density, Q_f : flowrate)

Mode	Fomula
Tube	$Re = \frac{\rho \cdot d \cdot U}{\mu}$ or $Re_Q = \frac{\rho \cdot Q}{\mu \cdot \pi \cdot r}$ (II.1)
Equivalent tube	$Re = \frac{\rho \cdot d_h \cdot U}{\mu}$ or $Re_Q = \frac{\rho \cdot Q}{\mu \cdot \pi \cdot r_h}$ (II.2)
Annulus tube	$Re = \frac{\rho \cdot (d_o - d_i) \cdot U}{\mu}$ (II.3)
Axial flow in annulus	$Re_a = \frac{2du_z}{v}$ (II.4)
Rotating system (mixing)	$Re_m = \frac{\rho N d_m^2}{\mu}$ (II.5)

Rotating system*	$Re_R = \frac{k \cdot \rho \cdot \omega \cdot r^2}{\mu}$	(II.6)
------------------	--	--------

Rotating cone	$Re_s = \frac{\omega(h + r \tan \alpha)^2}{\nu}$	(II.7)
---------------	--	--------

Gap based Ekman number	$E = \frac{1}{Re_s} = \frac{\mu}{\rho \cdot \omega \cdot s^2}$	(II.8)
------------------------	--	--------

Vibrating system	$Re_v = \frac{2\pi \cdot F \cdot h^2}{\rho}$	(II.9)
------------------	--	--------

3.1.1.1 Reynolds number in tube

The Reynolds number, Re , is a dimensionless quantity that is the ratio between inertia force and viscous force. It is used to define and predict similar flow patterns in complex fluid flow conditions. Reynolds number is defined as Eq.II.1 with flow in tube, where μ is the dynamic viscosity of the fluid, ρ is the density of fluid, d is the diameter of the tube. It also can be define as $Re = (d \cdot U)/\nu$, where ν is kinematic viscosity, defined as $\nu = \mu/\rho$. When fluid flow in a non-tube, Eq.II.3 and $Re = (d_h \cdot U)/\nu$, where d_h is the hydraulic diameter. As well as in annulus tube, Eq.II.5 is defined where d_h is equal to outer diameter of the tube minus inner diameter. According to the different operating parameters, Reynolds number also can be determined by flowrate Q , see Eq.II.2.

In an annulus tube, Reynolds number can be defined as Eq.II.3 according to equivalent diameter. However, when this annulus coaxial cylinder was fed by axial flow, Reynolds number can be defined as Eq.II.4, where u_z was the axial velocity [115,151].

3.1.1.2 Reynolds number in mixing and rotating system

In mixing system (with rotating mixer), it is known that Reynolds number is defined as Eq.II.6, Azimuthal Reynolds, where N is the rotation speed in Hz and d_m is the diameter of the mixer. According to the mixing system, Reynolds number can be developed by angular velocity ω as $Re = (\rho \cdot \omega \cdot r^2)/\mu$. According to this theory, four different pattern of flows in rotating disk in a housing system were proposed by researchers:[92,102], Re_s refers to axial Reynolds number and Re_r refers to radial Reynolds number. With a flowrate equal to zero ($Q=0$), four flow regimes may appear in the filtration cell and they have been described by Murkes & Carlsson (1988) [152]:

Laminar regime I : $Re_s < 4$, $Re_R < 2-3 \cdot 10^5$ and $E > 0,25$. Case corresponding to small gap, both limiting layer fuse and Couette flow is observed.

Laminar regime II : $Re_s > 4$, $Re_R < 2-3 \cdot 10^5$ and $E < 0,25$. The gap is then more important and limiting layers are developing at stator and rotor surfaces. Close to rotor, centrifugal forces eject the fluid outwardly compared to the shaft whereas, at membrane surface (stator), radial velocity induced centripetal forces in respect with continuity equation. The thickness of limiting layer on stator surface is then theoretically four times higher than on the stator for an infinite disk.

Turbulent regime III : $Re_R > 2-3 \cdot 10^5$ and $s/r > 0,05-0,06$.

Turbulent regime IV : $Re_R > 2-3 \cdot 10^5$ and $s/r < 0,05-0,06$. Limiting layers are separated like in laminar regime II.

Moreover, a local Reynolds number can be defined as Eq.II.6, represents the flow pattern in local fluid, where k is a velocity coefficient refers to the transmission of impeller velocity to the fluid ($0 < k < 1$). An axial Reynolds number of a rotating conical rotor system was also defined as Eq.II.7 where the rotor height h and the inclination angle were taken into account [107]. And a Reynolds number can be defined as a reverse of the Ekman number as Eq.II.8 shows. Ekman number characterizes the ratio of viscous drag forces in a fluid to the Coriolis forces[153].

3.1.1.3 Reynolds number for vibrating systems

In a different system, as vibration or oscillation, the flow is governed by various parameters. This system was early studied by Rosenblat [154], who used two parallel infinite plane disks, oscillate torsional driven by a common axis for Newtonian fluid. The Reynolds number is defined as function of oscillation frequency F and the distance between disks, shown as Eq.II.9. It has been applied to a vibrating membrane VSEP system, Re was of the order of 3×10^5 . [78,155].

3.1.2 Friction curve and power consumption curve

Power consumption curve is the representation of Power number against Re_{mixing} , it is an important specification to evaluate agitation and mixing performance by considering device properties and fluid rheological properties. The fluid dynamic behavior in an agitation and

mixing system can be described as a function of the rotational speed of the mixing Reynolds number (Eq.II.10), the power consumption P can be described by Power Number N_p (Eq.II.11).

$$Re_{mixing} = \frac{\rho N d_m^2}{\mu} \quad (II.10)$$

$$N_p = \frac{P}{\rho N^3 d_m^5} \quad (II.11)$$

The friction curve is the representation of Da against Re_Q Eq.II.12 and 13, it is an important specification use to predict the frictional energy lose in a pipe or equivalent pipe based on the velocity of the fluid and the resistance due to friction. The friction curve can be described using a unique expression based on Churchill's model, Eq.II.14. This general expression can be used for laminar, transitory or turbulent flow regime. Contribution of these three regime were considered in this expression.

$$Re_Q = \frac{\rho u_f d_h}{\mu} = \frac{2\rho Q}{\mu \pi d_h} \quad (II.12)$$

$$Da = \frac{8\tau_p}{\rho u^2} = \frac{\Delta p d_h}{4L\rho u^2} \quad (II.13)$$

$$Da = \left(((Da)_{tur}^{n1} + (Da)_{tran}^{n1})^{\frac{n2}{n1}} + (Da)_{lam}^{n2} \right)^{\frac{1}{n2}} \quad (II.14)$$

Research on friction curve and power consumption curve of RVF module were done previously [5], aimed to identify the flow regime of given operating conditions. The critical Reynolds numbers can be obtained to define flow regime as the following:

Laminar flow regime: $Re_Q < 3, Re_{mixing} < 2000$;

Transition flow regime: $3 < Re_Q < 50, 2000 < Re_{mixing} < 300000$;

Turbulent flow regime: $Re_Q > 50, Re_{mixing} > 300000$.

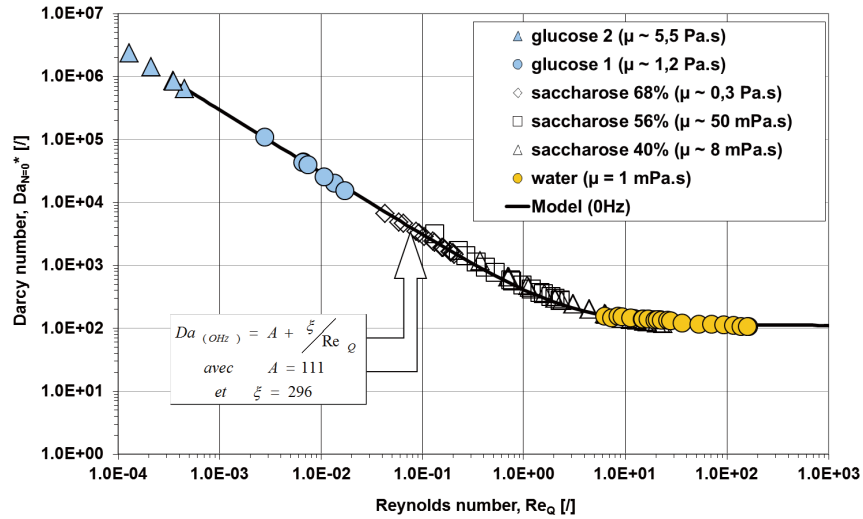


Fig.II. 7 Friction curve established with RVF lab-scale module [5]

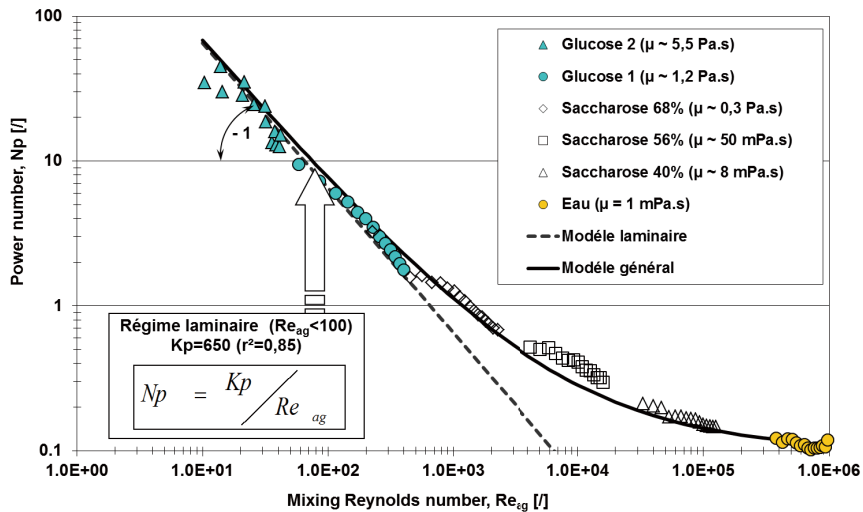


Fig.II. 8 Power consumption curve established with RVF lab-scale module [5]

3.2 Semi-local approaches

In dynamic filtration device, rotation module for instance, the movement of rotation generates additional/radial pressure. The core velocity coefficient appears as a key parameter to define the additional pressure, whose value is a complex function of gap, radial position, mixing rate and geometry of rotating disk (smooth disk, modified surface disk, flat blade mixer).

Another parameter, the shear rates on stator (membrane) and rotor (rotating disk) surfaces have been described, solved theoretically and then calculated numerically by several authors: Bodewadt (1940)[156], Daily et al. (1960)[157], Schlichting (1968)[158], Murkes & Carlsson

(1988)[152], Bouzerar (2000)[3]. Table II. 9 summarizes the expressions of shear rates on stator and rotor surfaces for each flow regime, reported into literature.

3.2.1 Radial pressure and core velocity coefficient induced by mixing

3.2.1.1 Radial pressure

The impact of additional pressure due to mixing was studied previously[4,5,144], Permeate flux (J) is calculated according to Darcy's law,

$$J = \frac{Q_p}{S} = \frac{\Delta P}{\mu_p \cdot Rh} = L_p \cdot \Delta P \quad \text{with} \quad \Delta P = \frac{(PR_{in} + PR_{out})}{2} - PP \quad (\text{II.15})$$

where J is flux [m/s], Q_p permeate flow-rate [m³/s], S membrane area [m²], ΔP the transmembrane pressure [Pa], μ_p the permeate viscosity [Pa·s], Rh the total hydraulic resistance [1/m], L_p the permeability [m/(s·Pa)], PR_{in} , PR_{out} and PP respectively inlet, outlet and permeate relative pressures [Pa].

Bouzerar et al. indicated that in the core fluid layer, fluid velocity can be calculated by $k \cdot 2 \cdot \pi \cdot N$, where k is the core velocity coefficient inferior to 1. The core velocity coefficient highly depends on system geometry such as configuration of the mixer, distance from mixer to membrane[3,24,159]. Therefore, radial pressure gradient in the core layer can be expressed by:

$$\frac{\partial p}{\partial R} = \rho \cdot R \cdot (k \cdot 2 \cdot \pi \cdot N)^2 \quad (\text{II.16})$$

$$p(R) = p_0 + \rho \cdot g \cdot z(R) + 2 \cdot \rho \cdot (k \cdot \pi \cdot N)^2 \cdot R^2 \quad (\text{II.17})$$

where ρ is the density [kg/m³], p is the pressure [Pa] and R is the radius [mm]. Pressure field is then obtained by integration of Eq.II.16 and the mean additional pressure is obtained by integration of Eq.II.17 over membrane area from R_0 to R_{max} . Due to the specification of impeller design, the hydrodynamic perturbation generated by this three-blade impeller in the gap (membrane to impeller) is different from a full flat disk. This perturbation is including the contribution of rotation speed (N) and additional pressure fluctuation (ΔP_{ag}) due to the impeller characteristics. Additional pressure ΔP_{ag} was deduced by measuring the flux versus the radial

position and the rotation speed (Fig.II. 9). The flux was measured versus the frequency and compared to the case rotation speed equal to zero (Eq.II.18):

$$J(0, R \text{ to } R + dR) = \frac{\Delta P}{\mu_p \cdot Rh_m} \quad (\text{II.18})$$

$$J(N, R \text{ to } R + dR) = \frac{(\Delta P + \Delta P_{ag}(N, R))}{\mu_p \cdot Rh_m} \quad (\text{II.19})$$

where Rh_m is the hydraulic resistance of clean membrane [1/m]. Trans membrane pressure can be expressed by $TMP = p(r) - \Delta P_{ag}(N, r)$.

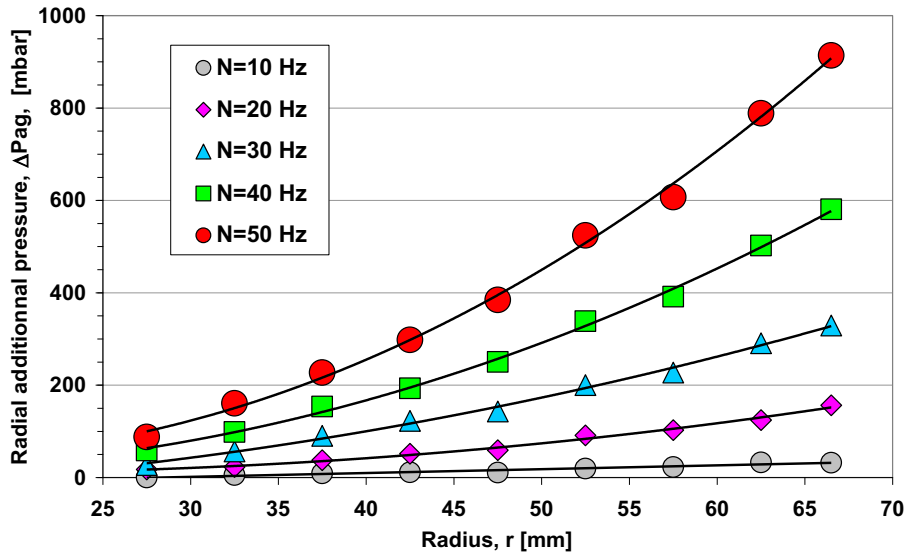


Fig.II. 9 Determination of hydrodynamic performances, evolution of the radial pressure distribution versus the radius and the rotational speed[4,5]

3.2.1.1 Discussion of core velocity coefficient

Core velocity coefficient, K_θ the ratio of mean fluid velocity to impeller velocity, is one of the key factors that present the mechanical efficiency of the RVF module, to quantify the mechanical efficiency as an indicator.

Flow between a stationary and a rotating disk system was early studied by Wilson et al. [127]. They proved that flow pattern between these two disk was different: radial flow close to

the rotor was centrifugally outwards, and it was directly inwards when close the stator, and also had different boundary layers respectively, suction reduced the boundary layer thickness. Then a concept of rotation rate was presented and equal to 0.3131 at $Re=10^4$, it characterized the fluid rotating at an angular velocity $0.3131 \times 2\pi N$ with the rotor rotating at $2\pi N$.

Flow field between a stationary membrane and a rotating disk was studied by Bouzerar et al. [3], resulting that velocity coefficient was influenced by system geometry and configuration, to be 0.34 for smooth flat disk, and rise to 0.62 for flat disk equipped with vanes. And this influence was further investigated by Brou et al. [79] by modifying the distance of disk to membrane, of 0.45 with smooth disk in 17 mm gap and rise to 0.84 in 15 mm gap for disk equipped with 8 pairs of 6 mm thickness vanes.

RVF module performed 0.71 of core velocity coefficient with a three-blade impeller in a 3 mm rotor-to-membrane gap. Numerical simulation was also conducted to estimate this value, of 0.895 and 0.795 for laminar and turbulent respectively [102].

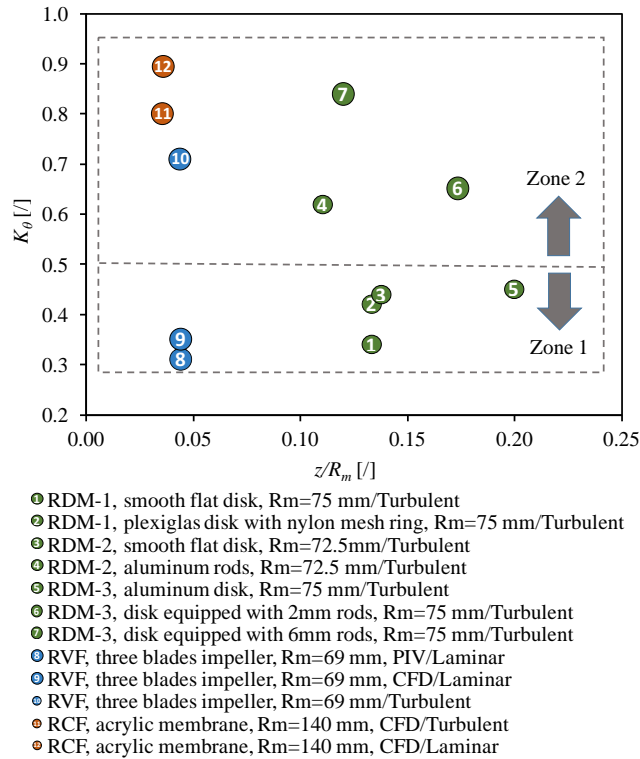


Fig.II. 10 Evolution of core velocity coefficient, K_θ as a function of gap-to-radius ratio, z/R_m . Values are reported from literature for DF modules using confined rotating impeller close to membrane and established under laminar or turbulent regimes

Fig.II. 10 compares K_θ value issued from experimental or numerical approaches among similar DF modules using confined rotating impeller close to membrane. Core velocity coefficients can be classified into the lowest values in Zone 1 ($K_\theta=0.3 - 0.5$) and into enhanced mechanical efficiency in Zone 2 ($K_\theta>0.5$). Geometry of the module is characterized by the ratio, z/R_m , where z is the minimal distance between impeller or disk (considering geometrical modification) and the membrane, R_m is the radius of the mixer. In general, when the values of z/R_m decrease, the core velocity coefficients K_θ increase. Wilson et al.[127] first reported that K_θ was close to 0.313 between a stationary and a rotating disk with suction in turbulent regime. Bentzen et al.[102] have conducted CFD simulations in laminar and turbulent regimes. They report $K_\theta = 0.8$ (turbulent) and 0.9 (laminar) for a rotating cross-flow MBR installed with a plastic disk rotor ($z/R_m=0.0357$). These values are very close which is unexpected for laminar regime. Researchers tended to improve K_θ by increasing surface roughness and by modifying device configuration in turbulent regime. Fig.II. 10 shows $K_\theta = 0.45$ in RDM-3 with aluminum disk (point 5); Bouzerar et al.[3] increased this coefficient up to 0.65 in the RDM-1 module, by

installing 2mm thickness rods on the rotating disk surface (point 6); and Brou. et al.[79] further increased up to 0.84 by installing 6mm thickness (point 7). Other improvements with RDM modules were also achieved by applying outer Nylon mesh ring, rods in different size and materials and so on[3,79,136].

In RVF module (with a 3 flat blades impeller), previous works based on mean pressure measurement [4] have identified K_θ equal to 0.71 in turbulent flow which is consistent with similar z/R_m ratio established with full disk. In all configurations, the increase of K_θ from Zone 1 to the Zone 2 are correlated with the gap reduction related to geometrical modifications. However, the magnitude of K_θ has not been correlated with the design and number of modifications (ex. number of rods). In this study (details of experiment set-up is given in *Chapter III 4 Local investigations: Particle Image Velocimetry*, more discussion is presented in), local K_θ ($\frac{\overline{U_\theta}}{\omega \cdot R}$) distribution was identified by PIV measurements and CFD simulation in laminar regime. CFD simulation provides a similar value equal to 0.35. K_θ values in laminar regime issued from PIV and CFD are coherent with velocity profiles.

Table II. 8 Core velocity coefficient of different DF filters

Introduction of the rotating device (without membrane)						
Research module	Rotating element (rotor)	Disk-to-membrane gap [mm]	Gap ratio s/r	Testing fluid	Core velocity coefficient	Ref.
Two parallel infinite disks	One disk rotates			(Reynolds numbers Re = 104)	0.3131	[127]
RDM-1 154 mm housing 150 mm disk	Smooth flat disk 150 mm	10	0.13	CaCO ₃ suspension, 60 kg/m ³	0.34	[3]
	A Plexiglas disk equipped with nylon mesh ring	10	0.13		0.42	
RDM-2 154 mm housing 145 mm disk	Smooth flat disk 145 mm	10	0.14		0.44	
	An aluminum disk welded with aluminum rods	10	0.14		0.62	
RDM 154 mm housing 150 mm disk	150 mm Aluminum Disk,	17	0.23	Baker yeast suspension, 3 g/L	0.45	[79]
	Disks equipped with 8 pairs of 2mm thickness rods.	15	0.2		0.65	

	Disks equipped with 8 pairs of 6mm thickness rods.				0.84	
Rotating and Vibrating module (RVF technology—patent no. FR-97-14825)	3-blade impeller 135 mm	3	0.04	Water	0.71	[4]

3.2.2 Shear rate and shear stress calculation

In dynamic filtration, separation efficiency and productivity are highly dependent on the selection of membrane types and materials. However, as mentioned previously, shear rates is one of the crucial factor, which can control membrane fouling and enhance permeate flux. Some theoretical and semi-empirical mathematical models for calculating shear rates in different systems are presented in this section.

3.2.2.1 Rotating systems

General model

In general, the shear rate between two disks can be estimated according to viscosity law, with velocity of the flow u and the distance of the gap y :

$$\dot{\gamma} = \frac{du}{dy} \quad (\text{II.20})$$

Or by shear stress τ and viscosity of the fluid μ :

$$\dot{\gamma} = \frac{\tau}{\mu} \quad (\text{II.21})$$

Vogel et al. [107] considered the average shear rate γ_{av} in the gap between the conical rotor and the membrane in CSF system, it could be estimated by angular velocity ω , radius of the rotating cone, distance between cone and the membrane h , and inclination angle of the cone α as Eq. II.22 shown. Result of maximum wall shear rate by Eq. III.21 was 12650 s^{-1} , while the average value by Eq.II.22 in the gap was 1246 s^{-1} .

$$\dot{\gamma}_{av} = \frac{\omega r}{h + r \tan \alpha} \quad (\text{II.22})$$

Lee et al. [114] calculated the shear rate in a annulus of coaxes cylindrical RO membrane system as Eq.II.23 shown, where f was a velocity factor. They considered the circumferential velocity was uniform in the center of the annulus at about $r_i\omega/2$. The maximum shear rate was generated close to the rotating inner cylinder.

$$\dot{\gamma} = f \left(\frac{\omega r_i}{r_0 - r_i} \right) \quad (\text{II.23})$$

Boundary theory with four flow regimes

In rotating systems, flow is governed by centrifugal forces that generated by rotors, and induce different flow pattern near the rotor and the stator. Four different flow regimes were presented, according to azimuthal Reynolds number and the gap to radius ratio, and shear rates on the rotor and stator were defined:

Table II. 9 Four different flow regimes in a rotation system

	Rotor	Stator
Regime I (L)	$\dot{\gamma}_w = \frac{\omega \cdot r}{s} \quad (\text{II.24})$	$\dot{\gamma}_w = \frac{\omega \cdot r}{s} \quad (\text{II.25})$
Regime II (L)	$\dot{\gamma}_w = 1,81 \cdot \frac{(k \cdot \omega)^{3/2} \cdot r}{\nu^{1/2}} \quad (\text{II.26})$	$\dot{\gamma}_w = 0,77 \cdot \frac{(k \cdot \omega)^{3/2} \cdot r}{\nu^{1/2}} \quad (\text{II.27})$
Regime III (T)	$\dot{\gamma}_w = 0,008 \cdot \frac{(\omega \cdot r)^{7/4} (\nu/s)^{1/4}}{\nu} \quad (\text{II.28})$	$\dot{\gamma}_w = 0,0115 \cdot \frac{(\omega \cdot r)^{7/4} (\nu/s)^{1/4}}{\nu} \quad (\text{II.29})$
Regime IV (T)	$\dot{\gamma}_w = 0,057 \cdot \frac{r^{8/5} (k \cdot \omega)^{9/5}}{\nu^{4/5}} \quad (\text{II.30})$	$\dot{\gamma}_w = 0,0296 \cdot \frac{r^{8/5} (k \cdot \omega)^{9/5}}{\nu^{4/5}} \quad (\text{II.31})$

Bouzerar et al. [3] obtained the same expression of Eq.II.27 and Eq.II.31 for laminar flow and turbulent flow for investigating RDM system. Bendick et al.[31] believed that, in a rotating membrane system HSR-MS, γ and Re might be as a function of steady state flux J_{ss} respectively, so they applied this theory to characterize shear rates γ on the rotating membrane surface with

membrane diameter of 267 mm using Eq.II.26 in laminar flow and Eq.II.30 in turbulent flow. They proved the J_{ss} - Re and J_{ss} - γ relationship and extended the model for further prediction.

Torras et al. [130] developed Eq.II.30 and 31 for estimating shear rates on the rotating metal disk and a stationary organic membrane. Considering the area-weighted averages of the azimuthal component for the wall shear stress τ_{disk} and $\tau_{membrane}$, both Eq.II.30 and 31 were integrated. Considering the geometry of the test system and properties of the test fluid (skim milk at 45 °C), they obtained,

$$\tau_{disk} = 0.0059 \cdot \omega^{1.8} = 1.02 \cdot 10^{-4} \cdot \Omega^{1.8} \quad (II.32)$$

$$\tau_{membrane} = 0.0037 \cdot \omega^{1.8} = 6.37 \cdot 10^{-5} \cdot \Omega^{1.8} \quad (II.33)$$

3.2.2.2 Vibrating systems

Torsional, vibrating or oscillating system with two parallel disks was with complicated parameters, which includes the complex geometry of the system, vibration frequency, amplitude and the properties.

VSEP module

Rosenblatt et al. early studied the flow between oscillating disks[154], Akoum et al. [78] calculated the shear rates on the membrane in a lab scale VSEP system by

$$\gamma_w(r, t) = \left. \frac{\partial V}{\partial Z} \right|_{z=0} = \left. \frac{\partial V}{\partial Z} \right|_{z=h} = \frac{r\Omega}{h} \sqrt{\frac{Re}{2}} G(t) \quad (II.34)$$

$$\text{with } G(t) = \cos(2\pi Ft) - \sin(2\pi Ft) \quad (II.35)$$

where r and h was the radius and gap of the disks, t was the operating times.

The shear rate occurred at the periphery ($r=R_2$, R_2 was the outer radius of the membrane), maximum shear rate could be calculated by

$$\gamma_{w \max} = \frac{R_2 \Omega Re^{1/2}}{h} = (2\pi F)^{1/2} R_2 \Omega \nu^{-1/2} = 2^{1/2} d(\pi F)^{3/2} \gamma^{-1/2} \quad (II.36)$$

Moreover, mean value of the shear rate can be defined by computing the average of the absolute value over a specific area, for example the annular limited by inner radius R_1 and outer radius R_2 in this case, showed as

$$\bar{\gamma}_w = \frac{2^{3/2}(R_2^3 - R_1^3)}{3\pi R_2(R_2^2 - R_1^2)} \gamma_{w \max} \quad (\text{II.37})$$

For VSEP system in this research, result showed that the maximum and mean shear rates at the membrane was of 112000 and 37000 s^{-1} , respectively, with water at 20°C. These expressions also had been used to estimate maximum shear rates with Eq.II.36 [49], and calculated mean shear rate with Eq.II.37 [48,71], in 45 °C milk solution.

Hollow fiber

Hollow fiber system is often applied with vibrating mechanical forces, shear rate in this membrane module was calculated by Beier et al. [58], they showed that the shear rates at the membrane surface should be

$$\gamma_s = v_0 \sqrt{\frac{\omega}{2\nu}} [\sin(\omega t) - \cos \omega t] \quad (\text{II.38})$$

where ω was angular frequency ($\omega = 2 \times \pi \times f$), v_0 was the amplitude of velocity ($v_0 = \text{amp} \times \omega$), t was times.

Base on this expression, a time mean average of shear rate was defined as

$$\bar{\gamma}_s = \frac{\sum_{i=0}^{1000} |\gamma_s(t = i/1000)|}{1000} \quad (\text{II.39})$$

Result showed that the maximum time mean value, computed by Eq.II.39, could up to approx. 2000 s^{-1} .

Gomaa et al. [122] investigated a flat vertical vibrating membrane unit with turbulence promoters. They gave a surface shear rate expression for surface shear rates estimation

$$\gamma(t) = \frac{aw^{1.5}}{2\nu^{0.5}} \left(\cos \omega t + \frac{\pi}{4} \right) \quad (\text{II.40})$$

$$\text{and the maximum shear rate is } \gamma_{max} = \frac{aw^{1.5}}{2\nu^{0.5}} \quad (\text{II.41})$$

Comparing these three systems as following,

$$\frac{\gamma_{max1}}{\gamma_{max2}} = \frac{d_1}{d_2} \left(\frac{\omega_1}{\omega_2} \right)^{1.5} \quad (\text{II.42})$$

Shear rate for VSEP (frequency 60 Hz, amplitude 30 mm) is of 28 fold higher than hollow membrane system (30 Hz, 3 mm)[30], and it is 4 fold higher than the vertical flat membrane unit.

3.3 Local approaches

In dynamic filtration system, complexity flow pattern is generated by the complexity of the geometrical configuration and the rheological behavior of the fluid. This flow pattern is also at the same time depending on the time and length scales. Global and semi-local approaches show their limitation for getting further information such local velocity, shear, temperature etc.

From experiment point of view, recently optical measurement/visualization technique are becoming more and more popular for accurate and reliable local measurement, resulting velocity field, concentration field, temperature field etc.

3.3.1 PIV/PTV

Imaging methods for measuring the velocities of particles in fluid flow fields capture two-dimensional or three-dimensional images of the particles at two or more instants and infer the particle velocity from the displacements of the images. These techniques are based on tracking the motion of seeded particle groups (PIV) or individual particles (PTV). Many researchers became interested in PIV [160-164] and PTV [165-167] because it offered a new and highly promising means of studying the structure of flow.

3.3.2 Molecular tagging velocimetry (MTV)/Planar laser-induced fluorescence imaging (PLIF)

MTV is a technique for determining the velocity of currents in fluids by tagging specific molecular and tracking its displacement by image technique. There are three optical ways via which these tagged molecules can be visualized: fluorescence, phosphorescence and laser induced fluorescence (LIF)[168].

3.3.3 Doppler velocimetry (LDV)

Laser Doppler velocimetry (LDV), also known as laser Doppler anemometry (LDA), is one of the techniques of using the Doppler shift in a laser beam to measure the velocity in transparent or semi-transparent fluid, or the linear or vibratory motion of opaque, reflecting, surfaces. The measurement with LDA is absolute, linear with velocity and requires no pre-calibration [169-171].

3.3.4 Electrochemical method

H. Ziouh et al. used an electrochemical method based on the reduction in the ferricyanide ion on an electrode surface to determine shear stress experimentally. This method is based on the determination of the limiting diffusion current at the surface of an electrode under conditions for which the chemical reaction rate is fast enough so that the concentration of the reacting ions is zero at the surface of the working electrode [172,173].

3.3.5 Computational Fluid Dynamics (CFD)

From numerical point of view, as an alternative to the experimental studies, Computational fluid dynamics (CFD) uses numerical analysis and data structures to solve and analyze problems that involve fluid flows, by solving Navier–Stokes equations. The geometrical domain and the associated set of governing equations for fluid should be defined, and specific numerical method should be added to better explain system problem. Moreover a proper calculation mesh should adapted to the geometry and the numerical method, according to the specific problem [174-176].

❖ **Summary of Chapter II: Literature review on Dynamic Filtration modules**

The general background of membrane filtration process was introduced, and the scientific production related to dynamic filtration process was described. A database interrogation was carried out to review scientific publications and gain insight into research hotspots (quantitative analysis). A total of 195 articles on the topic “dynamic filtration” and “shear enhanced filtration”. *Journal of Membrane Science* ranked the first place with 23.59 % of total articles published. University of Technology of Compiègne (France) published 38% articles out of the total and had a closer cooperation with China.

In the second part, a full inventory of existing DF modules (lab/pilot/industrial scales) produced by 29 manufacturers is discussed, including:

- their definition and classification (mobile and stationary membranes);
- their geometrical complexity and description (operating conditions);
- their field of applications (water treatment, food engineering, biological and medical engineering).

The cut-off size, material of the membranes and the product to filter are common factors affecting membrane processes. Specifically, DF performances were found to be highly dependent on the following parameters:

- the configuration and geometry of the system (cell configuration, mixer design, gap between membrane and mixer);
- the operating conditions and hydrodynamic parameters (rotating/vibrating frequency, local transmembrane pressure).

In the third part, the current research on global hydrodynamics was introduced concerning the developed methods including:

- Theory (dimensionless analysis)
- Experimental methods (semi-local: pressure measurement, local measurement: optical laser-based technique, electrochemical method, CFD simulation)
- Empirical correlation (wall shear model for rotating/vibrating module)

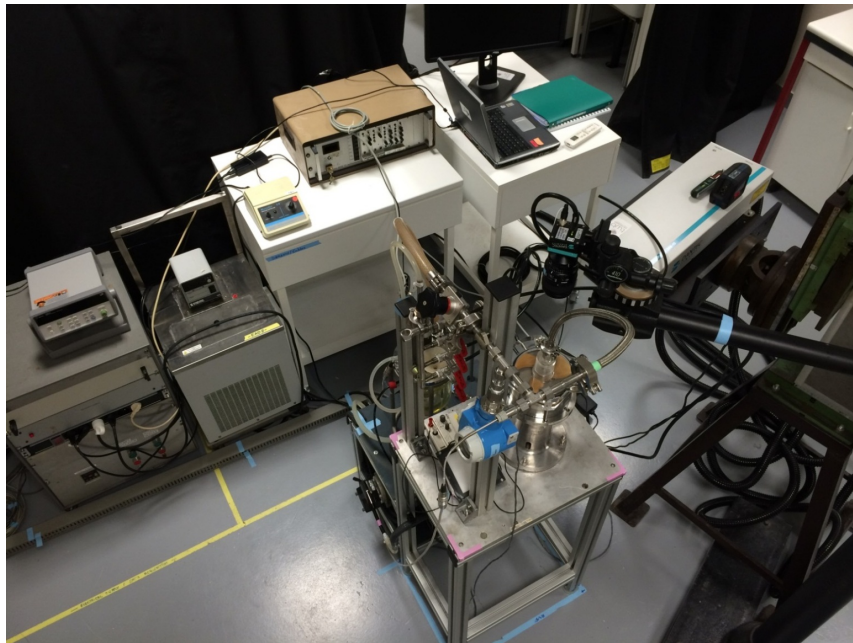
From 2005 to now, newly devices appeared as the second-generation DF filter by

optimizing design and scaling up. Overviewing the literature, majority of the scientific works are based on global approach (retention-permeation efficiency, core velocity coefficient). Local hydrodynamics are necessarily needed to better understand local phenomena and to define accurate and optimized operating conditions. This PhD thesis is thus motivated by the lack of knowledge about:

- the local and instantaneous hydrodynamics (velocity fields) within the filtration cell;
- the local shear stress/rate at membrane-fluids interface;
- the criteria to optimize filtration efficiency;
- the design and the scale-up of DF module.

Chapter III:

Materials and Methods



Overview of PIV set-up

Chapter III: Materials and methods

Dynamic filtration module, called Rotating and Vibrating Filtration (RVF) module, is investigated in this study. Scientific strategy is conducted with dedicated set-up for thermal balance, Residence Time Distribution (RTD), Particle Image Velocimetry (PIV) and Computational Fluid Dynamic (CFD) simulation.

This chapter firstly describes the RVF module, and the general set-up through all the experiment. A listing of all the devices and materials are presented in Fig.III. 2 and Table III. 1.

In the second section, experimental fluids (BREOX solutions and water) and tracers (salt solution, Rhodamine suspension and cell suspension) are presented. In abiotic conditions, salt solutions mixed with water and BREOX solutions, were used in RTD experiments as tracers, and Rhodamine suspensions were used as tracers in PIV experiments. In biotic conditions, *Escherichia coli* (*E. coli* WK6) cell suspensions were used in a filtration process.

1 RVF module and experimental set-up

A dynamic filtration technology, called rotating and vibrating filtration (RVF), was investigated in this study, involved experiments for investigating thermal balance, Residence Time Distribution (RTD), Particle Image Velocimetry (PIV) and Computational Fluid Dynamic (CFD) simulation. RVF is designed for filtration of highly concentrated liquids characterized with high fouling and/or clogging characteristics. It uses disc-shaped flat sheet membranes in the vicinity of the rotating bodies. These rotating bodies as well as the pulsating blows generate highly dynamic vortex movements of filtered liquid being in contact with the membrane surface resulting in high values of shear rates thus preventing any particles or molecules to accumulate on the surface of the membrane or to enter inside the pores. Flow rate through the pores remains stable and being at a high level even with highly concentrated liquids to be filtered[103].

1.1 Specification of RVF module

The RVF laboratory module consists of two identical filtration cells (Fig.III. 1a shows one filtration cell, volume 0.2 L per cell, 1.5 L in total) in series, including two flat disc membranes fixed onto porous substrates which drain the permeate, and impeller-shaped rotating bodies attached to a central shaft [4,5]. It can install 4 membranes in total (two for each filtration cell), with total filtration area 0.048 m² are installed. Each cell (Fig.III. 1b) includes a three-blade impeller (flat blade, diameter= 138 mm, thickness= 8mm) driven by a central shaft continuously rotating (up to 50 Hz) in a 14mm gap between two porous substrate plates (membrane support in metal) which drains the permeate. This configuration gives a 3-mm-gap between the impeller and the membrane surface. Feeding fluid flows into the system from the inlet at the bottom, and go through the filtration cells along the central shaft, then retentate flow goes out of the system from the outlet at the top (Fig.III. 1c). This simple mechanical device runs continuously and generates a high shear stress as well as a hydrodynamic perturbation in the small membrane-to-impeller gap TMP (up to 300 kPa) and rotation frequency can be adjusted to optimize the operating conditions.

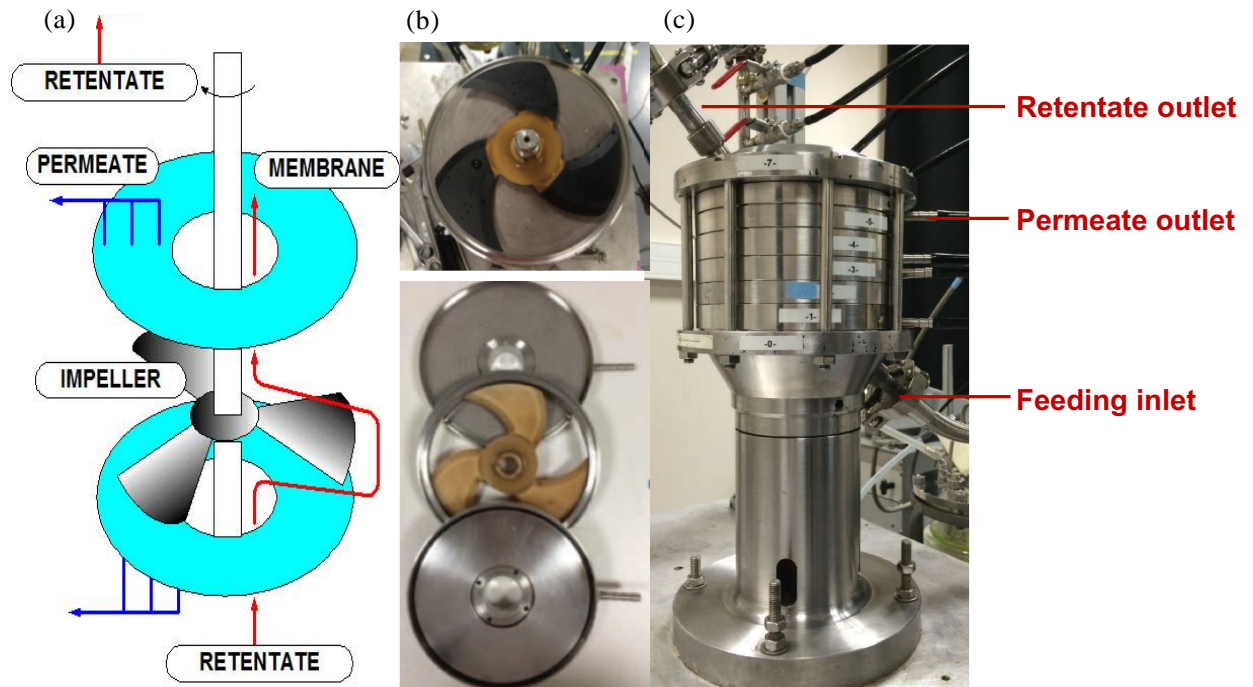


Fig.III. 1 Scheme and illustration of filtration cell and of RVF module.

1.2 Specification of membrane

Membranes were used only in the filtration of cell suspension. Hydrophilic polyethersulfone (PES, Pall, Supor®-200-6654) membranes were applied. These membranes were flat and crown-like discs, with an inner diameter of 50 mm and external diameter of 142 mm. It gave an effective filtration area $1.26 \times 10^{-2} \text{ m}^2$ per membrane by considering the correction due to the gasket (effective external diameter was about 136 mm). Manufacturer information introduces that the typical water permeability is of $6.2 \times 10^{-8} \text{ m} \cdot \text{s}^{-1} \cdot \text{Pa}^{-1}$ ($2.23 \times 10^4 \text{ L} \cdot \text{h}^{-1} \cdot \text{m}^{-2} \cdot \text{bar}^{-1}$) and a minimum bubble point (water) of 350 kPa.

1.3 General experimental set-up

As shown in Fig.III. 2, the RVF module is integrated in a fully instrumented closed circulation loop: outlet and bypass are linked back to the feeding tank. In general, in this circulation loop (4 L intotal), the feeding flow is pumped from a double-jacket feeding tank (2 L), which is connected with a thermostat to maintain a constant temperature. Flowrate is controlled by a volumetric pump (Head: TUTHILL CO., series A54739, Drive: GROSCOPP CO., series PM8014, 3800RPM, DC motor control unit: DART 250G series) and measured by a flow meter (Altometer IFM 1080/6). Temperature and pressure are measured by thermal sensor

Chapter III: Materials and Methods

(PT100) and pressure gauge (Endress Hauser Cerabar S PMC 731, $0-4 \times 10^3$ kPa), both installed at the inlet and outlet, respectively. A third thermal sensor is fixed in the feeding tank. Power consumption of the RVF module is calculated by the measurement of current (Ammeter, LEM Co. AC current transducer AT-B10) and tension (Voltmeter, SINEAX U 504 31 LD). All the sensors are connected to a digital data acquisition system (AGILENT 34972A LXI), and converted to numerical data record by a PC.

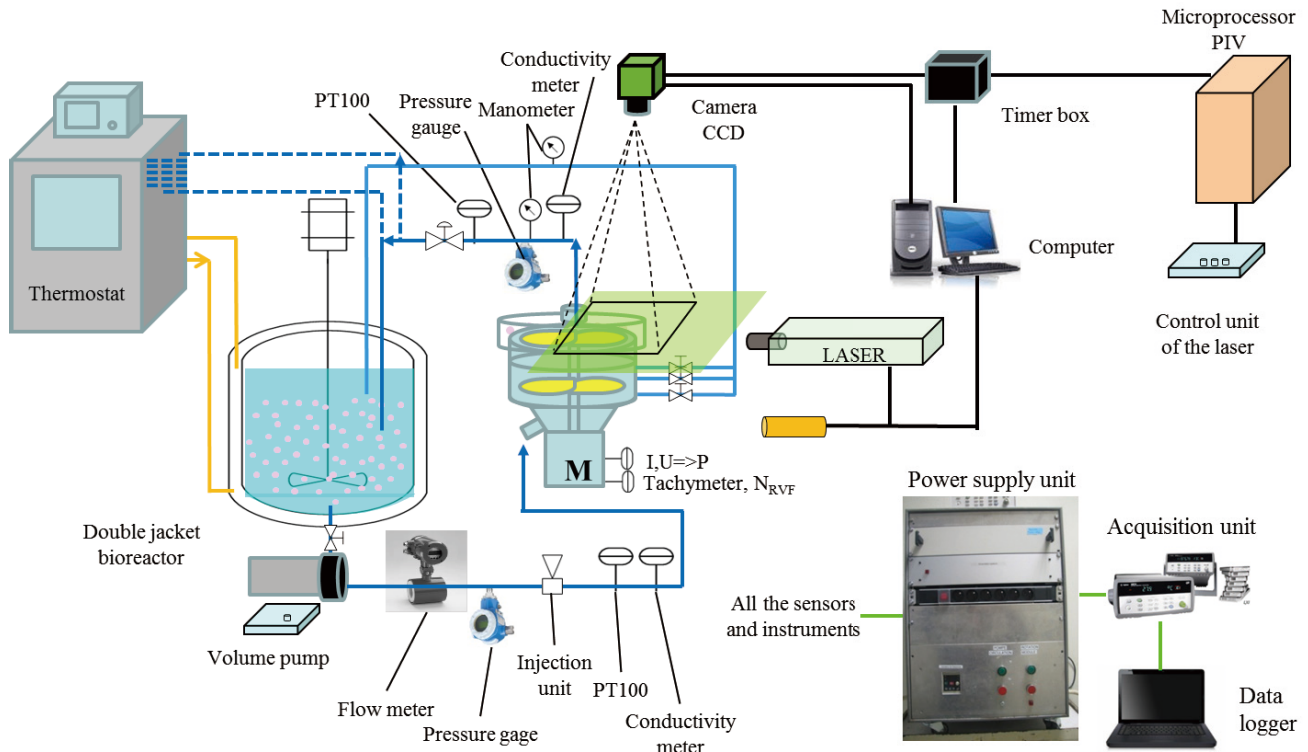


Fig.III. 2 All equipment used in this study

In this part, a list of all the material including devices, sensors and equipment are summarized in Table III. 1, information of usage are indicated by “○” in the given experiment.

Table III. 1 Devices and materials used in all experiments

Sensors/ devices	Ref.	Measure	Range- Precision	General	RTD	PIV	Cell
Feeding pump: Head: TUTHILL CO., series A54739, Drive: GROSCHOPP CO., series PM8014, 3800RPM, DC motor control unit: DART 250G series	Pump	/	0-300 L/h	○	○	○	○
Flowmeter Altometer IFM 1080/6 (Meter size : DN 15mm)	Q_f	Flowrate	5% error of flowrate (actual value), limit flow velocity at 0.4 m/s, reference conditions: water, 10-30°C	○	○	○	○
Pressure gauge Endress Hauser Cerabar S PMC 731	P _{in}	Pressure of inlet	To TD 10:1: $\pm 0.1\%$ of set span; for TD 10:1 to 20:1 $\pm 0.1\% \times [\text{normal value}/(\text{set span} \times 10)]$ of set span	○		○	○
	P _{out}	Pressure of outlet		○		○	○
Manometer	P	Manometer	0-6 bar	○	○	○	○
Temperature sensor PT100	T _{in}	Temperature of inlet	Ref. SFE50-A3-T-0, 15-4-100-R-IP68, -50°C - +260°C ($\pm 0.2^\circ\text{C}$)	○		○	○
	T _{out}	Temperature of outlet	Ref. SFE50-A3-T-0, 15-4-100-R-IP68, -50°C - +260°C ($\pm 0.2^\circ\text{C}$)	○		○	○
	T _{reactor}	Temperature of reactor		○		○	○
Conductimetre Conducell 4USF-PG325 (SN:238 999-2519)	σ_{in}	Conductivity of inlet	1-500000 $\mu\text{S}/\text{cm}$ ($\pm 1\%$ par decade), 4 - 20mA, 100W, 0.4 - 2V, 220 VAC		○		
	T- σ_{in}	Temperature of inlet	-20 / +150°C (Class A, $\pm 0,5^\circ\text{C}$), 4 - 20mA, 100W, 0.4 - 2V, 220 VAC		○		
Conductivity meter KEMOTRON type 9147 Integral flow (SN:36036) Box Knick type Stratos2402Cond (SN:66610/8214784/0614)	σ_{out}	Conductivity of inlet	5-200000 $\mu\text{S}/\text{cm}$ ($\pm 3\%$ per decade)		○		
	T- σ_{out}	Temperature of inlet	-20 / +150°C (Class A, $\pm 0,5^\circ\text{C}$)		○		
Ammeter AT 20 B 10 LEM KR 02	I	Current (RVF)	Input: 20A, Output: 0-10v, precision $\pm 0.3\text{A}$	○	○	○	○

Chapter III: Materials and Methods

Voltmeter Camille bauer Ref: Sineax u 504 31 Id 100 70/ 991602007/ 15	U	Voltage (RVF)	Tech. Info. Input: 0-250v 50Hz, Output: 0-20mA R: 750 Ohm, precision $\pm 0.2V$	<input type="radio"/>	<input type="radio"/>	<input type="radio"/>	<input type="radio"/>
Tachymeter Testo 460, Germany	N	Rotation speed	100-29999 RPM, $\pm 0.02\%$ of mv, resolution 0.1 RPM (100- 999.9 RPM) 1 RPM (1000 to 29999 RPM)	<input type="radio"/>	<input type="radio"/>	<input type="radio"/>	<input type="radio"/>
CCD Camera DANTEC Dynamic. Flow sense EO 4M (DENMARK)	Camer a	/	fps at full resolution 20.4, sensor resolution 2048 \times 2048, interframe time 200 ns, pixel size 7.4 μm			<input type="radio"/>	
Pulse laser LISTRON L200-15 PIV	Laser	/	Repetition Rate 0-15 Hz, Max output Energy at 532nm 1200 mJ, pulse duration 4 ns, wave length 1064 nm, 532 nm, laser medium Nd:YAG			<input type="radio"/>	
Data logger, Agilent 34972A LXI Acquisition / Switch Unit	Data logger	/	3-slot mainframe with built-in GPIB and RS232 interfaces, 6 1/2-digit (22-bit) internal DMM, scanning up to 250 channels per second	<input type="radio"/>	<input type="radio"/>	<input type="radio"/>	<input type="radio"/>
Thermostat PolyScience Model 9705-BB, serial No. GD6840	Therm ostat	/	Type: Refrig/Heat, temperature range: -45°C – 150°C , reservoir capacity: 13 L,	<input type="radio"/>	<input type="radio"/>	<input type="radio"/>	<input type="radio"/>
Bioreactor+motor Lenze D-32696 External Germany	Biorea ctor	/	Volume of reactor 2 L (installed with two impeller: rushon and marine), Motor: 55W, 3000 1/min, 0-5 A, 180 V	<input type="radio"/>	<input type="radio"/>	<input type="radio"/>	<input type="radio"/>
Optical trigger Monarch Instrument ROS Serial No.1898218	Trigger	/	Speed range 1-250,000RPM, working temperature -10°C - $+70^{\circ}\text{C}$, 40 mA, 3-15 V			<input type="radio"/>	
Membrane	Membr ane	/	/				<input type="radio"/>

2 Experiment fluids

Abiotic and biotic experimental fluids were used for global and local approaches. In this part, water and BREOX solution were used in RTD and PIV experiments to access to turbulent and laminar regimes; two tracers NaCl solution (for RTD experiment) and Rhodamine suspension (for PIV experiment) were introduced; *Escherichia coli* (*E. coli* WK6) cell suspension was presented and used in the filtration experiments.

2.1 Abiotic approach

2.1.1 Water

Water was used in RTD and PIV experiment to achieve turbulent flow regime. Properties of water are well known. Thermal – physical properties and their thermal dependency were taken from literature [177]. Properties of Water in the Range 0-100°C. At 20°C, their values are: density $\rho = 998.2 \text{ kg/m}^3$, specific heat capacity at constant pressure $C_p=4181.8 \text{ J/(kg}\cdot\text{°C)}$, viscosity $\mu=1.0 \text{ Pa}\cdot\text{s}$. (under 100 kPa).

2.1.2 BREOX solution

A water soluble and viscous transparent Newtonian fluid (BREOX® Polyalkylene Glycol 75 W 55000, BASF) was used in abiotic investigations. The thermo-physical properties including viscosity μ [Pa·s], density ρ [kg/m³], heat capacity C_p [J/(kg·°C)] were respectively measured with a rheometer (HAAKE Mars III, SN: 4201100100779, Thermo Scientific, Germany, torque range: 10⁻⁸ to 0.2 N·m, rotation speed range: 10⁻⁷ to 4500 RPM), a density meter (DE40, SN: MPK38384, Mettler Toledo, France, range: 10⁻⁴ to 3 g/cm³ ± 10⁻⁴ g/cm³, 4 to 90°C ± 0.05°C), and a differential scanning calorimeter (Micro DSC-III, SN: 60/50287.06.102, Setaram, France, temperature range: -20 to +120°C, thermal kinetics: 10⁻³ to +1.2°C and fluxmeter range: 0.2 μW to 20 mW, resolution: 40nW). These three properties μ , ρ and C_p are described as functions of temperature T [°C] (15 to 45°C) and mass concentration C [w/w, %] as follows:

$$\begin{cases} C_p = aT + b \\ a = -14.8C^2 + 16.3C - 1.46 \quad (R^2 = 0.974) \\ b = -2.17 \times 10^3 C + 4.30 \times 10^3 \quad (R^2 = 0.972) \end{cases} \quad (\text{III.1})$$

$$\begin{cases} \rho = dT + c \\ c = 0.185C + 1.00 \quad (R^2 = 0.999) \\ d = -9.74 \times 10^{-4}C - 2.58 \times 10^{-4} \quad (R^2 = 0.999) \end{cases} \quad (\text{III.2})$$

$$\begin{cases} \ln\mu = -\frac{Ea}{R} \left(\frac{1}{T + 273} - \frac{1}{T_r + 273} \right) + \ln\mu_r \\ Ea = -1.80 \times 10^4 C - 1.90 \times 10^4 \quad (R^2 = 0.964) \\ \ln(\mu_{20}) = -7.88C^2 + 19.7C - 6.78 \quad (R^2 = 0.999) \end{cases} \quad (\text{III.3})$$

where coefficients a, b, c, d are functions of C [w/w, %] in Eq.III.1 and 2; Temperature dependence of μ is fitted with the Arrhenius-type equation, with Ea is the activation energy in kJ/mol, R [$\text{J} \cdot \text{mol}^{-1} \cdot \text{K}^{-1}$] is the universal gas constant, μ_r is the viscosity in Pa·s at reference temperature, $T_r = 20^\circ\text{C}$. Then, properties of BREOX solutions are estimated by Eq.III.1, 2, 3. By knowing the properties of BREOX solution, two concentrations were used in RTD and PIV respectively, properties are shown as the follows:

(1) 35% w/w BREOX-water solution was used in RTD experiment, with $\mu = 0.35$ Pa·s, $C_p = 3650$ J/(kg·°C) and $\rho = 1040$ kg/m³ at $T=20^\circ\text{C}$.

(2) 40% w/w BREOX-water solution was used in PIV experiment, with $\mu = 0.85$ Pa·s, $C_p = 3274$ J/(kg·°C) and $\rho = 1067$ kg/m³ at $T=20^\circ\text{C}$.

2.1.3 Tracer solutions

2.1.3.1 Salt solutions (RTD)

RTD experiments are examined by introducing a non-reactive tracer into the system at the inlet, and the concentration of the tracer is changed according to a known function [177] and the response is found by measuring the concentration of the tracer at the outlet. The selected tracer should not modify the physical properties of the fluid and the hydrodynamic condition in the system. The tracer should have several properties (1) non-reactive (2) easily detectable (3) properties similar to the fluid in the system (4) completely soluble (5) should not adsorb [178].

In RTD experiment, 100 g/L NaCl solution was chosen and it was injected to the experiment loop with a 5 mL syringe. NaCl solution was prepared by dissolving NaCl in demineralized water for turbulent regime investigation, and dissolving in 20% BREOX solution for laminar regime investigation, although test fluid was 35% BREOX solution, 20% BREOX

solution was easier to be injected and we assumed that 5 mL injection quantity was negligible and it would not significantly change the properties of test fluid.

2.1.3.2 Rhodamine suspensions (PIV)

Fluorescent polymer particles called Rhodamine B (FPP-RhB-10, 1-20 μm , DANTEC DYNAMICS) were used, they have homogeneous distribution and good ability to present the flow motion and scatter the light from laser beams in fluid. Particles have spherical shape with a mean particle size 10 μm (range from 1-20 μm), a density of 1190 kg/m^3 and a refractive index of 1.479. Pretreatment was conducted with sonication (Elmasonic S 60 H, 50/60 Hz) for desegregating of particles in test fluid (water and BREOX solutions).

2.2 Escherichia coli (*E. coli* WK6) cell suspension (partnership with Hazar KRAIEM, PhD IPT/LISBP)

For prokaryote cell suspension cultivation, *E. coli* WK6 cells from a glycerol stock were initially plated on LB-agar plate containing appropriate antibiotics and incubated overnight at 37 °C, one single colony was later inoculated into 5 mL LB medium supplemented with appropriate antibiotics and cultured overnight at 37 °C with shaking at 225 RPM. Further transferred and cultured in 2000 mL Erlenmeyer flask of minimal medium culture used to inoculate 1.5L of MM media in a 5L bioreactor. At first the fermentation was run in batch mode, dissolved oxygen level was maintained at required saturation with increasing the stirring and aeration speed (VVM , RPM) proportionally to the need ($\text{PO}_2 > 20\%$). The Cultivation temperature and pH were set at 37 °C and 6.8 respectively by the addition of ammoniac solution (14%). Before switching to fed-batch/oxidative mode, the dissolved oxygen was used as a guide of the amount of Glucose, where the last one is completely consumed (10g/l), the PO_2 increase considerably. At the end of cultivations, fermentation broth was harvested from bioreactor. Biomass concentration was 7.61g CDW (cell dry weight) per liter determined by using Eppendorf for dry matter. 500 mL *E. coli* suspension was stored at 2°C in the refrigerator.

3 Global investigations: Residence Time Distribution (RTD) and thermal balance

Flow patterns in continuous systems are usually too complex to be experimentally measured or theoretically predicted from solutions of the Navier–Stokes equation or statistical mechanical considerations. The residence time of an element of fluid is defined as the time elapsed from its entry into the system until it reaches the exit [179]. RTD theory, experimental set-up and methodology are presented in this part.

3.1 Theory of RTD

The distribution of these times is called the RTD function of the fluid $E(t)$, or E -curve, and represents the fraction of fluid leaving the system at each time [179]. Practically, experimental injection cannot be a perfect and direct signal. In the experiment point of view, normalized signals $x(t)$ and $y(t)$ were defined for inlet and outlet, presents as Eq.III.4. The product of the convolution can be replaced in the Laplace domain by a simple product, where $X(s)$, $Y(s)$ and $G(s)$ are the Laplace transform of $x(t)$, $y(t)$ and $E(t)$, as Eq.III.5 presents:

$$y(t) = \int_0^t E(u)x(t-u)du \quad (\text{III.4})$$

and

$$Y(s) = G(s)X(s) \quad (\text{III.5})$$

Practically, $x(t)$ and $y(t)$ are calculated from experimental signal $C_{in}(t)$ and $C_{out}(t)$ respectively, expressed as Eq.III.6, and its cumulative function can be obtained as Eq.III.7.

$$E(t) = \frac{C_{out}(t)}{\int_0^{\infty} C_{out}(t)dt} \quad (\text{III.6})$$

$$F(t) = \int_0^{\infty} E(t)dt \quad (\text{III.7})$$

RTD function can be expressed by moments and centered moments of orders Γ [180].

The mean residence time, t_s , is characterized by a moment of first order, Γ^1 . The holding time, a theoretical value τ , is calculated by the volume of the test system and the feeding flow

Chapter III: Materials and Methods

rate, as Eq.III.9 shows. For most of the simple system, t_s and τ must be equal, the closer they are, the closer to the ideality. However, in some complex system, it is not the case. By knowing t_s - τ ratio k as Eq.III.10 presents, flow behavior can be diagnosed if system has a shortcut of exit or a circuit in the dead zone (volume V_2), effective volume V_1 is defined by t_s .

$$\Gamma^1 = t_s = \int_0^{\infty} tE(t)dt \quad (\text{III.8})$$

and

$$\tau = \frac{V}{Q_f} \quad (\text{III.9})$$

and

$$k = \frac{t_s}{\tau} \quad (\text{III.10})$$

The centered moments of second order, $\Gamma^{2'}$, presents the variance σ^2 , as Eq.III.11 shows, and its corresponding dimensionless term β^2 , as Eq.III.12 shows. The second centered moment is a very important parameter to describe the width of a distribution, ideal plug flow reactor has $\beta^2 = 0$, $\beta^2 > 0$ indicates an axial dispersion, the smaller the value the narrow the distribution curve and the lower the axial dispersion as well [181].

$$\Gamma^{2'} = \sigma^2 = \int_0^{\infty} (t - t_s)^2 E(t)dt = \int_0^{\infty} t^2 E(t)dt - t_s^2 \quad (\text{III.11})$$

and

$$\beta^2 = \frac{\sigma^2}{t_s^2} \quad (\text{III.12})$$

The centered moments of third order, $\Gamma^{3'}$, presents the skewness, as Eq.III.13 shows. It is helpful to determine the symmetry where $S=0$ indicates a symmetrical distribution, a left-skew distribution for $S<0$ and a right-skew distribution for $S>0$.

$$\Gamma^{3'} = S = \int_0^{\infty} (t - t_s)^3 E(t) dt \quad (\text{III.13})$$

The centered moments of fourth order, $\Gamma^{4'}$ as Eq.III.14 shows, estimates the spread of the RTD, indicates the kurtosis of the distribution function, it describes how heavy-tail (spread) the curve distributes.

$$\Gamma^{4'} = \int_0^{\infty} (t - t_s)^4 E(t) dt \quad (\text{III.14})$$

All moments and centered moments of order can be calculated. However, researchers point out the quality of the signals often leads to non-significant or unreliable results for the moment of higher order.

3.2 RTD set-up

Basic elements in RTD set-up was shown in *Chapter III 1.3 General experimental set-up*, see devices used in this experiment and their specification in Fig.III. 2 and Table III. 1.

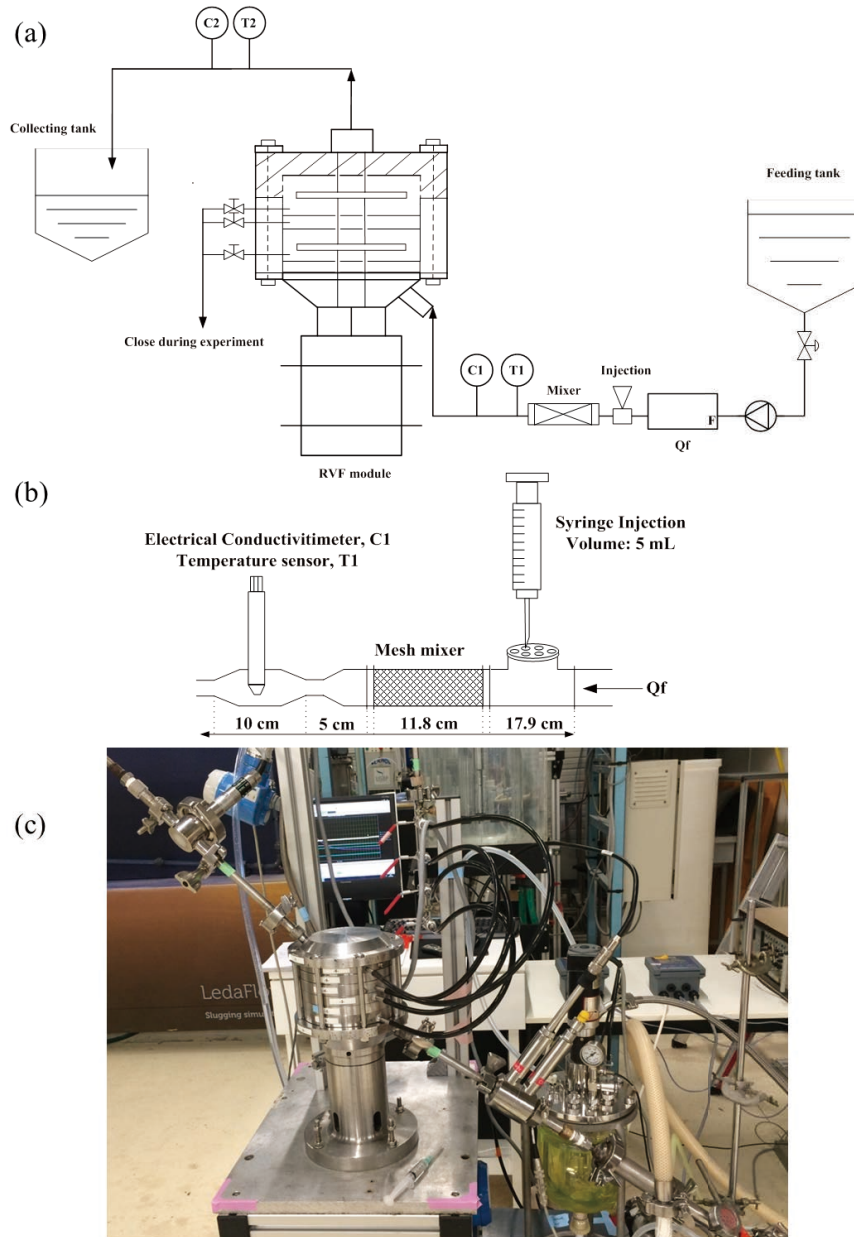


Fig.III. 3 Experimental set-up and injection device (a) C1, C2: Electrical conductivity measurement; T1, T2: Temperature measurement; Q_f : Feeding flow rate, (b) Injection device.

As the schematic Fig.III. 3 shows, this set-up was specifically implemented with:

- (1) an open loop configuration and specific inlet and outlet tank

For experiment in laminar regime, test fluid was stored in a 50 L plastic tank (feeding tank) and connected to the RVF inlet, outlet was connected to 50 L plastic tank (collecting tank)

for recycling. Whereas in turbulent regime, test fluid was directly from the tap, no recycling tank was used at the outlet.

(2) tracer injection unit

An injection device connected with a mixer was developed to achieve homogenous syringe injections of the tracer, both in turbulent and laminar flow regime. Tracer solution (100 g/L NaCl solution) was injected by a 5 mL syringe and perfectly mixed by a mesh mixer, see Fig.III. 3b, (close to an ideal pulse injection) and then the tracer were measured by electrical conductivity sensors at the inlet and outlet of the RVF module.

(3) conductivity sensors at the inlet and outlet of RVF module

Two identical stainless steel straight tubes (diameter 12 mm, length 125 mm, volume 14mL) were used to connect with the probes at the inlet and the outlet of RVF module (see Fig.III. 4a). Inlet and outlet signal were detected as it illustrates in Fig.III. 4b.

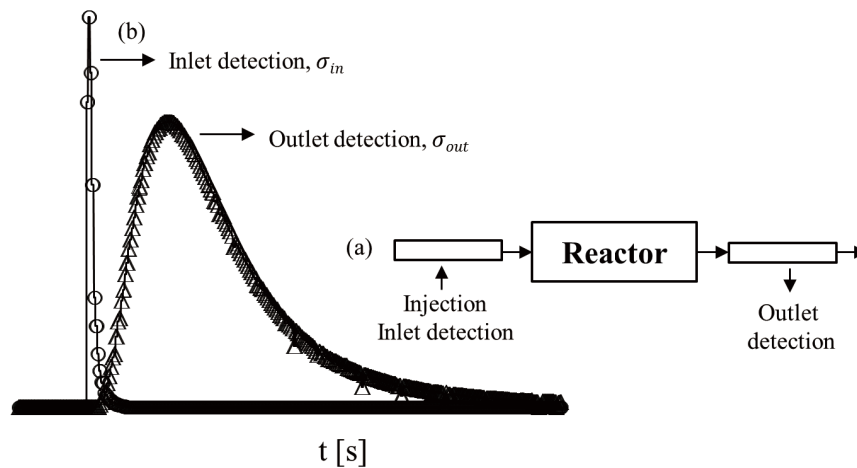


Fig.III. 4 Conductivity measurements at the inlet and outlet

3.3 Methodology

3.3.1 RTD: data treatment and analysis

In this study, the tracing experiments were carried out according to the methodology described by Thereska et al[182]. The experimental distribution functions must provide basic data to diagnose the functioning of industrial processes.

Chapter III: Materials and Methods

In the first step, a set-up with fluid circulation connected with RVF module and related sensors were conducted (concerning to optimize the experiments and the quality of the measurements).

In the second step, experiments were conducted with designed experiment protocol and data was acquired.

In the third step, experiment raw data processing was performed by smoothing, convolution, background noise reduction, data selection, normalization and standardization. Raw data of conductivity was acquired by data logger, expressed as σ_{in} and σ_{out} at temperature T_{in} and T_{out} , were recalculated at T_{ref} (25°C), based on equation $\sigma = \sigma_{25^\circ C} + a \cdot T_{25^\circ C}^n \cdot (T - 25)$, with $a=0.022$ and $n=0.93$ [183]. Base line was then subtracted and conductivity signal $\sigma - \sigma_0(t)$ were converted into concentration. Mass balance was established by comparing inlet and outlet signal. $q_{in} = \int_0^\infty C_{in}(t) \cdot Q(t) \cdot dt$ and $q_{out} = \int_0^\infty C_{out}(t) \cdot Q(t) \cdot dt$. Concentration signal was normalized by total amount of detection, normalized distribution function for inlet and outlet was identified by $x(t) = \frac{C_{in}(t)}{\int_0^\infty C_{in}(t)dt}$ and $y(t) = \frac{C_{out}(t)}{\int_0^\infty C_{out}(t)dt}$, by taking the contribution of injection effect into account (with perfect injection, x(t) can be ignored and distribution function can be expressed by $E(t) = \frac{C_{out}(t)}{\int_0^\infty C_{out}(t)dt}$). Thereafter, cumulative function can be calculated by $X(t) = \int_0^\infty x(t)dt$ and $Y(t) = \int_0^\infty y(t)dt$.

In the fourth step, moment (or center moment) was discussed concerning mean residence time, and the characteristics of RTD curve including symmetry, spreading, and dispersion. This distribution and analytical solutions enable to diagnose the behavior of the reactor as a function of various operating conditions.

In the fifth step, a systemic approach is then conducted by software (DTS Progepi, RTD Software Analysis). This step relies on the identification of parameters (Assumption of a model based on the interconnection of elementary reactors more or less complex) by adjusting the simulated response and experience. The relevance of such an approach is based both on the quality of the experimental measurements, and the interpretation of the related data with the structure of the reactor and the compact model proposal (minimization of degrees of freedom).

The evolution of the parameters identified according to the operating variables allows then to propose various simple predictive modes (details are reported in *Chapter III 3.3.3*).

In the sixth step, a CFD program was processed to simulate the flow streamlines and indicate the further information of mixing effect.

3.3.2 Power consumption and thermal balance

In order to realize thermal balance, power consumption of RVF module was measured during RTD experiment or estimated from power consumption curve.

3.3.2.1 Power consumption

Power consumption was measured at the RVF motor by recording current IC and voltage U signals, (see sensors in diagram Fig.III. 2, specification in Table III. 1), and it gives:

$$P_{RVF} = U \times IC \quad (II.15)$$

3.3.2.2 Thermal balance

The flow is supposed to be incompressible and stationary, and we neglect the gravity neglected. A non-slip condition is imposed on the walls and the inlet speed profile is the same as the outlet profile, then it gives:

$$\Delta P \cdot Q + \iint_A \sum_{j=1}^3 \sum_{i=1}^3 \tau_{if} n_i U_j ds + \iint_A \sum_{i=1}^3 (-P) n_i U_i ds = \iiint_D \rho \varepsilon_V dv \quad (III.16)$$

1st term: necessary pump power to drive the fluid in the circulation loop;

2nd term: external viscous forces of by the impeller;

3rd term: external forces of the pressure by the impeller;

4th term: total power dissipation in the field.

Moreover, we assume the uniform temperature at the input and output sections and the heat capacity independent of T, heat dissipation can be simplified by effective power:

$$P_{eff} = \iiint_D \rho \varepsilon_V dv = \rho C_p (T_{inlet} - T_{outlet}) Q_f \quad (III.17)$$

3.3.3 Experiment strategy and operating procedure

The hydrodynamic study of Residence Time Distribution were conducted according to a defined conditions and procedures. Each experiment was studied in function of the various operating conditions concerning different test fluids, feeding flowrates, and mixing rate of RVF module in both laminar and turbulent regimes. Friction and power consumption curves enable to identify a flow regimes [5], and experiments were conducted under both laminar ($Re_{mixing} < 1200$) and turbulent flow ($Re_{mixing} > 3 \times 10^4$). During all the measurements, the fluid properties and operating parameters were stable, inlet fluid temperature is at 13 - 15°C (+/- 0.1°C) under turbulent flow (tap water), 17 - 22°C (+/- 0.14°C) under laminar flow. Data acquisition rate is 0.167-0.2s Experimental conditions and procedures were presented in Table III. 2. This strategy allows determining the flow behavior according to the related variables. It also allows comparing the system characteristic with the existed model to predict the future operating conditions and optimize the performance of the system design.

Table III. 2 Operating procedure of RTD experiment

Laminar flow regime		Turbulent flow regime
Test fluid	BREOX 35% solution, $\mu = 0.35$ Pa·s	Tap water, $\mu = 1$ mPa·s
Step 1	Circulation with BREOX solution, close permeate loop (recycle fluid by collecting at the outlet to a tank) $Q_f = 25, 50, 100$ L/h	Circulation with water, close permeate loop (no recycling) $Q_f = 50, 100, 150, 300$ L/h
Step 2	Set rotation speed $N = 0, 2, 10, 25$ Hz	Set rotation speed $N = 0, 2, 10, 25, 50$ Hz
Wait until steady state (check $Q_f, N, T_{in}, T_{out}, P_{in}, P_{out}$)		
Step 3	Inject tracer (100 g/L NaCl+20% BREOX solution) with 5 mL syringe at injection point (Fig.III. 3)	Inject tracer (100 g/L NaCl+water solution) with 5 mL syringe at injection point (Fig.III. 3)
Wait until steady state (check $\sigma_{in}, \sigma_{out}$)		
Step 4	Each experiment was repeated 3 times (50 L 35% BREOX solution was reused during all the experiment)	Each experiment was repeated 3 times
Step 5	Take sample after each experiment for viscosity μ control. μ of these samples is measured by rheometer HAAKE Mars III)	/

3.3.4 Method of modeling: systematic analysis

A software (DTS Progepi v4.2,) was used to correctly simulate the experimental response to an input of any complex set-up consisted of connected elementary reactor [184]. The formulation of RTD constitutes an efficient means for a better understanding of the hydrodynamic phenomena which intervene in the RVF module which can be confronted either with numerical simulation (CFD) or with bio-performances concerning biological activity. This step is based on the identification of parameters (hypothesis of a model based on the interconnection of elementary reactors more or less complex) by adjusting the simulated response according to the experimental data. The relevance of such an approach depends on the quality of the experimental measurements, the interpretation of the data in relation to the reactor structure and the compact model proposal (minimization of degrees of freedom). The evolution of the parameters is identified according to the operating variables and enables to propose simple predictive RTD models for complex systems.

In terms of the type of flow encountered in a continuous reactor, there are two limiting cases, the ideal plug flow reactor (PFR) and the continuous stirred tank reactor (CSTR). In the PFR, the velocity profile at a given cross-section is flat without axial mixing of fluid elements, which therefore, all have the same residence time. In the CSTR, the fluid is perfectly stirred, which leads to a broad RTD. The flow pattern in a real reactor does not conform to the PFR or CSTR, and in some cases, it even converges. To consider the deviation from ideal flow behavior, simple models such as a cascade of N continuous stirred tank reactors (CSTR) or a dispersed plug flow (DPF) have been extensively used to model RTD experiments, in a large variety of flow systems.

System with multiple inputs or several outputs can be simulated after a convolution and a procedure of optimization. The software can also be used to calculate different models giving the same response, and the subsequent test of relevance of physical meaning of these parameters leads to the choice of realistic model. In addition, this automatic calculation requires both analysis of the distribution curves (peak, spreading, etc.) and the physical information on the process itself (volume, dimension, geometry, number of mixer, flowrate, dead volume, etc.). A good understanding about the system geometry is therefore necessary for establishing the model as similar as possible with the actual flows in the reactor to have a better prediction. The

Chapter III: Materials and Methods

software realizes optimization by Rosenbrock method, allowing simultaneously optimize up to 6 parameters in a reduced way, which corresponds to the difference, $\sum_0^{NP} [y(t)' - y(t)]^2$, between the distribution function $y(t)_{cal}$ calculated by the model and the experimental curve $y(t)$.

4 Local investigations: Particle Image Velocimetry (PIV)

PIV is one of the popular techniques to investigate local variables, which is based on the visualization measurement. PIV provides the local velocity distribution (or vector map) by tracking the particle displacement in a given time interval, which is one of the widely used technique. In DF filtration domain, PIV measurement was first applied in rotating cylindrical filters [185-187], giving details of particles path and streamlines spaced in different dimension and geometrical profile. This helped to explain the physical fouling mechanism due to the cylindrical Couette flow and the Taylor vortex flow. Figueredo-Cardero et al. [188] examined the flow field with in a thin gap between inner and outer cylinder, mainly focus on the radial behavior. Other PIV measurement have been conducted with a rotating cone filter [135], a rotating flat-sheet (wing-like) membrane bioreactor [189,190], a vibrating hollow fiber filter [123], a folded plate membrane module[191] to better explain their filter performances by flow motion. Therefore, in our study, we used this promising PIV technique to investigate local hydrodynamics.

4.1 Principle of PIV

Particle Image Velocimetry (PIV) is a visualization technique, providing instantaneous velocity vector measurements in a cross-section (target plane) of a flow, in real-time velocity maps. In general, three key elements are required: a Charge Coupled Device (CCD) camera, pulse laser source, and transparent flow field feed with tracer particles. The basic principle of PIV is that CCD camera records two images of a cross-section within a given time interval Δt , then the particle displacement between these two images was calculated via cross-correlation. With particles displacement and Δt , velocity is able to be calculated, two velocity components are also can be provided.

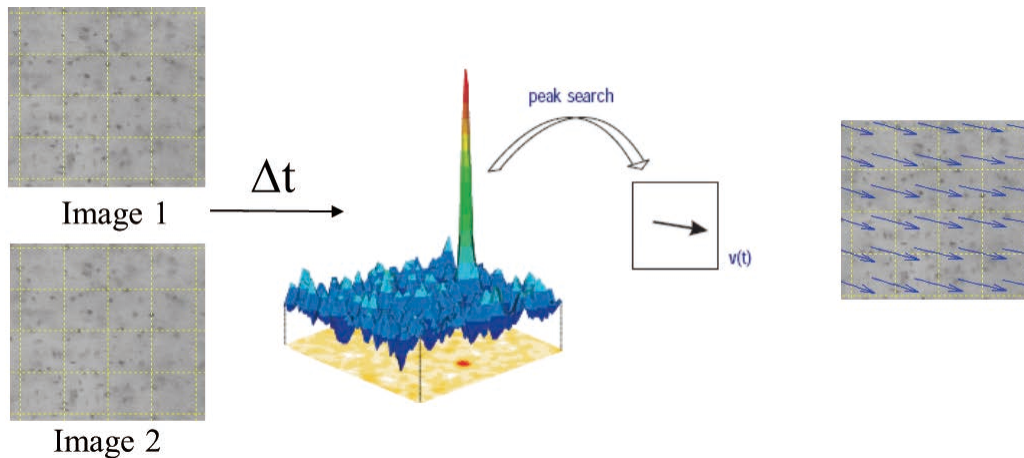


Fig.III. 5 Principle of Particle Image Velocimetry (PIV), figure modified from Nicolas DIETRICH's PhD thesis[192]

4.2 PIV set-up

In this part, experiments were conducted with PIV technique with specific set-up including horizontal and vertical measurements. Two strategy were applied for this PIV measurements, firstly, PIV system was synchronized with an optical trigger aims to measure the instantaneous velocity with the fixed impeller position; secondly, no trigger was used in the measurement in order to observe the velocity as function of time, with the rotation of impeller.

It was assumed that no impact of permeate flux on the local velocity distribution, due to its low quantity compare with the feeding flow, thus permeate loop was closed and no membrane was used.

4.2.2 Horizontal field configuration

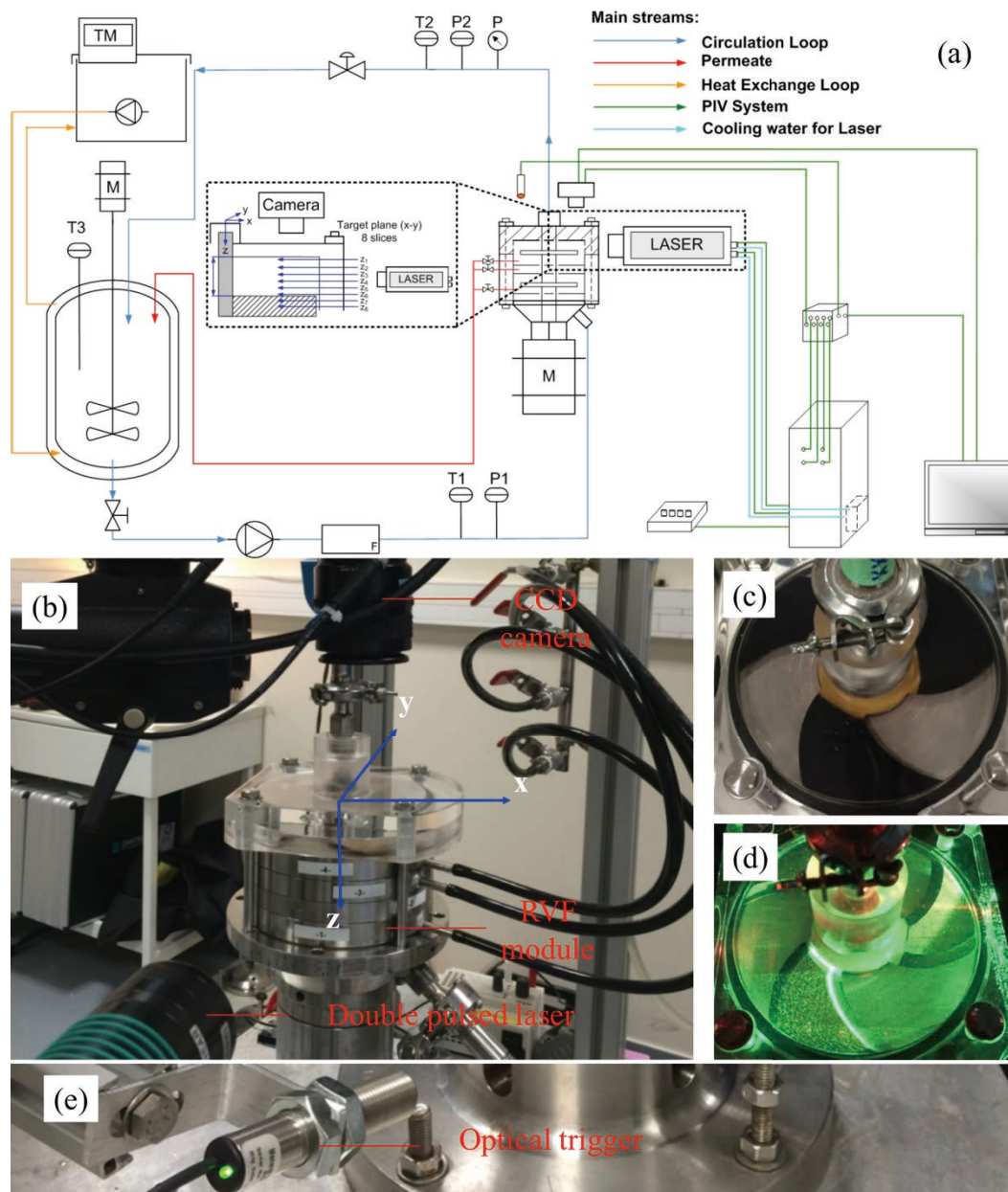


Fig.III. 6 Schematic diagram and apparatus used in the experiment (a) horizontal PIV schematic diagram (b) PIV system synchronized with a CCD camera, double pulsed laser and the RVF module with the transparent cell; (c) the transparent filtration cell installed with a black painted impeller; (d) the transparent filtration cell with laser beam (e) An optical trigger synchronized with the PIV system.

In the horizontal set-up, as it displays in Fig.III. 6a and b, the RVF module is integrated with the PIV system which has traditional elements. In this study, measurements were focused at

Chapter III: Materials and Methods

the horizontal plane (x - y plane) between the upper wall (of the filtration cell) and the impeller surface and the laser sheet could be adjusted to different slices (z_1 - z_8). PIV system was supported and maintained by DANTEC DYNAMICS Co. (Denmark), basic elements are required:

- The stainless-steel filtration cell is replaced by a transparent cell as shown in Fig.III. 6b;
- A flat light source to illuminate the target plane and the florescent particles;
- A CCD camera should focus on the target plane (perpendicular to the flat laser sheet);
- Since tracers were used in this case, a high pass red filter (>570 nm) is placed in front of the camera to allow only fluorescent light (reflected from particles) enter the camera, while reflection of the transparent cell is filtered out;
- A processor and timer box is needed to communicate with the camera and the pulsed laser.
- Importantly, with the trigger strategy, an optical trigger, as it shown in Fig.III. 6e, is connected to the timer box. In this case, acquisition signal was sent by this trigger when it detected a marker on the shaft (which drives the impeller), images were always taken with the same impeller position. With the no trigger strategy, images were always able to present the movement of the impeller.

4.2.3 Vertical field configuration

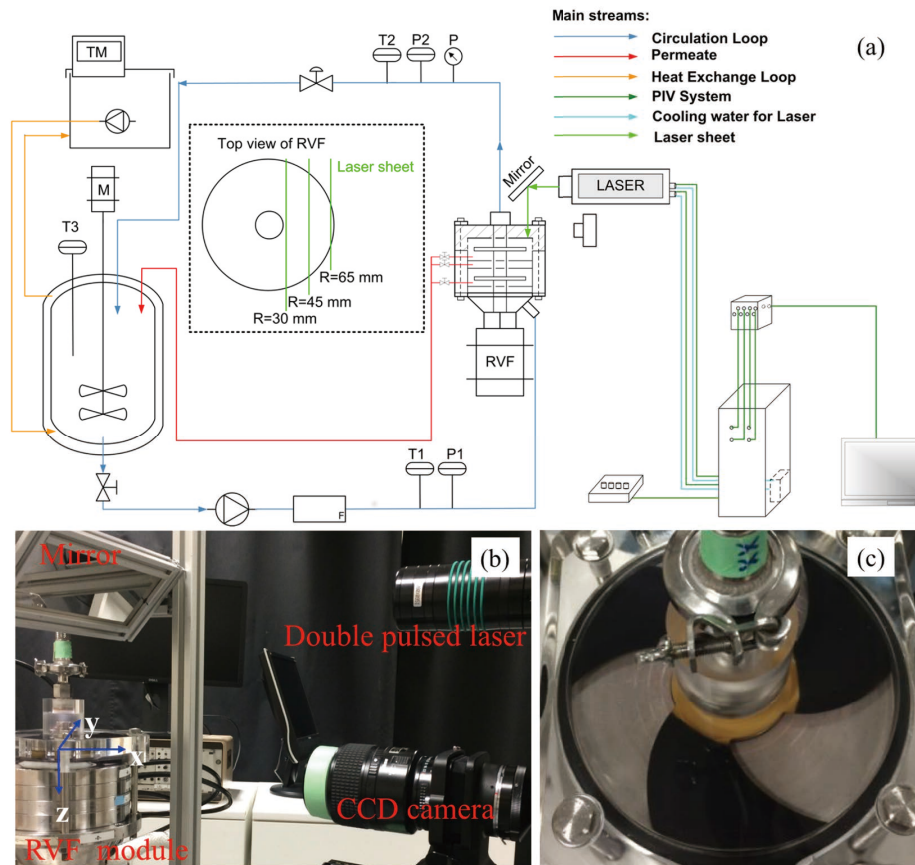


Fig.III. 7 Schematic diagram and apparatus used in the experiment (a) vertical PIV schematic diagram; (b) The PIV system synchronized with a CCD camera, double pulsed laser and the RVF module with the transparent cell; (c) the transparent filtration cell installed with a black painted impeller.

In the vertical set-up, basic elements of PIV measurement were the same with the horizontal set-up but the target plane. Target plane was shown in Fig.III. 7a, horizontal laser sheet was reflected by a mirror and then towards the vertical direction (z direction) at 3 position ($R=30$ mm, $R=45$ mm, $R=65$ mm) respectively. The CCD camera was set perpendicularly to the vertical target plane.

4.3 Experimental strategy and operating conditions

Brief experimental strategy is summarized as the follows:

- (1) for horizontal measurement, shown in Fig.III. 6a, laser sheet can be adjusted from z_1 to z_6 step by 0.5 mm in z direction from the wall to the impeller, $z_1=0.25$ mm, $z_2=0.75$ mm, $z_3=1.25$

Chapter III: Materials and Methods

mm, $z_4=1.75$ mm, $z_5=2.25$ mm, $z_6=2.75$ mm, with uncertainty ± 0.25 mm according to the thickness of laser sheet. Two additional slices were scrutinized at $z_7= 4.75$ mm and $z_8= 6.75$ mm in order to access to velocity fields between two blades;

(2) for vertical measurement, shown in Fig.III. 7a, laser sheet can be adjusted to $R=30$ mm, $R= 45$ mm and $R=65$ mm;

(3) experiments were conducted with and without optical trigger.

Table III. 3 Operating conditions

		Laminar (Breox)	Turbulent (Water)
With trigger	Horizontal	$\mu=0.8$ Pa.s 8 slices (6 gap+2) $N=2$ Hz, $Q_f = 25, 50$ L/h, 1000 pairs of images.	$\mu=1$ mPa.s 8 slices (6 gap+2) $N= 10$ Hz, $Q_f = 50, 100$ and 150 L/h, 1000 pairs of images.
	Vertical	$\mu=0.8$ Pa.s 3 slices ($R=30, 45, 65$ mm), $N= 2$ Hz, $Q_f = 50$ L/h, 300 pairs of images.	$\mu=1$ mPa.s 3 slices ($R=30, 45, 65$ mm), $N= 10$ Hz, $Q_f = 100$ L/h, 300 pairs of images.
No Trigger	Horizontal	$\mu=0.8$ Pa.s 3 slices (gap) $N=2$ Hz, $Q_f = 50$ L/h, 1000 pairs of images.	$\mu=1$ mPa.s 3 slices (gap) $N= 0, 2, 10, 25, 50$ Hz, $Q_f = 100$ L/h, 3000 pairs of images.
	Vertical	$\mu=0.8$ Pa.s 3 slices ($R=30, 45, 65$ mm), $N=2$ Hz, $Q_f = 50$ L/h, 1000 pairs of images.	$\mu=1$ mPa.s 3 slices ($R=30, 45, 65$ mm), $N= 10$ Hz, $Q_f = 100$ L/h, 1000 pairs of images.

4.4 Data treatments

4.4.1 From images to velocity fields

Taking example from the horizontal measurement with trigger strategy, experiment was performed in a field of 109×109 mm² view, and focused on one third of the filtration cell in x - y (horizontal) plane, this area was capturing one leading edge and one trailing edge. Flow field was assumed to be periodic since it was agitated by a 3-blades impeller. This 1/3 area was considered to represent the whole filtration cell. The raw image processing was evaluated by using commercial software DynamicStudio.2015a (by DANTEC DYNAMIC, Denmark). A statistical adaptive cross-relation algorithm was used to find average particles displacement with a mask input to filter the non-interested area, and iteratively adjust and determine an appropriate Interrogation Area (IA) size and shape (specified criteria is needed) to local seeding density and flow gradient. An adaptive IA window was used to start with 32×32 px² to 16×16 px² window

Chapter III: Materials and Methods

for the calculation, corresponding to $1.70 \times 1.70 \text{ mm}^2$ and $0.85 \times 0.85 \text{ mm}^2$, a 50% window overlapping was also applied to improve correlation. Therefore, each velocity map has theoretically 128×128 vectors, with about 9000 valid and 7389 disabled by the mask, while approximately 1% bad vectors had been rejected. The time interval between two images in each pair was controlled between 500-800 μsec according to different operating conditions, it only allowed the particle displacement move approximately a quarter of the window size. Other parameters can be found in Table III. 4.

Table III. 4 Acquisition parameters of PIV system (horizontal measurement)

Parameters	Setting
Calibration	Scale factor : 7.177 ; 1 pixel= $7.177 \times 7.4 = 53 \mu\text{m}$
Image size	$2048 \times 2048 \text{px}^2$ ($108 \times 108 \text{mm}^2$), 128×128 vectors (16384)
Interrogation window	adaptive PIV from $16 \times 16 \text{px}^2$ to $32 \times 32 \text{px}^2$, step size $16 \times 16 \text{px}^2$
Particle density	5-10 particles per interrogation window ($16 \text{px} \times 16 \text{px}$)
Particle size	Mean diameter of 10-20 μm
Time interval between consecutive images, Δt	500-800 μsec
Frequency of acquiring/ trigger rate	Synchronized/ Not synchronized with impeller rotation speed
Number of samples	1000 of image pairs

Same acquisition parameters of vertical measurement can be found in Table III. 5.

Table III. 5 Acquisition parameters of PIV system (vertical measurement)

Parameters	Setting
Calibration	Scale factor : 2.166 ; 1 pixel= $2.166 \times 7.4 = 16 \mu\text{m}$
Image size	$2048 \times 944 \text{px}^2$ ($32.8 \times 15.1 \text{mm}^2$), 128×59 vectors (7552)
Interrogation window	adaptive PIV from $16 \times 16 \text{px}^2$ to $32 \times 32 \text{px}^2$, step size $16 \times 16 \text{px}^2$
Particle density	2-5 particles per interrogation window ($16 \text{px} \times 16 \text{px}$)
Particle size	Mean diameter of 10-20 μm
Calibration	Scale factor : 2.166 ; 1 pixel= $2.166 \times 7.4 = 16 \mu\text{m}$
Time interval between consecutive images, Δt	10-300 μsec (depends on each case)
Frequency of acquiring/ trigger rate	Synchronized/ Not synchronized with impeller rotation speed
Number of samples	300-1000 of image pairs

4.4.2 Interpolation

Velocity profile at the given positions was calculated by Inverse Distance Weighting Interpolation (IDW) as the following equation:

$$U_m(x, y) = \frac{\sum_{j=1}^n [U_m(x_j, y_j) \cdot w_j]}{\sum_{j=1}^n w_j}, \quad \text{with } w_j = \frac{1}{h_j^p} \quad (\text{III.18})$$

where w_j is a weight factor assigned by the distances h_j between the reference points (value-known) and the interpolation point (value-unknown). $U_m(x, y)$ is the interpolation point and $U_m(x_j, y_j)$ is the neighbor vector as a reference input, n is the number of reference vectors and we put 4 in this case, p is an exponent value (power index, default value 2), determines how quickly the influence of neighboring points drops off, the higher value the closer vector influence more. By this method, velocity profiles at any given position in the gap can be reported.

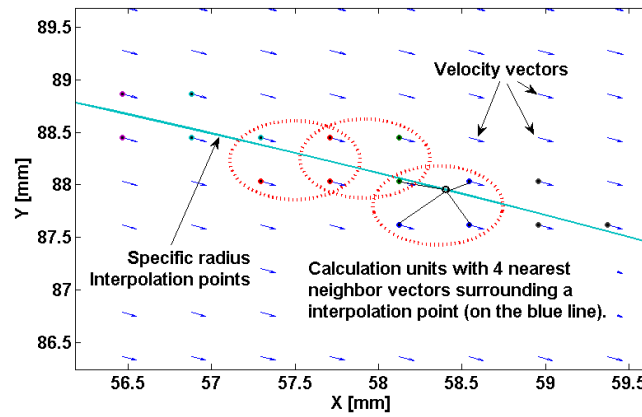


Fig.III. 8 Velocity calculation at the specific point by Inverse Distance Weighting Interpolation (IDW)

4.4.3 Statistical analysis: convergence

The proper amount of images on the flow statistics (mean values and standard deviation) was investigated by plotting the moving average of velocity, in order to determine and to optimize PIV measurements. The reliability and stability of velocity fields were verified to determine to the required minimum number of image pairs, both in the cases with trigger strategy and non-trigger strategy. In Fig.III. 9, the mean value of velocity magnitude $\overline{U_m}$ (Eq.III.19) and the standard deviation σ_I (Eq.III.20) are calculated from velocity field in random points, and are plotted as a function of image number (I). Similarly in Fig.III. 10, moving average of the velocity U (velocity in x direction), V (velocity in y direction) and their related σ_U and σ_V are presented.

$$\overline{U_{m_I}} = \frac{1}{I} \sum_{i=1}^I [U_{m_i}], \quad I = 1, 2, \dots, 1000. \quad (\text{III.19})$$

$$\sigma_I = \sqrt{\frac{1}{I} \sum_{i=1}^I (U_{m_i} - \overline{U_{m_I}})^2}, \quad I = 1, 2, \dots, 1000. \quad (\text{III.20})$$

where $\overline{U_{m_I}}$ is defined as an accumulative moving average. As well as σ_I , it is defined as an accumulative moving standard deviation.

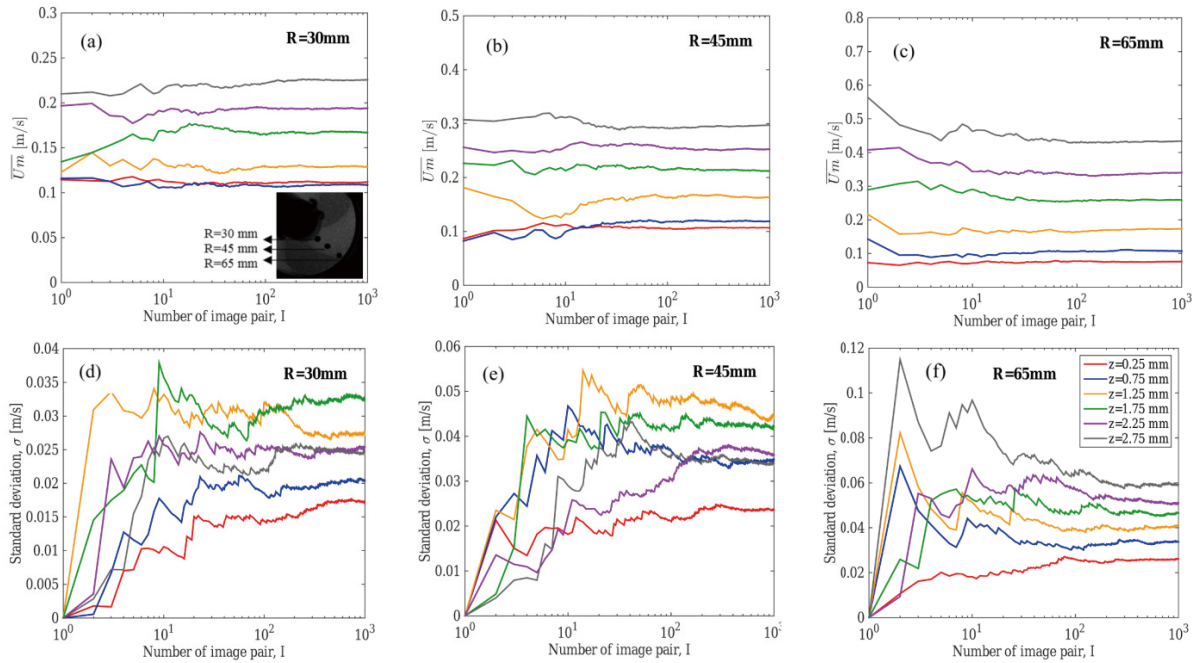


Fig.III. 9 Convergence of mean IDW velocity $\overline{U_{m_I}}$ (a, b and c) and the associated standard deviation σ_I (d, e and f) as a function of the number of image pairs I . Observations in this example are reported for 3 radius ($R=30, 45$ and 65 mm) for 6 different slices within the gap (z_1 to z_6) at $\theta=-50^\circ$, in horizontal measurement. Operating conditions: $N=2$ Hz, $Q_f=50$ L/h BREOX solution $\mu=0.80$ Pa.s, with optical trigger.

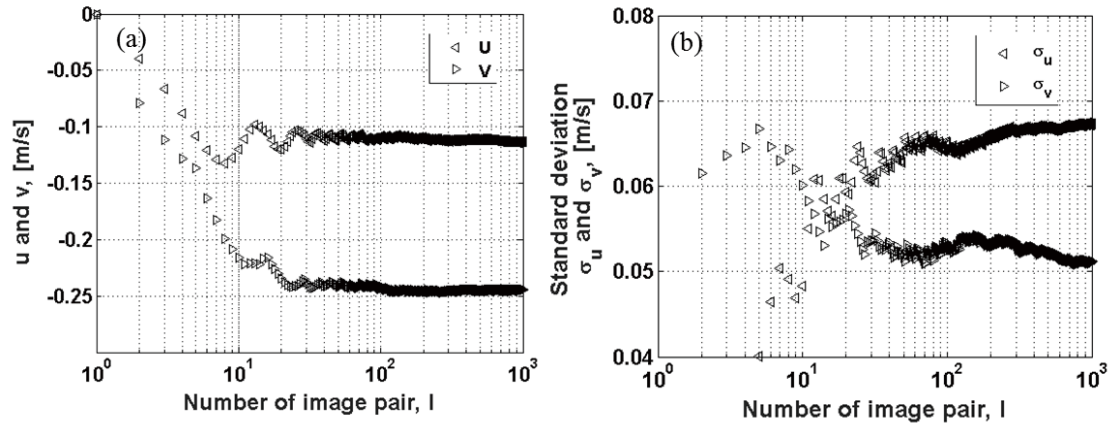


Fig.III. 10 Convergence of (a) velocity u (x direction) and v (y direction) and (b) the associated standard deviation σ_I as a function of the number of image pairs I . Observations in this example are reported for a random point in within the gap ($z=1.5$ mm) in horizontal measurement.

Operating conditions: $N=2$ Hz, $Q_f=50$ L/h, BREOX solution $\mu=0.80$ Pa·s, without optical trigger.

Result introduces by the trigger strategy, in Fig.III. 9a, b and c, an increase of mean velocity from the wall to the impeller (gap position) is observed whatever radius for position $\theta=50^\circ$. Fig.III. 9d, e and f indicate a large variation of standard deviation magnitude without correlation with gap position. For example, at $R=45$ mm for $z_I=0.25$, $z_3=1.75$ and $z_6=2.75$ mm, $\overline{U_{m_{100}}}$ values are respectively 0.1, 0.25 and 0.3 m/s whereas σ_{100} values are respectively 0.02, 0.04 and 0.035. Graphically, $\overline{U_{m_I}}$ and σ_I seems to converge to stable and constant values for $I > 50$ and $I > 100$ respectively. Some studies argued that large number of frames was needed, especially for turbulent flow characterization. Figueredo-Cardero et al. [188] proposed that 4000 image pairs had to be used, T. Li et al.[123] used a total of 300 image pairs for fouling investigation in a hollow fiber set-up, while T.Jiang et al.[193] and N.Liu et al.[194] used only a small amount around 50 image pairs for their analysis, while larger number of image pairs are required in other research fields like aeronautics and aerodynamics [195,196]. In our conditions, convergence criterion, $\left| \frac{d\overline{u_{m_I}}}{dI} \right|$ and $\left| \frac{d\sigma_I}{dI} \right|$ are defined. A constant decreasing slope of $\log \left| \frac{d\overline{u_{m_I}}}{dI} \right|$ and $\log \left| \frac{d\sigma_I}{dI} \right|$ vs $\log(I)$ is noticeable and absolute criterion, $\left| \frac{d\overline{u_{m_I}}}{dI} \right|$ and $\left| \frac{d\sigma_I}{dI} \right| < 10^{-4}$, are used to estimate the minimum requested number of image pairs. For $\overline{U_{m_I}}$ and σ_I , I superior to 200 is identified and $I=1000$ was retained, although it is overestimated.

Result introduces by the non-trigger strategy, in Fig.III. 10, instead of presenting with the IDW velocity magnitude, convergence are introduced with velocity U (velocity component in x direction) and V (velocity component in y direction). Since it is in laminar flow, velocity in both component are very stable and it converge around $I=100$. And, with the presence of impeller, it is normal that standard deviation tend to be more unstable, and it converges around $I=800$. In any case, $I=1000$ is sufficient to represent the flow statistics.

4.4.4 POD analysis

Recently, POD (Proper Orthogonal Decomposition) technique was used to extract more and more information from such huge source of experimental data [197-201]. POD is an efficient technique to process instantaneous velocity fields, enabling to reconstruct the velocity in terms of summation of modes, each mode contributing to the total kinetic energy. POD is thus a modal decomposition of instantaneous velocity fields. Modes can be derived from the Fredholm eigenvalue integral equation, adapted by Sirovich (1987)[202]. Knight & Sirovich (1990)[203] have shown that the POD eigenvalue spectrum (plot of eigenvalues versus mode number I) exhibit $I^{-11/9}$ trend characteristic of the inertial subrange of turbulence. The goal of this paper is to relate eigenvalue spectrum issued from POD to energy density spectrum. In the first part, energy density spectrum will be reconstructed from selected modes issued from POD. In the second part of the paper, the energy density spectrum (or probability density functions PDF of velocity fluctuations) will be derived in turbulent flow from “entropy information” [204,205].

4.4.4.1 Principle of POD analysis

We propose in this work to investigate POD in terms of reconstruction of instantaneous velocity fields measured by PIV technique in RVF module. POD is a modal decomposition method of instantaneous velocity fields, allows reconstructing the velocity in terms of modes, each mode contributing to the total kinetic energy. Mode can be derived from the Fredholm eigenvalue integral equation, adapted by Sirovich[203]. POD technique was enabling to extract more and more information from PIV instantaneous velocity field [197-199,201]. In this part, our objective is to reconstruct and isolate coherent structures from a series of instantaneous velocity field, to better understand the contribution of different velocity structure/motion (mean velocity, organized velocity, fluctuating velocity), and to further study the shear (mean shear, organized shear, fluctuating shear).

4.4.4.2 POD data treatment

PIV measurements were performed in the 2-D plane, x - z for example, on a regular mesh with L rows and C columns, leading to $NP = L C$ points per plane. Each instantaneous velocity field measurement constitutes a snapshot of the flow. The statistical analysis is performed on N snapshots taken in the same plane (PIV data). The number of grid points being LC , one obtains the matrix of instantaneous velocity vector data as:

$$\overrightarrow{U}_k^{(I)} = \begin{bmatrix} \overrightarrow{U}_k(x_1, z_1) & \overrightarrow{U}_k(x_1, z_2) & \overrightarrow{U}_k(x_1, z_C) \\ \overrightarrow{U}_k(x_2, z_1) & \overrightarrow{U}_k(x_2, z_2) & \overrightarrow{U}_k(x_2, z_C) \\ \overrightarrow{U}_k(x_L, z_1) & \overrightarrow{U}_k(x_L, z_2) & \overrightarrow{U}_k(x_L, z_C) \end{bmatrix} \quad (\text{III.21})$$

where k is the index of the instantaneous event ($k=1, N$). This matrix of vectors can be reshaped to build a vector \overrightarrow{U}_k with $2LC$ rows as follows:

$$\overrightarrow{U}_k = \begin{bmatrix} u_k(x_1, z_1) \\ u_k(x_2, z_1) \\ u_k(x_L, z_C) \\ v_k(x_1, z_1) \\ v_k(x_2, z_1) \\ v_k(x_L, z_C) \end{bmatrix} \quad (\text{III.22})$$

The snapshot method adopted in this eigenvalue problem was proposed by Sirovich (1987)[202]. This method is based on the snapshot matrix M corresponding to the N instantaneous velocity fields. The matrix M can be expressed as

$$M = \begin{bmatrix} u_1(x_1, z_1) & u_2(x_1, z_1) & \dots & u_N(x_1, z_1) \\ u_1(x_2, z_1) & u_2(x_2, z_1) & \dots & u_N(x_2, z_1) \\ \dots & \dots & \dots & \dots \\ u_1(x_L, z_C) & u_2(x_L, z_C) & \dots & u_N(x_L, z_C) \\ v_1(x_1, z_1) & v_2(x_1, z_1) & \dots & v_N(x_1, z_1) \\ v_1(x_2, z_1) & v_2(x_2, z_1) & \dots & v_N(x_2, z_1) \\ \dots & \dots & \dots & \dots \\ v_1(x_L, z_C) & v_2(x_L, z_C) & \dots & v_N(x_L, z_C) \end{bmatrix} \quad (\text{III.23})$$

The matrix M has $2LC$ rows and N columns, each column of the matrix M representing the k^{th} event of the instantaneous velocity field. The auto-covariance tensor R can be derived as:

$$R = \frac{1}{N} M.M^T = \begin{bmatrix} \overline{u^2(x_1, z_1)} & & \\ & \dots & \\ & & \overline{v^2(x_L, z_C)} \end{bmatrix} \quad (\text{III.24})$$

Modes can be derived from eigenvalue equation, adapted by Sirovich (1987) as:

$$R(x, z, x', z') \overline{\Phi^{(I)}}(x', z') = \lambda^{(I)} \overline{\Phi^{(I)}}(x, z) \quad (\text{III.25})$$

where R is the cross-correlation tensor and $\lambda^{(I)}$ are the eigenvalues. In the present problem, the eigenvalues are expressed in m^2/s^2 . $\overline{\Phi^{(I)}}(x, y, z)$ is a spatial eigenfunction associated to I^{th} mode. Usually eigenvalue series are ranked in decreasing order.

One of the issues of POD lies in the problem of reconstruction. Indeed, given \overline{U}_k a k^{th} event of instantaneous velocity field, it can be decomposed as:

$$\overline{U}_k(x, z) = \sum_{i=1}^N \overline{U}_k^{(I)}(x, z) = \sum_{i=1}^N a_k^{(I)} \overline{\Phi}^{(I)}(x, z) \quad (\text{III.26})$$

where $\overline{U}_k^{(I)}$ is the I^{th} component of the POD decomposition. For each mode I the POD decomposition generates temporal coefficients $a_k^{(I)}$ and spatial modes $\overline{\Phi}^{(I)}$. $a_k^{(I)}$ is an instantaneous (k) scalar (called POD coefficient of I^{th} mode); it is independent of space.

$\overrightarrow{\Phi}^{(I)}(x, z)$ is a spatial eigenfunction associated to I^{th} mode; it is independent of time (or instantaneous event k).

4.4.4.3 Reconstruction of instantaneous velocity field from POD

Each instantaneous velocity field or snapshot of the flow can be expanded in a series of POD modes. The POD coefficients $a_k^{(I)}$ are obtained by projecting each instantaneous velocity field on the I^{th} eigenfunction $\overrightarrow{\Phi}^{(I)}$:

$$a_k^{(I)} = \overrightarrow{U}_k \cdot \overrightarrow{\Phi}^{(I)} \quad (\text{III.27})$$

The coefficients $a_k^{(I)}$ are thus independent of space.

The I^{th} velocity vector $\overrightarrow{U}_k^{(I)}$ corresponding to the I^{th} decomposition is given by:

$$\overrightarrow{U}_k^{(I)} = a_k^{(I)} \overrightarrow{\Phi}^{(I)} \quad (\text{III.28})$$

One can thus reconstruct each instantaneous velocity field by:

$$\overrightarrow{U}_k(x, z) = \sum_{I=1}^N \overrightarrow{U}_k^{(I)}(x, z) = \sum_{I=1}^N a_k^{(I)} \overrightarrow{\Phi}^{(I)}(x, z)$$

which was presented in Eq. III.26.

5 Local investigation: CFD simulation in laminar flow

To simulate numerically the flow field in this dynamic filtration module, a model based on the finite element method was developed using commercial CFD software COMSOL Multiphysics (version 4.3a, U.S).

5.1 Governing equations and boundary conditions

The geometrical domain was simplified to one filtration cell of the RVF module. Assuming a periodic movement of the impeller, one third of the filtration cell is simulated and the governing equations are solved in a rotating reference frame. Considering a laminar and incompressible flow of a Newtonian fluid, mass and momentum balances were governed by the Navier Stokes equations expressed in a fixed reference frame as follows:

$$\nabla \cdot \mathbf{u} = 0 \quad (\text{III.29})$$

$$\rho \frac{\partial \mathbf{u}}{\partial t} + \rho(\mathbf{u} \cdot \nabla \mathbf{u}) = -\nabla P + \mu \nabla^2 \mathbf{u} \quad (\text{III.30})$$

where ρ is the fluid density in kg/m^3 , μ is the fluid dynamic viscosity in $\text{Pa}\cdot\text{s}$, P is the pressure in Pa, and \mathbf{u} is the velocity vector in m/s .

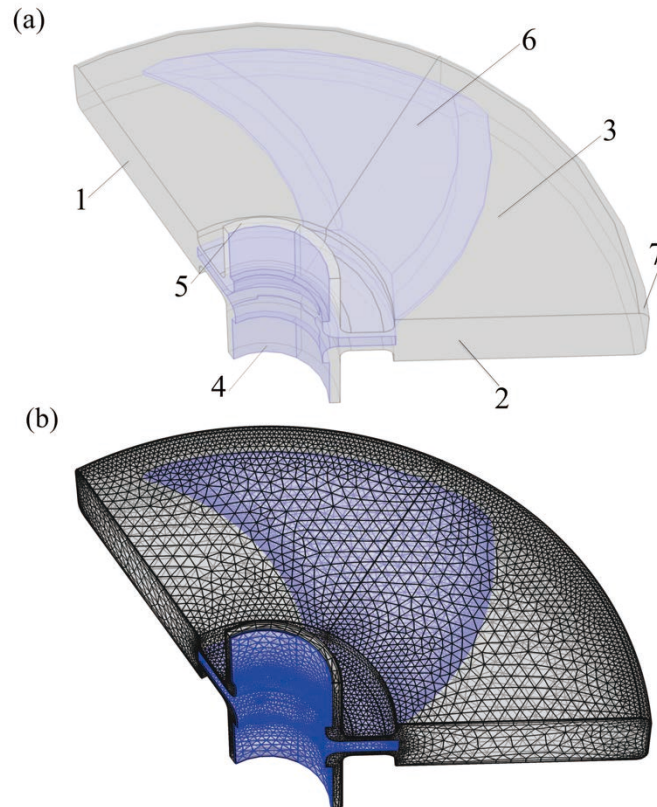


Fig.III. 11 Geometry of the RVF filtration cell (a) and calculation mesh (b) used in CFD software COMSOL 4.3a. 1 and 2: Fluid cross-sections (vertical periodic); 4 and 5: fluid cross-section for inlet (bottom) and outlet (top); 6: surface of the rotating solid impeller. 3: the upper and lower walls where the membrane are mounted; 7: surrounding wall of the filtration cell

Navier Stokes equations were solved under boundary conditions related to fluid domain, wall and impeller, which describe real working conditions:

- Simulation focused on one third of the filtration cell and flow fields were assumed to be periodic at $\theta = 0^\circ$ and 120° (Fig.III. 11a, cross-section 1 and 2);
- A mean pressure gradient, as the driving force, was imposed to the entire volume of the filtration cell across the whole length from the bottom to the top (Fig.III. 11a, cross-section 4 and 5);
- On the impeller surface (Fig.III. 11a, surface 6), radial velocity vector u_r and vertical velocity vector u_z were imposed to 0, angular velocity vector $u_\theta = 2\pi N r$, was expressed from rotation frequency of the impeller, where N is the rotation frequency [Hz] and r is the radial coordinate [m];

- Velocity vectors on all the walls, including membrane surfaces (upper and lower wall) and the surrounding wall (Fig.III. 11a, wall 3 and 7) were imposed to 0 m/s considering no-slip boundary conditions at fluid-solid interface;

5.2 Numerical method and calculation mesh

Eq. III.29 and Eq. III.30 were solved by the Rotating Machinery Model of COMSOL 4.3a, which was a time-dependent 3D problem. Selected mesh was a compromise between accuracy and reduction of the calculation time. For the simulations dealing purely with laminar flow, a physical controlled and refined mesh (automatically generated by COMSOL 4.3a) was chosen (Fig.III. 11b). Several element types were used, such as tetrahedral, pyramid, prism, triangular, quadrilateral, edge and vertex elements, with total number of 355362, total volume 55 mL. Large velocity gradient was carefully considered with local refined mesh close to the wall.

5.3 Operating conditions

For CFD simulation, a Newtonian fluid with a viscosity equal to 0.8 Pa·s was assumed to be incompressible and independent of temperature in agreement with test fluid for PIV measurements. Simulation conditions were imposed with rotation frequencies equal to 2, 5 and 10 Hz, associated with 50 L/h. One additional simulation with $Q_f=25$ L/h, $N=2$ Hz was performed to realize the impact of flowrate to the flow field.

6 Application of RVF module with *E.coli* suspension

The disruption of cells is an important step in many bioprocesses in which the target product is not secreted by a cell into the suspending solution. The level of disruption required will depend on the mechanical strength of the organism and the mechanical forces of disruption being employed [206].

The aim of this study is to determine the mechanical damage of the complex hydrodynamic to cells in dynamic filtration process. In order to achieve this, *Escherichia coli* (*E. coli* WK6) cell suspension was used in a filtration process of RVF module.

There is strong evidence that growth and differentiation of microbial cells are effected by several types of mechanical forces including stretch, strain, compression, and shear stress [207,208]. Due to the high rotation speed in the complex designed RVF module, we may wonder: What is the effect by this high shear stress when filtering cell suspensions? To answer this question, experiments were conducted with *E.coli* suspension, and different rotation speed were applied to realize the consequence.

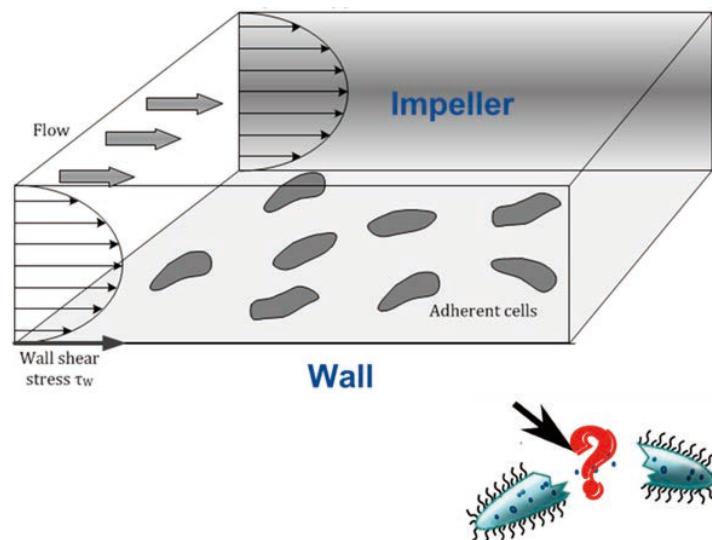


Fig.III. 12 Wall shear stress acting on adherent cells in a flow chamber with parallel plates.
(modified from [208,209])

6.1 Experiment strategy

Objective of this study is to quantify the mechanical impact by the complex hydrodynamic generated by RVF module, concerning its high shear in the system. This mechanical impact was realized by measuring particle size distribution and observation under microscope.

Particle size distribution of samples were analyzed by Diffraction Light Scattering (DLS) (Mastersizer 2000 Hydro, Malvern Instruments Ltd. SN: 34205-69, range from 0.01 to 1000 μm), repeated at least 3 time). DLS is a technique in physics that based on scattering of light, and can be used to determine the size distribution profile of small particles in suspension or polymers in solution [210]. Particles scatter light in a size-dependent way where bigger particles scatter more intensely at smaller angles and smaller particles scatter with lesser intensity at wider angles [211]. In laser diffraction technique, the scattering of light is expressed as a function of scattering angle which in turn is used to measure particle size. In this experiment, 50 mL sample was added to the DLS circulation loop. Analysis are conducted at room temperature (20°C) with obscuration rates (red $\lambda=632.8\text{nm}$ and blue $\lambda=470.0\text{nm}$ lights) ranging between 10 and 40%. Particle volume distribution and the associated cumulative curve versus particle diameter were determined. Laser diffraction analysis converts the detected scattered light into a particle size distribution.

Then samples were also analyzed by a microscope (Olympus BH2 Research Microscope, $\times 100$, oil, contrast phase).

6.2 Operating procedures

To carry out a filtration process, 4 PES membrane (specification was reported in *Chapter III 1.2 Specification of membrane*) were installed in RVF module to simulate a filtration environment. 100 mL *E.coli* suspension was inoculated to 4 L circulation loop (see general set-up in Fig.III. 2 and devices in Table III. 1), each experiment was carried out in function of various mixing rate (0-50 Hz, RVF module) for 5 hours. 50 mL Samples were taken every 1 hour.

Step 1: Feed circulation loop ($Q_f=100\text{ L/h}$) with demineralized water (4 L in total), and run the loop for 15 minutes;

Chapter III: Materials and Methods

Step 2: Simulate a filtration environment by adjusting inlet, outlet and permeate pressure (P_{in} , P_{out} , P_p). Experiment was controlled at $P_{out} \sim 2000$ mbar, $P_p \sim 200$ mbar;

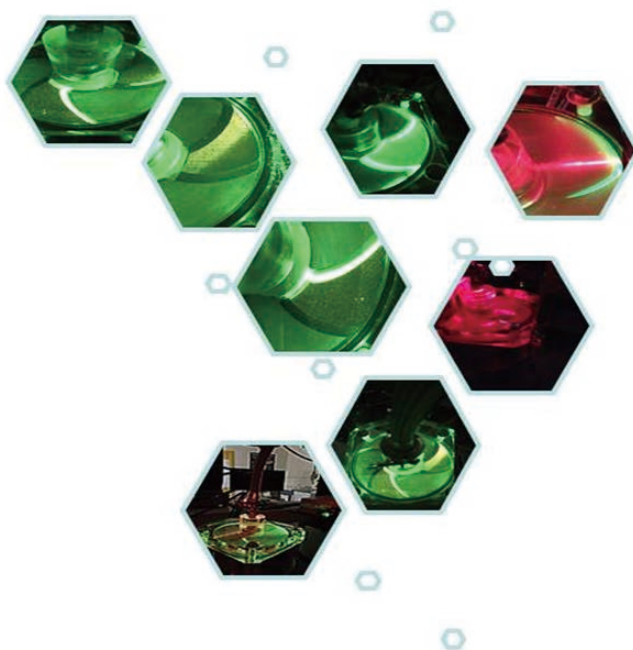
Step 3: Feed 100 mL *E.coli* suspension into reactor and run the circulation at $N=0$ Hz till parameters P_{in} , P_{out} , P_p reach steady state;

Step 4: Set rotation speed ($N= 0, 2, 10, 25, 50$ Hz) and run for 5 hours;

Step 5: Take 50 mL sample with every 1 hour (Sample was analyzed with DLS at the same time) and labeled time and rotation speed as '0 h, 0 Hz' to '5 h, 50 Hz';

Step 6: Rinsing the pilot with tap water and 10 mL 0.5 mol/L NaOH solution to the circulation loop (pH=11) for 1 hour, and 80°C water for 0.5 hour.

Chapter IV:
Results and Discussion



Chapter IV: Results and Discussion

The objective of this study is to investigate hydrodynamics in RVF module, in order to improve filtration and overall industrial bioprocess performances. To answer scientific questions (*Chapter I Introduction*), it is planned to perform experiments and numerical simulations at global and local scales in laminar and turbulent regimes under biotic and abiotic conditions:

(1) For global approach, investigation of Residence Time Distribution (RTD) and thermal balance will be carried out and compared to the previous global study (power consumption and friction curves).

(2) For the local approach, Particle Image Velocimetry (PIV) will be carried out and compared to CFD simulation. PIV preliminary study will be conducted with a trigger strategy to access through angle-resolved measurements to an averaged velocity field. PIV further study will be performed with a non-trigger strategy and applied to POD analysis in order to identify the coherent structure of the flow by decomposing the organized and turbulent fluctuations.

(3) For the bioprocess application, an exploratory work will characterize the effect of Dynamic Filtration on prokaryote cell population (*Escherichia coli*) by quantifying cell integrity or damage as a function of time and rotation speed during filtration process in turbulent regime. Table IV. 1 provides an overview of obtained results that will be discussed in this chapter.

Table IV. 1 Overview of obtained and discussed results in Chapter IV

	Global approach				Local approach			Bioprocess
	Re_Q , Re_{mixing} , Da_Q , N_p	ΔP_{ag}	Thermal balance	RTD	PIV with trigger (velocity analysis)	PIV without trigger (POD analysis)	CFD simulation	Morphology analysis
Laminar regime	II	II	IV-1	IV-1	IV-2.1	IV-2.2	IV-2.1 and 2.2	/
Turbulent regime	II	II	IV-1	IV-1	IV-2.1	IV-2.2	/	IV-3

1 Global approach: Thermal balance and RTD

Experiments were conducted under both laminar ($Re_{mixing} < 1200$) and turbulent flow ($Re_{mixing} > 3 \times 10^4$) in agreement with experimental strategy and associated experimental set-up described in Chapter III 3.

1.1 Thermal balance

Thermal balance (heat dissipation) is highly correlated to mixing power (power consumption curve). Paying attention to the thermal effect during the RTD experiments, temperature increases significantly with the increase of mixing rate and the reduction of flowrate. As Fig.IV. 1 shows, in laminar flow (BREOX solution) with $Q_f = 25$ L/h and $N = 25$ Hz, temperature increased 11°C ; in turbulent flow (water), with $Q_f = 50$ L/h and $N = 50$ Hz, temperature increased 9°C .

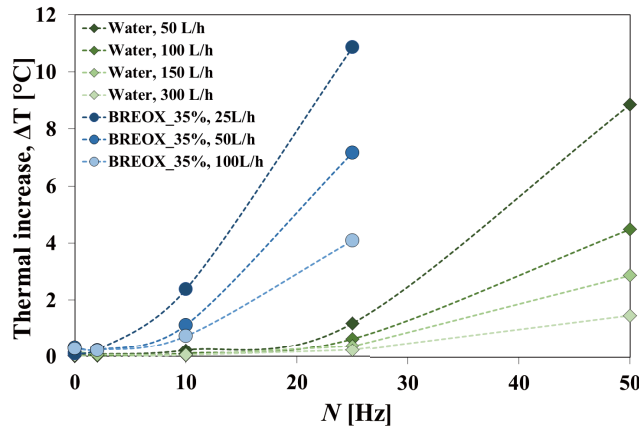


Fig.IV. 1 Temperature variation of the test fluid with different mixing rate

In agreement with theory (Eq.III.16 and 17), Fig.IV. 2 shows the variation of heat dissipation and efficient power consumption [W] under different mixing rate in both laminar and turbulent regimes. Due to its higher viscous force (2nd term of Eq.III.16) in laminar regime, temperature (as well as heat dissipated) increases faster than in turbulent regime (for example $Q_f = 50$ and 100 L/h). As indicates with the solid curves, the effective power consumption is estimated from a power consumption curve model showed in Fig.II. 8, $Np = \left(B \frac{1}{n} + \right.$

$$\left. \left(\frac{Kp}{Re_{mixing}} \right)^{\frac{1}{n}} \right)^n \cong \frac{Kp}{Re_{mixing}}, \text{ where } n=2, B=0.10, Kp=520, \text{ by knowing mixing Reynolds.}$$

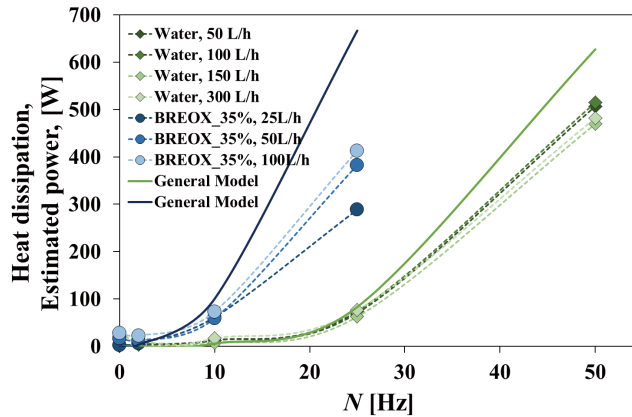


Fig.IV. 2 Heat dissipation and estimated power consumption as a function of mixing rate

In a bioprocess context, maintaining ideal culture temperatures is vital for optimal cell growth. Which temperature is selected will depend on the nature of the cells to be cultured. In addition to culturing, there are temperature considerations when it comes to storing cells. The maximum temperature for growth depends on the thermal sensitivity of secondary and tertiary structures of proteins and nucleic acids. The minimum temperature depends mainly on the freezing temperature. Different physiological groups of microorganisms adapt to different temperature. Psychrophiles have optimal temperatures for growth below 15°C. Mesophilic have optimal growth temperatures in the range between 20 and 40 °C. thermophiles grow best between 50 and 70°C. There are known thermoextremophyles growing at temperature higher than 70°C [212]. For example, prokaryote cells *E. coli*'s optimal temperature to live in is around 37°C and *Streptomyces griseus* is at 25 to 35C; for eukaryote cell *Saccharomyces cerevisiae* is 31 to 35°C and *Saccharomyces uvarum* around 36 to 30°C [213].

Considering a temperature increase limited to 4°C (compatible with cell culture), restricted operating conditions (minimum flowrate and maximum mixing rate) can be estimated from Eq.III.17 including thermal balance and power consumption.

1.2 Residence Time Distribution (RTD)

RTD experiments were conducted as described in *Chapter III.3*. Analytical studies concerning experimental observations is firstly reported and moments are discussed. Then reactor modeling through systemic approach is proposed.

1.2.1. Analytical studies

Analytical results will be discussed concerning distribution and cumulative distribution functions, and moments. Two flow regimes (Laminar regime $Re_{mixing} < 1200$; Turbulent $Re_{mixing} > 3 \times 10^4$), different flow rate Q_f and rotation speed N (Laminar regime: $Q_f = 25, 50, 100$ L/h, $N = 0, 2, 10, 25$ Hz; turbulent regime: $Q_f = 50, 100, 150, 300$ L/h, $N = 0, 2, 10, 25, 50$ Hz) were scrutinized in agreement with established friction curves and power consumption curves, and corresponding to industrial practice.

1.2.1.1 Distribution and cumulative distribution functions

Following Thereska (1998) [182], experimental inlet and outlet RTD signals, $x(t)$ and $y(t)$ are formulated. The measured conductivity values were converted into concentration values for a reference temperature (*Chapter IV: 3.3.1 General approach*). The concentration profiles were obtained as a function of time and Fig.IV. 3 shows typical inlet and outlet RTD normalized signals, in laminar and turbulent regimes respectively.

Qualitative comparison on inlet and outlet RTD signals and mass balance

Inlet signals, $x(t)$ is only affected by nominal flowrate (from 25 up to 300L/h in laminar and turbulent regimes). Inlet curves, $x(t)$ at given operating conditions indicates a good repeatability. Considering normalized inlet signals, $\tau \cdot x(t) = f(t/\tau)$ almost identical functions were observed in laminar and turbulent regime which indicates an accurate reproducibility (control of injected volume and tracer amount, injection time and repetition). However, $x(t)$ peak values in laminar regime are significantly inferior to turbulent regime whereas spreading is larger. Differences are attributed to injection device (efficiency of static mixer), injection time and flow regime. In turbulent flow, tracer solution was well-mixed and homogenized in bulk before passing through the measurement cell, then detection was accurate. In laminar regime, tracer solutions were poorly mixed in laminar regime, with inhomogeneous concentration along a cross-section, then detection might present slight deviation between experiments.

Outlet signals, $y(t)$ are affected by mixing rate and flowrate and express the RVF behavior. Fig.IV. 3a and b illustrate the impact of mixing rates on outlet functions. In laminar flow, $y(t)$ at 0 Hz appears as a sharp and unsmoothed signal. Under these conditions, RVF module exhibits none mixing efficiency and our remarks are similar to inlet signal. For $N > 0$ Hz, $y(t)$ present a

stable outlet signal with a lower peak and consequently a larger spreading. In turbulent flow, smooth signals were obtained due to turbulence, internal geometrical complexity and mixing rate. The increase in mixing rate generates a larger asymmetric Gaussian curve.

Duration of inlet and outlet signals stand as a qualitative criteria of tracing experiments. The ratios of inlet/outlet signal duration are considered for $F = 0.95$ and are equal to 10 s (± 3) and 3 s (± 2) in laminar and turbulent regimes respectively. Mean residence time and the dispersion of inlet signals are negligible compared to outlet signals ($t_{sin}/t_{sout} < 10\%$). Therefore, we may assume that the inlet signal acts as a Dirac function (pulse injection). In such condition the inlet signal may be assimilated to a Dirac signals and it can be neglected during systemic analysis. This assumption will be further discussed by comparing RTD treatment with and without convolution.

Finally, the mass balance between inlet and outlet indicates values of 92.4% (± 5.3) and 54% (± 23) in turbulent (out of 60 experiments) and laminar (out of 36 experiments) regimes respectively.

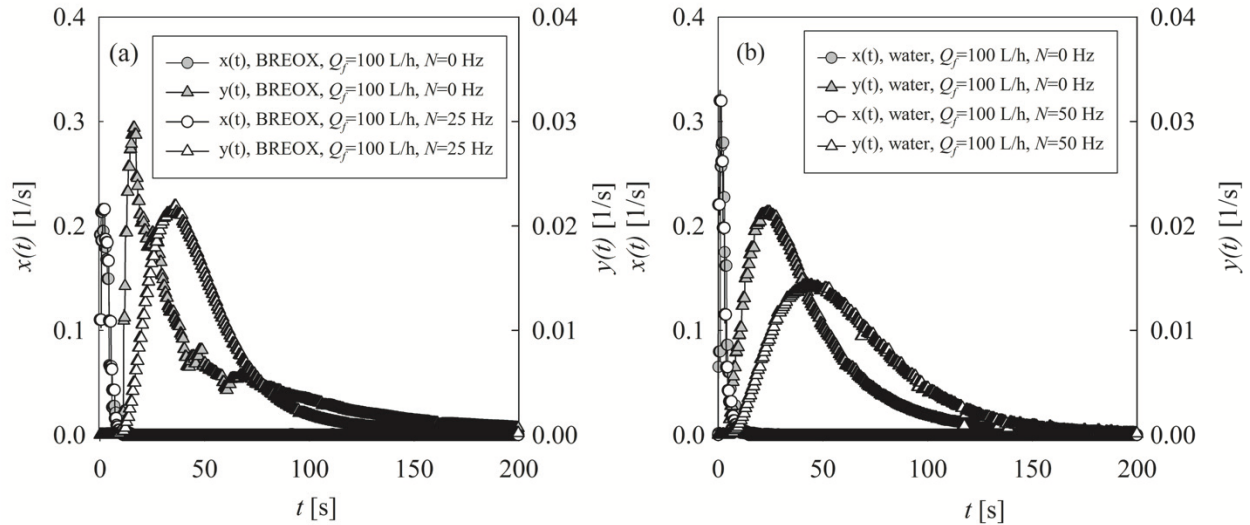


Fig.IV. 3 Inlet and outlet distribution function $x(t)$ and $y(t)$ in (a) laminar flow regime, operating condition: 35% BREOX solution, $\mu=0.35$ Pa·s, $Q_f=100$ L/h, $N=0$ ($T_{in}=22.7 \pm 0.01^\circ\text{C}$, $T_{out}=23.0 \pm 0.02^\circ\text{C}$) and 25 Hz ($T_{in}=22.2 \pm 0.14^\circ\text{C}$, $T_{out}=26.3 \pm 0.13^\circ\text{C}$); and in (b) turbulent flow regime, operating condition: water, $\mu=1$ mPa·s, $Q_f=100$ L/h, $N=0$ ($T_{in}=13.0 \pm 0.12^\circ\text{C}$, $T_{out}=13.1 \pm 0.11^\circ\text{C}$) and 50 Hz ($T_{in}=14.8 \pm 0.02^\circ\text{C}$, $T_{out}=19.3 \pm 0.02^\circ\text{C}$).

Impact of mixing rate and flowrate in turbulent and laminar regimes

Fig.IV. 4a and b compare the outlet RTD signals, $y(t)$ as a function of mixing rate and regime for a given flowrate (100 L/h).

In turbulent regime, it shows the sliding of peak value from 0.037 to 0.021 1/s, with the rotation speed increase from 0 to 25 Hz. In laminar regime, peak value slides from 0.021 to 0.014 1/s with the rotation speed increase from 0 to 50 Hz.

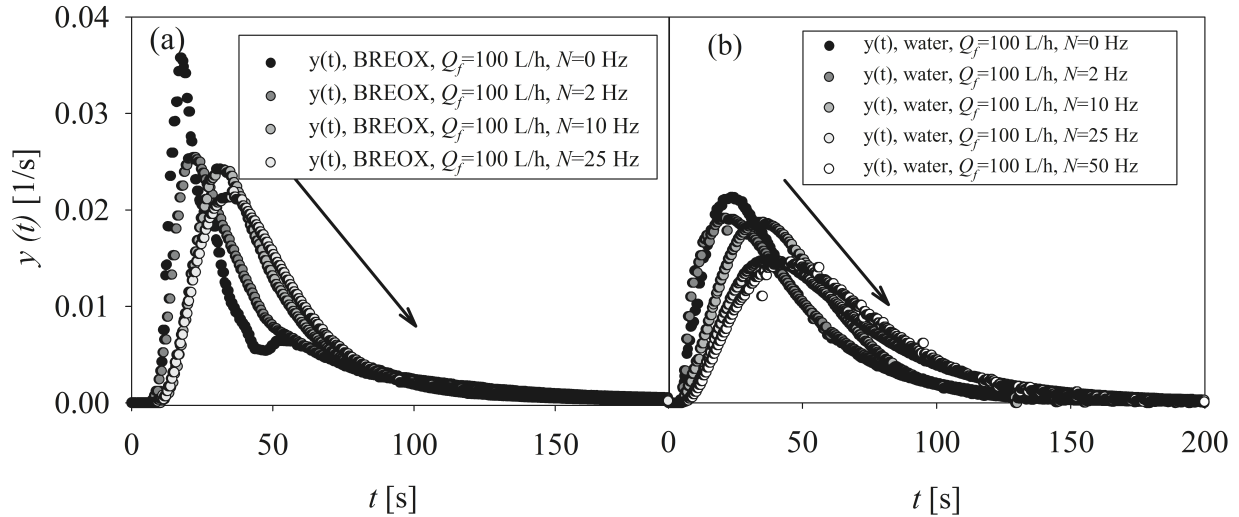


Fig.IV. 4 Outlet distribution function $y(t)$ for (a) laminar flow regime, operating condition: 35% BREOX solution, $\mu=0.35 \text{ Pa}\cdot\text{s}$, $Q_f=100 \text{ L/h}$, $N=0, 2, 10, 25 \text{ Hz}$; and for (b) turbulent flow regime, operating condition: water, $\mu=1 \text{ mPa}\cdot\text{s}$, $Q_f=100 \text{ L/h}$, $N=0, 2, 10, 25, 50 \text{ Hz}$.

Cumulative distribution functions, $Y(t)$ were plotted in Fig.IV. 5a and b as a function of mixing rate and flowrate. With various flowrates, it can be clearly seen in both flow regime, $Y(t)$ of higher flowrate has steeper acceleration than the lower flowrate as expect, consider that the molecule flow out from the RVF module faster when it was driven by a higher flowrate. On the other hand, with various rotation speed, $Y(t)$ of turbulent flow (Fig.IV. 5b) has a noticeable growth: in each cluster of colored curves, with the increase of N , the $Y(t)$ turn to be flatter, and slowly reach the plateau of the curve. Yet there is also a large difference of rotation speed in laminar flow regime (Fig.IV. 5a), it has no such significant impact.

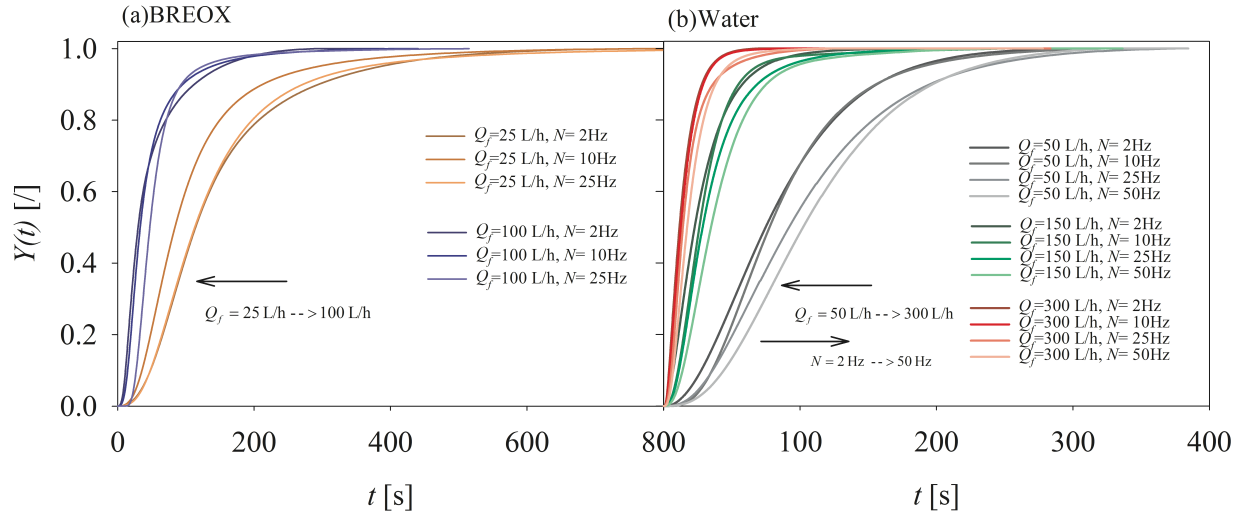


Fig.IV. 5 Cumulative function $Y(t)$ at the outlet for (a) laminar flow regime, operating condition: 35% BREOX solution $\mu=0.35$ Pa·s, $Q_f=25, 100$ L/h, $N= 2, 10, 25$ Hz; and for (b) turbulent flow regime, operating condition: water, $\mu=1$ mPa·s, $Q_f=50, 150, 300$ L/h, $N=2, 10, 25, 50$ Hz

1.2.1.2 Discussion of moments

Table IV. 2 and 3 reports the average operating conditions and calculated RTD parameters in laminar and turbulent regimes.

Table IV. 2 Operating conditions and calculated RTD parameters in laminar flow (SD: standard deviation)

Re_{mixing}	N [Hz]	T_{in} [°C]	T_{out} [°C]	Laminar flow				
				V_l [L]	Mean ts [s]	SD (ts) [s]	β^2	SD(β^2)
$Q_f=25$ L/h								
0	0	17.6	17.7	1.07	152.33	0.95	0.690	0.015
106	2	17.7	18.0	1.18	168.31	4.35	0.461	0.443
528	10	17.8	20.2	1.07	152.33	2.03	0.598	0.068
1320	25	19.3	30.2	1.14	162.58	3.95	0.508	0.099
$Q_f=50$ L/h								
0	0	23.9	24.2	1.34	94.78	1.80	0.969	0.249
106	2	21.7	22.0	1.30	92.37	3.23	0.680	0.030
528	10	20.7	21.8	1.18	83.78	1.31	0.745	0.044
1320	25	21.1	28.3	1.24	88.18	0.51	0.616	0.057
$Q_f=100$ L/h								
0	0	22.7	23.0	1.36	51.09	2.75	0.906	0.116
106	2	21.7	22.0	1.32	49.82	1.50	0.844	0.063
528	10	21.3	22.1	1.34	50.48	1.87	0.765	0.076
1320	25	22.2	26.3	1.32	49.86	2.00	0.733	0.046

Table IV. 3 Operating conditions and calculated RTD parameters in turbulent flow(SD: standard deviation)

Re_{mixing}	N [Hz]	T_{in} [°C]	T_{out} [°C]	Turbulent flow			β^2	SD(β^2)
				V_l [L]	Mean t_s [s]	SD (ts) [s]		
$Q_f=50L/h$								
0	0	14.1	14.1	1.14	81.16	0.27	0.346	0.029
33800	2	14.7	14.7	1.19	84.57	1.40	0.355	0.010
169000	10	14.6	14.9	1.23	87.48	0.77	0.314	0.011
422500	25	14.1	15.3	1.55	110.24	0.25	0.331	0.008
845000	50	13.9	22.8	1.63	116.26	2.56	0.257	0.003
$Q_f=100L/h$								
0	0	13.0	13.1	1.06	39.29	0.69	0.563	0.005
33800	2	13.8	13.8	1.14	41.97	2.26	0.561	0.041
169000	10	13.8	14.0	1.2	44.31	1.19	0.452	0.005
422500	25	13.4	14.0	1.53	56.55	1.75	0.476	0.062
845000	50	14.8	19.3	1.60	58.86	0.54	0.331	0.013
$Q_f=150L/h$								
0	0	13.3	13.4	1.1	27.41	0.38	0.531	0.018
33800	2.1	14.1	14.1	1.15	28.78	1.14	0.618	0.065
169000	10	13.5	13.5	1.2	29.85	1.26	0.497	0.144
422500	25	14.0	14.3	1.47	36.75	0.03	0.530	0.010
845000	50.1	14.0	16.9	1.68	41.84	1.08	0.456	0.068
$Q_f=300L/h$								
0	0	13.1	13.1	1.09	13.57	0.17	0.486	0.031
33800	2.1	13.0	13.0	1.12	13.91	0.43	0.550	0.034
169000	10	13.5	13.5	1.12	13.93	0.13	0.540	0.006
422500	25	13.5	13.8	1.44	17.88	0.88	0.708	0.152
845000	50.1	13.6	15.0	1.6	19.94	0.11	0.486	0.054

Moment of 1st order (mean residence time)

Moment of first order Γ^1 represents the mean residence time t_s in the system, as expressed by Eq. III.8. These mean residence time, t_s , will be compared to the holding, τ .

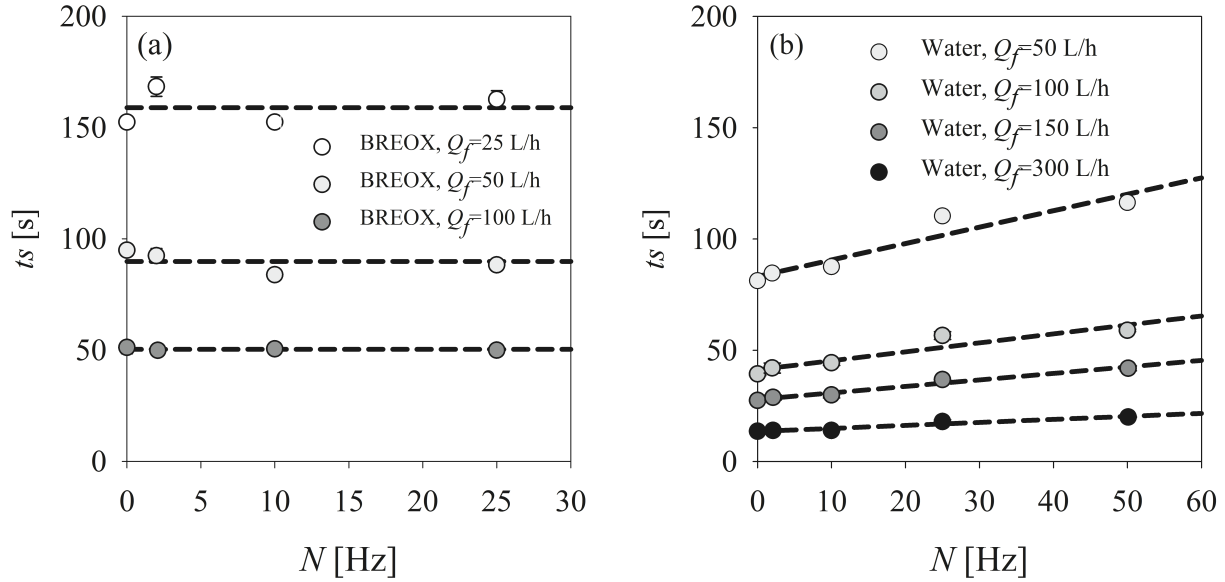


Fig.IV. 6 Mean residence time t_s as a function of rotation speed N for (a) laminar flow regime, operating condition: BREOX solution $\mu=0.35 \text{ Pa}\cdot\text{s}$, $Q_f=25, 50, 100 \text{ L/h}$, $N=0, 2, 10, 25 \text{ Hz}$; and for (b) turbulent flow regime, operating condition: water, $Q_f=50, 100, 150, 300 \text{ L/h}$, $N=0, 2, 10, 25, 50 \text{ Hz}$.

Fig.IV. 6a and b plot t_s as a function of N in laminar and turbulent regimes. As expected, t_s decrease as Q_f increases.

In laminar flow, t_s remain constant at a given Q_f , whatever the N is. The product $t_s \cdot Q_f$ indicates that the effective volume: for $Q_f=25 \text{ L/h}$, $V_I = 1.12 \text{ L} \pm 0.06$; for $Q_f=50 \text{ L/h}$, $V_I=1.27 \text{ L} \pm 0.07$; for $Q_f=100 \text{ L/h}$, $V_I=1.34 \text{ L} \pm 0.02$. Effective volume is only flow rate dependent, the mixing rate do not seem to have impact.

In turbulent flow, t_s increases linearly as a function of N at a given Q_f . In this case, the effective volume is only mixing rate dependent whereas flow rate does not have any effect. V_I can be described by a semi-empirical relation with Q_f and N considering the mean residence time, t_s :

$$t_s = \alpha N + \tau_0, \text{ (or } V_I = \alpha N + V_0) \quad (\text{IV.1})$$

where α (or τ_0) is as function of $1/Q_f$ ($R^2 \geq 99\%$), t_s and V_I can be generally described by Q_f and N , with an initial volume of 1.15 L , which is close to the effective volume V_I in laminar flow.

$$V_1 = t_s \cdot Q_f = \alpha N + V_0 = 0.0106 \cdot N + 1.15 \quad (IV.2)$$

where α and τ_0 are as function of $1/Q_f$ ($R^2 \geq 99\%$), t_s and

It is noticeable that effective volume will just depend on mixing rate in turbulent regime.

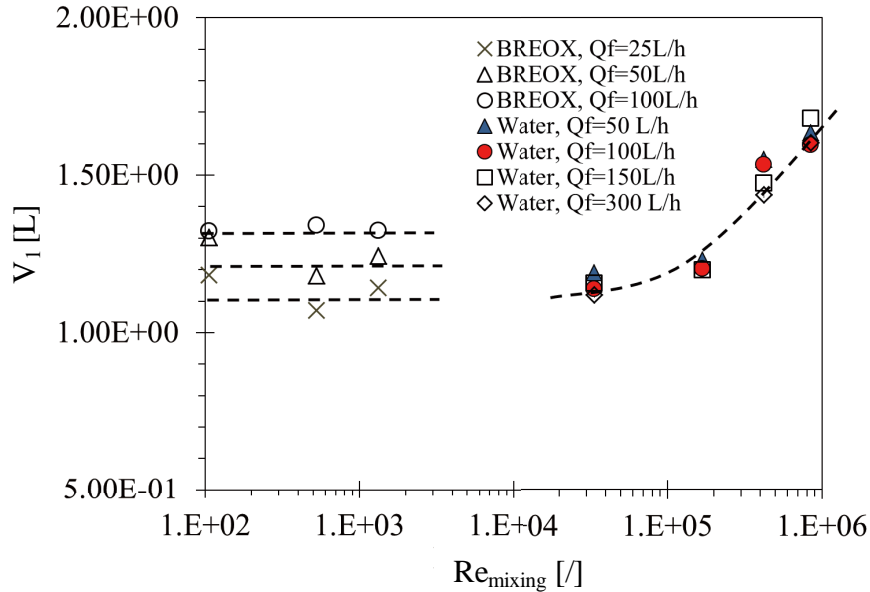


Fig.IV. 7 Used volume V_1 as a function of mixing Reynolds number. Laminar flow regime $Re_{mixing} < 1200$, operating condition: BREOX solution $\mu = 0.35 \text{ Pa}\cdot\text{s}$, $Q_f = 25, 50, 100 \text{ L/h}$, $N = 0, 2, 10, 25 \text{ Hz}$; Turbulent flow $Re_{mixing} > 3 \times 10^4$ operating condition: water, $Q_f = 50, 100, 150, 300 \text{ L/h}$, $N = 0, 2, 10, 25, 50 \text{ Hz}$

Mean residence time, t_s reflects the real movement of the tracers in RVF module (including shortcut, bypass, dead-zone may if existing), while τ represents the holding time based on the assumption that tracer molecules ideally move all volume of RVF module. Therefore, ratios, t_s / τ or V_1 / V_{RVF} , can be one of the important parameters to diagnose efficient volume. The closer are the ratio to 1, the closer the system feet to ideal case. As it is illustrated in Fig.IV. 7, in laminar flow ($Re_{mixing} < 1200$), used volume remains constant as a function of mixing Reynolds number at each flowrate. The main contributor that improves the used ratio is the increase of the flowrate Q_f , rotation speed N doesn't drive the flow to reach all over the system. To explain, at first, N was limited to 0-25 Hz which might be not high enough to drive the fluid. Besides, it probably due to that laminar flow is very stable as widely known, the mixing effect in this kind of flow is poor. However, in turbulent flow ($Re_{mixing} > 3 \times 10^4$), generally, initial used ratio

is almost the same value as laminar flow at low rotation speed, and it has a rapid growth of used ratio as the increase of rotation speed. Moreover, flowrate in turbulent flow somehow affects the used ratio as the opposite way as in laminar flow: in laminar flow, used ratio increase from 0.76 to 0.90 with the increase of flowrate from 25 to 100 L/h; in turbulent flow, apparently, flow with lower flowrate seems has higher used ratio. Special attention should be paid for the used ratio which is higher than 1, the reason to explain this behavior is that the tracer molecule goes into the dead-zone and it is slowly mixed out of the system. Overall, these observations lead to the fact that, in laminar flow, mixing driving force is mainly the Q_f ; while in turbulent flow, mixing driving force is largely improve by the rotation speed, and lower Q_f may help to have a better mixing.

Centered moment of 2nd order, (reduced variances, β^2)

In Fig.IV. 8, experimental reduced variance, β^2 is analysed versus mixing Reynolds. There is a significant decrease in reduced variance under both the laminar and turbulent regime. It is noticeable that with higher flowrate the system seems closer to a perfect mixer, and with higher Re_{mixing} it has lower value which may tend to more similar as a plug flow reactor. Considering $Q_f= 50$ and 100 L/h in both flow regime, two logarithmic regressions are plotted, which denotes that β^2 and mixing effect (Re_{mixing}) are somehow related.

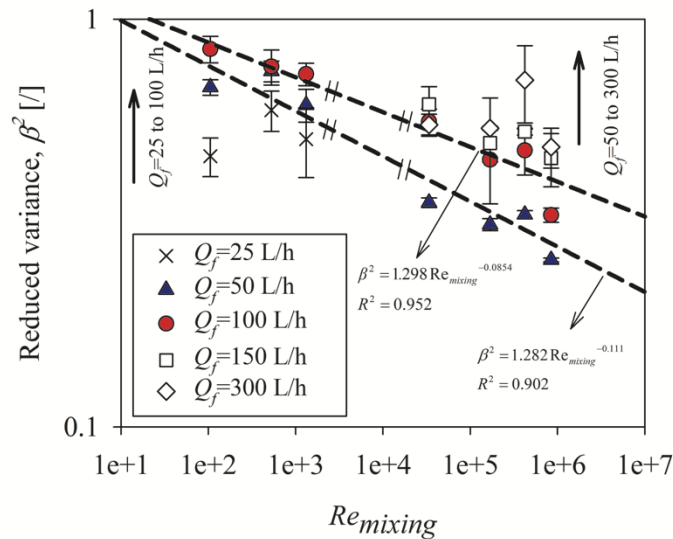


Fig.IV. 8 Reduced variance β^2 as a funtion of mixing Reynolds number. Laminar flow regime: $Re_{mixing} < 1200$, operating condition: BREOX solution $\mu = 0.35$ Pa·s, $Q_f = 25, 50, 100$ L/h, $N = 0, 2$,

Chapter IV: Results and Discussion

10, 25 Hz; Turbulent flow regime: $Re_{mixing} > 3 \times 10^4$ operating condition: water, $Q_f = 50, 100, 150, 300$ L/h, $N = 0, 2, 10, 25, 50$ Hz

Centered moment of 3rd and 4th order estimates the skewness and the spreading of RTD curves. In our case, Γ^3 and Γ^4 of all the experiments have positive values, indicating that, generally, RTD curves in RVF module is right-skewed and has a tail spreading. Mixing effect appears as the predominant effectors compared to flow rate, and values are significantly higher in laminar than in turbulent regimes. For instance, Γ^3 and Γ^4 are equal to 4.4×10^6 ($\pm 1.5 \times 10^6$), 8.8×10^9 ($\pm 2.1 \times 10^9$) (operating condition: BREOX, $Q_f = 25$ L/h, $N = 25$ Hz) and 1.9×10^5 ($\pm 1.3 \times 10^4$), 6.8×10^8 ($\pm 6.4 \times 10^7$) (operating condition: water, $Q_f = 50$ L/h, $N = 50$ Hz) for laminar and turbulent regimes respectively. However, further interpretation is limited by these poorly significant and reliable calculations.

1.2.1.3 Reduced signal of outlet distribution function

Through data and moment analyses, we demonstrate that in laminar ($Re_{mixing} < 1200$) and turbulent ($Re_{mixing} < 3 \times 10^4$), hydrodynamics in RVF module differs.

In laminar regime, effective volume appears to be correlated to flowrate whereas in turbulent regime, the mixing rate (Re_{mixing}) acts as the dominant parameters. In order to confirm or to refute the uniqueness of hydrodynamics behavior of RVF module, the reduced distribution functions, $y(t/t_s) \cdot t_s$ are normalized by experimental mean residence time t_s instead of holding time, τ . Fig.IV. 9 presents the reduced distribution functions, $y(t/t_s) \cdot t_s$ for both regimes considering the effect of flow and mixing. In laminar flow at given flowrate, $Q_f = 100$ L/h, (Fig.IV. 9a1) reduced distribution functions are separated and the peak values slide from 1.83 to 1.07 with the increase of mixing rate.

Furthermore, for three flowrates at given mixing rate (Fig.IV. 9a2), reduced distribution function are perfectly overlapped (OVL coefficient = 0.86). Fig.IV. 9a1 and a2 indicate that RVF behavior is the same at a given rotation speed whatever the flowrate is. In turbulent regime, reduced distribution functions, $y(t/t_s) \cdot t_s$ are overlapped in all conditions indicating the uniqueness of hydrodynamics behaviors. In Fig.IV. 9b, four curves are shown exhibiting an OVL coefficient equal to 0.85. It can be reasonably assumed that flow behavior in turbulent flow is always the same, whatever the flowrate and rotation speed are. Since the flow behaviors show its

uniqueness in whole or in part in different flow regime, flow behaviors in the RVF module can be explained by a unique model with the equivalent system.

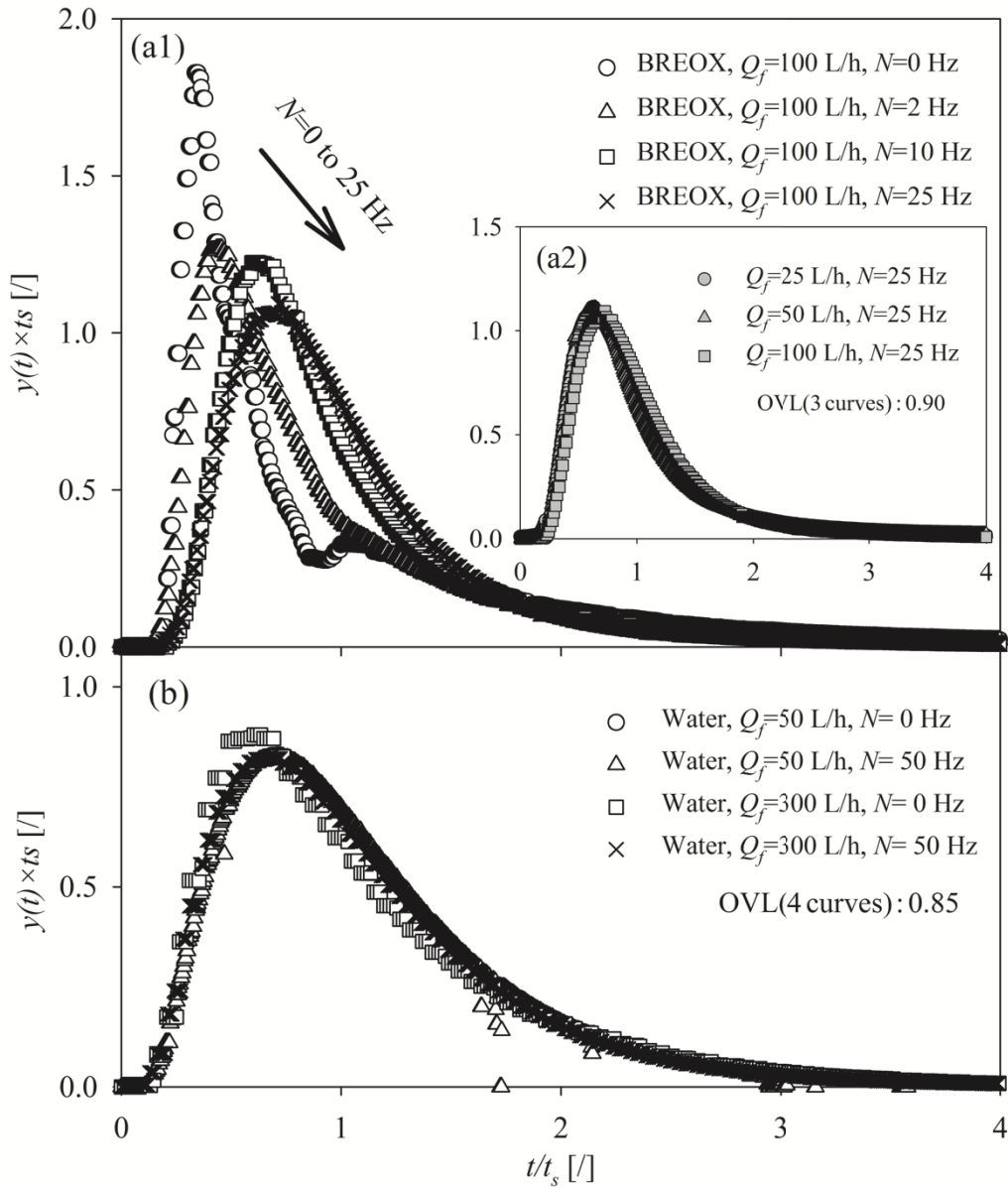


Fig.IV. 9 Reduced $y(t/t_s) \cdot t_s$ as a function of reduced time t'/t_s , for (a) laminar flow regime, operating conditions for a1: BREOX solution $\mu=0.35$ Pa·s, $Q_f=100$ L/h, $N=0, 2, 10, 25$ Hz, operating conditions for a2: BREOX solution $\mu=0.35$ Pa·s, $Q_f=25, 50, 100$ L/h, $N=25$ Hz; for (b) Turbulent flow regime, operating conditions: water, $Q_f=50, 300$ L/h, $N=0, 50$ Hz

1.2.2 Systemic analysis and modeling of RTD

After the analytical studies of RTD, in the second step, the hydrodynamic behaviors of the RVF module was describe by a systematic analysis of the RTD modeling signals, by using DTS Progepi v4.2 (Leckerc et al., 1995). Our objective is to model and to establish an analytical solution of RTD functions considering the complexity of RVF module.

1.2.2.1 Proposal of reactor models

4 models were proposed to fit the outlet function $y(t)$ of RVF module in order to obtain a better agreement. Inlet function $x(t)$ was taken into account due to the imperfect injection. The objective of this modeling is to find the analytical solution to represent the complex designed RVF module. To this aim, conventional models, such as Plug Flow reactor, continuous flow stirred-tank reactor (CSTR) or their combine forms PFR+(J) CSTR, are proposed, with the ideal PF reactor equivalent to the real tubes before and after the RVF module, describes as Fig.IV. 10 shows:

Model 1: PFR+PFR reactor open to diffusion by imposing V_{RVF} and adjusting Peclet number Pe_L , shown in Fig.IV. 10a. Model 1 considered the association in serie of 2 PF reactor. The first one behave as an ideal plug (pure delay) whereas the 2nd one is open to diffusion and its volume is imposed by V_{RVF} . Consequently, this model exhibit only 1 degree of freedom by adjusting Peclet number, Pe_L . RTD function is described by an analytical solution (Eq.IV.4). The current model considers mass transport in the axial direction as a diffusion-like process (analogous to Fick's diffusion law) in terms of an effective longitudinal diffusivity, D_{ax} (axial dispersion coefficient), which is superimposed on the plug flow. The concentration C , of the tracer injected uniformly over the cross-section at the inlet of the system, is given as a function of time t , and the streamwise coordinate z , by Eq.IV.3. The axial dispersion coefficient is assumed to be independent of the concentration and the position. The first assumption is usually verified if molecular diffusion can be neglected, and the second can be used when a fully developed flow is obtained at the inlet and outlet of the process. This choice for the boundary conditions (called "open-open") leads to the following expression

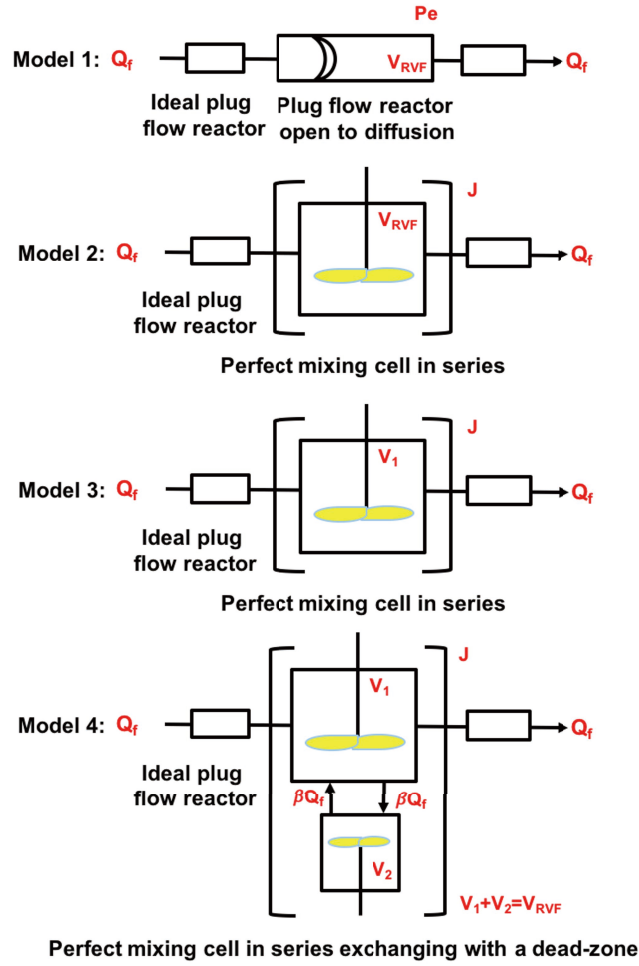


Fig.IV. 10 Proposed models equivalent to RVF model, with the ideal plug flow reactor equivalent to the real tubes

$$\frac{\partial C}{\partial t} = D_{ax} \frac{\partial^2 C}{\partial z^2} - U \frac{\partial C}{\partial z} \quad (IV.3)$$

$$E(t) = \frac{1}{2} \left(\frac{Pe_L}{\pi t \tau} \right)^{1/2} \exp \left(- \frac{Pe_L (\tau - t)^2}{4 t \tau} \right), \text{ where } \tau = \frac{V_{RVF}}{Q_f} \quad (IV.4)$$

$$\text{with } \frac{t_s}{\tau} = 1 + \frac{2}{Pe_L}, \beta^2 = \frac{\sigma^2}{t_s^2} = \frac{2}{Pe_L} + \frac{8}{Pe_L^2} \quad (IV.5)$$

$$\text{and } Pe_L = \frac{LU}{D_{ax}} \quad (IV.6)$$

PeL is calculated from the pipe length and is a dimensionless measure of the axial dispersion, Dax . The DPF model is supposed to yield the best agreement between numerical and experimental results. Furthermore, it has the advantage of necessitating the estimation of only one parameter, i.e., the Peclet number, PeL, Eq.IV.6.

Model 2: PFR+(J) CSTR model by imposing V_{RVF} and this model exhibit only 1 degree of freedom adjusting the number of mixing cell J . In order to obtain a better agreement, a second model defined by a cascade of a plug reactor (τ_p) in series with 2 CSTR (τ_{cs}) was investigated (Fig.IV. 10b). This model was chosen because it is simple and correlates closely to the physical structure of the process. However, other models can also be used as reported by Ham and Platzter [180]. The corresponding expressions for the transfer function, $G(s)$ and $E(t)$ are formulated by Eq.IV.7 and Eq.IV.8:

$$G(s) = \frac{\exp(-s\tau_p)}{\left(1 + \left(\frac{s\tau_{cs}}{2}\right)\right)^2}, \text{ where } \tau = \frac{V_{RVF}}{Q_f} \quad (\text{IV.7})$$

$$E(t) = H(t - \tau_p) \left(\frac{J}{\tau_{cs}}\right)^2 (t - \tau_p) \exp\left(\frac{-J(t - \tau_p)}{\tau_{cs}}\right), \text{ with } \tau = \frac{V_1}{Q_f} \quad (\text{IV.8})$$

The main advantage of this simple model is that only one parameter a , is used, which is the plug reactor contribution, in terms of residence time, Eq. IV.9. Van Laar's equation leads to a simple relationship between a and β^2 , Eq.IV.10:

$$a = \frac{\tau_p}{\tau_p + \tau_{cs}} \quad (\text{IV.9})$$

$$\beta^2 = \frac{(1 - a)^2}{2} \quad (\text{IV.10})$$

Model 3: PFR+(J) CSTR model. Instead of imposing the total volume of RVF module, this model is based on imposing V_l (value from experiments) to the mixing cells volume and it exhibits only 1 degree of freedom by adjusting J , governing equation presents as Eq.IV.8, with

$$\tau = \frac{V_l}{Q_f};$$

Chapter IV: Results and Discussion

Model 4: PFR+(J) CSTR model exchanging with a dead-zone. Considering a dead-zone may exist in the system, this model taking the exchanging flow by imposing V_1 to the mixing cell (with $\tau = \frac{V_1}{Q_f}$) and it exhibits 2 degree of freedom by adjusting J and β (the ratio between the exchanging flowrate in the dead zone and the feeding flowrate).

1.2.2.2 Model adjustment and comparison

Even if inlet signals can be neglected, we observed injection may slightly differed from ideal Dirac functions, especially in laminar regime. Consequently to fit the experimental functions, $y(t)$, the inlet functions, $x(t)$ were considered with all models to simulate $E(t)$. The function $E(t)$ was obtained for all the experiment.

Special attention should be paid to the result of Model 4, it was proved that average value of β is inferior to 2%. It means that only 2% of the main flow has exchange with the dead-zone, which can be neglected. In this case, Model 4 is equivalent to Model 3. Therefore, Fig.IV. 11 plots the modeling curve $y(t)'$ of Model 1, Model 2 and Model 3 fitting with the experimental data $y(t)$. Result shows that, to fit the experimental data of laminar flow, Model 1 has an overlapping coefficient OVL=0.66, Model 2 OVL=0.77 and Model 3 OVL= 0.89; whereas in turbulent flow, Model 1 OVL=0.66, Model 2 OVL=0.87 and Model 3 OVL= 0.98. Significantly, Model 3 is preferred in both laminar and turbulent flow. The adjustable parameter J is reported in Table IV. 4. To conclude, PFR+(J) CSTR model by imposing effective volume V_1 and $J=2.5\pm 0.6$ is chosen to describe flow behavior in RVF module.

Table IV. 4 J value in Model 3

	N [Hz]	25 L/h	50 L/h	100 L/h	150 L/h	300 L/h
Laminar	0	1.84	1.52	1.32		
	2	2.86	2.31	1.66		
	10	2.33	2.75	2.74	/	/
	25	1.88	2.62	3.41		
Turbulent	0	/	3.11	1.95	1.93	2.28
	2		2.41	1.71	1.72	1.74
	10		3.20	3.16	2.74	1.84
	25		2.94	2.88	2.53	2.20
	50		3.56	3.47	3.00	2.58

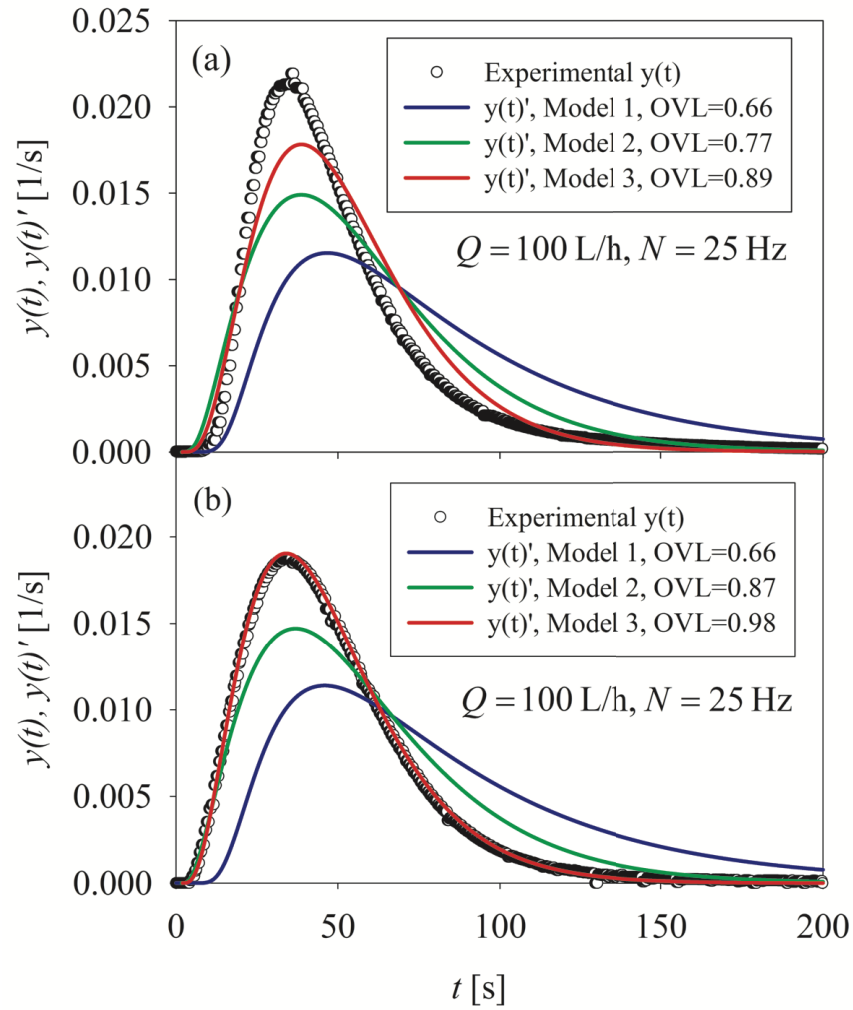


Fig.IV. 11 Comparison of curves fitting from Model 1, Model 2 and Model 3. (a) in laminar regime (b) in turbulent regime

1.3 Simulation of fluid streamlines by CFD under laminar flow regime

So far, results mainly presented in global scale including thermal balance and RTD. To complete this hydrodynamic analysis, it requires some transition information such as the track of fluid, which can lead the discussion to further study local flow pattern and the mixing effect within the RVF filtration cell. Therefore, we pay attention to streamlines issued from CFD. Comparison between PIV experiments and CFD simulations has proved simulation approach was validated in laminar flow, which also indicated the access to streamlines is feasible, whereas experimental approaches are hardly possible. (Simulation for turbulent flow will be included in the future works.)

The streamlines are the lines tangential to velocity vectors at a given time.. Simulation of Fig.IV. 12 was conducted with $Q_f= 45$ L/h, $N=2$ Hz, corresponding to vertical mean pressure gradients ($\frac{\partial \langle P \rangle}{\partial z}$) 1.17 Pa/m. Fig.IV. 13a introduces the streamline start from cross-section1 within the whole filtration cell, while Fig.IV. 12b presents part of the streamlines that follow the impeller movement. These streamlines seem to be almost parallel to each other, indicating a well-organized flow motion. However, by comparing these two figures, it seems streamlines are more organized following the impeller rotation (in the same fluid layer with the impeller) than the streamlines close to the wall. It may be explained by the effect of the low mixing efficiency close to the wall, especially close to the central shaft. In Fig.IV. 12c, as expected, streamlines velocity is found almost equal to zero close to the surrounding wall and it remained rotating in the same radial annular; it highly refers to a low mixing dead-zone without exchange flow to the rest of the fluid. Nevertheless, a large magnitude of velocity between the streamlines is noticeable.

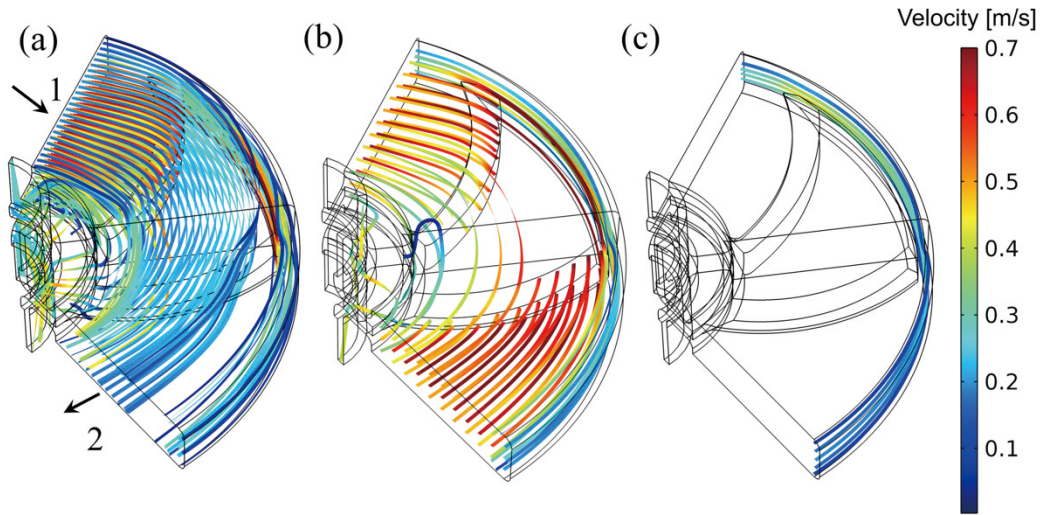
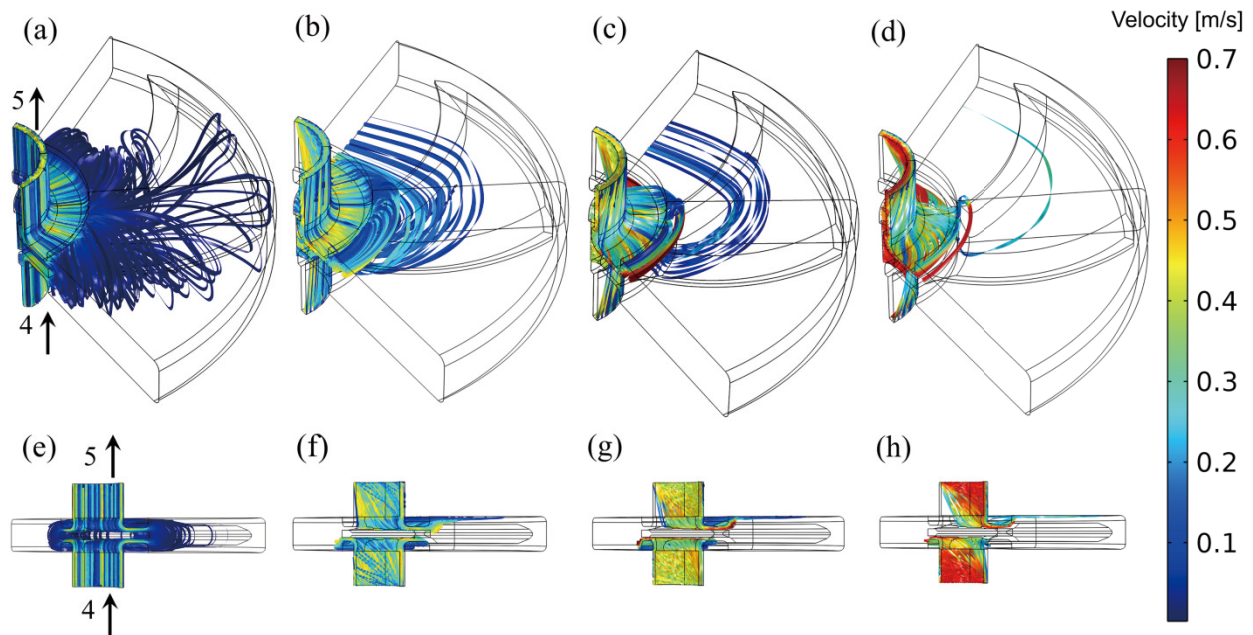


Fig.IV. 12 Illustration of streamlines start from cross-section 1 issued from CFD simulation (a) within the whole filtration cell; (b) streamlines follow the impeller rotation; and (c) close to the surrounding wall $R=69$ mm; Direction of the streamline: from cross-section 1 to 2; Operating conditions: $Q_f= 45$ L/h, $N=2$ Hz; $\mu=0.85$ Pa·s and $T=20^\circ\text{C}$

In addition, Fig.IV. 13 presents the streamlines corresponding to inlet and outlet cross-section (4 and 5). These simulations were performed to investigate the effect of mixing rate, to realize the contribution of the impeller to mixing effect in the system. Simulation were performed with 0, 2, 5 and 10 Hz, associated with vertical mean pressure gradients equal to 1.20, 1.17, 1.10 and 1.02 Pa/m, according to nominal flowrate $Q_f=45$ L/h. It is clear that shortcut effect along the shaft is a dominant phenomenon: graphically, less streamlines pass over the entire filtration cell from (a) to (d), which has an increase rotation speed with from 0 to 10Hz. It seems the flow has a shortcut straight from the inlet to the outlet. Moreover, it is further proved by the streamlines in the vertical view (e), (f), (g) and (h): with the increase of rotation speed, vertical streamlines have higher velocity, it means that fluid left the system faster in this zone, and the flow in the rest of the cell hold steady and remain rotating in stable.

To sum up, streamlines confirm that a dominant shortcut flux may exist along the shaft, consequently less flux flow into the filtration cell; the contribution of the shortcut in vertical direction became more prevalent with the increase of rotation speed, it may cause a risk of dead-zone in the filtration cell. Recall of the results from RTD investigation, effective volume V_I is constant at each flowrate (for $Q_f= 25$ L/h, $V_I= 1.12$ L \pm 0.06; for $Q_f=50$ L/h, $V_I=1.27$ L \pm 0.07; for

$Q_f=100$ L/h, $V_I=1.34$ L \pm 0.02; \sim 82.8% out of total volume), it leads to a conclusion that: fluid may have a shortcut to flow through the system and dead-zone may exist in laminar flow.



*Fig.IV. 13 Illustration of streamlines in the filtration cell issued from CFD simulation in 3D (a, b, c, d) and 2D (e, f, g, h) view with rotation frequency $N=0$ Hz (a, e), $N=2$ Hz (b, f), $N=5$ Hz (c, g), $N=10$ Hz (d, h). Direction of the streamline: from cross-section 4 to 5; Operating conditions: $Q_f= 45$ L/h; $\mu=0.85$ Pa·s and $T=20^\circ\text{C}$. * Notice each figure has 500 streamlines*

Additional simulation with $Q_f=25$ L/h, $N= 2$ Hz (corresponding to vertical mean pressure gradients 0.76 Pa/m) indicated that Q_f had no significant impact on velocity fields and streamlines.

❖ **Summary of Global approach (Thermal balance and RTD)**

Objectives:

- (1) to investigate the thermal effect and the impact of processing conditions (flowrate Q_f , rotation speed N) on RTD in RVF module;
- (2) to compare the different flow pattern in laminar and turbulent regimes;
- (3) to evaluate the homogeneity within the device.

Highlights:

(1) Thermal balance

- Temperature variation and heat dissipation are reported as a function of operating conditions (rotation speed, flowrate) and correlated with viscous dissipation (mixing power). Due to its higher viscous force in laminar regime, temperature (as well as heat dissipated) increases faster than in turbulent regime;
- Considering a temperature increase limitation (compatible with cell culture), restricted operating conditions (minimum flowrate and maximum mixing rate) can be estimated from thermal balance and power consumption.

(2) Distribution and cumulative distribution functions $x(t)$, $y(t)$, $X(t)$ and $Y(t)$ indicate that:

- Mass balance between inlet and outlet indicates values of 92.4% (± 5.3) and 54% (± 23) in turbulent (out of 60 exp.) and laminar (out of 36 exp.) regimes respectively;
- Inlet signals, $x(t)$ is only affected by nominal flowrate (from 25 up to 300L/h) in laminar and turbulent regimes;
- Outlet signals, $y(t)$ are affected by mixing rate and flowrate and expressed the RVF behavior. Inlet signals are always negligible compared to outlet signals ($t_{Sin}/t_{Sout} < 10\%$);
- Distribution $y(t)$ and cumulative $Y(t)$ functions are effected by feeding flowrate Q_f in both laminar flow and turbulent regimes; but mixing rate has more impact in

turbulent regime.

(3) Moment of 1st and centered moment of 2nd orders informed:

In laminar flow, moment of 1st order, t_s , remains constant at a given Q_f , whatever N is. Effective volume V_I is only flowrate dependent, the mixing rate does not seem to impact. In turbulent regime, t_s , increases linearly as a function of N at a given Q_f . The effective volume V_I is only mixing rate dependent whereas flowrate has no effect.

Centered moments of 2nd order, reduced variances β^2 , are as a linear function of mixing Reynolds number for the given flowrate, β^2 slightly increased with Q_f .

(4) Reduced signal $y(t/t_s) \cdot t_s$ of outlet distribution function indicated the global reactor behavior:

- In laminar regime, reduced signals are unique at a given mixing rate N , it is assumed that flow behavior is the same at a given N .
- In turbulent regime, reduced signals are unique whatever Q_f and N , it is assumed that flow behavior is the same and can be describe by a single model.

(5) A systemic analysis was used to describe the hydrodynamic behaviors of the RVF module. By using DTS Progepi v4.2 software, 4 models were proposed to fit the outlet functions $y(t)$. PFR+(J)CSTR model with an effective volume V_I and $J=2.5\pm 0.6$ is the most appropriate model to fit the experimental results.

(6) A CFD simulation of fluid streamlines was done under laminar regime. Combining CFD and RTD observations, it leads to demonstrate that a shortcut and a dead-zone may exist in laminar flow.

2 Local approach with Particle Image Velocimetry (PIV)

Brief recall of PIV set-up:

In this part, experiments were conducted in horizontal plane and vertical plane. Brief schematic is given in Fig.IV. 14 and Fig.IV. 15 (see detail in *Chapter III: Materials and Methods*, Fig.III. 6 and Fig.III. 7, operating conditions in Table III. 3).

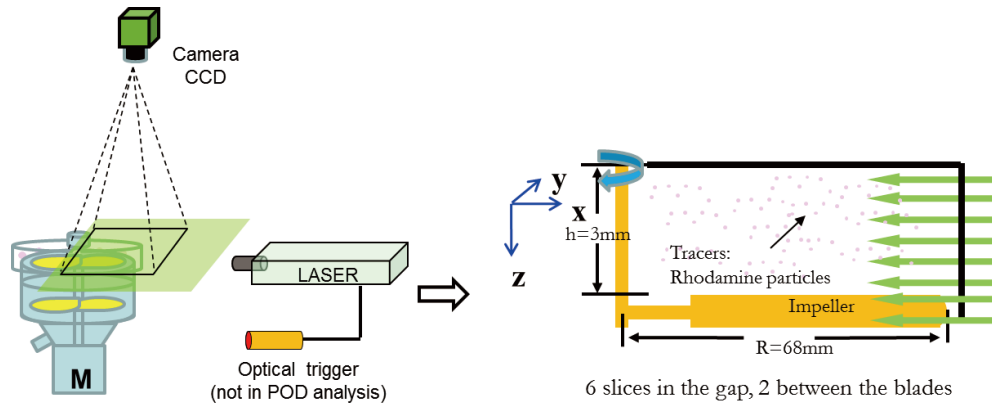


Fig.IV. 14 Brief schematic of horizontal measurement

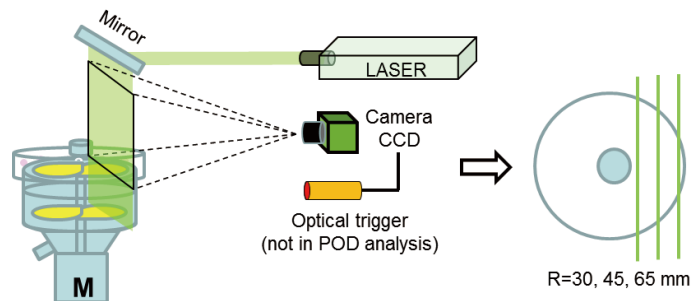


Fig.IV. 15 Brief schematic of vertical measurement

Chapter IV: Results and Discussion

Hydrodynamics in the cell was investigated by Particle Image Velocimetry (PIV). PIV technique enables to achieve a noninvasive measurement and determine 2D instantaneous velocity field. Laminar and turbulent flows were investigated. And two solutions were investigated:

- Conditional averaging (angle-resolved measurements, fixed with trigger strategy, *Chapter IV 2.1 Preliminary study-PIV with trigger strategy*)
- Reconstruction of organized motion based on POD processing (non-trigger strategy, *Chapter IV 2.2 POD analysis (with non-trigger strategy)*)

2.1 Preliminary study-PIV with trigger strategy

2.1.1 Laminar regime

To achieve pure laminar flow regime, 40% (w/w) diluted BREOX solution was chosen as a test fluid (with $\mu = 0.81\text{-}0.85$ Pa·s, $C_p = 3274$ J/(kg·°C) and $\rho = 1067$ kg/m³ at $T=20^\circ\text{C}$), impeller rotation speed was controlled at $N=2$ Hz. Temperature of the feeding tank was controlled at 20°C by adjusting the thermostat (room temperature was air controlled at $20 \pm 1^\circ\text{C}$).

2.1.1.1 Velocity field

By analyzing the PIV raw images, the instantaneous velocity fields (from single images pair) and time averaged mean velocity fields (from 1000 image pairs) were computed at 6 horizontal plane (x - y plane within membrane-impeller gap) and 3 vertical plane (x - z plane at different radius). To acquire the mean velocity fields in this rotating system, the optical trigger plays a key role in these measurements because it synchronizes and governs the laser generator and the camera with the position of one specific blade. Image processing and statistical quantities (\overline{U}_m , σ_I) were detailed and proved the measurement reliability in *Chapter III 4.4.2*.

Horizontal plane

Fig.IV. 16 provides an overview of the magnitude of velocity fields. In our experimental conditions, maximal impeller velocity is equal to 0.87 m/s at $R=69$ mm ($d_m=138$ mm). Raw PIV images, Fig.IV. 16a and d show the constant position of impeller and the homogeneous surface density of florescent particles for $z_I=0.25$ (close to membrane) and $z_0=2.75$ (close to impeller) mm.

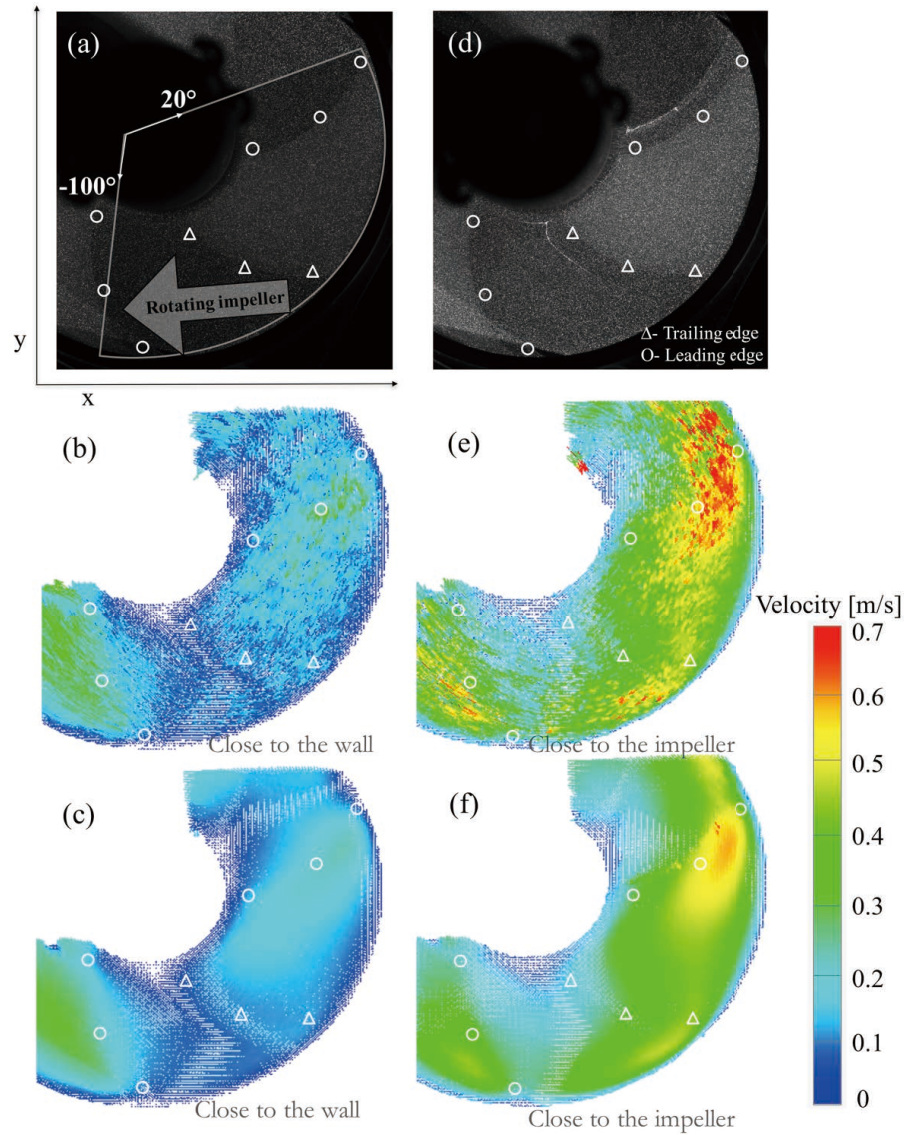


Fig.IV. 16 Illustration of PIV raw images in horizontal measurement (a, d), instantaneous velocity fields (b, e, issued from single image pair) and time-averaged velocity fields (c, f, averaged of 1000 image pairs) in the RVF module. Slice positions: z_1 close to the wall (a, b and c) and z_6 close to the impeller (d, e and f); Operating conditions: $Q_f= 45 \text{ L/h}$, $N=2 \text{ Hz}$; $\mu=0.85 \text{ Pa}\cdot\text{s}$ and $T=20^\circ\text{C}$. Symbols: \circ , leading edge and \triangle , trailing edge of blade

In terms of flow pattern, instantaneous (Fig.IV. 16b and e) and mean (Fig.IV. 16c and f) velocity fields can be compared. Fig.IV. 16b and c present the lowest velocity magnitudes whereas Fig.IV. 16e and f exhibit the highest values (close to the impeller velocity). As expected, mean velocity fields present a uniform and regular flow pattern. Jiang.T et al.[189,193] also introduced a PIV measurement by using pine pollen tracing in water (turbulent flow) with a

rotating membrane bioreactor. This membrane module was consisted of 9 identical flat sheets vertically in a cylindrical reactor, with internal diameter of 240 mm and effective volume of 13 L. In their conditions, mean velocity fields show a clear and stable velocity gradient in radial direction with time-averaged velocity plot. In our study, similar observation can be established:

- It is found that the velocity around the central shaft is regular and organized being close to zero. As it described in Introduction part, feeding fluid goes through the RVF module along the central shaft vertically (z direction) from the bottom to the top, governing velocity vector is at the z direction, so, velocity close to the central shaft in horizontal (x - y) plane is almost zero;
- Velocity gradient increases in radial direction from inner to outer diameters, but velocity remains nearly equal to zero at the maximum diameter $R=70$ mm (fluid is at rest close to the surrounding wall, no-slip boundary conditions at fluid-solid interface). This observation is verified for both position, $z_1=0.25$ and $z_6=2.75$ mm;
- Velocity magnitude close to the inner diameter, $R=25$ mm, remains inferior to 0.1 m/s whereas shaft velocity is equal to 0.31 m/s;
- Velocity fields likely have periodic movements generated by the specific shape of impeller. Maximum fluid velocities (Fig 5c and f) were found near the leading edge of the blade. At $R=65$ mm, the maximum values were 0.15 and 0.45 m/s for $z_1=0.25$ and $z_6=2.75$ mm respectively, while the impeller velocity was 0.82 m/s. However, maximum value in the velocity field $z_1=0.25$ and $z_6=2.75$ mm are at $R=55-60$ mm, with 0.21 and 0.58 respectively.
- Local K_θ ($\frac{\langle U_\theta \rangle}{\omega \cdot R}$) varies from 0.08 up to 0.54 within the gap. Mean value at each radius ($R=25$ to $R=65$) is equal to 0.32 ± 0.08 and remains constant except at the surrounding wall ($R=65$ mm) where a decrease from 0.35 to 0.2 is observed.

Vertical plane

Fig.IV. 17 plots an overview of the raw images and velocity fields by vertical measurement in laminar flow, experiment was conducted at $N=2$ Hz, maximum velocity is equal to 0.87 m/s. Measurements were carried out at $R=30$, 45 and 65 mm, raw observation images are displayed as Fig.IV. 17a, b and c: this vertical plane was fixed between two blades.

Instantaneous velocity fields are presented in (d-f), and the time-average velocity fields are presented in (g-i). This vertical measurement is in agreement with horizontal observation:

- Velocity gradient increases in radial direction from inner to outer diameters (from $R=30$ mm to 65 mm), but velocity remains nearly equal to zero at the surrounding wall;
- Velocity fields have periodic movements generated by the specific shape of impeller, see figure g to i;
- As we expected, in the 3 mm wall-to-impeller gap, velocity close to the wall (membrane) is nearly zero.

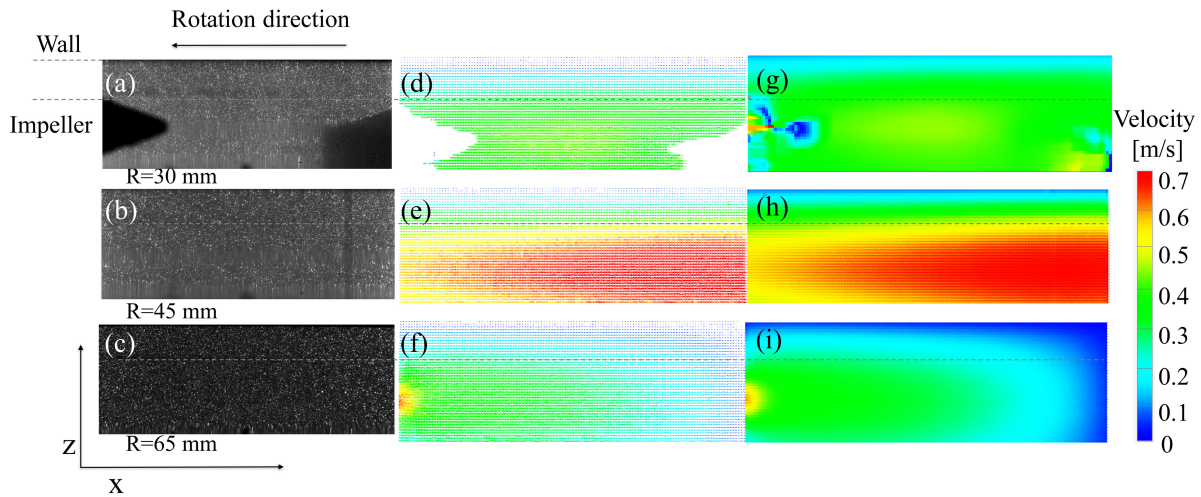


Fig.IV. 17 Vertical measurement in laminar flow. Illustration of PIV raw images (a, b, c), instantaneous velocity fields (d, e, f, issued from single image pair) and time-averaged velocity fields (g, h, i, averaged of 300 image pairs). Vertical positions: $R=30$ mm (a, d, g), $R=45$ mm (b, e, h), $R=65$ mm (c, f, i); Operating conditions: $Q_f= 50$ L/h, $N=2$ Hz; $\mu=0.85$ Pa·s and $T=20^\circ\text{C}$

2.1.1.2. Velocity profiles

Horizontal plane

From horizontal velocity fields, velocity profiles can be more specifically analyzed. Fig.IV. 18a presents the evolution of IDW mean velocity magnitude \overline{U}_m profiles at 3 given radius (30, 45 and 65 mm) for 6 axial positions ($z_1= 0.25$ to $z_6=2.75$ mm). From this overview, However, the unexpected velocity peaks (about 0.35 m/s) which locate at $R=30$ mm $z_6=2.75$ mm can be pointed out as they have the same magnitude as impeller velocity (0.38 m/s). This fact

was most likely caused by the fluorescent particles accumulated on the blade edge, and PIV system considered those particles in data treatment.

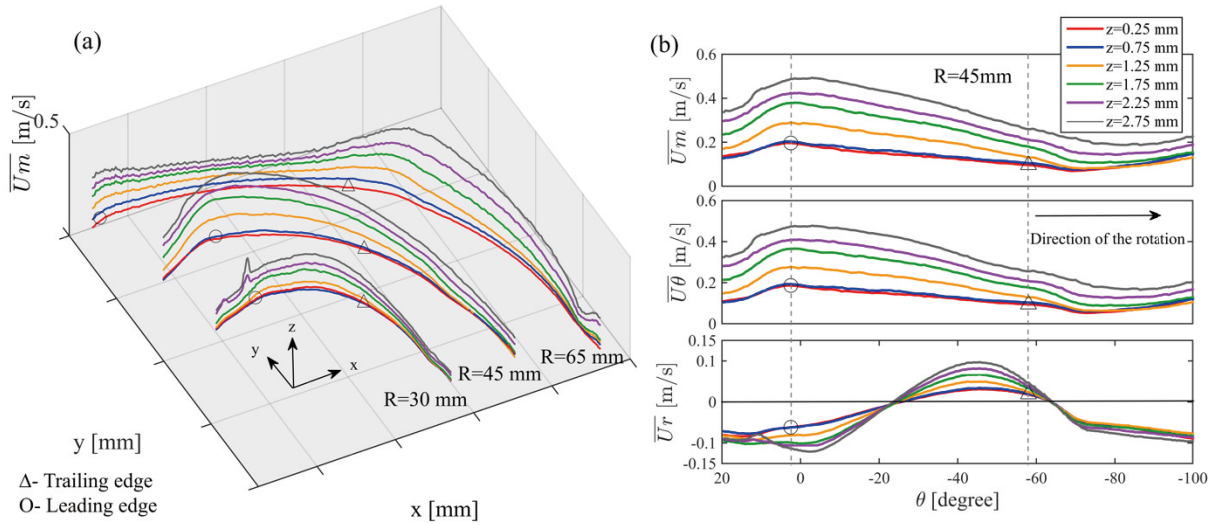


Fig.IV. 18 Evolution of mean velocity profiles \overline{U}_m and their radial and angular components \overline{U}_θ , \overline{U}_r as a function of angular position for 6 horizontal planes (z_1 to z_6) within the membrane-impeller gap. (a): IDW mean velocity at $R=30, 45$ and 65 mm; (b): mean, radial and angular velocity profiles, \overline{U}_m , \overline{U}_θ and \overline{U}_r , at $R=45$ mm. Operating conditions: $Q_f=45$ L/h, $N=2$ Hz; $\mu=0.85$ Pa·s and $T=20^\circ\text{C}$. Symbols: \circ , leading edge and \triangle , trailing edge of blade

In Fig.IV. 18b, mean velocity profiles versus angular position ($-100^\circ < \theta < +20^\circ$) in one third of filtration cell are presented at $R=45$ mm within a reconstructed polar coordinate centered at the middle of the rotating shaft. Both components were derived from the Cartesian velocity by decomposing the velocity vector into radial and tangential components. Profiles were observed to be periodic and sustain previous observation with velocity fields. As expected, maximum velocity occurs close to the impeller ($z_6=2.75$ mm), and decrease gradually from the impeller to the wall without any disruption between the layers. It indicated that laminar flow within the gap was highly stable and well organized. Specific remarks can be summarized from Fig.IV. 18b:

- \overline{U}_m and \overline{U}_θ are statistically similar. Since the RVF module is an rotating mixing device with an impeller equipped with three flat blades, the dominant velocity component is \overline{U}_θ ;
- Some noticeable waves appear at the leading edge (symbol O), probably due to the shape blades. It might imply that this impeller design could periodically generate

Chapter IV: Results and Discussion

regular variations along the angular direction, and tended to remove the membrane fouling even with highly viscous fluids;

- \overline{U}_r has a negligible contribution in value but oscillated with a highly organized ebbs and flows, probably due to the impeller design as well;

Besides, velocity profiles were also compared with two feed flowrates (25 and 45 L/h). Results showed that velocity profiles are 99% percent similar, no significant impact was observed. It corroborated one of the advantages of DF compare to the conventional filtration (DE, CF) with an internal flow pattern independent from feed flowrate.

Vertical plane

Fig.IV. 19 plots a vertical velocity profile from the velocity field Fig.IV. 17g-i (R=30 mm to 60 mm), and compare to the CFD simulation (solid and dotted curves). This profile is located at the center of the measurement window, it is also the middle between two blade, (-25° in Fig.IV. 18) Standard deviation of each curve are around: $\overline{\sigma}_{R=30} = 0.09$, $\overline{\sigma}_{R=45} = 0.21$, $\overline{\sigma}_{R=60} = 0.15$ This vertical measurement gives evidence that:

- Vertical velocity profile in this gap (membrane-to-membrane) is parabolic;
- Velocity at R=45 mm seems to have higher value than R=30 mm and 60 mm, it verified the observation in Fig.IV. 17;
- Simulation at R=45 mm seems well fit the experiment curve. However, simulations results for R=30 mm and R= 65 mm are over estimated while the trend are the same as experiments result $U_{R=45} > U_{R=30} > U_{R=65}$.

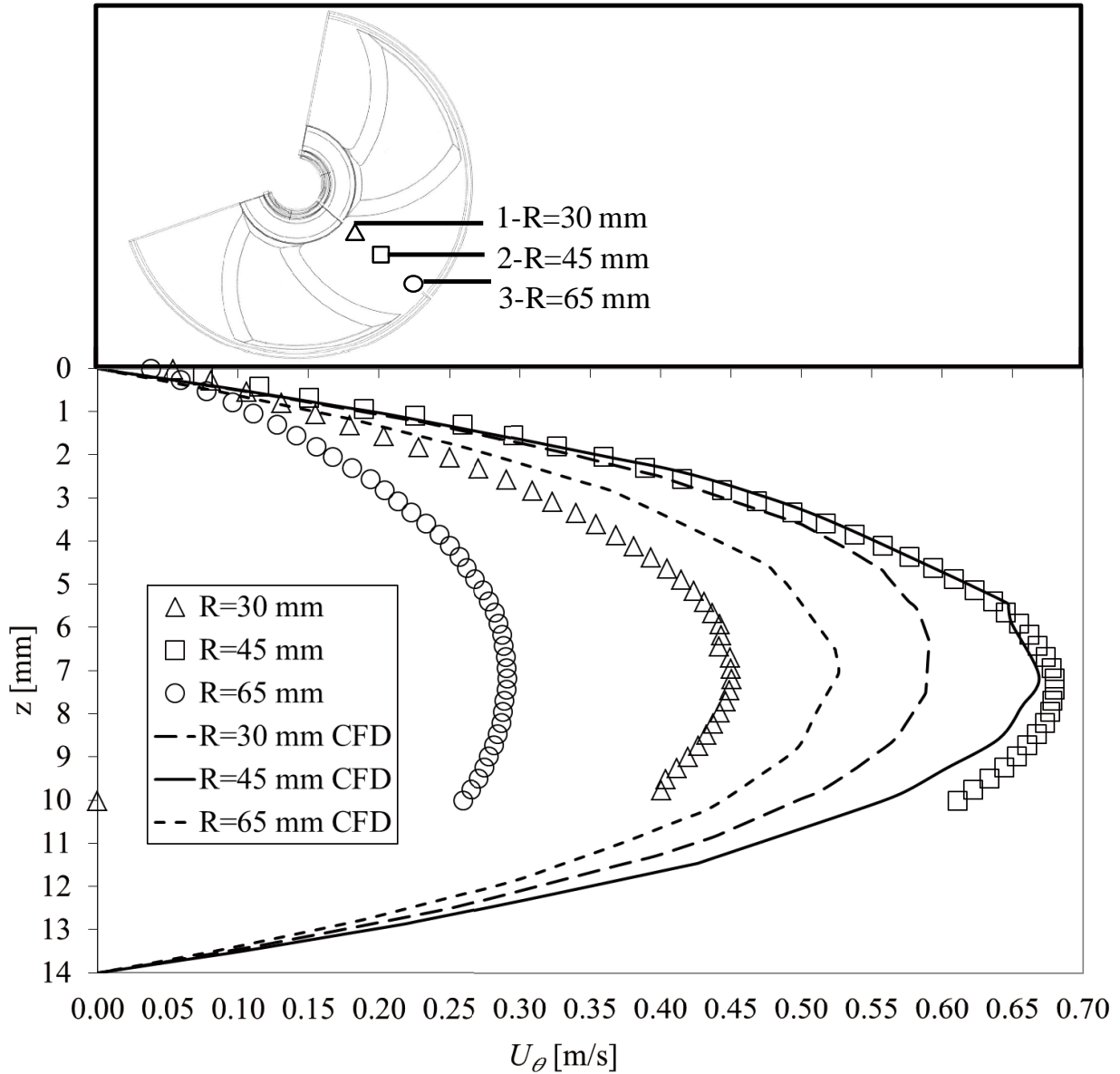


Fig.IV. 19 Vertical velocity profile at z direction at $R=30$ mm, $R=45$ mm and $R=65$ mm (between two blades) and compare to the CFD simulation. Operating conditions: $Q_f= 50$ L/h, $N=2$ Hz; $\mu=0.85$ Pa·s and $T=20^\circ\text{C}$

2.1.1.3 Comparison with CFD simulation

Simulation in laminar flow is already well developed in commercial software. It is easier to have more accurate results than in turbulent flow. So, in our study, simulation was presented only in laminar flow.

2.1.1.2.1 Simulated velocity and shear fields

Navier-Stokes equations can be easily and rigorously solved in laminar regime without any approximation. On the contrary it is not possible to perform DNS (direct Numerical Simulations) in turbulent regime except for very simplified geometries. Even if there exists a number of models for turbulent flow generally based on Reynolds decomposition, such as the common used k-eps model, we restrict the numerical study to laminar flow.

In this case, CFD give access to velocity in x , y and z coordinate, results present in this part is velocity magnitude in the x - y plane associated with PIV measurements.

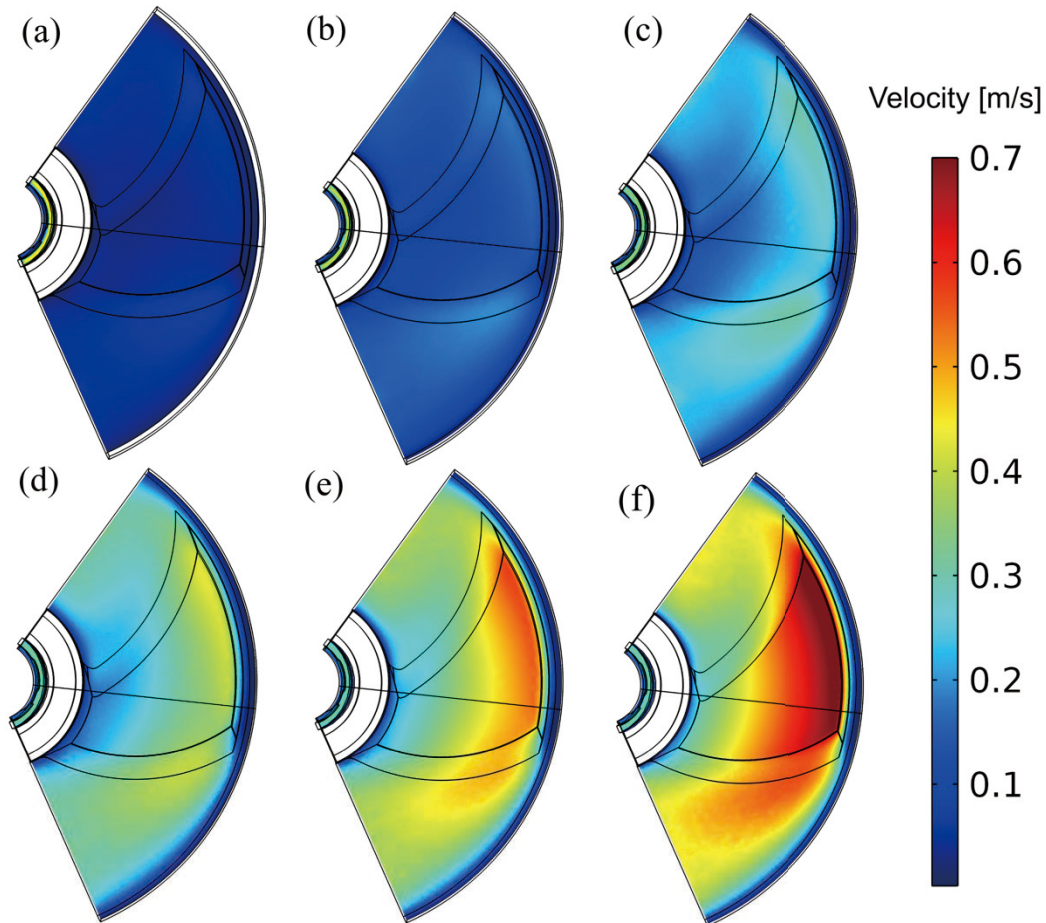


Fig.IV. 20 Velocity fields in CFD simulation with 6 slices, from z_1 (a) to z_6 (f). Operating conditions: $Q_f= 45$ L/h, $N=2$ Hz; BREOX solution, $\mu=0.85$ Pa·s and $T=20^\circ\text{C}$

In Fig.IV. 20a, velocity fields at 6 slices are plotted to appreciate velocity magnitude and deviation. A first qualitative approach (Fig.IV. 16 and Fig.IV. 20) is presented to compare the simulated and experimental velocity fields:

Chapter IV: Results and Discussion

- Velocities are nearly equal to zero when the flow layers are close to the wall (z_1), while the closest to the impeller present the highest values (z_6);
- Velocity is nearly zero close to the central shaft and the surrounding wall ($R=70$ mm) of the filtration cell;
- Maximum velocities occur at leading edge at $R=55-60$ mm of the impeller for (a) (b) (c) and (d) which has been found also in Fig.IV. 16, but for (e) and (f), it is found above the blade body;
- Differences between PIV and CFD may come from the precision and uncertainty of measurement, as we described, adjusting the measuring plane may have ± 0.25 mm error due to the laser thickness.

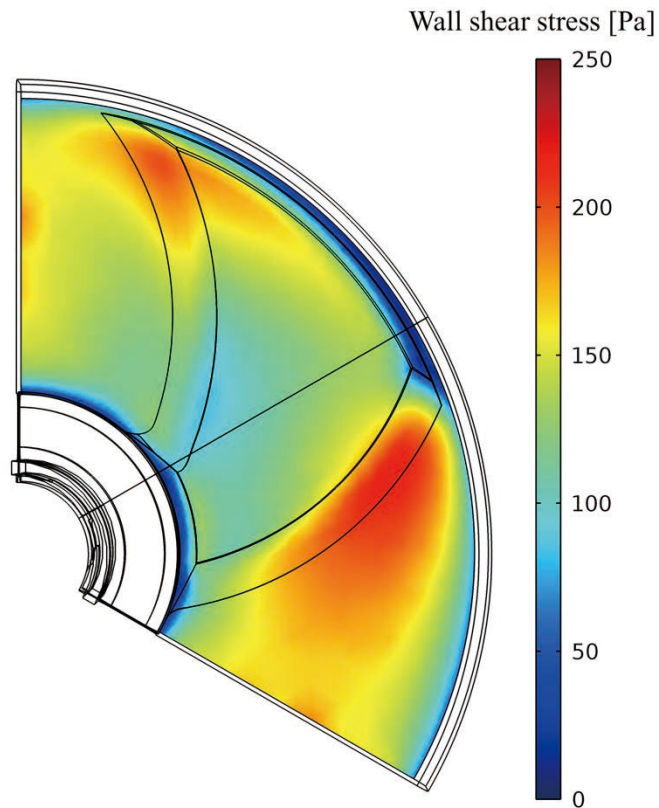


Fig.IV. 21 Field of wall shear stress ($z=0$ and 14 mm) calculated from CFD simulations. Operating conditions: $Q_f= 45$ L/h, $N=2$ Hz; $\mu=0.85$ Pa·s and $T=20^\circ\text{C}$ (Notice: $z=0$ and 14 mm is at the surface of the walls where membranes are mounted)

Velocity magnitudes and parabolic shapes sustain the accurate fitting between PIV and CFD, local shear stress can be estimated from CFD to introduce the hydrodynamic phenomena in

the filtration cell. Therefore, wall shear stress field is reported in Fig.IV. 21, it is the tangential component of the stress vectors applied on the wall surface (absolute values are almost the same at $z=0$ and 14 mm), and calculated by $\tau_w = \mu \sqrt{\left(\frac{\partial u}{\partial z} + \frac{\partial w}{\partial x}\right)^2 + \left(\frac{\partial w}{\partial y} + \frac{\partial v}{\partial z}\right)^2}$, where τ_w is the wall shear stress; u , v , and w are the velocity vectors in m/s at x , y and z direction respectively. In our operating conditions ($Q_f= 45$ L/h, $N=2$ Hz; $\mu=0.85$ Pa·s and $T=20^\circ\text{C}$), high values of τ_w are found at two areas: the leading edge of the impeller ($\tau_{w_max} = 225$ Pa) and the tip of the impeller trailing edge ($\tau_{w_max} = 200$ Pa). This result almost corresponds to the velocity field in PIV (Fig.IV. 16) and CFD (Fig.IV. 20): the area with higher velocity value has the higher shear stress value. This information may indicate a complex hydrodynamics at the membrane surface, which is intensified by the complex shape of the impeller and its rotation.

2.1.1.2.2 Vertical profile of velocity magnitude comparing PIV and CFD

As mentioned, PIV measurements were performed in half of the filtration cell from z_1 to z_8 . Due to optical obstruction of laser beam, velocity field in z_7 and z_8 can only measure between 2 blades and provided very limited information, while CFD simulations were applied to the entire filtration cell (within 14 mm gap $0 < z < 14$ between both membranes, including upper gap $0 < z < 3$ impeller thickness $3 < z < 11$, and lower gap $11 < z < 14$).

Fig.IV. 22 compares velocity profiles at radius $R=45$ mm between PIV measurements and CFD simulation. All curves issued from CFD simulations present a typical parabolic laminar profile between two fixed walls for point 1 (leading edge at $\theta=0^\circ$), 2 (between two blades at $\theta=-30^\circ$) and 3 (trailing edge at $\theta=-60^\circ$). Between 2 blades, the maximum velocities were located at the parabolic vertex corresponding to the middle of filtration cell ($z=7$ mm). Between blade and membrane, the maximum velocity can be observed at blade surface (Fig.IV. 18b). Velocity at leading edge (Point 1) is higher than the two other points (2 and 3) with a maximum velocity of 0.757 ± 0.029 m/s in PIV and 0.778 m/s in CFD. For points, 2 and 3, maximum velocities were respectively 0.678 ± 0.027 m/s and 0.517 ± 0.046 m/s for PIV and 0.641 m/s and 0.556 m/s for CFD. However, theoretical angular velocity of the impeller is 0.56 m/s at $R=45$ mm, a tentative inference on this result is that special configuration (narrow gap, confined volume with rotating three-blade impeller) have great influence in local velocity field and thus has complex hydrodynamic in the filtration cell, according to author's limited knowledge. Regarding

maximum velocities, the consistency between PIV and CFD is well established. Considering whole velocity profiles, the same trends could be observed even if the profile at trailing edge is slightly overestimated with CFD. Slight deviations are justified by uncertainty of experimental measurements regarding laser sheet location and velocity.

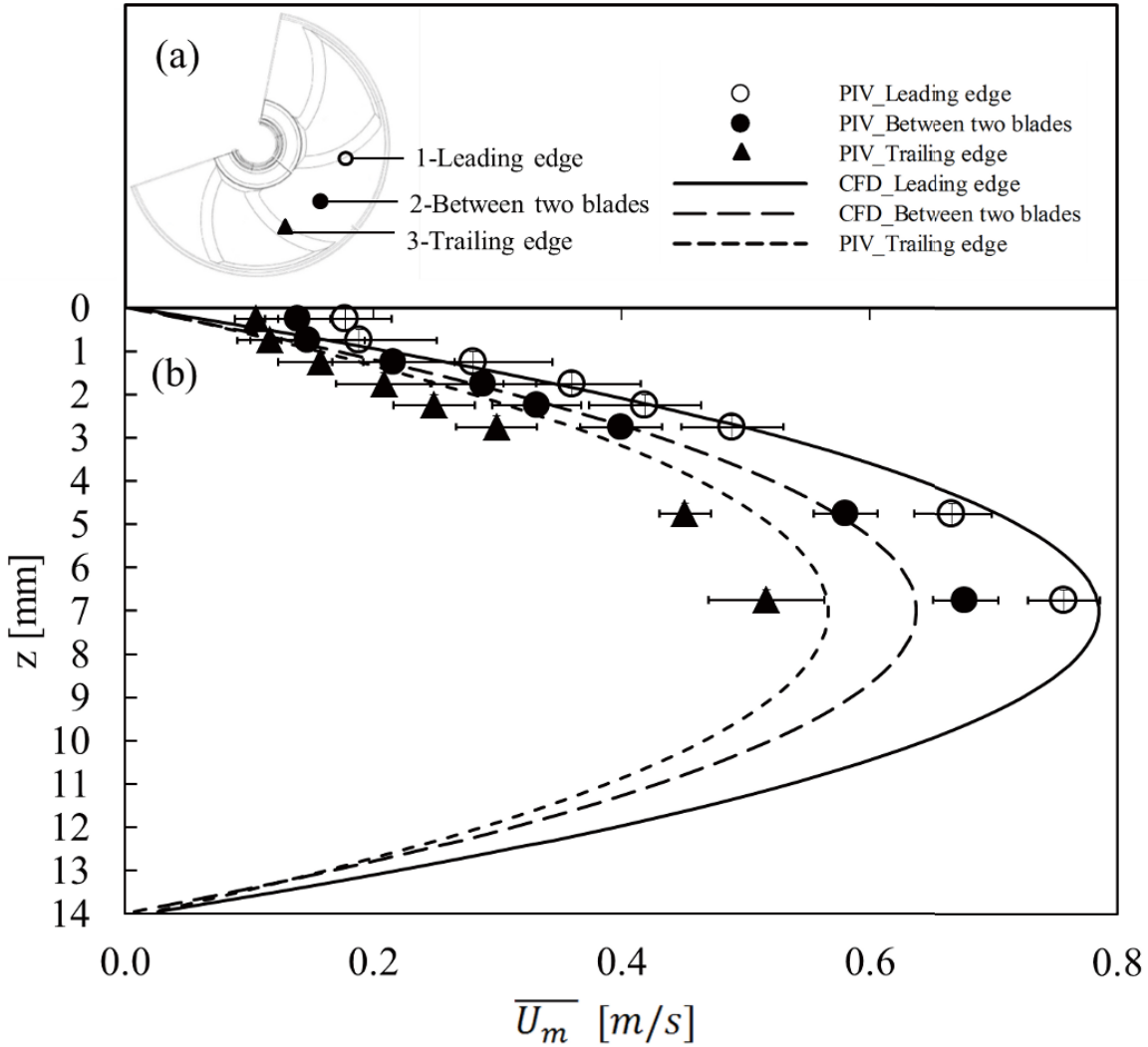


Fig.IV. 22 Evolution of mean velocity \overline{U}_m issued from PIV horizontal measurement and CFD simulations as a function of z , for 3 points, at radius $R=45$ mm (point 1: leading edge, point 2: between two blades, point 3: trailing edge). Operating conditions: $Q_f= 45$ L/h, $N=2$ Hz; $\mu=0.85$ Pa·s and $T=20^\circ\text{C}$. (Notice: $z=0$ and 14 mm is at the surface of the walls where membranes are mounted, this 14 mm gap is including upper gap $0 < z < 3$ impeller thickness $3 < z < 11$, and lower gap $11 < z < 14$)

Chapter IV: Results and Discussion

To review, in horizontal measurements, velocity was presented at θ -R plane at limited z level at a fixed impeller position; in vertical measurements, velocity was presented at θ - z plane at limited R position and a fixed impeller position. To conclude PIV experiment with trigger strategy:

- (1) It gives velocity distribution at a certain condition (impeller position);
- (2) But it doesn't give information in time span and the impact of impeller movement;
- (3) It also gives insufficient information to access to wall shear stress because it was a challenge and technical limitation to precisely realize the distance between the target plane and the wall/membrane.

Therefore, PIV measurements connected with optical trigger helps to well understand the velocity deviation at a given impeller position. To get further information such as the evolution of velocity and shear affected by the impeller movement, PIV experiments without the optical trigger are necessarily needed.

2.1.2 Turbulent regime

2.1.2.1 Velocity field analyses

By analyzing the PIV raw images, the instantaneous velocity fields (from single images pair) and time averaged mean velocity fields (from 1000 image pairs) were computed at 6 horizontal plane (x - y plane within membrane-impeller gap) and 3 vertical plane (x - z plane at different radius).

Horizontal plane

PIV measurement within turbulent flow (similar presentation as in laminar flow, see Fig.IV. 16), Fig.IV. 23 provides an overview of the magnitude of velocity fields. Raw PIV images, figure a and d show the constant position of impeller and the homogeneous surface density of florescent particles for $z_I=0.25$ (close to membrane) and $z_6=2.75$ (close to impeller) mm. In terms of flow pattern, instantaneous (figure b and e) and mean velocity fields (figure c and f) are presented. In this experimental condition, maximum impeller velocity is equal to 4.3 m/s at $R=69$ mm. Main observations are:

- As expected, mean velocity fields present a uniform and regular flow pattern;
- Velocity around the central shaft is regular and organized being close to zero because the governing velocity vector is at the z direction, which could not be measured in horizontal plane;
- Velocity gradient increases in radial direction from inner to outer diameters, maximum velocity was found at the trailing edge of the impeller, which is different from observation in laminar flow.
- Velocity fields seems similar close to the wall/membrane and close to the impeller, it is likely to have a constant velocity along the z direction;
- Local K_θ ($\frac{\langle \overline{U_\theta} \rangle}{\omega \cdot R}$) varies from 0.52 up to 0.65 within the gap. Mean value at each radius ($R=30$ to $R=65$) is equal to 0.58 ± 0.06 .

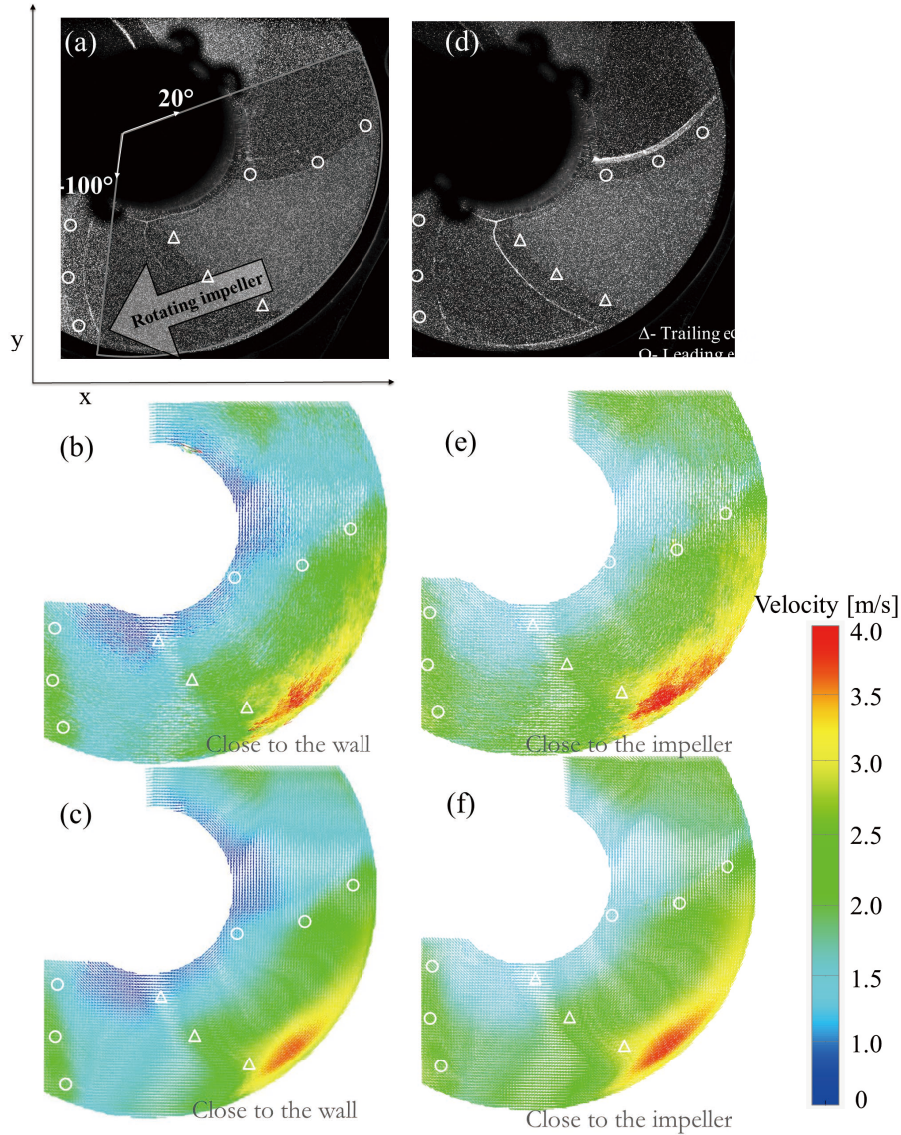


Fig.IV. 23 Illustration of PIV raw images in horizontal measurement (a, d), instantaneous velocity fields (b, e, issued from single image pair) and time-averaged velocity fields (c, f, averaged of 1000 image pairs) in the RVF module. Slice positions: z_1 close to the wall (a, b and c) and z_6 close to the impeller (d, e and f); Operating conditions: $Q_f=100$ L/h, $N=10$ Hz; water, $\mu=1$ mPa·s and $T=20^\circ\text{C}$. Symbols: \circ , leading edge and \triangle , trailing edge of blade

Vertical plane

Fig.IV. 24 plots an overview of the raw images and velocity fields by vertical measurement in turbulent flow, experiment was conducted at $N=10$ Hz, maximum velocity is equal to 4.3 m/s (same operating condition as horizontal measurement). Experiments were carried out at $R=30, 45$ and 65 mm, raw images are displayed as figure (a- c): this vertical plane

was fixed between two blades. Instantaneous velocity fields are presented in (d-f). This vertical measurement is in agreement with horizontal observation:

- Velocity gradient increases in radial direction from inner to outer diameters (from $R=30$ mm to 65 mm, see d-f);
- As we expected, velocity fields have constant value at a given radius;

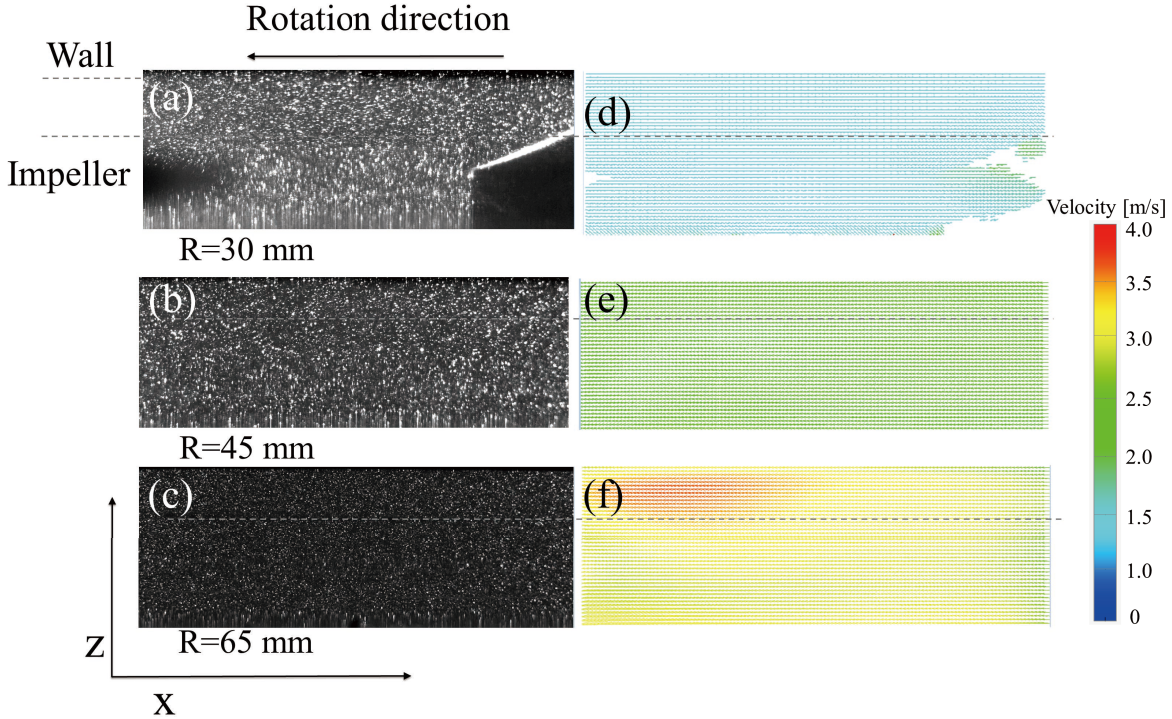


Fig.IV. 24 Vertical measurement in turbulent flow. Illustration of PIV raw images (a, b, c), instantaneous velocity fields (d, e, f, issued from single image pair). Vertical positions: $R=30$ mm (a, d), $R=45$ mm (b, e), $R=65$ mm (c, f); Operating conditions: $Q_f= 100$ L/h, $N=10$ Hz; water, $\mu=01$ mPa·s and $T=20^\circ\text{C}$

2.1.2.2. Velocity profiles

Horizontal plane

Fig.IV. 25a presents the evolution of \overline{U}_m profiles at 3 given radius (30, 45 and 65 mm) for 6 axial positions ($z_1= 0.25$ to $z_6=2.75$ mm).

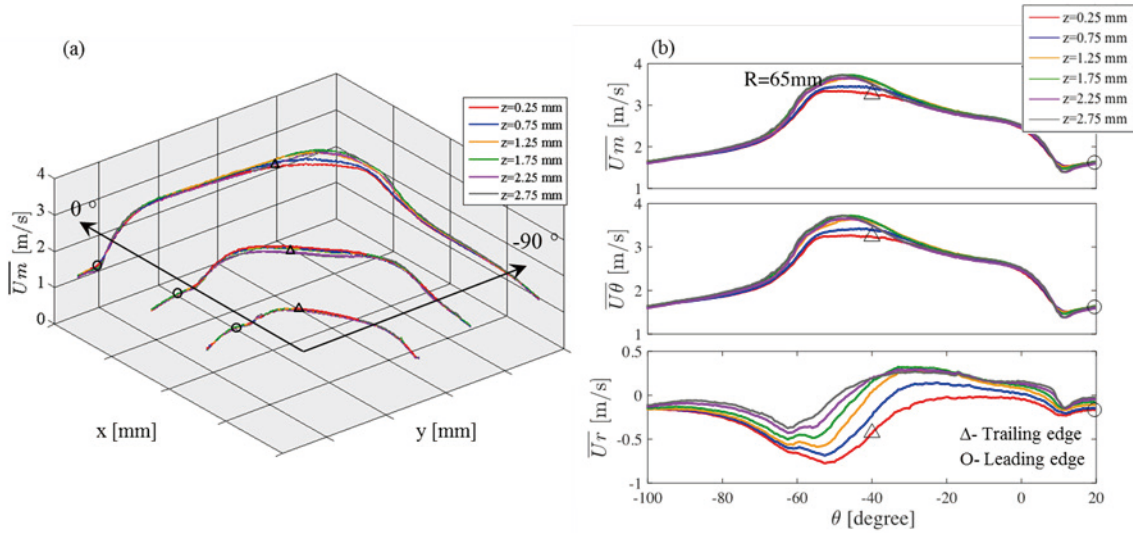


Fig.IV. 25 Evolution of mean velocity profiles \overline{U}_m and their radial and angular components \overline{U}_θ , \overline{U}_r as a function of angular position for 6 horizontal planes (z_1 to z_6) within the membrane-impeller gap. (a) IDW mean velocity at $R=30, 45$ and 65 mm; (b): mean, radial and angular velocity profiles, $\overline{U}_m, \overline{U}_\theta$ and \overline{U}_r , at $R=65$ mm. Operating conditions: $Q_f= 100$ L/h, $N=10$ Hz; water, $\mu=1$ mPa·s and $T=20^\circ\text{C}$. Symbols: O, leading edge and Δ , trailing edge of blade

In Fig.IV. 25b, mean velocity profiles versus angular position ($-100^\circ < \theta < +20^\circ$) in one third of filtration cell are presented at $R=65$ mm. Profiles \overline{U}_m and \overline{U}_θ were observed to be uniform at each z position. Along the angular position, we found the velocity is periodic (same value at $\theta = -100$ and 20), the maximum velocity is located at the trailing edge of the impeller, which verifies the observation in Fig.IV. 23. It indicated that the mixing in turbulent flow within the gap was highly homogenous. Specific remarks can be summarized from Fig.IV. 25b:

- \overline{U}_m and \overline{U}_θ are statistically similar;
- \overline{U}_r has a negligible contribution in value but it has a well-organized motion;
- Besides, velocity profiles were also compared with two feed flowrates (50 and 100 L/h). Results showed that no significant impact on velocity profiles was observed. It once again proves the advantage of DF module that flowrate is uncoupled with velocity distribution in this kind of filtration system.

Vertical plane

Fig.IV. 26 plots a vertical velocity profile from the velocity field Fig.IV. 24d-f ($R=30$ mm to 60 mm). This profile is located at the center of the measurement window, it is also the middle

Chapter IV: Results and Discussion

between two blade, (-15° in Fig.IV. 18) Standard deviation of each curve are around: $\overline{\sigma_{R=30}} = 0.08$, $\overline{\sigma_{R=45}} = 0.12$, $\overline{\sigma_{R=65}} = 0.64$. The main observation in this vertical measurement is that vertical velocity profile in this gap (membrane-to-membrane) is almost uniform, and it verify the observation in Fig.IV. 23;

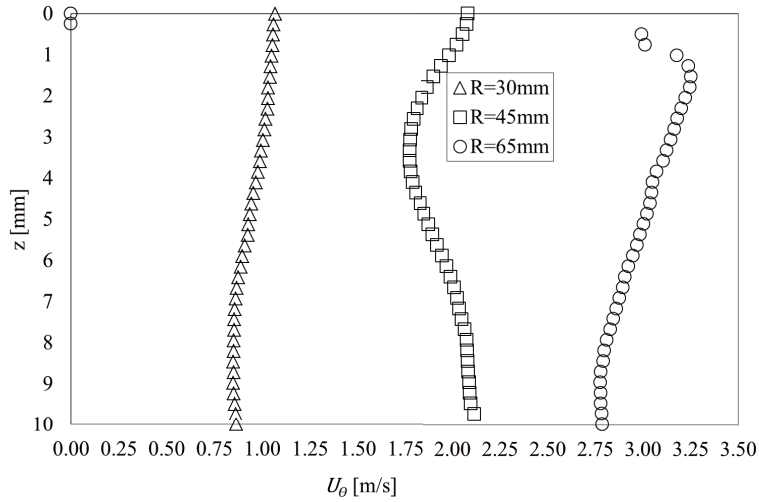


Fig.IV. 26 Vertical velocity profile at z direction at R=30 mm, R=45 mm and R=65 mm. Operating conditions: $Q_f= 100$ L/h, $N=10$ Hz; water, $\mu=1$ mPa·s and $T=20^\circ\text{C}$

❖ **Summary: local approach PIV with trigger strategy**

Objectives:

To study local hydrodynamics under laminar and turbulent flow at a fixed condition by using the optical trigger.

To compare experiments with CFD simulation to validate numerical model in laminar regime.

Highlights:

In laminar regime:

(1) Velocity fields: Horizontal velocity fields close to the wall/membrane and close to the impeller are presented respectively. Maximum velocity is found at the leading edge of the impeller; Vertical velocity fields are presented at R=30, 45 and 65 mm radial position;

(2) Velocity profiles: Angular velocity profiles (velocity magnitude versus angular position) are presented at 6 slices (z_1 to z_6), deduced from horizontal measurements. These profiles are highly organized; vertical velocity profiles (velocity magnitude versus z direction) are plotted at R=30, 45 and 65mm, and they exhibit a parabolic distribution;

(3) CFD simulation: CFD result is only compared with velocity fields and profiles which are calculated from horizontal measurements. Results compare the velocity magnitude at 3 positions: at the leading edge, between two blades and at the trailing edge which are located at R=45 mm.

In turbulent regime:

(1) Velocity fields: Horizontal velocity fields close to the wall/membrane and close to the impeller are presented respectively. Maximum velocity is found at the trailing edge of the impeller; Vertical velocity fields are presented at R=30, 45 and 65 mm radial position;

(2) Velocity profiles: Angular velocity profiles (velocity magnitude versus angular position) are presented at 6 slices (z_1 to z_6), deduce from horizontal measurement, these profiles at different slices seem the same distribution; vertical velocity profiles (velocity magnitude versus z direction) are plotted at R=30, 45 and 65mm, and they exhibit an almost constant distribution.

2.2 POD analysis (with non-trigger strategy)

Hydrodynamics in the cell was investigated by Particle Image Velocimetry (PIV). PIV technique enables to achieve a noninvasive measurement and determine 2D instantaneous velocity field. Laminar and turbulent flows were investigated.

Due to the presence of the impeller, both in laminar and turbulent regimes, it is essential to account for velocity fluctuations induced by the periodic motion of the impeller. Two solutions were investigated:

- Conditional averaging (angle-resolved measurements, fixed with trigger strategy, *Chapter IV 2.1 Preliminary study-PIV with trigger strategy*)
- Reconstruction of organized motion based on POD processing (non-trigger strategy, *Chapter IV 2.2 POD analysis (with non-trigger strategy)*)

In laminar flow, each instantaneous velocity should be split into two contributions:

$$U_i = \bar{U}_i + \tilde{u}_i \quad (\text{IV.11})$$

In turbulent flow, a triple decomposition of the instantaneous velocity can be considered as:

$$U_i = \bar{U}_i + \tilde{u}_i + u'_i \quad (\text{IV.12})$$

where the instantaneous velocity component is U_i and the angle-resolved averaged component is $\bar{U}_i + \tilde{u}_i$, the turbulent fluctuation being u'_i . \bar{U}_i is the mean velocity (both organized and turbulent fluctuations are filtered) whereas \tilde{u}_i is the periodic (or organized) fluctuation induced by the impeller blade.

Based on a statistic of instantaneous 2D velocity fields, POD enables to generate a series of eigenvalues and eigenvectors. $\lambda^{(I)}$ is the I^{th} eigenvalue and $\overrightarrow{\Phi}^{(I)}(x, y)$ is the I^{th} associated eigenvector or eigenvector. Each instantaneous velocity field can be reconstructed as:

$$\vec{U}(x, y, z, t) = \sum_{I=1}^K a^{(I)}(t) \overrightarrow{\Phi}^{(I)}(x, y, z) \quad (\text{IV.13})$$

Chapter IV: Results and Discussion

I is the I^{th} mode of POD (total mode number equal to K), while $a^{(I)}(t)$ is the corresponding POD coefficient; the series of coefficient $a_k^{(I)}$ (or $a^{(I)}(t)$ in case of resolved PIV) is given by the projection of each instantaneous velocity field on the I^{th} eigen vector:

$$a_k^{(I)} = \left(\overrightarrow{U}_k, \overrightarrow{\Phi}^{(I)} \right) \quad (\text{IV.14})$$

By this way, one can thus reconstruct the velocity field and in particular, the mean flow and the organized motion by Eq.III 26: $\overrightarrow{U}_k(x, y, z, t) = \sum_{I=1}^N \overrightarrow{U}_k^{(I)}(x, y, z) = \sum_{I=1}^N a_k^{(I)} \overrightarrow{\Phi}^{(I)}(x, y, z)$

2.2.1 Laminar regime

It is essential to account for velocity fluctuations induced by the periodic motion of the impeller. Each instantaneous velocity should be split into two contributions as Eq.IV.11 shows: $U_i = \bar{U}_i + \tilde{u}_i$, where \bar{U}_i stands for mean value (periodic fluctuation being filtered) and \tilde{u}_i accounts for periodic fluctuations induced by the impeller blades.

In a first part, we will focus on laminar mean flow; then fluctuation contributions will be analyzed.

2.2.1.1 Mean laminar flow

The case presented here corresponds to a viscous fluid ($\rho = 1067 \text{ kg/m}^3$; $\mu = 0.85 \text{ Pa.s}$) and low frequency ($N = 2 \text{ Hz}$). Thus the Reynolds number is:

$$Re_{mixing} = \frac{\rho N d_m^2}{\mu} = 42$$

Horizontal plane

Three horizontal planes were investigated by PIV. Radial profiles of tangential mean velocities are plotted. Classical laminar flow profiles are exhibited in Fig.IV. 27, the tangential velocity component increases with radial position up to a maximum then decreases towards the external static wall ($R=70 \text{ mm}$).

The radial profiles of tangential velocity component are mainly controlled by the upper and lower boundary conditions: the upper wall ($z=0.25 \text{ mm}$) is fixed and the lower boundary

Chapter IV: Results and Discussion

($z=2.75$ mm) corresponds to the impeller. The three radial profiles exhibit the same trend, increasing between $R = 20$ mm up to $R=55$ mm, then decreasing towards the external static wall.

The maximum velocity ($R=55$ mm) linearly decreases from high value close to the impeller (0.52 m/s) to intermediate value in the middle plane (0.32 m/s) and to low value close to the upper static wall (0.12 m/s).

From these profiles, one can estimate the radial profile of viscous shear stress by:

$$\tau_{r\theta}(r) = \mu r \frac{\partial}{\partial r} \left(\frac{U_\theta}{r} \right) \quad (\text{IV.15})$$

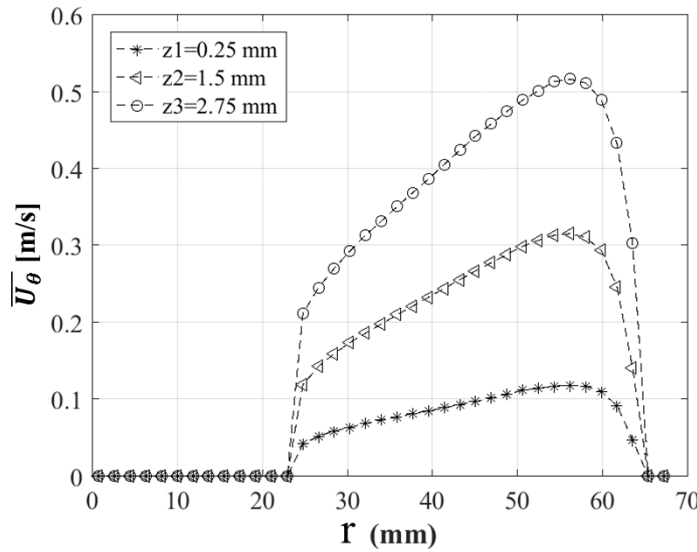


Fig.IV. 27 Radial profiles of tangential mean velocities at 3 planes, $z=0.25, 1.5$ and 2.75 mm (distance from the upper wall). Operating conditions: horizontal measurements at $Q_f= 50$ L/h, $N=2$ Hz; BREOX solution, $\mu=0.85$ Pa·s, $Re_{mixing}=42$, and $T=20^\circ\text{C}$

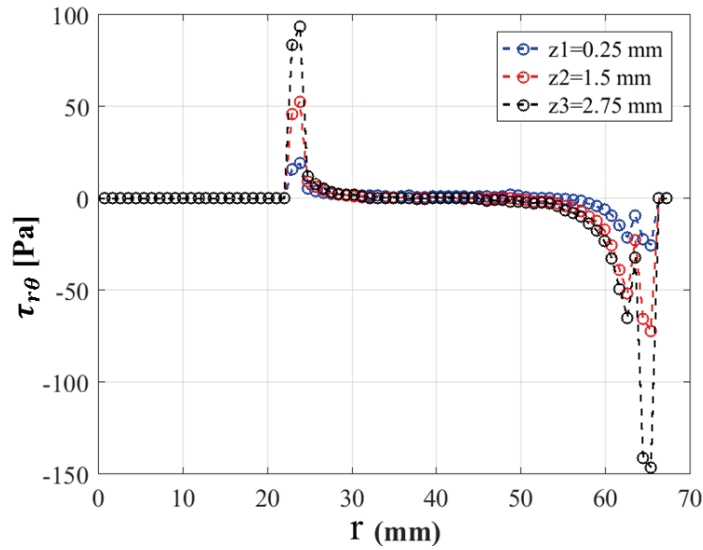


Fig.IV. 28 Radial profiles of viscous mean shear at 3 planes, $z=0.25, 1.5,$ and 2.75 mm (distance from the upper wall). Operating conditions: horizontal measurements at $Q_f= 50$ L/h, $N=2$ Hz; BREOX solution, $\mu=0.85$ Pa·s, $Re_{mixing}=42$, and $T=20^\circ\text{C}$

From Fig.IV. 28, one can estimate the mean shear stress at the external wall ($R = R_{ext}$) from each shear stress profile. Near the upper wall of the cell (z_1), the shear stress at the external wall is low and equal to 25 Pa. In the middle plane (z_2), the shear stress at the external wall is higher and equal to 75 Pa whereas close to the impeller (z_3), it is highest and equal to 150 Pa. The vertical distribution of wall shear stress is thus almost linear.

Then the torque can be estimated resulting from the distribution of wall shear stress along the external cylinder, above and below the impeller assuming a mean value of $\tau_{ecu} = 75$ Pa:

$$T_{extcyl_{upper}} = 2 \pi R_e \varepsilon_u \tau_{ecu} R_e = 0.007 \text{ N.m}$$

where $R_e = 70$ mm is the external radius of the filtration cell, $\varepsilon_u = 3$ mm is the gap between the upper wall/membrane and the impeller.

The same torque is applied along the external cylinder below the impeller:

$$T_{extcyl_{lower}} = 2 \pi R_e \varepsilon_l \tau_{ecl} R_e = 0.007 \text{ N.m}$$

where $\varepsilon_l = 3$ mm is the gap between the lower wall/membrane and the impeller.

Chapter IV: Results and Discussion

One can consider that the wall shear stress in the region of the impeller at the external cylinder is constant and equal to:

$$\tau_{eci} = \mu \frac{R_m 2 \pi N}{R_e - R_m} = 280 \text{ Pa}$$

where $R_m=67.5$ mm is the radius of the impeller, $R_e - R_m$ indicates a gap between the external wall and the impeller.

The resultant torque is thus:

$$T_{extcyl_{impeller}} = 2 \pi R_e \varepsilon_m \tau_{eci} R_e = 0.07 \text{ N.m}$$

Consequently, the total torque along the external cylinder is

$$T_{extcyl_{total}} = 0.085 \text{ N.m}$$

Vertical planes

Three vertical planes were investigated by PIV at three radial positions ($R= 30, 45$ and 65 mm). Vertical profiles of tangential mean velocities are plotted.

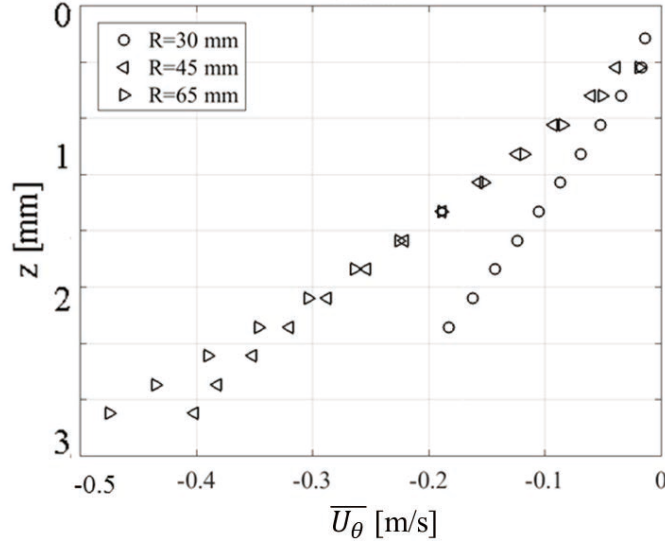


Fig.IV. 29 Vertical profiles of tangential mean velocities at 3 radius, $R=30, 45$ and 65 mm. Operating conditions: vertical measurements at $Q_f= 50$ L/h, $N=2$ Hz; BREOX solution, $\mu=0.85$ Pa·s, $Re_{mixing}=42$, and $T=20^\circ\text{C}$

Chapter IV: Results and Discussion

Clearly, the vertical profiles measured in the 3 mm gap above the impeller are quasi-linear. This is consistent with previous observations. The velocity is equal to zero at the static wall. Close to the impeller, it is maximum and probably proportional to the local tangential velocity of the impeller.

Dimensionless velocity profiles can be deduced by dividing the tangential velocity of the local rotation speed equal to: $2 \pi N r$. Characteristic results are plotted:

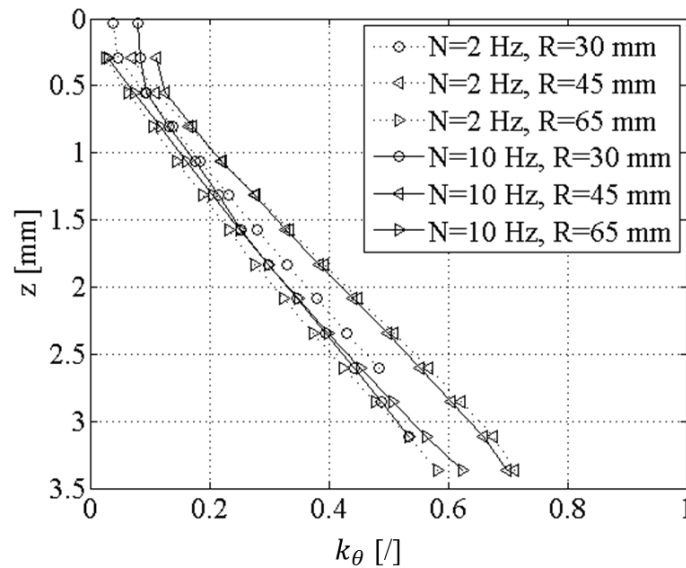


Fig.IV. 30 Vertical profiles of dimensionless velocity k_θ (local velocity coefficient) at 3 radius $R=30, 45$ and 65 mm with $N=2$ and 10 Hz. Operating conditions: vertical measurements at $Q_f=50$ L/h; BREOX solution, $\mu=0.85$ Pa·s, $Re_{mixing}=42$ and 210 , and $T=20^\circ\text{C}$

From these plots, vertical profiles of viscous mean shear stress can be plotted and the viscous shear stress at the upper wall can be estimated.

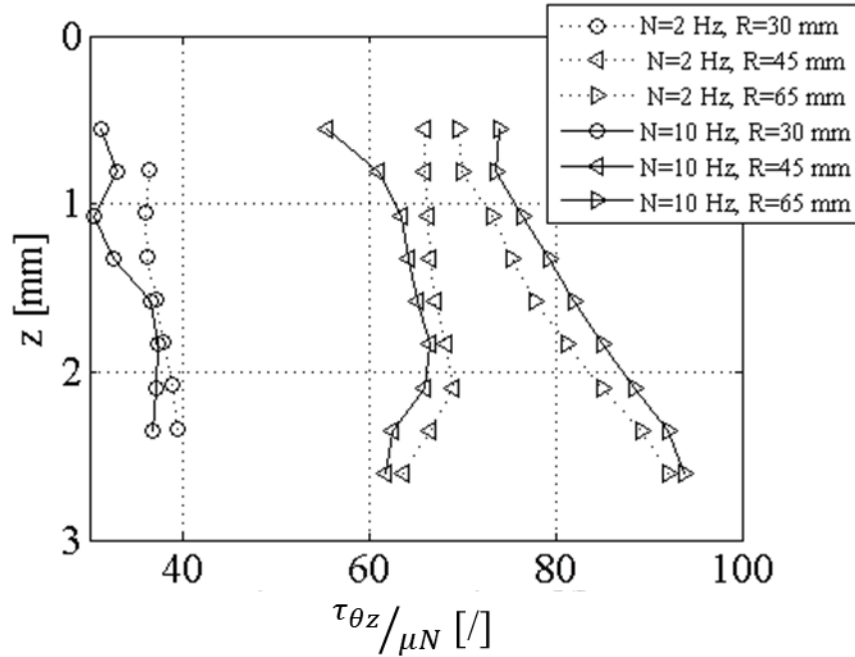


Fig.IV. 31 Vertical profiles of viscous mean shear stress at 3 radius $R=30, 45$ and 65 mm with $N=2$ and 10 Hz. Operating conditions: vertical measurements at $Q_f= 50$ L/h; BREOX solution, $\mu=0.85$ Pa·s, $Re_{mixing}=42$ and 210 , and $T=20^\circ\text{C}$

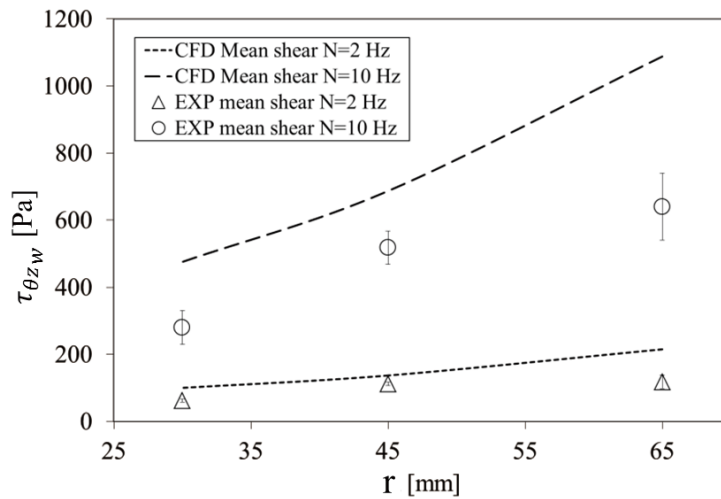


Fig.IV. 32 Radial profiles of wall shear stress compare to CFD, at 3 radius $R=30, 45$ and 65 mm with $N=2$ and 10 Hz. Operating conditions: vertical measurements at $Q_f= 50$ L/h; BREOX solution, $\mu=0.85$ Pa·s, $Re_{mixing}=42$ and 210 , and $T=20^\circ\text{C}$

Clearly, the radial profile of wall viscous shear stress is linear, CFD result shows the same trend although the values are overestimated. One can deduce:

Chapter IV: Results and Discussion

$$\tau_{\theta z}(r) = \mu \frac{\partial U_{\theta}}{\partial z} \cong \mu \frac{(r 2 \pi N)}{\varepsilon_u} \quad (\text{IV.16})$$

One can then estimate the torque at the upper wall:

$$T_{upperwall} = 2 \pi \int_{R_i}^{R_e} \tau_{\theta z}(r) r^2 dr = 2 \pi^2 \mu \frac{N}{\varepsilon_u} \int_{R_i}^{R_e} r^3 dr \cong \frac{\pi^2 \mu N R_e^4}{2 \varepsilon_u} \quad (\text{IV.17})$$

The same torque is exerted on the lower wall.

Thus the total torque is:

$$T_{total} = T_{extcyl_{total}} + 2 \times T_{upperwall} \quad (\text{IV.18})$$

An equal torque is exerted along the rotating impeller and shaft. Thus one can estimate the power needed to rotate the impeller and shaft:

$$Power = T_{total} 2 \pi N \quad (\text{IV.19})$$

It corresponds to a power number:

$$N_p = \frac{Power}{\rho N^3 d_m^5} \quad (\text{IV.20})$$

Table IV. 5 Value of the parameters deduced from velocity measurements (N=2 and 10 Hz for example)

Rotation speed	τ_{eci}	$T_{extcyl_{total}}$	$\tau_{\theta z(R=65)}$	$T_{upperwall}$	T_{total}	Power	N_p
N=2 Hz	280 Pa	0.085 N.m	115 Pa	0.134 N.m	0.35 N.m	4.4 W	15
N=10 Hz	1400 Pa	0.34 N.m	580 Pa	0.67 N.m	1.68 N.m	105 W	2.6

The value of N_p is relatively close to the power number measured in the first part of this work and plotted on Fig.II. 8. It is important to underline that the main contribution to the torque is related to the shear along the upper and lower walls, where the membranes are installed.

2.2.1.2 Fluctuations in laminar flow (at N = 2 Hz)

Based on a statistic of instantaneous 2D velocity fields, POD enables to generate a series of eigenvalues and eigenvectors. $\lambda^{(l)}$ is the l^{th} eigenvalue and $\overline{\Phi^{(l)}}(x, z)$ is the l^{th} associated

Chapter IV: Results and Discussion

eigenvector or eigenvector. Each instantaneous velocity field can be reconstructed by Eq.III 26:

$$\vec{U}(x, y, z, t) = \sum_{I=1}^N a^{(I)}(t) \overline{\Phi^{(I)}}(x, y, z)$$

I is the I^{th} mode of POD (total mode number equal to N), while $a^{(I)}(t)$ is the corresponding POD coefficient; the series of coefficient $a_k^{(I)}$ (or $a^{(I)}(t)$ in case of resolved PIV) is given by the projection of each instantaneous velocity field on the I^{th} eigenvector: $a_k^{(I)} = \left(\overline{U_k}, \overline{\Phi^{(I)}} \right)$

Thus velocity field can be reconstructed and in particular, the mean flow and the organised motion. We will focus on organised motion in this case.

Example of POD data processing of horizontal measurement at plane z_2

(1) Eigenvalue spectrum

The eigenvalue spectrum is plotted in Fig.IV. 33. This eigenvalue are normalized by the sum of the eigenvalues (indicating the total kinetic energy) and it was plotted as the function of mode number I . Liné et al.[200] indicated that those normalized eigenvalues correspond to the contribution of each mode to the total kinetic energy in the plane of measurement. Concerning the first mode, its contribution to the total kinetic energy is dominant, about 90%. It corresponds to the mean flow. The 4 following modes, it is easy to observe that modes 2 & 3, and modes 4 & 5 are close to each other. They respectively contribute 6-7% and 0.7-0.8% of the total kinetic energy. These 4 modes are likely associated with organized motions generated by the impeller blades rotation contributes to about 8% of the total energy.

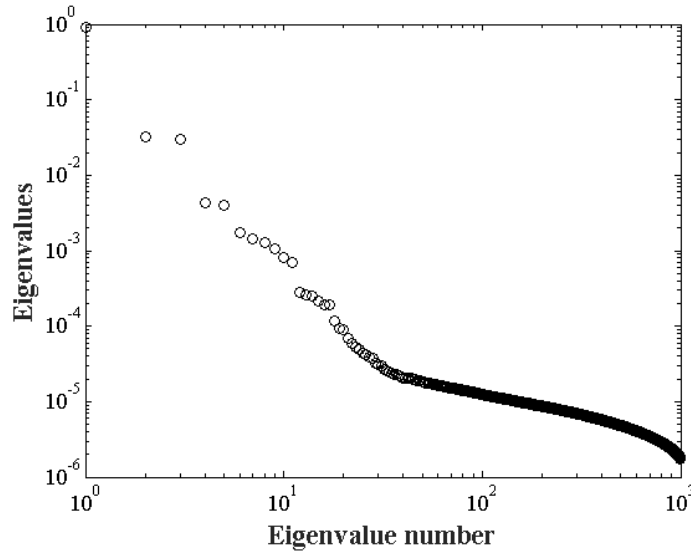


Fig.IV. 33 Eigenvalue spectrum. Operating conditions: horizontal measurement at plane $z_2=1.5$ mm, $Q_f= 50$ L/h, $N=2$ Hz, $Re_{mixing}=42$; BREOX solution, $\mu=0.85$ Pa·s and $T=20^\circ\text{C}$, data acquisition rate 7 Hz, 1000 pairs of images

(2) First mode analysis, the mean flow

The reshaped eigenvector corresponding to mode 1 is plotted in Fig.IV. 34a. It looks like a velocity field but it is not, since the eigenvector has no dimension. The instantaneous velocity field associated to the first mode is given by:

$$\overline{U}_k^{(1)}(x, y, t) = a_k^{(1)}(t) \Phi^{(1)}(x, y) \quad (\text{IV.21})$$

for each k realization of the velocity. Fig.IV. 34b plots the probability density (pdf) function of the coefficient $a_k^{(1)}$. The coefficient $a_k^{(1)}$ is given by $a_k^{(1)} = \left(\overline{U}_k, \overline{\Phi^{(1)}} \right)$.

And it can be normalized by the square root of the first eigenvalue $\lambda^{(1)}$ expressed in m^2/s^2 . The first remark is that the pdf is centered on the unity value; the second remark is the dispersion of the N realization $a_k^{(1)}$ is weak, meaning that $a_k^{(1)}$ is almost constant. One can thus reconstruct the velocity field associated to the first mode as:

$$\overline{U}_k^{(1)}(x, y, t) = \sqrt{\lambda_R^{(1)}} \overline{\phi}^{(1)}(x, y) \cong cst \quad \forall k \quad (\text{IV.22})$$

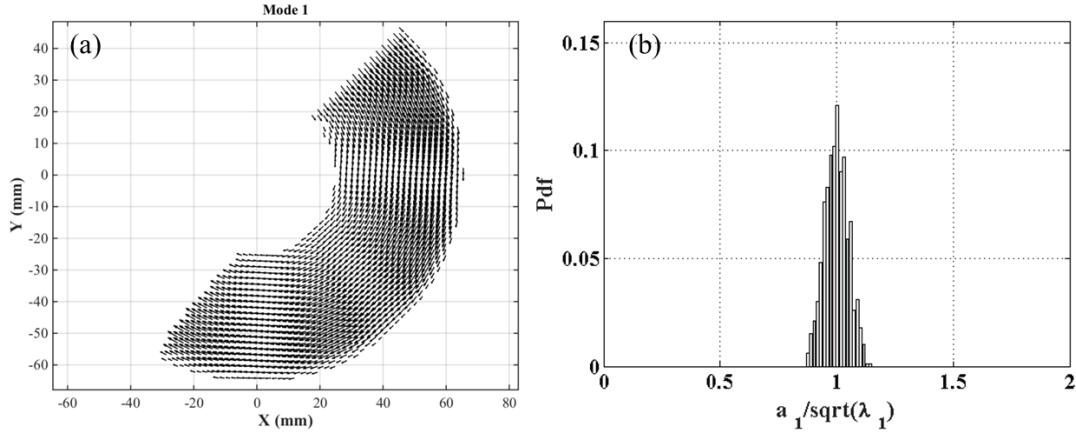


Fig.IV. 34 First mode (a) eigen function, and (b) pdf of normalized POD coefficient. Operating conditions: horizontal measurement at plane $z_2=1.5$ mm, $Q_f= 50$ L/h, $N=2$ Hz, $Re_{mixing}=42$; BREOX solution, $\mu=0.85$ Pa·s and $T=20^\circ\text{C}$, data acquisition rate 7 Hz, 1000 pairs of images

This reconstructed velocity field is highly close to the mean velocity according to many studies concerning POD analysis[197,201]. In order to prove, in Fig.IV. 1, the velocity reconstructed with the first mode is compared to the statistical average of the velocity. The two profiles are similar. It confirms that the first mode corresponds exactly to the mean flow.

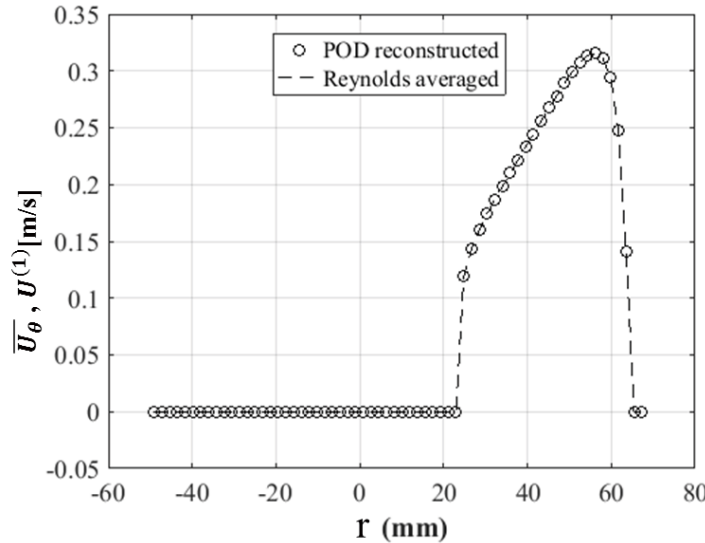


Fig.IV. 35 Reconstructed velocity with the first mode (POD reconstructed) compared to the statistical average of the velocity (Reynolds averaged). Operating conditions: horizontal measurement at plane $z_2=1.5$ mm, $Q_f= 50$ L/h, $N=2$ Hz, $Re_{mixing}=42$; BREOX solution, $\mu=0.85$ Pa·s and $T=20^\circ\text{C}$, data acquisition rate 7 Hz, 1000 pairs of images

(3) Organized motion associated to mode 2 and 3

Chapter IV: Results and Discussion

As aforementioned, the eigenvalues $\lambda^{(2)}$ and $\lambda^{(3)}$ have similar orders of magnitude, suggesting that they may correspond to organized motions and both modes are somehow related. The eigen vectors corresponding to modes 2, $\overline{\phi^{(2)}}(x, y)$ and 3, $\overline{\phi^{(3)}}(x, y)$, are plotted in Fig.IV. 36a and c. The structures exhibited in these two modes, are almost symmetrical with respect to the shape of the impeller, indicating some organization in the flow. Once again, these plots are not velocity fields. The velocity fields associated to the sum of these modes can be written:

$$\overline{U}_k^{(2,3)}(x, y, t) = \sum_{I=2}^3 \overline{U}_k^{(I)}(x, y, t) = a_k^{(2)}(t) \overline{\phi^{(2)}}(x, y) + a_k^{(3)}(t) \overline{\phi^{(3)}}(x, y) \quad (\text{IV.23})$$

Where the coefficients are again given by

$$a_k^{(2)} = \left(\overline{U}_k, \overline{\Phi^{(2)}} \right) \quad \text{and} \quad a_k^{(3)} = \left(\overline{U}_k, \overline{\Phi^{(3)}} \right)$$

One can plot in Fig.IV. 36b and d the probability density function of the normalized coefficients $a_k^{(2)} / \sqrt{\lambda^{(2)}}$ and $a_k^{(3)} / \sqrt{\lambda^{(3)}}$. The distributions are centered on the origin and their shape can be related to sinusoidal distribution, as expected from the literature[201].

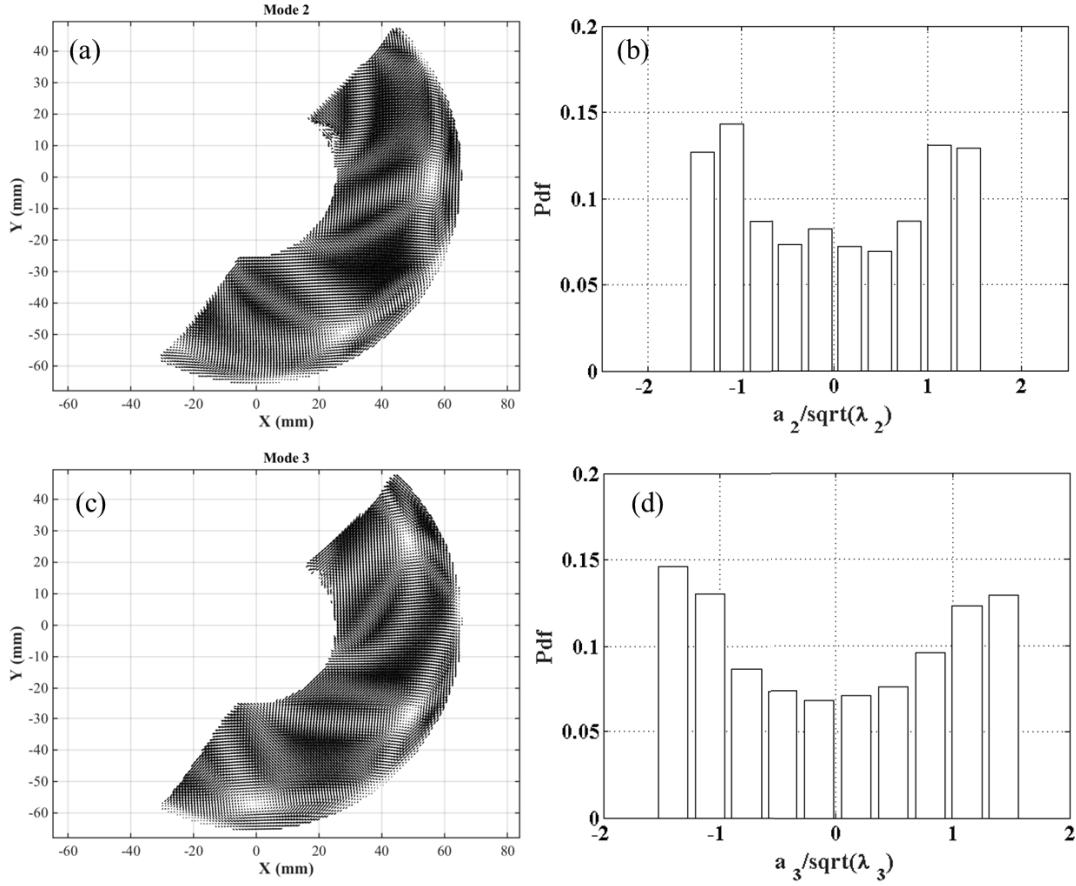


Fig.IV. 36 Second and third mode (a, c) eigen function, and (b, d) pdf of normalized POD coefficient. Operating conditions: horizontal measurement at plane $z_2=1.5$ mm, $Q_f= 50$ L/h, $N=2$ Hz, $Re_{mixing}=42$; BREOX solution, $\mu=0.85$ Pa·s and $T=20^\circ\text{C}$, data acquisition rate 7 Hz, 1000 pairs of images

In order to highlight the link between modes 2 and 3, the k realization of POD coefficient $a_k^{(2)}$ were plotted versus the k realization of POD coefficient $a_k^{(3)}$ in Fig.IV. 37. A 2D projection of the phase portrait in the $(a_k^{(2)}, a_k^{(3)})$ plane is thus obtained. The set of data show an organized shape; for sake of simplicity, it will be considered as an ellipse. The coefficients can thus be related by the expression:

$$\frac{a_k^{(2)2}}{2\lambda^{(2)}} + \frac{a_k^{(3)2}}{2\lambda^{(3)}} = 1 \quad (\text{IV.24})$$

where the eigenvalues are expressed in m^2/s^2 . The periodic nature of these coherent structures associated with modes 2 and 3 could be expressed as sinusoidal variations [198,199,214,215].

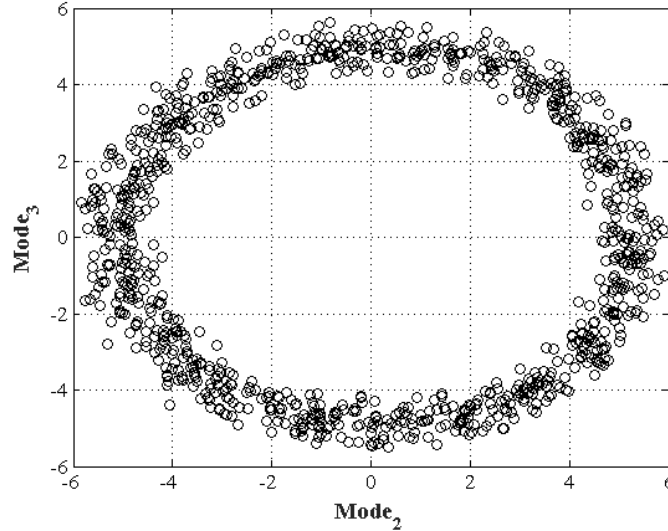


Fig.IV. 37 Portrait of phase between coefficients of mode 2 and 3. Operating conditions: horizontal measurement at plane $z_2=1.5 \text{ mm}$, $Q_f= 50 \text{ L/h}$, $N=2 \text{ Hz}$, $Re_{mixing}=42$; BREOX solution, $\mu=0.85 \text{ Pa}\cdot\text{s}$ and $T=20^\circ\text{C}$, data acquisition rate 7 Hz , 1000 pairs of images

(4) Organized motion associated to mode 4 and 5

As aforementioned, the eigenvalue $\lambda^{(4)}$ and $\lambda^{(5)}$ have also similar orders of magnitude and may thus contribute to organized motions. The eigen function corresponding to mode 4 and 5, $\overline{\phi^{(4)}}(x, y)$ and $\overline{\phi^{(5)}}(x, y)$, are plotted in Fig.IV. 38a and c. Compare to modes 2 and 3, modes 4 and 5 show again vortical structures but the length-scale seem to be roughly half of the length-scales of modes 2 and 3. One can plot in Fig.IV. 38b and d the probability density function of the normalized coefficients $a_k^{(4)} / \sqrt{\lambda^{(4)}}$ and $a_k^{(5)} / \sqrt{\lambda^{(5)}}$. The distributions are centered on the origin whereas the pdf distributions reveal slightly noisy sinusoidal distribution.

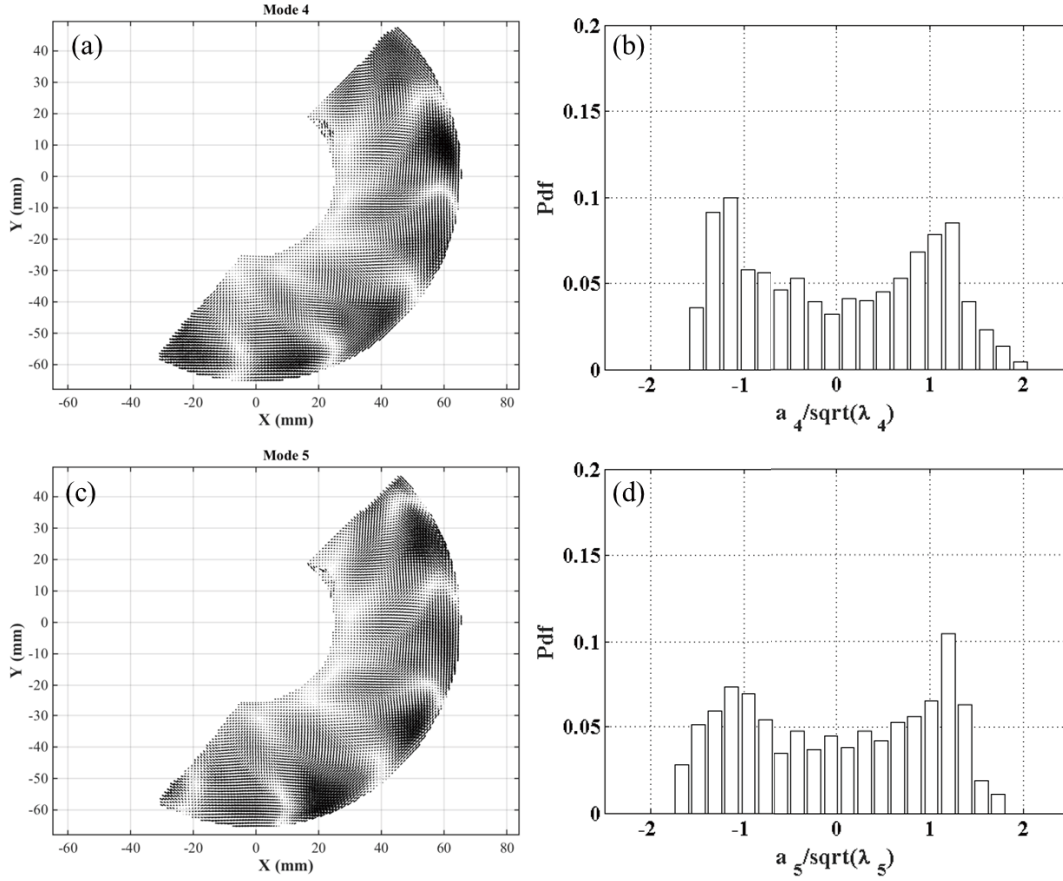


Fig.IV. 38 Fourth and fifth mode (a, c) eigen function, and (b, d) pdf of normalized POD coefficient. Operating conditions: horizontal measurement at plane $z_2=1.5$ mm, $Q_f= 50$ L/h, $N=2$ Hz, $Re_{mixing}=42$; BREOX solution, $\mu=0.85$ Pa·s and $T=20^\circ\text{C}$, data acquisition rate 7 Hz, 1000 pairs of images

Similarly to the previous analysis of modes 2 and 3, the k realizations of $a_k^{(4)}$ were plotted verses the k realization of $a_k^{(5)}$ in Fig.IV. 39 and it exhibits a strong relation between mode 4 and 5 although the pdf distributions reveal noisy sinusoidal distribution.

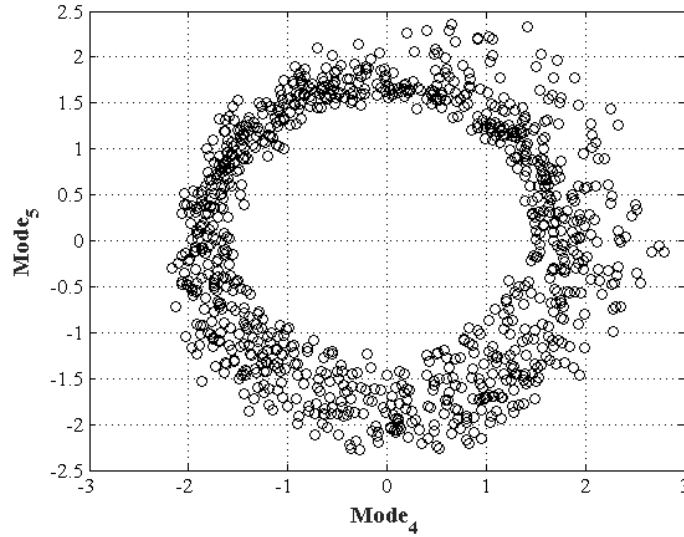


Fig.IV. 39 Portrait of phase between coefficients of mode 4 and 5. Operating conditions: horizontal measurement at plane $z_2=1.5$ mm, $Q_f= 50$ L/h, $N=2$ Hz, $Re_{mixing}=42$; BREOX solution, $\mu=0.85$ Pa·s and $T=20^\circ\text{C}$, data acquisition rate 7 Hz, 1000 pairs of images

(5) Potential organized motion associated to mode 6 and 7

In the eigen spectrum, the eigenvalue $\lambda^{(6)}$ and $\lambda^{(7)}$ are less close to each other compare to the mode 2 and 3, mode 4 and 5. Their contribution to organized motions is smaller (see eigen spectrum). However, one can have a look at their eigen functions, $\overline{\phi^{(6)}}(x, y)$ and $3, \overline{\phi^{(7)}}(x, y)$. They are plotted in Fig.IV. 40a and c. Compare to modes 4 and 5, modes 6 and 7 show new structures whose length-scale seem to be roughly half of the length-scales of modes 4 and 5. One can again plot in Fig.IV. 40b and d the probability density function of the normalized coefficients $a_k^{(6)}/\sqrt{\lambda^{(6)}}$ and $a_k^{(7)}/\sqrt{\lambda^{(7)}}$. The distributions are again centered on the origin as the previous modes.

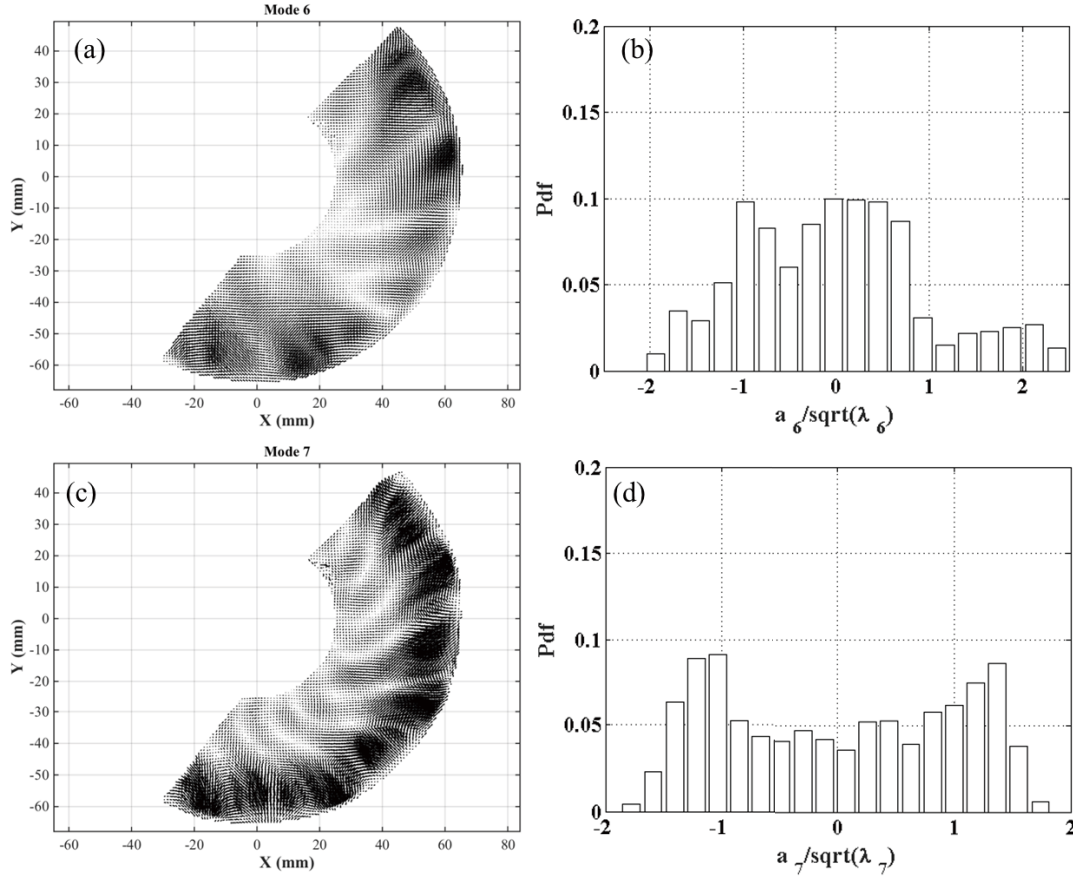


Fig.IV. 40 Sixth and seventh mode (a, c) eigen function, and (b, d) pdf of normalized POD coefficient. Operating conditions: horizontal measurement at plane $z_2=1.5$ mm, $Q_f= 50$ L/h, $N=2$ Hz, $Re_{mixing}=42$; BREOX solution, $\mu=0.85$ Pa·s and $T=20^\circ\text{C}$, data acquisition rate 7 Hz, 1000 pairs of images

(6) Reconstruct organized motion based on mode 2-5

Considering the previous results, in particular the eigen spectrum, we propose to reconstruct the organized motion by accounting for modes 2 to 5.

$$\overline{U}_k^{(2,5)}(x, y, t) = \sum_{l=2}^5 \overline{U}_k^{(l)}(x, y, t) = \sum_{l=2}^5 a_k^{(l)}(t) \overline{\phi}^{(l)}(x, y)$$

From this reconstruction, one can plot any instantaneous reconstructed velocity field in Fig.IV. 41;

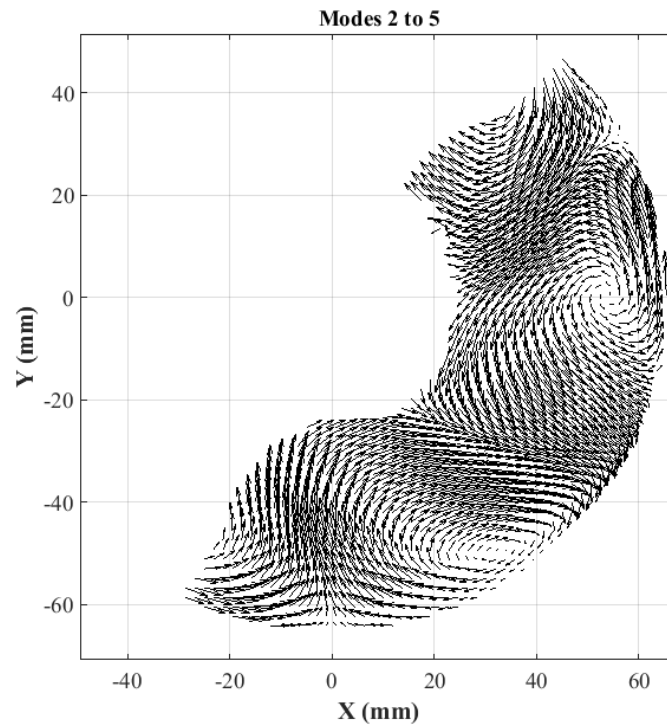


Fig.IV. 41 Instantaneous reconstructed velocity field based on mode 2 to 5. Operating conditions of the raw data: horizontal measurement at plane $z_2=1.5$ mm, $Q_f= 50$ L/h, $N=2$ Hz, $Re_{mixing}=42$; BREOX solution, $\mu=0.85$ Pa·s and $T=20^\circ\text{C}$, data acquisition rate 7 Hz, 1000 pairs of images

From these data, one can estimate the radial profile of fluctuating shear stress. Its mean value is equal to zero but one can estimate its Root Mean Square (RMS) distribution. For example, vertical profile of RMS shear stresses are plotted on Fig.IV. 42 for different radial position and for two impeller speed; From these profile, one can extrapolate towards the wall and deduce the values of RMS wall shear stresses. The radial profiles of RMS wall shear stresses are plotted in Fig.IV. 43.

The order of magnitude of RMS wall shear stress is close to 25 Pa at $N = 2$ Hz, and varies between 100 and 200 Pa at $N = 10$ Hz. One can plot the ratio of RMS wall shear stress divided by the mean wall shear stress. This percentage is plotted on Fig.IV. 44. The trends are similar for the two frequencies. The ratio ranges between 20 to 40 %. It is thus difficult to conclude whether the mean viscous shear stress or its RMS value is more efficient to reduce membrane fouling.

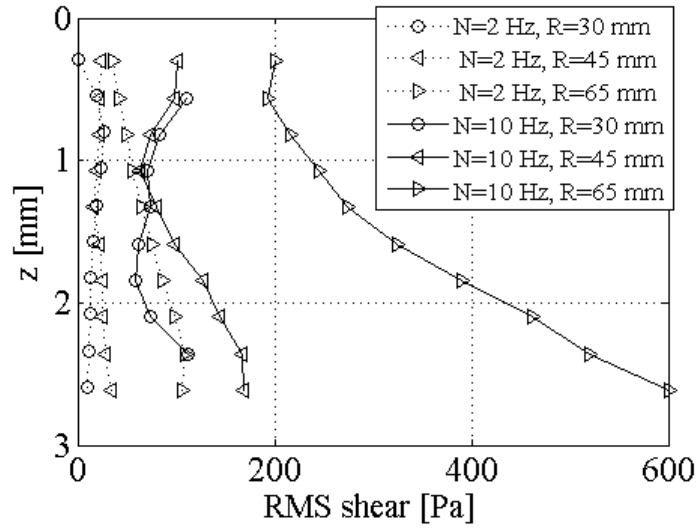


Fig.IV. 42 Vertical profiles of Root Mean Square (RMS) shear at 3 radius $R=30, 45$ and 65 mm with $N=2$ and 10 Hz. Operating conditions: vertical measurements at $Q_f= 50$ L/h; BREOX solution, $\mu=0.85$ Pa·s, $Re_{mixing}=42$ and 210 , and $T=20^\circ\text{C}$

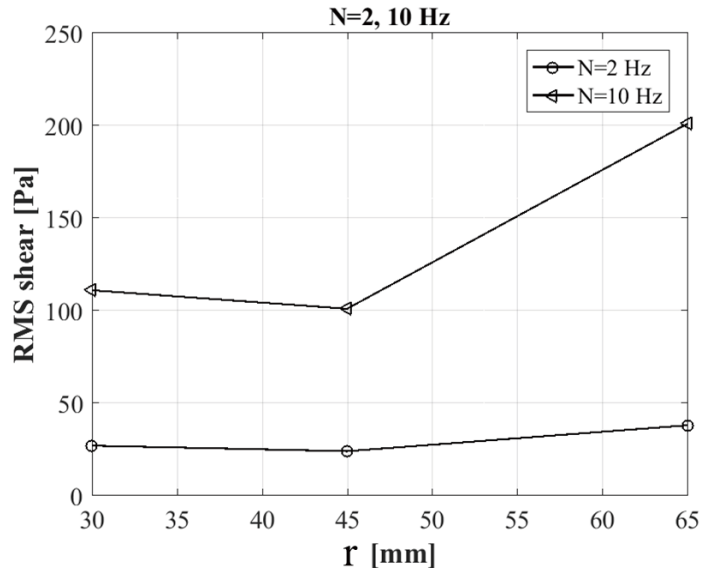


Fig.IV. 43 Radial profiles of viscous mean shear stress at $N=2$ and 10 Hz. Operating conditions: vertical measurements at $Q_f= 50$ L/h; BREOX solution, $\mu=0.85$ Pa·s, $Re_{mixing}=42$ and 210 , and $T=20^\circ\text{C}$

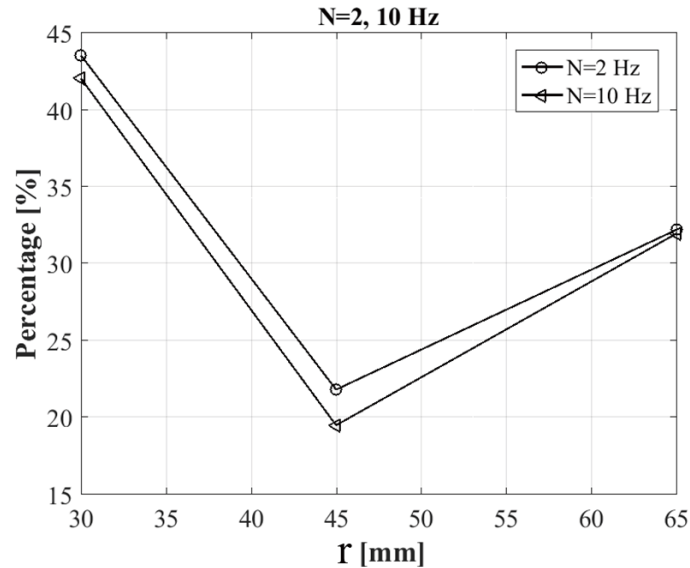


Fig.IV. 44 Radial profiles of the weight of RMS shear (out of viscous mean shear stress) at N=2 and 10 Hz. Operating conditions: vertical measurements at $Q_f= 50$ L/h; BREOX solution, $\mu=0.85$ Pa·s, $Re_{mixing}=42$ and 210, and $T=20^\circ\text{C}$

In conclusion, PIV data were processed to get:

- Mean velocity profiles, both radial profiles and vertical profiles
- Mean shear stress profiles

From these profiles, it was possible to estimate:

- Wall shear stress distributions along the upper and lower boundaries as well as along the external cylinder
- Associated torques.

The total torques was then estimated. Considering angular momentum balance, the torque along the rotating impeller was deduced and the associated power was calculated. The power number resulting from this analysis was compared to global values estimated previously and comparisons were more than satisfactory.

In addition, the analysis of the local hydrodynamics enables us to better understand how the flow was organized and how the wall shear stresses and corresponding to torques were distributed. The main contribution is due to the upper and lower wall (40 % each), the lateral (external) wall contributing for 20%.

Chapter IV: Results and Discussion

Finally, the fluctuating part of the velocity was investigated. POD enabled to reconstruct such organized motion, based on the modes 2 to 5. Both fluctuating velocity fields and shear stresses were estimated. The RMS of fluctuating wall shear stresses was calculated. It was shown to be quite important and up to 45 % of the mean value. Consequently, the periodic fluctuations of the wall shear stress induced by the impeller motion may contribute to the fouling limitation.

2.2.2 Turbulent regime

As it was mentioned, in turbulent flow, a triple decomposition of the instantaneous velocity should be considered as: $U_i = \bar{U}_i + \tilde{u}_i + u'_i$

Where the instantaneous velocity component is U_i and the mean velocity is \bar{U}_i (both organized and turbulent fluctuations are filtered); the periodic (or organized) fluctuation is \tilde{u}_i and the turbulent fluctuation is u'_i . Recall that the periodic (or organized) fluctuation \tilde{u}_i is induced by the impeller blade.

In the following, we will first focus on mean velocities and total fluctuating Reynolds stress components; then respective contributions of turbulence and periodic motion will be analyzed.

2.2.2.1. Mean turbulent flow

The case presented here corresponds to water ($\rho=1000 \text{ kg/m}^3$; $\mu = 1 \text{ mPa}\cdot\text{s}$) and frequency ($N=10 \text{ Hz}$). Thus the Reynolds number is:

$$Re = \frac{\rho N d_m^2}{\mu} = 182,250$$

Vertical planes

Vertical planes were investigated by PIV at three radial positions ($R= 30, 45$ and 65 mm). Vertical profiles of tangential mean velocities are plotted.

One can see that the vertical profiles of tangential velocity in Fig.IV. 45 are quite constant, corresponding to classical bulk flow. Indeed, strong velocity gradients are probably located close to the static upper wall and close to the rotating impeller. One can compare the values of bulk velocities to the local (radial) velocities of the impeller:

$$\text{At } R= 65 \text{ mm} \quad U_{\theta_{bulk}} = 2.5 \text{ m/s} \quad U_{\theta_{impeller}} = R 2 \pi N = 4.1 \text{ m/s}$$

$$\text{At } R= 45 \text{ mm} \quad U_{\theta_{bulk}} = 1.75 \text{ m/s} \quad U_{\theta_{impeller}} = R 2 \pi N = 2.8 \text{ m/s}$$

$$\text{At } R= 30 \text{ mm} \quad U_{\theta_{bulk}} = 0.9 \text{ m/s} \quad U_{\theta_{impeller}} = R 2 \pi N = 1.9 \text{ m/s}$$

The order of magnitude of the bulk velocity is half the local (radial) impeller velocity.

Chapter IV: Results and Discussion

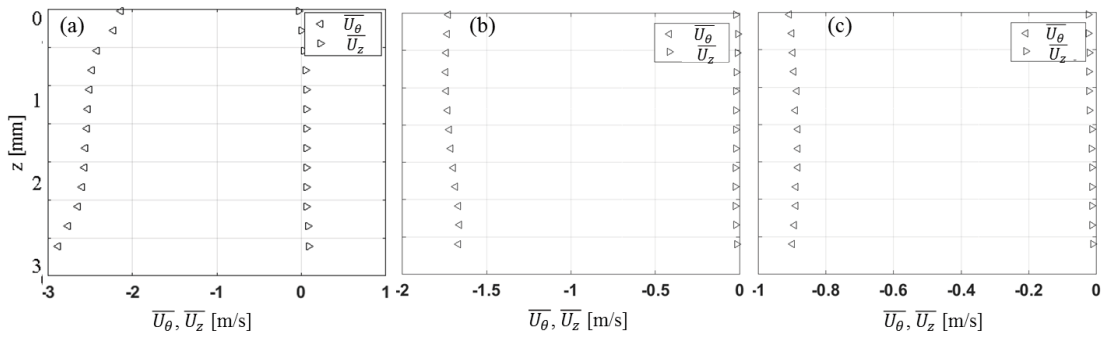


Fig.IV. 45 Vertical profiles of mean tangential velocity (\overline{U}_θ) and mean vertical velocity (\overline{U}_z). Operating conditions: vertical measurements at $R= 65(a)$, $45(b)$ and $30(c)$ mm with $Q_f= 100$ L/h; water, $\mu=1$ mPa·s, $N=10$ Hz, $Re_{mixing}=182,250$, and $T=20^\circ C$

Considering that all the fluctuations are “turbulent”, one can estimate the turbulent shear stress and plot it.

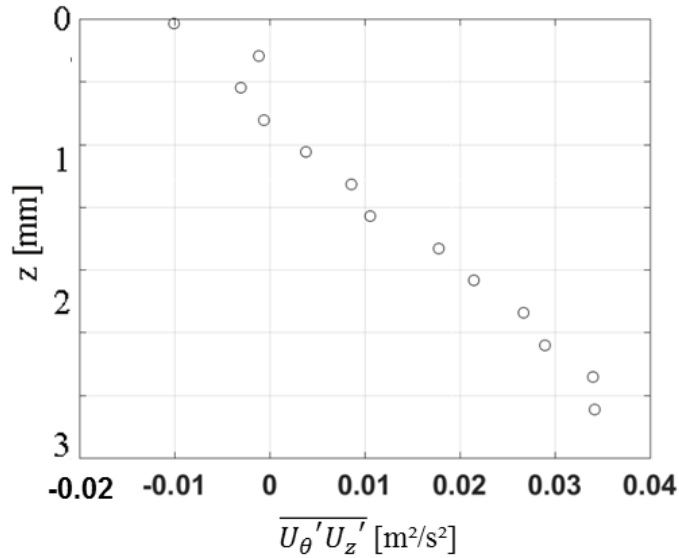


Fig.IV. 46 Vertical profiles of mean Reynolds shear stress at $R=65$ mm. Operating conditions: vertical measurements at $Q_f= 100$ L/h; water, $\mu=1$ mPa·s, $N=10$ Hz, $Re_{mixing}=182,250$, and $T=20^\circ C$

At $R=65$ mm, the vertical profile of Reynolds shear stress $\overline{U_\theta' U_z'}$ is linear. One can extrapolate the profile to deduce the wall value. It comes $U^{*2}= 0.015$ m²/s².

Chapter IV: Results and Discussion

Thus the friction velocity is $U^*=0.0125$ m/s; it can be compared to 5% of the bulk velocity ($5\% \times 2.5 = 0.0125$ m/s). Thus the profile of turbulent shear stress is consistent with the profile of mean velocity.

The local wall shear stress is thus $\tau_{upperwall}(R = 65 \text{ mm}) = \rho U^{*2} = 15 \text{ Pa}$

Similar processing can be performed for the other vertical planes at $R=45$ and 30 mm:

$$\tau_{upperwall}(R = 45 \text{ mm}) = \rho U^{*2} = 5 \text{ Pa}$$

$$\tau_{upperwall}(R = 30 \text{ mm}) = \rho U^{*2} = 1 \text{ Pa}$$

Clearly, the wall shear stress is quadratic with the bulk velocity. For sake of simplicity, let consider that:

$$\tau_{upperwall}(r) = \rho U^{*2} = \rho (5\%)^2 \left(\frac{2 \pi N r}{2} \right)^2$$

One can deduce the torque on the upper wall:

$$T_{upperwall} = \int_0^{2\pi} \int_{R_i}^{R_m} \tau_{upperwall}(r) r r dr d\theta$$

After calculation, one can derive:

$$T_{upperwall} = 2 \pi \rho (5\% \pi N)^2 \frac{R_m^5 - R_i^5}{5} \cong \frac{2 \pi^3 (5\%)^2}{5} N^2 R_m^5$$

Similar torque is exerted on the lower wall. Thus the sum is:

$$T_{upper\&lowerwalls} \cong \frac{4 \pi^3 (5\%)^2}{5} \rho N^2 R_m^5$$

Considering angular momentum balance, the torque along the impeller is equal to the torque on static walls. The corresponding power is:

$$Power = T_{upper\&lowerwalls} 2 \pi N \cong \frac{\pi^4 (5\%)^2}{20} \rho N^3 D_m^5$$

The power number is thus:

$$N_P = \frac{Power}{\rho N^3 d_m^5} \cong \frac{\pi^4 (5\%)^2}{20} \cong 0.01$$

Chapter IV: Results and Discussion

Unfortunately, this is one order of magnitude lower than global values obtained from previous experiments Fig.II. 8. It means that the contribution of the external lateral wall may be much more important than the upper and lower walls. Thus, horizontal PIV planes are now considered.

Horizontal planes

Three horizontal planes were investigated by PIV. Radial profiles of tangential mean velocities are plotted.

A first radial profile of tangential mean velocity is plotted close to the upper wall ($z_1 = 0.25$ mm). One can see that the radial profile is again linear and almost equal to half the impeller local (radial) velocity (see Fig.IV. 47.)

The turbulent shear stress component uv can also be estimated. Its profile is plotted on Fig.IV. 48. It is almost linear; one can thus extrapolate to get the wall shear stress value. It is close to $0.075 \text{ m}^2/\text{s}^2$, corresponding to a friction velocity equal to 0.27 m/s . The wall shear stress is thus close to 75 Pa .

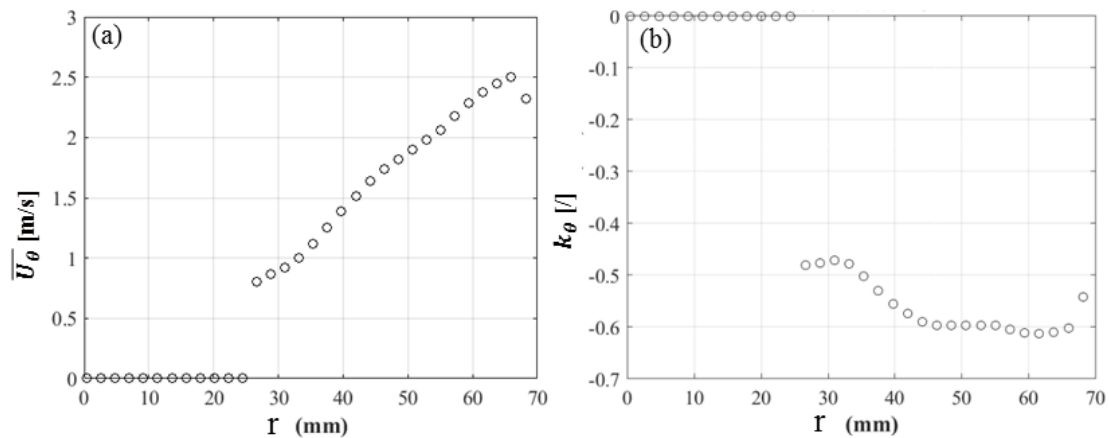


Fig.IV. 47 Radial profile of tangential mean velocity (a) and its normalized profile (b) close to the upper wall ($z_1 = 0.25$ mm). Operating conditions: horizontal measurements at $Q_f = 100 \text{ L/h}$; water, $\mu = 1 \text{ mPa}\cdot\text{s}$, $N = 10 \text{ Hz}$, $Re_{mixing} = 182,250$, and $T = 20^\circ\text{C}$

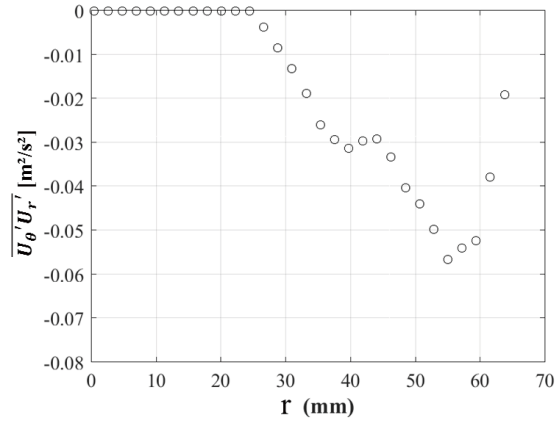


Fig.IV. 48 Radial profile of turbulent shear close to the upper wall ($z_1 = 0.25$ mm). Operating conditions: horizontal measurements at $Q_f = 100$ L/h; water, $\mu = 1$ mPa·s, $N = 10$ Hz, $Re_{mixing} = 182,250$, and $T = 20^\circ\text{C}$

A second horizontal profile of tangential mean velocity is plotted in the middle plane between the impeller and the upper wall ($z_2 = 1.5$ mm). One can see that the radial profile is linear and almost equal to half the impeller local (radial) velocity (see

Fig.IV. 49.)

The turbulent shear stress component $\overline{U'_\theta U'_r}$ can also be estimated. Its profile is plotted on Fig.IV. 50. It is almost linear; one can thus extrapolate to get the wall shear stress value. It is close to 0.1 m^2/s^2 , corresponding to a friction velocity equal to 0.33 m/s. The wall shear stress is thus close to 100 Pa.

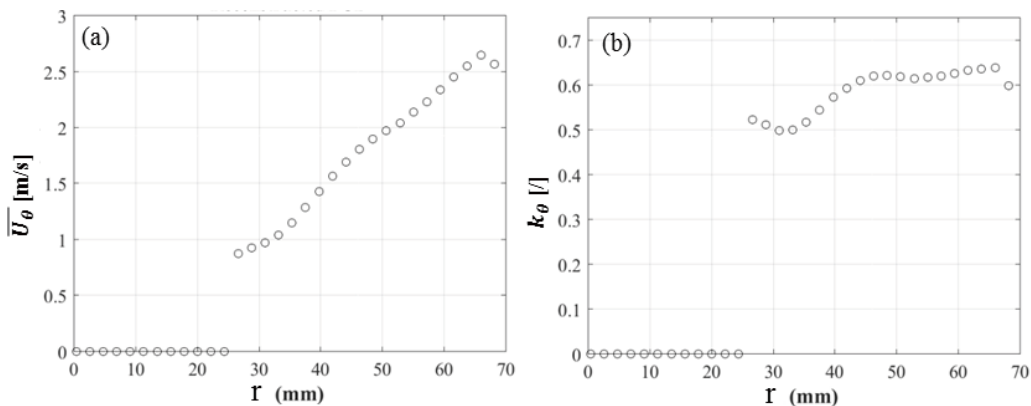


Fig.IV. 49 Radial profile of tangential mean velocity (a) and its normalized profile (b) close to the upper wall ($z_2 = 1.5$ mm). Operating conditions: horizontal measurements at $Q_f = 100$ L/h; water, $\mu = 1$ mPa·s, $N = 10$ Hz, $Re_{mixing} = 182,250$, and $T = 20^\circ\text{C}$

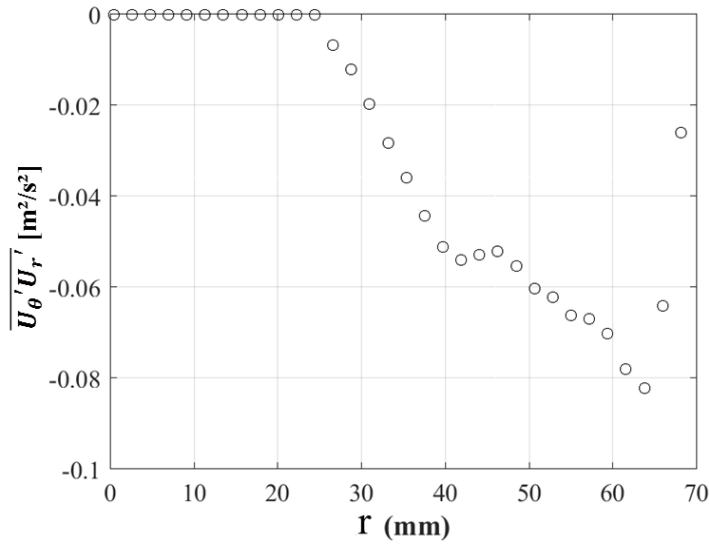


Fig.IV. 50 Radial profile of turbulent shear close to the upper wall ($z_2= 1.5$ mm). Operating conditions: horizontal measurements at $Q_f= 100$ L/h; water, $\mu= 1$ mPa·s, $N=10$ Hz, $Re_{mixing}=182,250$, and $T=20^\circ C$

We can consider that the wall shear stress along the external wall is roughly uniform and equal to $\tau_{ec} = 100$ Pa.

Thus the torque can be estimated:

$$T_{extcyl} = 2 \pi R_e \varepsilon_{ul} \tau_{ec} R_e = 0.043 \text{ N.m}$$

where $\varepsilon_{ul}=14$ mm is the distance between the upper and the lower wall. This torque should be compared to the previous one (upper & lower walls):

$$T_{upper\&lowerwalls} \cong \frac{4 \pi^3 (5\%)^2}{5} \rho N^2 R_m^5 = 0.01 \text{ N.m}$$

The total torque is thus 0.05 N.m, the lateral wall contributing to 80%.

Considering again angular momentum balance, the torque along the impeller is equal to the torque on static walls. The corresponding power is:

$$Power = T_{total} 2 \pi N \cong 3.14 \text{ W}$$

The power number is thus:

$$N_p = \frac{Power}{\rho N^3 d_m^5} \cong 0.06$$

Chapter IV: Results and Discussion

This is of the order of magnitude lower than global values obtained from previous experiments. Due to the main weight of the torque exerted on the external cylinder (80 %) compared to the torque exerted on upper and lower walls, it seems necessary to analyze the respective contributions of periodic (organized) motions and turbulence, in a horizontal plane.

2.2.2.2 Organized flow versus turbulence

In the previous part, for sake of simplicity we considered together organized and turbulent fluctuations. In this part, we will consider both separately. In order to discriminate organized motion from fluctuations, POD is now applied.

We will only present processing of horizontal plane. First, eigenvalue spectrum is plotted.

(1) Eigenvalue spectrum

The eigenvalue spectrum is plotted in Fig.IV. 51. Concerning the first mode, its contribution to the total kinetic energy is dominant, about 95% (90% in laminar flow, see Fig.IV. 33). The 8 following modes, it is easy to observe that mode 2 and 3, mode 4 and 5, mode 6 and 7, mode 8 and 9 are close to each other. They respectively contribute 4-5%, 0.3-0.4%, 0.1-0.15% and 0.06-0.07% of the total energy. These 8 modes are likely associated with organized motions generated by the impeller blades rotation contributes to about 5% of the total energy (8% in laminar flow). Relation between the rest modes is not so obvious.

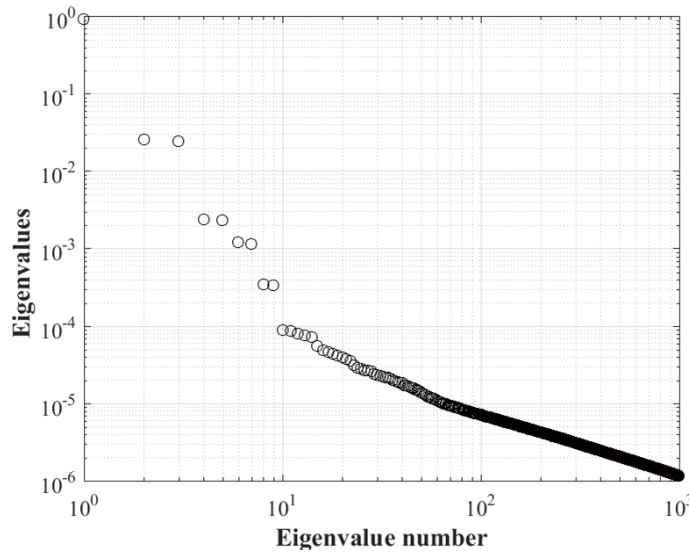


Fig.IV. 51 Eigenvalue spectrum. Operating conditions: horizontal measurement plane $z_2=1.5$ mm, $Q_f=100$ L/h, $N=10$ Hz; water, $\mu=1$ mPa·s and $T=20^\circ\text{C}$, data acquisition rate 7 Hz, 3778 pairs of images

(2) First mode analysis, the mean flow

The first mode corresponds to the mean flow. The eigen vector is plotted in Fig.IV. 52a. It looks like a velocity field but it is not, since the eigen-function has no dimension. The instantaneous velocity field associated to the first mode is given by: $\overline{U}_k^{(1)}(x, y, t) = a_k^{(1)}(t)\Phi^{(1)}(x, y)$, for each k realization of the velocity. The coefficient $a_k^{(1)}$ is given by $a_k^{(1)} = \left(\overline{U}_k, \overline{\Phi^{(1)}}\right)$

Fig.IV. 52b plots the probability density (pdf) function of the coefficient $a_k^{(1)}$ expressed in m^2/s^2 mentioned previously. The first remark is that the pdf is centered on the unity value; the second remark is the dispersion of the N realizations $a_k^{(1)}$ is weak, meaning that $a_k^{(1)}$ is almost constant.

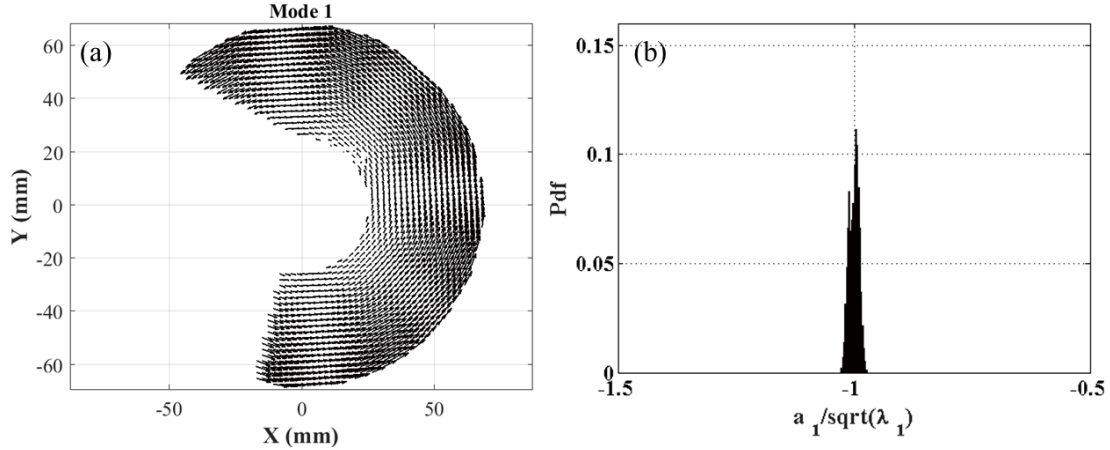
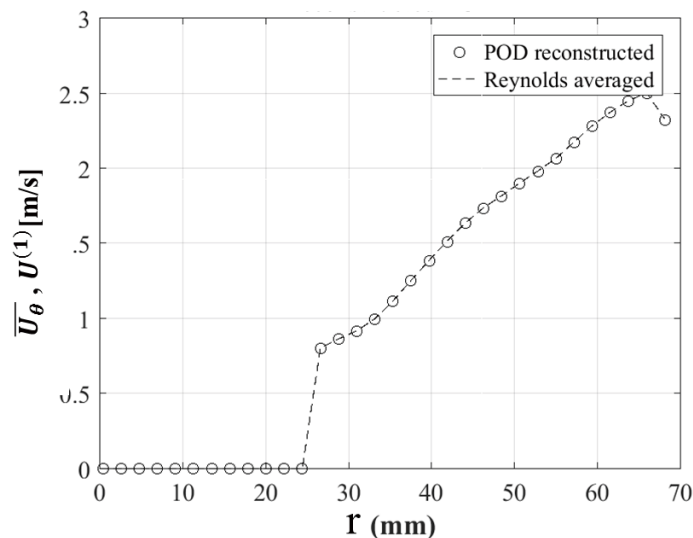


Fig.IV. 52 First mode (a) eigenvector, and (b) pdf of normalized POD coefficient. Operating conditions: horizontal measurement plane $z_2=1.5$ mm, $Q_f= 100$ L/h, $N=10$ Hz; water, $\mu=1$ mPa·s and $T=20^\circ\text{C}$, data acquisition rate 7 Hz, 3778 pairs of images

Thus the velocity field associated to the first mode can be reconstructed. It corresponds to tangential flow induced by the impeller. One can plot a radial profile of tangential component of both the velocity reconstructed with the first mode and the statistical averaged (see Fig.IV. 53) mean velocity. The radial profile of tangential velocity is linear. This reconstructed velocity field is highly close to the mean velocity according to many studies concerning POD analysis [197,201]. We thus believe that the first mode is a steady-state field corresponding to the mean flow. Considering the abscissa of this last plot, the coefficient a_1 is almost constant and equal to the square root of the first eigenvalue.



Chapter IV: Results and Discussion

Fig.IV. 53 Reconstructed velocity with the first mode (POD reconstructed) compared to the statistical average of the velocity (Reynolds averaged). Operating conditions: horizontal measurement plane $z_2=1.5$ mm, $Q_f=100$ L/h, $N=10$ Hz; water, $\mu=1$ mPa·s and $T=20^\circ\text{C}$, data acquisition rate 7 Hz, 3778 pairs of images

(3) Organized motions analysis (mode 2-9), the organized fluctuations

Clearly from the eigen spectrum, organized motion appears since modes 2&3, 4&5, 6&7 8&9 have similar contribution to global kinetic energy. The corresponding eigenvectors are plotted below (see Fig.IV. 54).

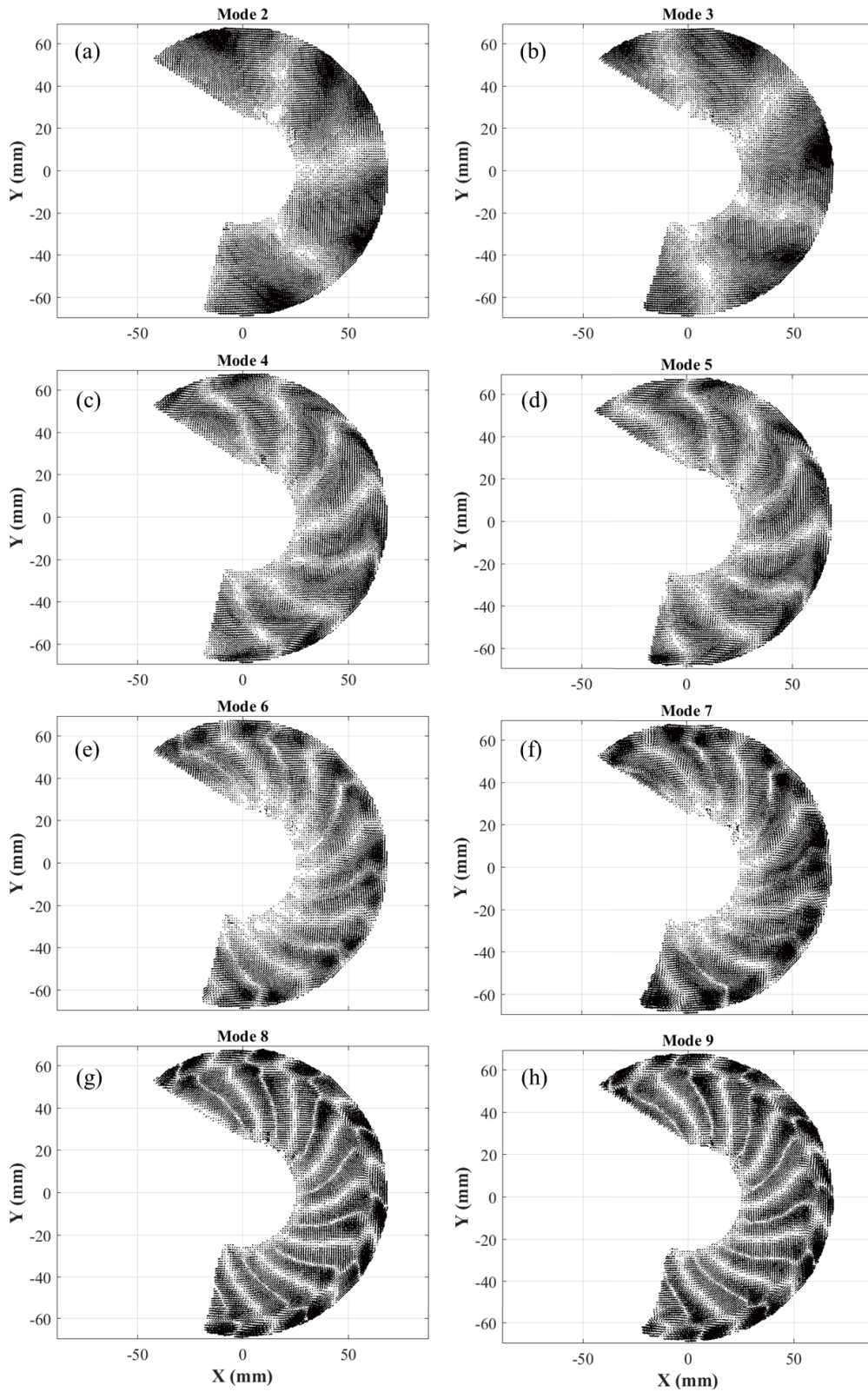


Fig.IV. 54 Eigenvectors related to mode 2-9. Same operating conditions with the previous figure

Chapter IV: Results and Discussion

Two comments are pointed out here:

- The structure of the modes 2&3 are similar, as 4&5, 6&7, 8&9; they exhibit spatial wavelengths;
- Clearly, the wavelength depends on the mode numbers: modes 2&3 exhibit wavelength similar to impeller blades, whereas modes 4&5 show half wavelength, and so on with increasing mode number. Such e behavior was explained in Gabelle *et al.*, (2017).

One can also derive mode coefficients that are given by

$$a_k^{(2)} = (\overrightarrow{U_k}, \overrightarrow{\Phi^{(2)}}) \quad \text{and} \quad a_k^{(3)} = (\overrightarrow{U_k}, \overrightarrow{\Phi^{(3)}})$$

And then plot the phase portrait of these two series Fig.IV. 55a.

It shows a perfect circle, the radius being between 35 & 40. Recall that the radius should be equal to $\sqrt{2} \lambda = 35$.

One can plot also the phase portraits of upper pair mode coefficients Fig.IV. 55b-d.

Remarkably, circular shapes are obtained. If we consider the radius, they decrease from around 40 for modes 2&3 to around 10 for modes 4&5, around 7 for modes 6&7 and around 4 for modes 8&9. This decrease corresponds to the decrease of eigenvalues given in the eigen spectrum; from POD derivation, one can report that $\sqrt{2} \lambda_4 = 12$, $\sqrt{2} \lambda_6 = 9$ and $\sqrt{2} \lambda_8 = 5$.

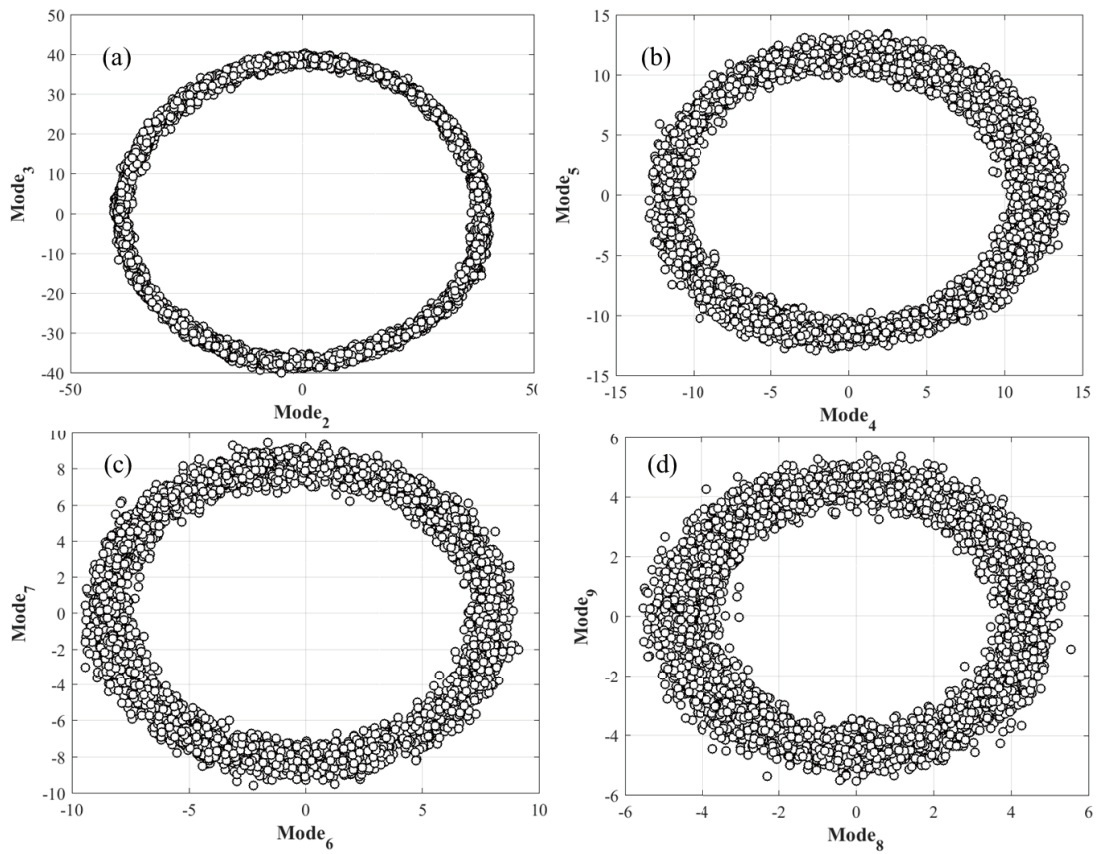


Fig.IV. 55 Portrait of phase between coefficients of mode 2&3, 4&5, 6&7 and 8&9. Operating conditions: horizontal measurement plane $z_2=1.5$ mm, $Q_f= 100$ L/h, $N=10$ Hz; water, $\mu=1$ mPa·s and $T=20^\circ\text{C}$, data acquisition rate 7 Hz, 3778 pairs of images

This organization of the fluctuating flow induced by the periodic motion of the impeller can be confirmed by plotting higher coefficients versus smaller ones:

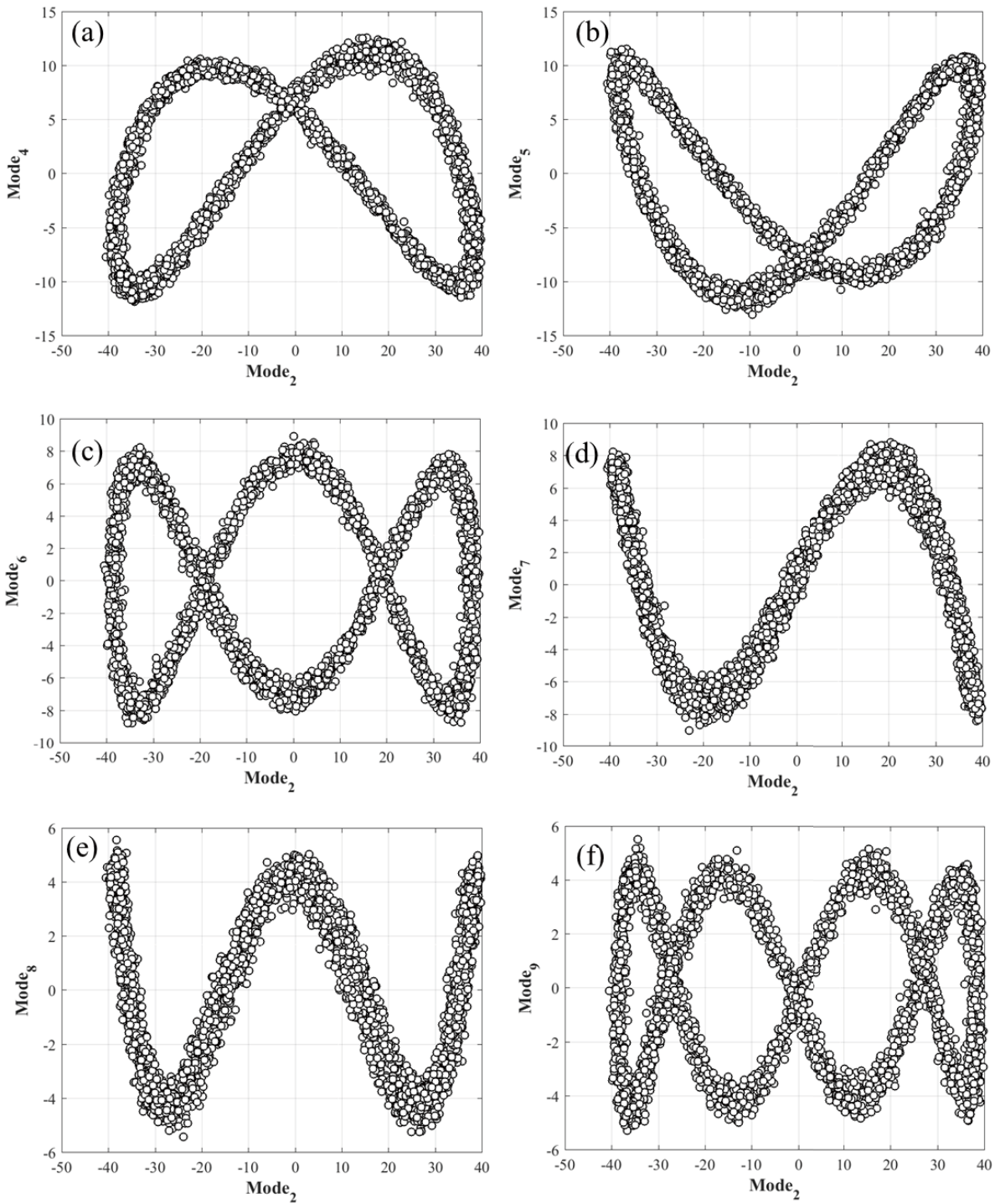


Fig.IV. 56 Portrait of phase between coefficients of mode 2&4, 2&5, 2&6, 2&7, 2&8 and 2&9. Operating conditions: horizontal measurement plane $z_2=1.5$ mm, $Q_f=100$ L/h, $N=10$ Hz; water, $\mu=1$ mPa·s and $T=20^\circ\text{C}$, data acquisition rate 7 Hz, 3778 pairs of images

Chapter IV: Results and Discussion

Here again, the shapes are remarkably well organized and consistent with previous analysis. From eigenvectors, it was shown half wavelength and from mode coefficients half periods are clearly exhibited.

The sinusoidal structure of the mode coefficients can also be confirmed by the plot of their pdf.

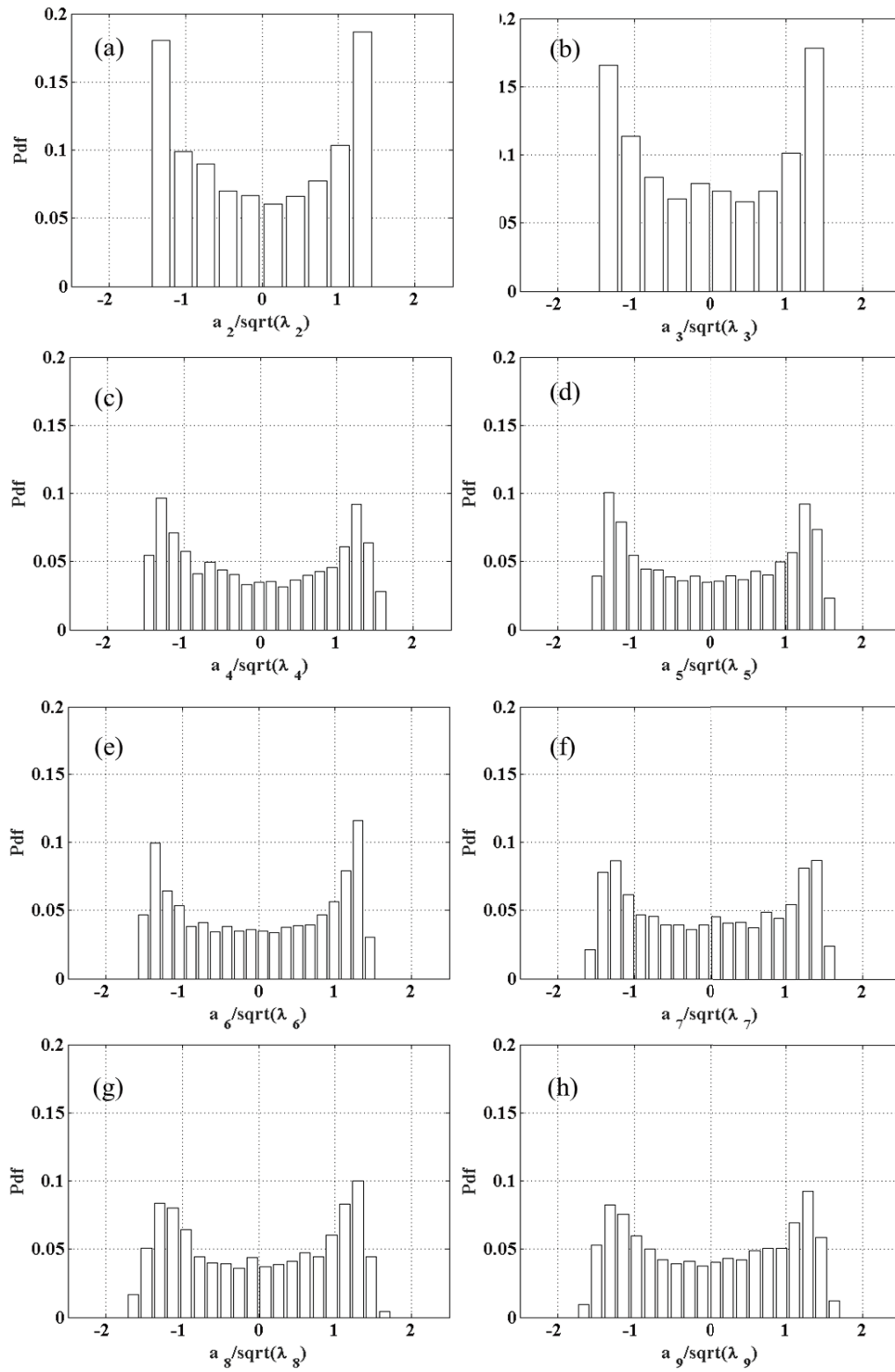


Fig.IV. 57 pdf of normalized POD coefficient from mode 2 to 9. Same operating conditions with the previous figure

Chapter IV: Results and Discussion

Finally, one can reconstruct the organized motion. We tested several sets of modes. (2 to 9 and 2 to 14, we get the same results.)

Given the reconstructed organized motion defined as:

$$\overline{U}_k^{(2,9)}(x, y, t) = \sum_{l=2}^9 \overline{U}_k^{(l)}(x, y, t) = \sum_{l=2}^9 a_k^{(l)}(t) \overline{\phi}^{(l)}(x, y)$$

From this reconstruction, one can plot any instantaneous reconstructed velocity field in Fig.IV. 58;

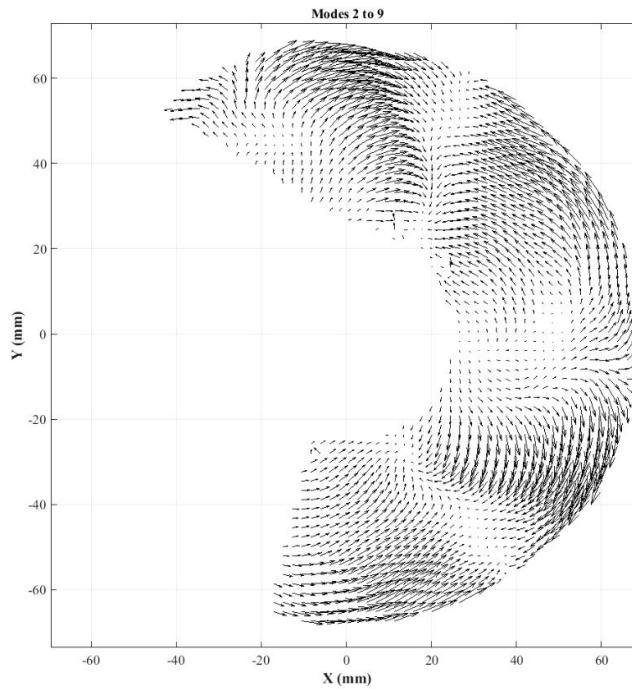


Fig.IV. 58 Instantaneous reconstructed velocity field based on mode 2 to 9. Raw data operating conditions: horizontal measurement plane $z_2=1.5$ mm, $Q_f= 100$ L/h, $N=10$ Hz; water, $\mu=1$ mPa·s and $T=20^\circ\text{C}$, data acquisition rate 7 Hz, 3778 pairs of images

Real turbulent contribution can be calculated as: $\vec{u}_k^t = \vec{U}_k - \vec{U} - \overline{U}_k^{2,9}$

One can thus derive turbulent Reynolds and organized shear stress components. The radial profiles of shear stresses are plotted on Fig.IV. 59. The shear stress based on total fluctuation is compared to the shear stress limited to turbulence.

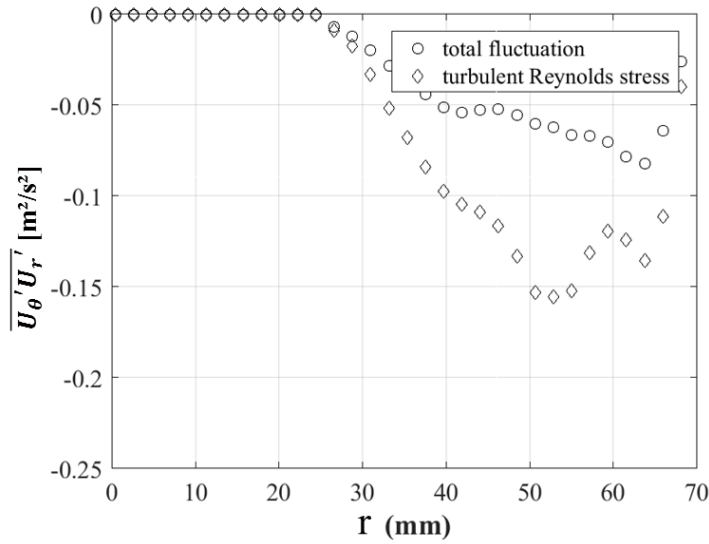


Fig.IV. 59 Turbulent Reynolds and organized shear stress components (based on mode 2-9). Operating conditions: horizontal measurement plane $z_2=1.5$ mm, $Q_f= 100$ L/h, $N=10$ Hz; water, $\mu=1$ mPa·s and $T=20^\circ\text{C}$, data acquisition rate 7 Hz, 3778 pairs of images

One can see that the organized motion should not be neglected. From this turbulent Reynolds shear stress profile, one can correct the previous estimation of the wall shear stress.

We can consider that the wall shear stress along the external wall is roughly uniform and now equal to $\tau_{ec} = 250$ Pa.

Thus the torque can be estimated:

$$T_{extcyl} = 2 \pi R_e \varepsilon_{ul} \tau_{ec} R_e = 0.1 \text{ N.m}$$

This torque should be compared to the previous one (upper & lower walls):

$$T_{upper\&lowerwalls} \cong \frac{4 \pi^3 (5\%)^2}{5} \rho N^2 R_m^5 = 0.01 \text{ N.m}$$

The total torque is thus 0.11 N.m, the lateral/external wall contributing to close to 90%.

Considering again angular momentum balance, the torque along the impeller is equal to the torque on static walls. The corresponding power is:

$$Power = T_{total} 2 \pi N \cong 7.8 \text{ W}$$

The power number is thus:

Chapter IV: Results and Discussion

$$N_P = \frac{\text{Power}}{\rho N^3 d_m^5} \cong 0.15$$

To conclude, PIV data were processed to get:

- Mean velocity profiles, both radial profiles and vertical profiles
- Mean fluctuating or Reynolds shear stress profiles

From these profiles, it was possible to estimate:

- Wall shear stress distributions along the upper and lower boundaries as well as along the external cylinder
- Associated torques.

Finally, the fluctuating part of the velocity was investigated. POD enabled to reconstruct the organized motion, based on the modes 2 to 9, in a horizontal plane.

The total torques was estimated. Considering angular momentum balance, the torque along the rotating impeller was deduced and the associated power was calculated. The power number resulting from this analysis was compared to global values estimated previously and comparisons were more than satisfactory.

In particular, the analysis of the local hydrodynamics enable us to better understand how was organized the flow and how were distributed the wall shear stresses and corresponding torques. In turbulent flow, the structure is quite different from what was observed in laminar flow: the main contribution to the torque is due to the lateral wall.

❖ **Summary of local approach PIV: POD approach**

Objectives:

To better understand the flow pattern and coherent structure of flow behavior in this confined filtration system by Proper Orthogonal Decomposition.

To split instantaneous velocity into mean flow and the fluctuation (organized fluctuation and turbulence).

Highlights:

Important local parameters including velocity, shear stress (wall shear stress, mean viscous shear, fluctuating shear (RMS shear), and torque). Moreover, global power consumption were deduced from local parameters and compared to the previous global measurement (power consumption curve).

(1) POD analysis conducted under laminar flow shows:

- Mean velocity profiles, both radial profiles and vertical profiles
- Mean shear stress profiles

From these profiles, it was possible to estimate:

- Wall shear stress distributions along the upper and lower boundaries as well as along the external cylinder
- Associated torques

The total torques and power consumption were then estimated. The power number resulting from this analysis was compared to global values estimated previously and comparisons were more than satisfactory.

The analysis shows how the flow was organized and how the wall shear stresses and corresponding torques were distributed. The main contribution is due to the upper and lower wall (40 % each), the lateral (external) wall contributing for 20%.

Finally, the fluctuating part of the velocity was investigated. POD enabled to reconstruct such organized motion, based on the modes 2 to 5. Both fluctuating velocity fields and shear stresses were estimated. The RMS of fluctuating wall shear stresses was calculated. It was shown to be quite important and up to 45 % of the mean value. Consequently, the periodic fluctuations

of the wall shear stress induced by the impeller motion may contribute to the fouling limitation.

(2) POD analysis conducted under turbulent flow shows:

- Mean velocity profiles, both radial profiles and vertical profiles
- Mean fluctuating or Reynolds shear stress profiles

From these profiles, it was possible to estimate:

- Wall shear stress distributions along the upper and lower boundaries as well as along the external cylinder
- Associated torques

The fluctuating part of the velocity was investigated. POD enabled to reconstruct the organized motion, based on the modes 2 to 9 in a horizontal plane.

The total torques and power consumption was estimated. The power number resulting from this analysis was compared to global values estimated previously and comparisons were more than satisfactory.

In turbulent flow, the structure is quite different from what was observed in laminar flow: the main contribution to the torque is due to the lateral (external) wall.

3 Application to cell suspensions

Interactions between biological matrices and DF filtration must be studied to intensify bioprocesses [207,216]. Thermal balanced and power consumption informed about temperature increase within RVF module and its compatibility with microorganism activity (optimal growth temperature for example). In a final step, the potential mechanical damage of microbial cells which can be generated by RVF module is investigated. As an exploratory step, *Escherichia coli* (*E. coli* WK6) cell suspensions were used and different rotation speed were applied up to 5h. Experiment was controlled at $P_{out} \sim 2000$ mbar, $P_p \sim 200$ mbar, TMP differs with rotation speed (*Chapter II 3.2*). The mechanical impact was characterized by observing samples under microscope (and by measuring particle size distribution by Dynamic Light Scattering (DLS)).

3.1 Observation of integrate and disrupted cells by microscopy

Mechanical impact is realized by comparing the samples of the initial case and the extreme case (5h). Two samples were chosen: (i) one sample is labeled '0h, 0 Hz', which means the sample is from the beginning of filtration process without rotation ($N=0$ Hz); (ii) the other one is from '5h, 50 Hz', which means at the end of operating time with $N=50$ Hz.

Fig.IV. 60 shows the cells images from initial sample '0h, 0 Hz'. Cells keep their integrity ($N=0$ Hz, $Q_f=100$ L/h). Cells are separated from each other with size about $2-3\mu\text{m}$. However, some of them are clustered together and forms a cluster with size about $8\mu\text{m}$.

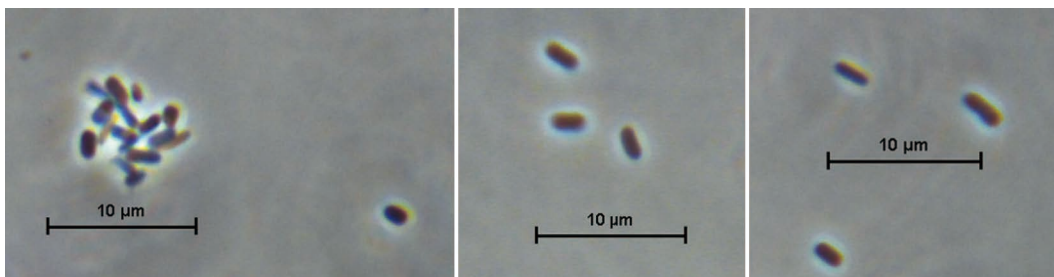


Fig.IV. 60 Sample of cells which from '0h, 0 Hz'. Operating condition:sampling time beginning of the experiment, $N=0$ Hz, $Q_f=100$ L/h, $T=20^\circ\text{C}$. (Microscopic view $\times 100$, contrast phase, oil) Image has been rescaled

Fig.IV. 61 illustrates the cell images from sample '5h, 50 Hz' corresponding to the most stressful environment. Observation indicates that cells still keep their integrity. However, some of cells likely have been damaged under condition $N=50$ Hz, $Q_f=100$ L/h. At 5th hour, they are

probably easier to be clustered and aggregates with disrupted cell seems to be observed. This was not observed with eukaryote cells in food bioprocessing (brewing and wine making) [4,144]. Consequently, cell damage induced by mechanical stress needs to be further explored in the light of local and global hydrodynamics.

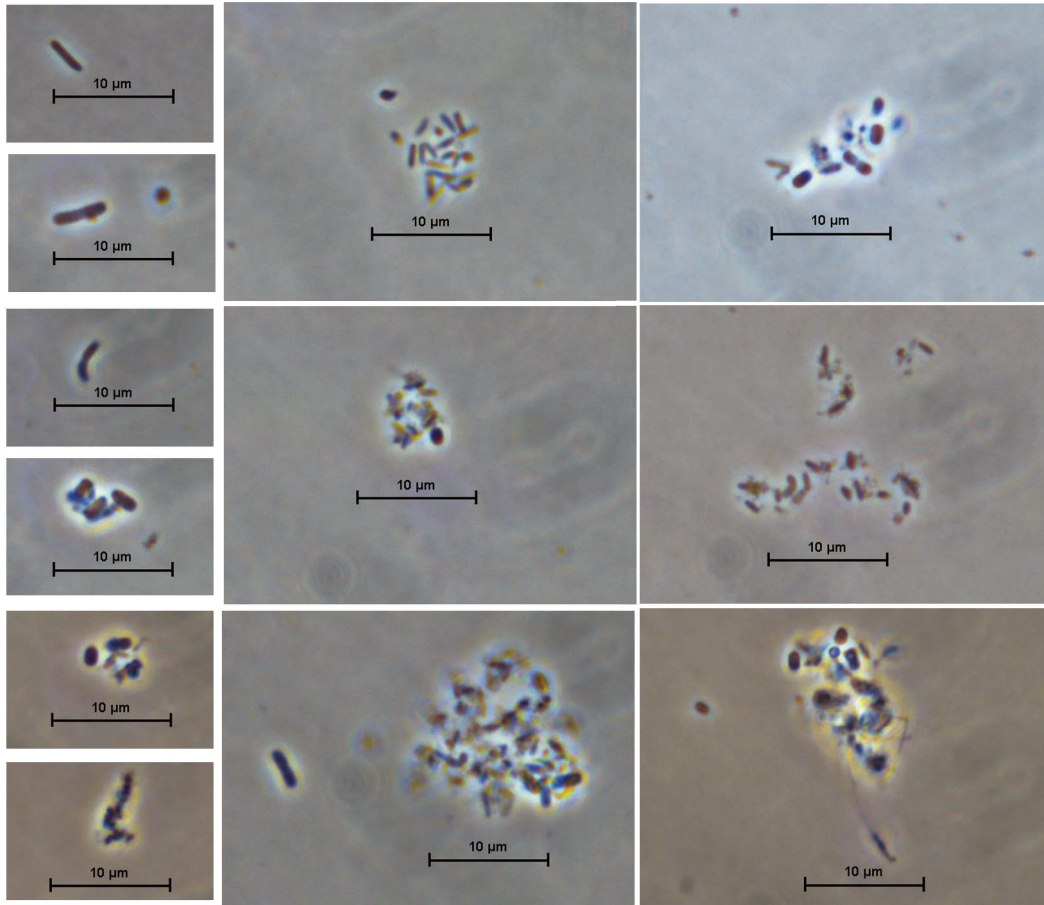


Fig.IV. 61 Sample of cells which from '5h, 50 Hz'. Operating condition:sampling time the 5th hour of the experiment, $N=50$ Hz, $Q_f=100$ L/h, $T=20^\circ\text{C}$. (Microscopic view: $\times 100$, contrast phase, oil) image has been rescaled

3.2 Particle size distribution (PSD) by DLS, impact of time and mixing rate

Fig.IV. 62 shows the PSD under two extrem operating conditions $N=0$ and 50 Hz. It is clear (Fig.IV. 61a) that during 5 hours experiment with no mixing, *E. coli* cells have no significant change in volume distribution function. It reveals that the feeding pump doesn't have impact on *E. coli* cells (reference state). In (Fig.IV. 61b) corresponding to 50 Hz, it is found that particle distribution has evolved and that larger particles seems to appear. This trend seems consistent with microscopic observation in which agglomerate of disrupted cell are present.

Fig.IV. 63 plots the accumulative volume of particle with $dp > 3.80 \mu\text{m}$. The threshold $dp > 3.80 \mu\text{m}$ was defined by the initial PSD at $N=0 \text{ Hz}$, $t=0 \text{ h}$. In this case, particles diameter ranges from 0.5 to $3.80 \mu\text{m}$). So, any diameter that superior to this value will be calculated. By this method, the differences between initial and other distribution functions can be quantified, the higher value the larger diameter it indicates. As expected, during 5 hours experiment, *E. coli* cells remain the same distribution under operating condition $N=0 \text{ Hz}$, no diameter deviations are observed. However, samples are likely to have larger/longer particles under higher rotation speed, although the case under $N=25 \text{ Hz}$ has no significant difference during the first 4 hours.

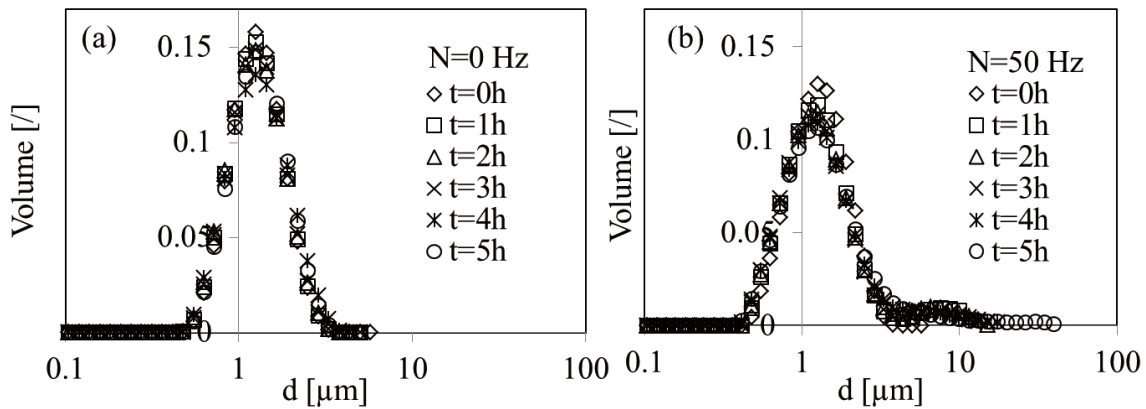


Fig.IV. 62 PSD as a function of time for two extrem operating conditions: (a) $N=0 \text{ Hz}$, $Q_f=100 \text{ L/h}$, $T=20^\circ\text{C}$; (b) $N=50 \text{ Hz}$, $Q_f=100 \text{ L/h}$, $T=20^\circ\text{C}$

To explain these observations, it is assumed that:

(1) *E. coli* cells were disrupted or stretched by the high shear (with $N \neq 0$), and it formed an elongated shape physically or aggregates;

(2) *E. coli* cells secreted Extracellular Polymeric Substances (EPS) colloid under extreme situation, and this substance helps to cluster cells or fragments. It is known that, EPS comprising the microbial biofilms in membrane bioreactor (MBR) systems, and it is considered as the most significant factor affecting the membrane fouling in separation process[217]. Since EPS exhibits a high flocculation properties [218], we strongly believe that the clusters, which were shown in Fig.IV. 61, have the major contribution in the calculation of Fig.IV. 63.

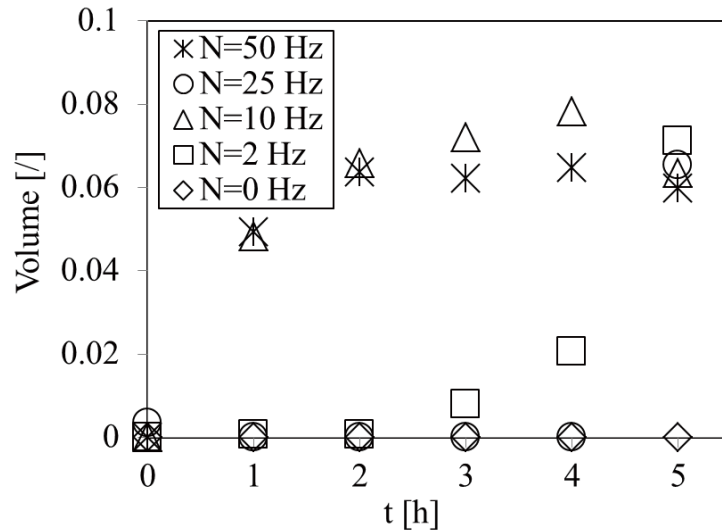


Fig.IV. 63 Cumulative volume of particle with $dp > 3.80 \mu\text{m}$ as a function of time and mixing rate

In this part, we investigated the mechanical impact on cell integrity by DF filtration. For the further study, configuration of biological processes is another factor to optimize their overall performance. Two scientific bottlenecks emerge in connection with the DF filtration: (i) knowledge of complex and evolving culture media (FCV, cell growth), and (ii) intensification of microbial cultures in high cell density condition (cellular activity and viability). Under the biotechnology point of view, our future work may include:

- (1) The scientific and technical bottlenecks related to retention / permeation issues (catalytic biomass and physic-chemical components) associated with complex biological matrices;
- (2) Interactions between matrices and membrane materials (nature, porosity and cut-off threshold);
- (3) The impact of the DF on the performance of bioprocesses (biological activity, cell lysis, etc.) for the specific strains.

❖ **Summary: application of dynamic filtration to cell suspensions**

Objectives:

To study the potential mechanical damage of microbial cells in complex hydrodynamic conditions (RVF module).

Highlights:

Prokaryote cell suspensions (*E.coli*) were investigated with $N=0$ to 50 Hz, $t=0$ to 5h, under $Q_f=100$ L/h and permeation (FCV=1).

- Observation under microscope indicates that cells still keep their integrity at initial condition $N=0$ Hz, $t=0$ h; and cells were damaged and disrupted under condition $N=50$ Hz, $t=5$ h. At $N=50$ Hz, clusters and aggregates with disrupted cell were observed;
- From the PSD study, result shows that larger particles may appear with higher rotation speed N . Our explanation assumes that (1) *E. coli* cells were disrupted or stretched by the high shear (with $N \neq 0$), and it formed some elongated aggregates; (2) *E. coli* cells secreted Extracellular Polymeric Substances (EPS) colloid under extreme situation, and this substance helps to cluster cells or fragments.

Perspectives:

Future work may characterize the impact of mechanical influence (RVF module) on the performance of different microorganisms (biological activity, viability, cell lysis, etc.) and relate to the specific shear stress.

Chapter V:
Conclusions

Chapter V: Conclusions

In this closing chapter, the general contexts and scientific actions of this work are briefly sum-up. Emphasis is given to the scientific questions and problematics as well as the investigated domain. A second part synthesizes the overall discussion and main results issued from the experimental strategy and data analysis. It draws attention to the main discoveries and the limits of this PhD thesis regarding bioprocess. A final part opens a discussion on the scientific perspectives and future works by considering the methodology, the tested fluids and the application to industrial bio-products.

Scientific and industrial context

Recently, membrane bioreactors (MBR) were largely applied in biotechnology field (eg. food biotechnology: rough beer clarification, wine making, dairy process). Dynamic Filtration stands as an alternative and efficient filtration technology compares to dead-end and crossflow filtration. Rotating and Vibrating Filtration (RVF) is a promising dynamic filtration module, and it has been investigated in our laboratory for bioprocess engineering. Reviewing the literature, hydrodynamic behaviors and the geometrical configuration of these filtration devices are the determinant factors to optimize the overall performances. Most of the researches were focusing on global performances (efficiency, fouling reduction, retention-permeation locks, etc.); whereas few works were associated with local parameters (hydrodynamics, fouling nature and structure).

Therefore, this PhD was motivated by the lack of knowledge related to local and global hydrodynamics. Measurements and analysis on local parameters such as local velocity, shear stress, flow pattern/ coherent structure and so on contribute to a better understanding of local phenomena and their efficiency.

Scientific questions and Research strategy

Research was dedicated to a better understanding of the complex hydrodynamics within RVF module into bioprocess context. Several scientific questions were identified (mentioned in *Chapter I*):

Chapter V: Conclusions

- How global performances (power consumption, friction curve, heat dissipation, Residence Time Distribution) can be characterized and interpreted?
- How long will a cell suffer in such stressful environment?
- What will be the magnitude of this mechanical stress?
- Does it damage microbial cell population?
- What is the local flow pattern in the filtration cell? And how does it organize and structure in the filtration cell?
- Is it possible to identify local and instantaneous velocity and shear stress?
- Are experimental measurements and simulations consistent at global and local scales?

To answer to these scientific questions, experiments and numerical simulations were performed at global and local scales in laminar and turbulent regimes with Newtonian fluid under biotic and abiotic conditions (Fig.V 1):

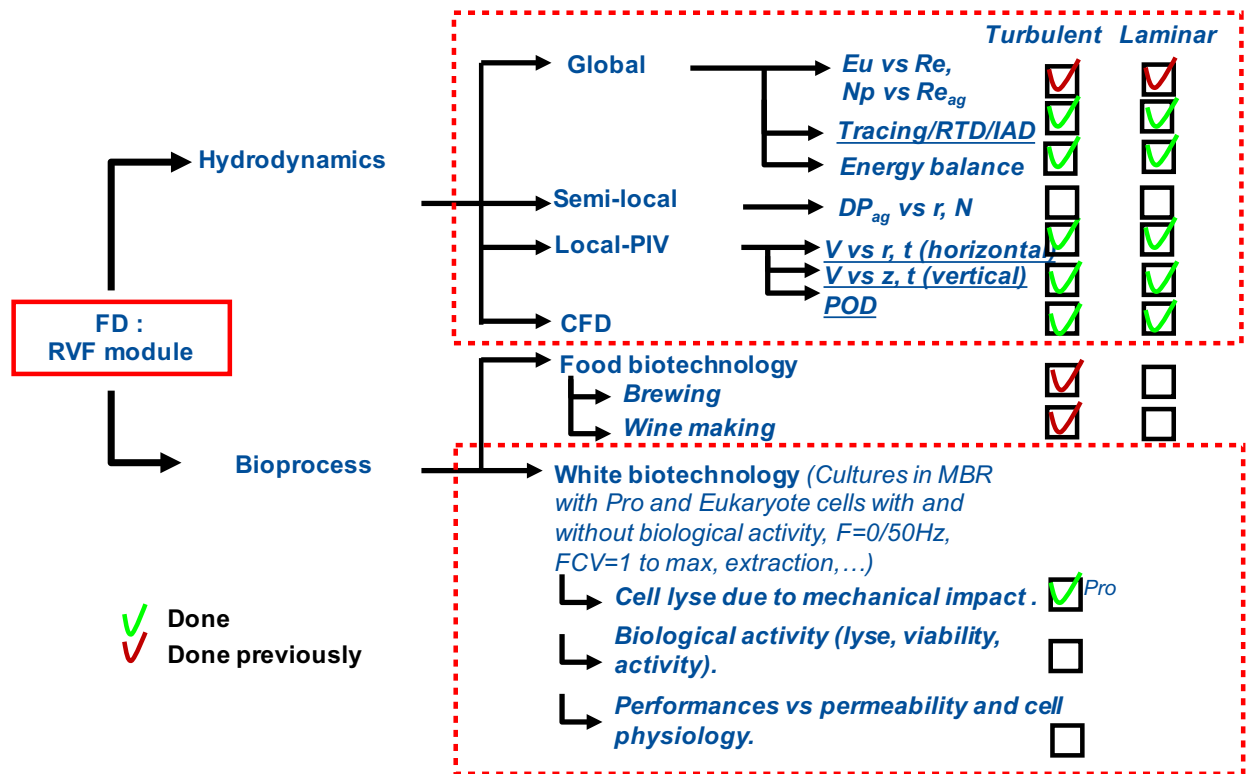


Fig.V 1 Overview of scientific strategy and obtained results with RVF module

Chapter V: Conclusions

(1) For global approach, investigation of Residence Time Distribution (RTD) and thermal balance has been carried out and compared to the previous global study (power consumption and friction curves).

(2) As a major part in this PhD work, for the local approach, Particle Image Velocimetry (PIV) was carried out and compared to CFD simulation. PIV preliminary study was conducted with a trigger strategy to access through angle-resolved measurements to an averaged velocity field. Further study was performed with a non-trigger strategy and applied to POD analysis in order to identify the coherent structure of the flow by decomposing the mean contribution, the organized and turbulent fluctuations.

(3) For the bioprocess application, an exploratory work characterized the effect of Dynamic Filtration on prokaryote cell population (*Escherichia coli*) by quantifying cell integrity or damage as a function of time and rotation speed during filtration process in turbulent regime.

Main results and highlights

These actions and related discoveries combined multi-scale and multidisciplinary approaches, which gave more information on the impact of DF on bioprocess, such as:

- thermal and mechanical effect on microbial cells;
- diagnosing the functioning of global flow behaviors, in order to apply better operating conditions, leading to optimize industrial processes, as well as the DF design;
- introducing the flow pattern and coherent structures, as well as giving support to better understand the mechanism of fouling removal by examining the local parameters including local velocity fields/profiles, local shear stress, fluctuations (organized motion and turbulence).

Among these results, some contributions related to bioprocess can be mentioned:

(1) Thermal balance (heat dissipation) is highly correlated to mixing power (power consumption curve). The temperature increased dramatically at high rotation speed, especially in laminar flow (ex. +11°C under operating conditions $Q_f=25$ L/h and $N=25$ Hz). In turbulent flow, with $Q_f=50$ L/h and $N=50$ Hz, temperature increased up to 9°C. Considering a temperature increase limited to 4°C (compatible with cell culture), restricted operating conditions (minimum

Chapter V: Conclusions

flowrate and maximum mixing rate) can be estimated from thermal balance and power consumption curve.

(3) In RTD study, results indicated that in laminar flow, mean residence time t_s remained constant at a given Q_f , whatever N was. Effective volume V_I was almost constant, slightly affected by flowrate, with a mean value at 1.3 L (87% out of the RVF total volume). In turbulent regime, t_s increased linearly as a function of N at a given Q_f . The effective volume V_I was only mixing rate dependent, whereas flowrate had no effect. The effective volume ranged from 1.1 up to 1.6 L (74 up to 100% out of the RVF total volume). Combining with the CFD simulations in laminar regime, it indicated that a short-cut and dead-zone might exist in the RVF module. Modeling of RTD by PFR+(J) CSTR model (effective volume V_I and $J=2.5\pm 0.6$) enabled to access to the mean residence time and its distribution for cells in a stressful environment.

(4) In the PIV experiments with optical trigger, results in laminar regime showed that velocity fields and their related profiles were well organized at different horizontal slices. A typical parabolic profile was observed and simulated in the vertical measurements, and shear stress field was established by CFD. In turbulent regime, velocities were highly uniform (bulk), and exhibited an almost linear profile along vertical direction.

(5) In PIV experiments without the optical trigger and applying POD analysis, important local parameters including velocity, shear stress (wall shear stress, mean viscous shear, fluctuating shear) and torque were investigated. It enabled to decompose the instantaneous velocity into mean flow (mode 1) and the fluctuations (including organized and turbulent contributions):

- In laminar regime (ex. $N=2$ Hz), the main contribution for the total torque was due to the upper and lower wall (40 % each), the lateral (external) wall contributing for 20%. Contribution of each mode to the total kinetic was discussed. Mode 1 represented the mean contribution (90% of the total kinetic energy). Organized motion was based on modes 2 to 5 (7-8% of the total kinetic energy), and the related RMS wall shear stress were shown to be quite important and up to 45% of the mean wall shear stress;
- In turbulent regime (ex. $N=10$ Hz), the lateral (external) wall shear stress with value 250 Pa contributed 90% of the total torque. Mode 1 represented the mean contribution (95% of the total kinetic energy). POD analysis showed that the organized

Chapter V: Conclusions

fluctuations were based on the modes 2-9 (4.4-5.5% of the total kinetic energy), and their coherent structure were remarkably organized.

(6) Observation with prokaryote cell suspensions (*E.coli*) indicated that cells were damaged and disrupted under extrem conditions, $N=50$ Hz and $t=5$ h. Moreover, at $N=50$ Hz, clusters and agregates with disrupted cell were observed. This was not observed with eukaryote cells in food bioprocessing (brewing and wine making). Consequently, cell damage induced by mechanical stress needs to be further explored in the light of local and global hydrodynamics.

Perspectives

Interactions between biological matrices and Dynamic Filtration must be deeply studied to intensify bioprocesses. Realizing the lack of knowledge on complex and evolving culture media (FCV, cell growth, bio-production), and (ii) intensification of microbial cultures under high cell density conditions (cellular activity and viability), future works related to dynamic filtration may be focused on:

- (1) the scientific and technical bottlenecks related to retention / permeation issues (catalytic biomass and physico-chemical components) associated with complex biological matrices;
- (2) interactions between matrices and membrane materials (nature, porosity and cut-off threshold);
- (3) the impact of the DF on the performances of prokaryote and eukaryote strains (biological activity, viability, cell lysis, etc.).

Scientific investigations may also include further works into hydrodynamics:

- (4) other local techniques can be applied to investigate local parameters such as temperature to analyze local thermal effects coupled with internal age distribution;
- (5) Electrochemical methods may be applied to quantify the instantaneous and local wall shear stress at membrane surface.
- (6) experiments can be carried out with non-Newtonian fluids to explore shear thinning/thickening and/or visco-plastic behaviors in laminar and turbulent regimes;

Chapter V: Conclusions

- (7) CFD simulations with more complex conditions (transitional and turbulent regimes with Newtonian and Non-Newtonian fluids) need to be explored and validated to design DF modules.

Reference

- [1] V.K. Pareek, Z. Yap, M.P. Brungs, A.A. Adesina, Particle residence time distribution (RTD) in three-phase annular bubble column reactor, *Chemical Engineering Science*. 56 (2001) 6063–6071. doi:10.1016/S0009-2509(01)00270-6.
- [2] C.A. Serra, M.R. Wiesner, A comparison of rotating and stationary membrane disk filters using computational fluid dynamics, *Journal of Membrane Science*. 165 (2000) 19–29. doi:10.1016/S0376-7388(99)00219-7.
- [3] R. Bouzerar, M.Y. Jaffrin, L. Ding, P. Paullier, Influence of geometry and angular velocity on performance of a rotating disk filter, *AIChE Journal*. 46 (2000) 257–265. doi:10.1002/aic.690460206.
- [4] L. Fillaudeau, B. Boissier, A. Moreau, P. Blanpain-avet, S. Ermolaev, N. Jitariouk, et al., Investigation of rotating and vibrating filtration for clarification of rough beer, *Journal of Food Engineering*. 80 (2007) 206–217. doi:10.1016/j.jfoodeng.2006.05.022.
- [5] Fillaudeau L., Boissier B., Ermolaev S., Jitariouk N., Gourdon A. Etude hydrodynamique d'un module de filtration dynamique, *Revue des Industries, Alimentaires & Agricole*, Septembre / Octobre, 124 (9), (2007) 8-16. [2].
- [6] M. Cheryan, *Ultrafiltration and microfiltration handbook* (1998), CRC press, Washington D.C, USA, ISBN: 9781566765985, 552p.
- [7] G. Daufin, J.P. Escudier, H. Carrère, S. Bérot, L. Fillaudeau, M. Decloux, Recent and Emerging Applications of Membrane Processes in the Food and Dairy Industry, *Food and Bioproducts Processing*. 79 (2001) 89–102. doi:10.1205/096030801750286131.
- [8] M.Y. Jaffrin, Dynamic filtration with rotating disks, and rotating and vibrating membranes: an update, *Current Opinion in Chemical Engineering*. 1 (2012) 171–177. doi:10.1016/j.coche.2012.01.002.
- [9] P.D.S. Wroński, D.E. Molga, L. Rudniak, Dynamic filtration in biotechnology, *Bioprocess Engineering*. 4 (1989) 99–104. doi:10.1007/BF00369757.
- [10] A.S. Jönsson, O. Wallberg, Cost estimates of kraft lignin recovery by ultrafiltration, *Desalination*. 237 (2009) 254–267, doi:10.1016/j.desal.2007.11.061.
- [11] W.P. Eagles, R.J. WAKEMAN, Interactions between dissolved material and the fouling layer during microfiltration of a model beer solution, *Journal of Membrane Science*. 206 (2002) 253–264. doi:10.1016/S0376-7388(01)00772-4.
- [12] L. Fillaudeau, H. Carrère, Yeast cells, beer composition and mean pore diameter impacts on fouling and retention during cross-flow filtration of beer with ceramic membranes, *Journal of Membrane Science*. 196 (2002) 39–57. doi:10.1016/S0376-7388(01)00568-3.
- [13] Q. Gan, R.W. Field, M.R. Bird, R. England, J.A. Howell, M.T. Mckechnie, et al., Beer Clarification by Cross-Flow Microfiltration: Fouling Mechanisms and Flux Enhancement, *Chemical Engineering Research and Design*. 75 (1997) 3–8. doi:10.1205/026387697523327.
- [14] P. Riddell, A. Kelly, The Effect of Microporous Membrane Filtration on Beer Foam Stability, *MBAA TQ*, 41, 4 (2004), pp. 379-385.

Reference

- [15] M. Taylor, Quantitative determination of fouling layer composition in the microfiltration of beer, *Separation and Purification Technology*. 22-23 (2001) 133–142. doi:10.1016/S1383-5866(00)00157-X.
- [16] Z. Wang, J. Ma, C.Y. Tang, K. Kimura, Q. Wang, X. Han, Membrane cleaning in membrane bioreactors: A review, *Journal of Membrane Science*. 468 (2014) 276–307. doi:10.1016/j.memsci.2014.05.060.
- [17] J. Jiang, Z. Liu, Y. He, Development Trend: Rotary fibre disk filtration in the treatment of oilfield wastewater, *Filtration & Separation*. 51 (2014) 32–34. doi:10.1016/S0015-1882(14)70034-5.
- [18] D.E. Hadzismajlovic, C.D. BERTRAM, Flux enhancement in laminar crossflow microfiltration using a collapsible-tube pulsation generator, *Journal of Membrane Science*. 142 (1998) 173–189. doi:10.1016/S0376-7388(97)00319-0.
- [19] M. Sarioglu, G. Insel, D. Orhon, Dynamic in-series resistance modeling and analysis of a submerged membrane bioreactor using a novel filtration mode, *Desalination*. 285 (2012) 285–294. doi:10.1016/j.desal.2011.10.015.
- [20] L. Xia, A.W.-K. Law, A.G. Fane, Hydrodynamic effects of air sparging on hollow fiber membranes in a bubble column reactor, *Water Research*. 47 (2013) 3762–3772. doi:10.1016/j.watres.2013.04.042.
- [21] M. Cai, S. Zhao, H. Liang, Mechanisms for the enhancement of ultrafiltration and membrane cleaning by different ultrasonic frequencies, *Desalination*. 263 (2010) 133–138. doi:10.1016/j.desal.2010.06.049.
- [22] R.P. Castro, H.G. Monbouquette, Y. Cohen, Shear-induced permeability changes in a polymer grafted silica membrane, *Journal of Membrane Science*. 179 (2000) 207–220. doi:10.1016/S0376-7388(00)00509-3.
- [23] E.-H. Kim, M. Dwidar, R.J. Mitchell, Y.-N. Kwon, Assessing the effects of bacterial predation on membrane biofouling, *Water Research*. 47 (2013) 6024–6032. doi:10.1016/j.watres.2013.07.023.
- [24] M.Y. Jaffrin, L.H. Ding, O. Akoum, A. Brou, A hydrodynamic comparison between rotating disk and vibratory dynamic filtration systems, *Journal of Membrane Science*. 242 (2004) 155–167. doi:10.1016/j.memsci.2003.07.029.
- [25] S. Chang and A.G. Fane, Techniques to Enhance Performance of Membrane Processes, in: *Handbook of Membrane Separations: Chemical, Pharmaceutical, Food, and Biotechnological Applications* (2008), Edited By Anil K. Pabby, Syed S.H. Rizvi, Ana Maria Sastre Requena, ISBN: 9781466555587, pp. 1–40.
- [26] Liu Y, Li M. (2016) BibeR: A Web-based tool for bibliometric analysis in scientific literature. *PeerJ Preprints* 4:e1879v1, <https://doi.org/10.7287/peerj.preprints.1879v1>.
- [27] L.Y. Ng, A.W. Mohammad, C.P. Leo, N. Hilal, Polymeric membranes incorporated with metal/metal oxide nanoparticles: A comprehensive review, *Desalination*. 308 (2013) 15–33. doi:10.1016/j.desal.2010.11.033.
- [28] K.P. Lee, T.C. Arnot, D. Mattia, A review of reverse osmosis membrane materials for desalination—Development to date and future potential, *Journal of Membrane Science*. 370 (2011) 1–22. doi:10.1016/j.memsci.2010.12.036.
- [29] M.M. Dal-Cin, C.N. Lick, A. Kumar, S. Lealess, Dispersed phase back transport during ultrafiltration of cutting oil emulsions with a spinning membrane disc geometry Issued as NRCC No. 41962.1, *Journal of Membrane Science*. 141 (1998) 165–181. doi:10.1016/S0376-7388(97)00304-9.

Reference

- [30] M.Y. Jaffrin, Dynamic shear-enhanced membrane filtration: A review of rotating disks, rotating membranes and vibrating systems, *Journal of Membrane Science*. 324 (2008) 7–25. doi:10.1016/j.memsci.2008.06.050.
- [31] J. Bendick, B. Reed, P. Morrow, T. Carole, Using a high shear rotary membrane system to treat shipboard wastewaters: Experimental disc diameter, rotation and flux relationships, *Journal of Membrane Science*. 462 (2014) 178–184. doi:10.1016/j.memsci.2014.02.015.
- [32] S.D. Ríos, J. Salvadó, X. Farriol, C. Torras, Antifouling microfiltration strategies to harvest microalgae for biofuel, *Bioresource Technology*. 119 (2012) 406–418. doi:10.1016/j.biortech.2012.05.044.
- [33] S.D. Ríos, E. Clavero, J. Salvadó, X. Farriol, C. Torras, Dynamic Microfiltration in Microalgae Harvesting for Biodiesel Production, *Ind. Eng. Chem. Res.* 50 (2011) 2455–2460. doi:10.1021/ie101070q.
- [34] Diva Envitec, Modular Spin Disk Filter MSDF, website: <http://divaenvitec.com/divaenvitec/products/modular-spin-disk-filter-msdf> (2014).
- [35] Fraunhofer IGB, Rotating disk filter for low energy wastewater treatment, website: https://www.igb.fraunhofer.de/en/research/competences/environmental-biotechnology/wastewater_purification/water-purification-and-bioreactor-concepts/cost-optimized-filtration.html (2018).
- [36] L. Ding, M. Jaffrin, M. Mellal, G. HE, Investigation of performances of a multishaft disk (MSD) system with overlapping ceramic membranes in microfiltration of mineral suspensions, *Journal of Membrane Science*. 276 (2006) 232–240. doi:10.1016/j.memsci.2005.09.051.
- [37] Mio Vigneto, Automatic Hi-Tech Filter System, website: <https://www.winesandvines.com/suppliernews/article/117021/Rocket-M7-and-M77-wine-and-lees-filters>.
- [38] M. Ebrahimi, O. Schmitz, S. Kerker, F. Liebermann, P. Czermak, Dynamic cross-flow filtration of oilfield produced water by rotating ceramic filter discs, *Desalination and Water Treatment*. 51 (2013) 1762–1768. doi:10.1080/19443994.2012.694197.
- [39] HUBER Technology, Vacuum Rotation Membrane Filtration- Unique, rotating membrane filtration for MBR applications, website: <http://www.huber.de/products/membrane-filtration-mbr/huber-membrane-filtration-vrmr.html>. (2018).
- [40] D. Sarkar, D. Datta, D. Sen, C. Bhattacharjee, Simulation of continuous stirred rotating disk-membrane module: An approach based on surface renewal theory, *Chemical Engineering Science*. 66 (2011) 2554–2567. doi:10.1016/j.ces.2011.02.056.
- [41] D. Sarkar, S. Bardhan, A. Bandyopadhyay, M. Chakraborty, C. Bhattacharjee, Simulation of continuous stirred ultrafiltration process: an approach based on surface renewal theory, *Asia-Pacific Journal of Chemical Engineering*. 7 (2012) 279–294. doi:10.1002/apj.534.
- [42] L. Liu, B. Gao, J. Liu, F. Yang, Rotating a helical membrane for turbulence enhancement and fouling reduction, *Chemical Engineering Journal*. 181-182 (2012) 486–493. doi:10.1016/j.cej.2011.12.007.
- [43] A. Sarkar, D. Sarkar, C. Bhattacharjee, Design and performance characterization of

Reference

- a new shear enhanced module with inbuilt cleaning arrangement, *J. Chem. Technol. Biotechnol.* 87 (2012) 1121–1130. doi:10.1002/jctb.3728.
- [44] A. Sarkar, S. Moulik, D. Sarkar, A. Roy, C. Bhattacharjee, Performance characterization and CFD analysis of a novel shear enhanced membrane module in ultrafiltration of Bovine Serum Albumin (BSA), *Desalination.* 292 (2012) 53–63. doi:10.1016/j.desal.2012.02.009.
- [45] D. Sarkar, A. Sarkar, A. Roy, C. Bhattacharjee, Performance characterization and design evaluation of spinning basket membrane (SBM) module using computational fluid dynamics (CFD), *Separation and Purification Technology.* 94 (2012) 23–33. doi:10.1016/j.seppur.2012.03.034.
- [46] A. Sarkar, D. Sarkar, M. Gupta, C. Bhattacharjee, Recovery of Polyvinyl Alcohol from Desizing Wastewater Using a Novel High-Shear Ultrafiltration Module, *Clean-Soil Air Water.* 40 (2012) 830–837. doi:10.1002/clen.201100527.
- [47] K.H. Kroner, V. Nissinen, Dynamic filtration of microbial suspensions using an axially rotating filter, *Journal of Membrane Science.* 36 (1988) 85–100. doi:10.1016/0376-7388(88)80009-7.
- [48] O. Al-Akoum, L.H. Ding, R. Chotard-Ghodsnia, M.Y. Jaffrin, G. Gesan-Guiziou, Casein micelles separation from skimmed milk using a VSEP dynamic filtration module, *Desalination.* 144 (2002) 325–330. doi:10.1016/S0011-9164(02)00337-5.
- [49] O. Akoum, M.Y. Jaffrin, L.H. Ding, Concentration of total milk proteins by high shear ultrafiltration in a vibrating membrane module, *Journal of Membrane Science.* 247 (2005) 211–220. doi:10.1016/j.memsci.2004.09.021.
- [50] M. Frappart, M.Y. Jaffrin, L.H. Ding, V. Espina, Effect of vibration frequency and membrane shear rate on nanofiltration of diluted milk, using a vibratory dynamic filtration system, *Separation and Purification Technology.* 62 (2008) 212–221. doi:10.1016/j.seppur.2008.01.025.
- [51] J. Postlethwaite, S.R. Lamping, G.C. Leach, M.F. Hurwitz, G.J. Lye, Flux and transmission characteristics of a vibrating microfiltration system operated at high biomass loading, *Journal of Membrane Science.* 228 (2004) 89–101. doi:10.1016/j.memsci.2003.07.025.
- [52] H.G. Gomaa, S. Rao, Analysis of flux enhancement at oscillating flat surface membranes, *Journal of Membrane Science.* 374 (2011) 59–66. doi:10.1016/j.memsci.2011.03.011.
- [53] H. Gomaa, A.M. Al-Taweel, Dynamic analysis of mass transfer at vertically oscillating surfaces, *Chemical Engineering Journal.* 102 (2004) 71–82. doi:10.1016/j.cej.2004.02.004.
- [54] H.G. Gomaa, R. Sabouni, Energetic consideration and flux characteristics of roughed-surface membrane in presence of reversing shear, *Chemical Engineering Research and Design.* 92 (2014) 1771–1780. doi:10.1016/j.cherd.2013.12.009.
- [55] H.G. Gomaa, Flux characteristics at oscillating membrane equipped with turbulent promoters, *Chemical Engineering Journal.* 191 (2012) 541–547. doi:10.1016/j.cej.2012.03.026.
- [56] H.G. Gomaa, S. Rao, M.A. Taweel, Flux enhancement using oscillatory motion and turbulence promoters, *Journal of Membrane Science.* 381 (2011) 64–73. doi:10.1016/j.memsci.2011.07.014.
- [57] H.G. Gomaa, S. Rao, A.M. Al-Taweel, Intensification of membrane microfiltration

Reference

- using oscillatory motion, *Separation and Purification Technology*. 78 (2011) 336–344. doi:10.1016/j.seppur.2011.01.007.
- [58] S. Beier, M. Guerra, A. Garde, G. Jonsson, Dynamic microfiltration with a vibrating hollow fiber membrane module: Filtration of yeast suspensions, *Journal of Membrane Science*. 281 (2006) 281–287. doi:10.1016/j.memsci.2006.03.051.
- [59] S. Beier, G. Jonsson, Separation of enzymes and yeast cells with a vibrating hollow fiber membrane module, *Separation and Purification Technology*. 53 (2007) 111–118. doi:10.1016/j.seppur.2006.06.019.
- [60] S.P. Beier, G. Jonsson, Critical Flux Determination by Flux-Stepping, *AIChE Journal*. 56 (2010) 1739–1747. doi:10.1002/aic.12099.
- [61] G. Genkin, T. Waite, A. Fane, S. Chang, The effect of vibration and coagulant addition on the filtration performance of submerged hollow fibre membranes, *Journal of Membrane Science*. 281 (2006) 726–734. doi:10.1016/j.memsci.2006.04.048.
- [62] L. Qin, Z. Fan, L. Xu, G. Zhang, G. Wang, D. Wu, et al., A submerged membrane bioreactor with pendulum type oscillation (PTO) for oily wastewater treatment: Membrane permeability and fouling control, *Bioresource Technology*. 183 (2015) 33–41. doi:10.1016/j.biortech.2015.02.018.
- [63] W. Zhang, L. Ding, Investigation of membrane fouling mechanisms using blocking models in the case of shear-enhanced ultrafiltration, *Separation and Purification Technology*. 141 (2015) 160–169. doi:10.1016/j.seppur.2014.11.041.
- [64] W. Zhang, N. Grimi, M.Y. Jaffrin, L. Ding, Leaf protein concentration of alfalfa juice by membrane technology, *Journal of Membrane Science*. 489 (2015) 183–193. doi:10.1016/j.memsci.2015.03.092.
- [65] L. Ding, W. Zhang, A. Ould-Dris, M.Y. Jaffrin, B. Tang, Concentration of Milk Proteins for Producing Cheese Using a Shear-Enhanced Ultrafiltration Technique, *Ind. Eng. Chem. Res.* 55 (2016) 11130–11138. doi:10.1021/acs.iecr.6b02738.
- [66] J. Luo, L. Ding, Y. Wan, P. Paullier, M.Y. Jaffrin, Application of NF-RDM (nanofiltration rotating disk membrane) module under extreme hydraulic conditions for the treatment of dairy wastewater, *Chemical Engineering Journal*. 163 (2010) 307–316. doi:10.1016/j.cej.2010.08.007.
- [67] J. Luo, L. Ding, Y. Wan, M.Y. Jaffrin, Flux decline control in nanofiltration of detergent wastewater by a shear-enhanced filtration system, *Chemical Engineering Journal*. 181–182 (2012) 397–406. doi:10.1016/j.cej.2011.11.101.
- [68] L.H. Ding, O. Al-Akoum, A. Abraham, M.Y. Jaffrin, Milk protein concentration by ultrafiltration with rotating disk modules, *Desalination*. 144 (2002) 307–311. doi:10.1016/S0011-9164(02)00334-X.
- [69] L. Li, L. Ding, Z. Tu, Y. Wan, D. Clause, J.-L. Lanoiselle, Recovery of linseed oil dispersed within an oil-in-water emulsion using hydrophilic membrane by rotating disk filtration system, *Journal of Membrane Science*. 342 (2009) 70–79. doi:10.1016/j.memsci.2009.06.023.
- [70] M. Frappart, O. Akoum, L.H. Ding, M.Y. Jaffrin, Treatment of dairy process waters modelled by diluted milk using dynamic nanofiltration with a rotating disk module, *Journal of Membrane Science*. 282 (2006) 465–472. doi:10.1016/j.memsci.2006.06.005.
- [71] O. Akoum, M.Y. Jaffrin, L.H. Ding, M. Frappart, Treatment of dairy process waters

Reference

- using a vibrating filtration system and NF and RO membranes, *Journal of Membrane Science*. 235 (2004) 111–122. doi:10.1016/j.memsci.2004.01.026.
- [72] J. Luo, W. Cao, L. Ding, Z. Zhu, Y. Wan, M.Y. Jaffrin, Treatment of dairy effluent by shear-enhanced membrane filtration: The role of foulants, *Separation and Purification Technology*. 96 (2012) 194–203. doi:10.1016/j.seppur.2012.06.009.
- [73] L. Ding, M.Y. Jaffrin, J. Luo, Dynamic Filtration with Rotating Disks, and Rotating or Vibrating Membranes, in: *Progress in Filtration and Separation*, Elsevier, 2015: pp. 27–59.
- [74] J. Luo, L. Ding, Y. Wan, P. Paullier, M.Y. Jaffrin, Fouling behavior of dairy wastewater treatment by nanofiltration under shear-enhanced extreme hydraulic conditions, *Separation and Purification Technology*. 88 (2012) 79–86.
- [75] Z. Tu, L. Ding, Microfiltration of mineral suspensions using a MSD module with rotating ceramic and polymeric membranes, *Separation and Purification Technology*. 73 (2010) 363–370. doi:10.1016/j.seppur.2010.04.024.
- [76] Z. Zhu, J. Luo, L. Ding, O. Bals, M.Y. Jaffrin, E. Vorobiev, Chicory juice clarification by membrane filtration using rotating disk module, *Journal of Food Engineering*. 115 (2013) 264–271. doi:10.1016/j.jfoodeng.2012.10.028.
- [77] J. Luo, L. Ding, Influence of pH on treatment of dairy wastewater by nanofiltration using shear-enhanced filtration system, *Desalination*. 278 (2011) 150–156. doi:10.1016/j.desal.2011.05.025.
- [78] O.A. Akoum, M.Y. Jaffrin, L. Ding, P. Paullier, C. Vanhoutte, An hydrodynamic investigation of microfiltration and ultrafiltration in a vibrating membrane module, *Journal of Membrane Science*. 197 (2002) 37–52. doi:10.1016/S0376-7388(01)00602-0.
- [79] A. Brou, L. Ding, P. Boulnois, M.Y. Jaffrin, Dynamic microfiltration of yeast suspensions using rotating disks equipped with vanes, *Journal of Membrane Science*. 197 (2002) 269–282. doi:10.1016/S0376-7388(01)00642-1.
- [80] Z. Zhu, S. Ladeg, L. Ding, O. Bals, Nadji Moulai-Mostefa, M.Y. Jaffrin, et al., Study of rotating disk assisted dead-end filtration of chicory juice and its performance optimization, *Industrial Crops and Products*. 53 (2014) 154–162. doi:10.1016/j.indcrop.2013.12.030.
- [81] R. Bouzerar, Local permeate flux–shear–pressure relationships in a rotating disk microfiltration module: implications for global performance, *Journal of Membrane Science*. 170 (2000) 127–141. doi:10.1016/S0376-7388(99)00348-8.
- [82] J. Luo, L. Ding, Y. Wan, M.Y. Jaffrin, Threshold flux for shear-enhanced nanofiltration: Experimental observation in dairy wastewater treatment, *Journal of Membrane Science*. 409–410 (2012) 276–284. doi:10.1016/j.memsci.2012.03.065.
- [83] W. Zhang, L. Ding, N. Grimi, M.Y. Jaffrin, B. Tang, Application of UF-RDM (Ultrafiltration Rotating Disk Membrane) module for separation and concentration of leaf protein from alfalfa juice: Optimization of operation conditions, *Separation and Purification Technology*. 175 (2017) 365–375. doi:10.1016/j.seppur.2016.11.059.
- [84] Z. Zhu, H. Mhemdi, W. Zhang, L. Ding, O. Bals, M.Y. Jaffrin, et al., Rotating Disk-Assisted Cross-Flow Ultrafiltration of Sugar Beet Juice, *Food Bioprocess Technol.* 9 (2015) 493–500. doi:10.1007/s11947-015-1644-3.
- [85] L.H. Ding, O. Akoum, A. Abraham, M.Y. Jaffrin, High shear skim milk ultrafiltration using rotating disk filtration systems, *AIChE Journal*. 49 (2006) 2433–

Reference

2441. doi:10.1002/aic.690490918.
- [86] N. Moulai-Mostefa, O. Akoum, M. Nedjihoui, L. Ding, M.Y. Jaffrin, Comparison between rotating disk and vibratory membranes in the ultrafiltration of oil-in-water emulsions, *Desalination*. 206 (2007) 494–498. doi:10.1016/j.desal.2006.04.061.
- [87] V.S. Espina, M.Y. Jaffrin, L.H. Ding, Comparison of rotating ceramic membranes and polymeric membranes in fractionation of milk proteins by microfiltration, *Desalination*. 245 (2009) 714–722. doi:10.1016/j.desal.2009.02.042.
- [88] V. Espina, M.Y. Jaffrin, L. Ding, B. Cancino, Fractionation of pasteurized skim milk proteins by dynamic filtration, *Food Research International*. 43 (2010) 1335–1346. doi:10.1016/j.foodres.2010.03.023.
- [89] J. Luo, Z. Zhu, L. Ding, O. Bals, Y. Wan, M.Y. Jaffrin, et al., Flux behavior in clarification of chicory juice by high-shear membrane filtration: Evidence for threshold flux, *Journal of Membrane Science*. 435 (2013) 120–129. doi:10.1016/j.memsci.2013.01.057.
- [90] A. Brou, M.Y. Jaffrin, L.H. Ding, J. Courtois, Microfiltration and ultrafiltration of polysaccharides produced by fermentation using a rotating disk dynamic filtration system, *Biotechnology and Bioengineering*. 82 (2003) 429–437. doi:10.1002/bit.10584.
- [91] O. Akoum, D. Richfield, M.Y. Jaffrin, L.H. Ding, P. Swart, Recovery of trypsin inhibitor and soy milk protein concentration by dynamic filtration, *Journal of Membrane Science*. 279 (2006) 291–300. doi:10.1016/j.memsci.2005.12.030.
- [92] S.S. Lee, A. Burt, G. Russotti, B. Buckland, Microfiltration of recombinant yeast cells using a rotating disk dynamic filtration system, *Biotechnology and Bioengineering*. 48 (1995) 386–400. doi:10.1002/bit.260480411.
- [93] U. Frenander, A.S. Jönsson, Cell harvesting by cross-flow microfiltration using a shear-enhanced module, *Biotechnology and Bioengineering*. 52 (1996) 397–403. doi:10.1002/(SICI)1097-0290(19961105)52:3<397::AID-BIT5>3.0.CO;2-F.
- [94] F. Meyer, I. Gehmlich, R. Guthke, A. Gorak, W.A. Knorre, Analysis and simulation of complex interactions during dynamic microfiltration of *Escherichia coli* suspensions, *Biotechnology and Bioengineering*. 59 (1998) 189–202. doi:10.1002/(SICI)1097-0290(19980720)59:2<189::AID-BIT7>3.0.CO;2-D.
- [95] R. Bott, T. Langeloh, E. Ehrfeld, Dynamic cross flow filtration, *Chemical Engineering Journal*. 80 (2000) 245–249. doi:10.1016/S1383-5866(00)00097-6.
- [96] J. Nuortila-Jokinen, M. Nyström, Comparison of membrane separation processes in the internal purification of paper mill water, *Journal of Membrane Science*. 119 (1996) 99–115. doi:10.1016/0376-7388(96)00118-4.
- [97] J. Nuortila-Jokinen, A. Kuparinen, M. Nyström, Tailoring an economical membrane process for internal purification in the paper industry, *Desalination*. 119 (1998) 11–19. doi:10.1016/S0011-9164(98)00083-6.
- [98] T. Huuhilo, P. Väisänen, J. Nuortila-Jokinen, M. Nyström, Influence of shear on flux in membrane filtration of integrated pulp and paper mill circulation water, *Desalination*. 141 (2001) 245–258. doi:10.1016/S0011-9164(01)85003-7.
- [99] S. Judd, The status of membrane bioreactor technology, *Trends in Biotechnology*. 26 (2008) 109–116. doi:10.1016/j.tibtech.2007.11.005.
- [100] M. Mänttari, J. Nuortila-Jokinen, M. Nyström, Evaluation of nanofiltration membranes for filtration of paper mill total effluent, *Filtration & Separation*. 34

Reference

- (1997) 275–280. doi:10.1016/S0015-1882(97)84794-5.
- [101] M. Mänttari, J. Nuortila-Jokinen, M. Nyström, Influence of filtration conditions on the performance of NF membranes in the filtration of paper mill total effluent, *Journal of Membrane Science*. 137 (1997) 187–199. doi:10.1016/S0376-7388(97)00223-8.
- [102] T.R. Bentzen, N. Ratkovich, S. Madsen, J.C. Jensen, S.N. Bak, M.R. Rasmussen, Analytical and numerical modelling of Newtonian and non-Newtonian liquid in a rotational cross-flow MBR, *Water Science and Technology*. 66 (2012) 2318–2327. doi:10.2166/wst.2012.443.
- [103] RVF, RVF – dynamic membrane filtration in the nonstationary flux, website: <Http://swww.Environmental-Expert.comproductsrvf-Rotating-Vibrating-Filtration-System> (2016).
- [104] K. Kim, J.-Y. Jung, J.-H. Kwon, J.-W. Yang, Dynamic microfiltration with a perforated disk for effective harvesting of microalgae, *Journal of Membrane Science*. 475 (2015) 252–258. doi:10.1016/j.memsci.2014.10.027.
- [105] BKT, Membrane Filtration System (FMS) - Anti-fouling Membrane Filtration System, website: <https://bkt21.com/fmx/>. (2017).
- [106] Miltenyi Biotec, LIFE 18™ – Disk Separator, website: <http://www.miltenyibiotec.com/en/clinical-applications/therasorb-therapeutic-apheresis/disposables/life-18--disk-separator.aspx>. (2018).
- [107] J.H. Vogel, K.H. Kroner, Controlled shear filtration: A novel technique for animal cell separation, *Biotechnology and Bioengineering*. 63 (1999) 663–674. doi:10.1002/(SICI)1097-0290(19990620)63:6<663::AID-BIT4>3.0.CO;2-0.
- [108] T.K. Sherwood, P.L.T. Brian, R.E. Fisher, Desalination by Reverse Osmosis, *Ind. Eng. Chem. Fund.* 6 (1967) 2–12. doi:10.1021/i160021a001.
- [109] B. Hallström, M. Lopez-Leiva, Description of a rotating ultrafiltration module, *Desalination*. 24 (1977) 273–279. doi:10.1016/S0011-9164(00)88089-3.
- [110] M. Mateus, J. Cabral, Steroid Recovery by a Rotary Membrane System, *Biotechnology Techniques*. 5 (1991) 43–48. doi:10.1007/BF00152754.
- [111] A. Adach, S. Wroński, M. Buczkowski, W. Starosta, B. Sartowska, Mechanism of microfiltration on the rotating track membrane, *Separation and Purification Technology*. 26 (2002) 33–41. doi:10.1016/S1383-5866(01)00114-9.
- [112] T. Murase, C. Pradistsuwana, E. Iritani, K. Kano, Dynamic Microfiltration of Dilute Slurries with a Rotating Ceramic Membrane, *Journal of Membrane Science*. 62 (1991) 187–199. doi:10.1016/0376-7388(91)80061-A.
- [113] S. Lee, R.M. Lueptow, Experimental verification of a model for rotating reverse osmosis, *Desalination*. 146 (2002) 353–359. doi:10.1016/S0011-9164(02)00512-X.
- [114] S. Lee, R.M. Lueptow, Control of scale formation in reverse osmosis by membrane rotation, *Desalination*. (2003). doi:10.1016/j.biortech.2012.05.044.
- [115] J.Y. Park, C.K. Choi, J.J. Kim, A study on dynamic separation of silica slurry using a rotating membrane filter 1. Experiments and filtrate fluxes, *Journal of Membrane Science*. 97 (1994) 263–273. doi:10.1016/0376-7388(94)00167-W.
- [116] C. Bhattacharjee, P.K. Bhattacharya, Ultrafiltration of black liquor using rotating disk membrane module, *Separation and Purification Technology*. 49 (2006) 281–290. doi:10.1016/j.seppur.2005.10.011.
- [117] S. Bhattacharjee, S. Datta, C. Bhattacharjee, Performance study during ultrafiltration

Reference

- of Kraft black liquor using rotating disk membrane module, *Journal of Cleaner Production*. 14 (2006) 497–504. doi:10.1016/j.jclepro.2005.02.004.
- [118] B. Gao, L. Liu, J. Liu, F. Yang, A photo-catalysis and rotating nano-CaCO₃ dynamic membrane system with Fe-ZnIn₂S₄ efficiently removes halogenated compounds in water, *Applied Catalysis B-Environmental*. 138 (2013) 62–69. doi:10.1016/j.apcatb.2013.02.023.
- [119] C. Nurra, E. Clavero, J. Salvadó, C. Torras, Vibrating membrane filtration as improved technology for microalgae dewatering, *Bioresource Technology*. 157 (2014) 247–253. doi:10.1016/j.biortech.2014.01.115.
- [120] C. Nurra, C. Torras, E. Clavero, S. Rios, M. Rey, E. Lorente, et al., Biorefinery concept in a microalgae pilot plant. Culturing, dynamic filtration and steam explosion fractionation, *Bioresource Technology*. 163 (2014) 136–142. doi:10.1016/j.biortech.2014.04.009.
- [121] N. Moulai-Mostefa, M. Frappart, O. Akoum, L. Ding, M.Y. Jaffrin, Separation of water from metal working emulsions by ultrafiltration using vibratory membranes, *Journal of Hazardous Materials*. 177 (2010) 978–982. doi:10.1016/j.jhazmat.2010.01.014.
- [122] H.G. Goma, S. Rao, A.M. Al-Taweel, Intensification of membrane microfiltration using oscillatory motion, *Separation and Purification Technology*. 78 (2011) 336–344. doi:10.1016/j.seppur.2011.01.007.
- [123] T. Li, A.W.-K. Law, M. Cetin, A.G. Fane, Fouling control of submerged hollow fibre membranes by vibrations, *Journal of Membrane Science*. 427 (2013) 230–239. doi:10.1016/j.memsci.2012.09.031.
- [124] T. Li, A.W.-K. Law, A.G. Fane, Submerged hollow fibre membrane filtration with transverse and longitudinal vibrations, *Journal of Membrane Science*. 455 (2014) 83–91. doi:10.1016/j.memsci.2013.12.042.
- [125] A. Kola, Y. Ye, A. Ho, P. Le-Clech, V. Chen, Application of low frequency transverse vibration on fouling limitation in submerged hollow fibre membranes, *Journal of Membrane Science*. 409-410 (2012) 54–65. doi:10.1016/j.memsci.2012.03.017.
- [126] S.P. Beier, G. Jonsson, Dynamic microfiltration with a vibrating hollow fiber membrane module, *Desalination*. 199 (2006) 499–500. doi:10.1016/j.desal.2006.03.114.
- [127] L.O. Wilson, N.L. Schryer, Flow between a stationary and a rotating disk with suction, *Journal of Fluid Mechanics*. 85 (1978) 479–496. doi:10.1017/S0022112078000750.
- [128] C. Harscoat, M.Y. Jaffrin, R. Bouzerar, J. Courtois, Influence of fermentation conditions and microfiltration processes on membrane fouling during recovery of glucuronane polysaccharides from fermentation broths, *Biotechnology and Bioengineering*. 65 (1999) 500–511. doi:10.1002/(SICI)1097-0290(19991205)65:5<500::AID-BIT2>3.0.CO;2-N.
- [129] M. Frappart, A. Masse, M.Y. Jaffrin, J. Pruvost, P. Jaouen, Influence of hydrodynamics in tangential and dynamic ultrafiltration systems for microalgae separation, *Desalination*. 265 (2011) 279–283. doi:10.1016/j.desal.2010.07.061.
- [130] C. Torras, J. Pallares, R. Garcia-Valls, M.Y. Jaffrin, Numerical simulation of the flow in a rotating disk filtration module, *Desalination*. 235 (2009) 122–138.

Reference

- doi:10.1016/j.desal.2008.02.006.
- [131] Z. Tu, L. Ding, M. Frappart, M.Y. Jaffrin, Studies on treatment of sodium dodecyl benzene sulfonate solution by high shear ultrafiltration system, *Desalination*. 240 (2009) 251–256. doi:10.1016/j.desal.2008.01.051.
- [132] M. Mellal, M.Y. Jaffrin, L.H. Ding, C. Delattre, P. Michaud, J. Courtois, Separation of oligoglucuronans of low degrees of polymerization by using a high shear rotating disk filtration module, *Separation and Purification Technology*. 60 (2008) 22–29. doi:10.1016/j.seppur.2007.07.041.
- [133] R. Bouzerar, M.Y. Jaffrin, A. Lefevre, P. Paullier, Concentration of ferric hydroxide suspensions in saline medium by dynamic cross-flow filtration, *Journal of Membrane Science*. 165 (2000) 111–123. doi:10.1016/S0376-7388(99)00226-4.
- [134] N. Moulai-Mostefa, L.H. Ding, M. Frappart, M.Y. Jaffrin, Treatment of aqueous ionic surfactant solutions by dynamic ultrafiltration, *Separation Science and Technology*. 42 (2007) 2583–2594. doi:10.1080/01496390701526612.
- [135] P. Francis, D.M. Martinez, F. Taghipour, B.D. Bowen, C.A. Haynes, Optimizing the rotor design for controlled-shear affinity filtration using computational fluid dynamics, *Biotechnology and Bioengineering*. 95 (2006) 1207–1217. doi:10.1002/bit.21090.
- [136] R. Bouzerar, P. Paullier, M.Y. Jaffrin, Concentration of mineral suspensions and industrial effluents using a rotating disk dynamic filtration module, *Desalination*. (2003). doi:doi:10.1016/S0011-9164(03)00436-3.
- [137] M. Frappart, M. Jaffrin, L.H. Ding, Reverse osmosis of diluted skim milk: Comparison of results obtained from vibratory and rotating disk modules, *Separation and Purification Technology*. 60 (2008) 321–329. doi:10.1016/j.seppur.2007.09.007.
- [138] V.S. Espina, M.Y. Jaffrin, M. Frappart, L.H. Ding, Separation of casein micelles from whey proteins by high shear microfiltration of skim milk using rotating ceramic membranes and organic membranes in a rotating disk module, *Journal of Membrane Science*. 325 (2008) 872–879. doi:10.1016/j.memsci.2008.09.013.
- [139] Z. Tu, L. Ding, Microfiltration of mineral suspensions using a MSD module with rotating ceramic and polymeric membranes, *Separation and Purification Technology*. 73 (2010) 363–370. doi:10.1016/j.seppur.2010.04.024.
- [140] M. Mellal, L.H. Ding, M.Y. Jaffrin, C. Delattre, P. Michaud, J. Courtois, Separation and fractionation of oligouronides by shear-enhanced filtration, *Separation Science and Technology*. 42 (2007) 349–361. doi:10.1080/01496390601069903.
- [141] V. Espina, M.Y. Jaffrin, M. Frappart, L.H. Ding, Separation of casein from whey proteins by dynamic filtration, *Desalination*. 250 (2010) 1109–1112. doi:10.1016/j.desal.2009.09.119.
- [142] V. Espina, M.Y. Jaffrin, L. Ding, Extraction and Separation of alpha-lactalbumin and beta-Lactoglobulin from Skim Milk by Microfiltration and Ultrafiltration at High Shear Rates: A Feasibility Study, *Separation Science and Technology*. 44 (2009) 3832–3853. doi:10.1080/01496390903183238.
- [143] Z. Zhu, H. Mhemdi, L. Ding, O. Bals, M.Y. Jaffrin, N. Grimi, et al., Dead-End Dynamic Ultrafiltration of Juice Expressed from Electroporated Sugar Beets, *Food Bioprocess Technol*. 8 (2015) 615–622. doi:10.1007/s11947-014-1427-2.
- [144] Y.E. Rayess, Y. Manon, N. Jitariouk, C. Albasi, M.M. Peuchot, A. Devatine, et al.,

Reference

- Wine clarification with Rotating and Vibrating Filtration (RVF): investigation of the impact of membrane material, wine composition and operating conditions, *Journal of Membrane Science*. (2016). doi:10.1016/j.memsci.2016.03.058.
- [145] R. Bott, T. Langeloh, E. Ehrfeld, Dynamic cross flow filtration, *Chemical Engineering Journal*. 80 (2000) 245–249. doi:10.1016/S1383-5866(00)00097-6.
- [146] K.-J. Hwang, S.-E. Wu, Disk structure on the performance of a rotating-disk dynamic filter: A case study on microalgae microfiltration, *Chemical Engineering Research and Design*. 94 (2015) 44–51. doi:10.1016/j.cherd.2014.12.009.
- [147] G. Zakrzewska-Trznadel, M. Harasimowicz, A. Miskiewicz, A. Jaworska, E. Dluska, S. Wronski, Reducing fouling and boundary-layer by application of helical flow in ultrafiltration module employed for radioactive wastes processing, *Desalination*. 240 (2009) 108–116. doi:10.1016/j.desal.2007.10.091.
- [148] C. Cojocar, G. Zakrzewska-Trznadel, A. Miskiewicz, Removal of cobalt ions from aqueous solutions by polymer assisted ultrafiltration using experimental design approach Part 2: Optimization of hydrodynamic conditions for a crossflow ultrafiltration module with rotating part, *Journal of Hazardous Materials*. 169 (2009) 610–620. doi:10.1016/j.jhazmat.2009.03.148.
- [149] R. Bouzerar, Local permeate flux-shear-pressure relationships in a rotating disk microfiltration module: implications for global performance, *Journal of Membrane Science*. 170 (2000) 127–141. doi:10.1016/S0376-7388(99)00348-8.
- [150] M.C. Porter, Concentration Polarization with Membrane Ultrafiltration, *Ind. Eng. Chem. Prod. Res. Dev.* 11 (1972) 234–248. doi:10.1021/i360043a002.
- [151] S. Chandrasekhar, The Stability of Spiral Flow Between Rotating Cylinders, *Proceedings of the Royal Society of London a: Mathematical, Physical and Engineering Sciences*. 265 (1962) 188–197. doi:10.1098/rspa.1962.0003.
- [152] Jakob Murkes, Claes-Göran Carlsson, *Crossflow filtration: theory and practice* (1988), Wiley, New York, USA, ISBN: 0471920975, 133p.
- [153] D. Cébron, P. Maubert, M. Le Bars, Tidal instability in a rotating and differentially heated ellipsoidal shell, *Geophys. J. Int.* 182 (2010) 1311–1318. doi:10.1111/j.1365-246X.2010.04712.x.
- [154] S. Rosenblat, Flow between torsionally oscillating disks, *Journal of Fluid Mechanics*. 8 (1960) 388–399. doi:10.1017/S0022112060000682.
- [155] C.S. Slater, M.J. Savelski, P. Kostetsky, M. Johnson, Shear-enhanced microfiltration of microalgae in a vibrating membrane module, *Clean Techn Environ Policy*. (2015) 1–13. doi:10.1007/s10098-015-0907-z.
- [156] U.T. Bödewadt, Die Drehströmung über festem Grunde, *ZAMM - Journal of Applied Mathematics and Mechanics / Zeitschrift Für Angewandte Mathematik Und Mechanik*. 20 (1940) 241–253. doi:10.1002/zamm.19400200502.
- [157] J.W. Daily, R.E. Nece, Chamber Dimension Effects on Induced Flow and Frictional Resistance of Enclosed Rotating Disks, *J. Basic Eng.* 82 (1960) 217–230. doi:10.1115/1.3662532.
- [158] Herrmann Schlichting, Klaus Gersten, *Boundary layer theory* (2000), 6th edition, Springer, Berlin, Germany, ISBN: 3-540-66270-7
- [159] E. Hoek, A.S. Kim, Influence of crossflow membrane filter geometry and shear rate on colloidal fouling in reverse osmosis and nanofiltration separations, *Environmental Engineering* 19 (2002) 357–372. doi:10.1089/109287502320963364.

Reference

- [160] R.J. Adrian, Bibliography of Particle Image Velocimetry Using Imaging Methods: 1917–1995, Symposium 25 Years of Particle Image Velocimetry in Aerodynamics, Institute of Aerodynamics and Flow Technology, Göttingen, September 23 - 25 (2009).
- [161] R.J. Adrian, J. Westerweel, Particle Image Velocimetry (Cambridge Aerospace Series) (2010), 1st ed., Cambridge University Press, ISBN: 978-0-521-44008-0, 535p.
- [162] R.J. Adrian, Twenty years of particle image velocimetry, Experiments in Fluids, August 2005, Volume 39, Issue 2, pp 159–169.
- [163] A.K. Prasad, Particle Image Velocimetry. Current Science-Bangalore, 79, 51-60. (2000).
- [164] Markus Raffel, Christian E. Willert, Steven T. Wereley, Jürgen Kompenhans, Particle Image Velocimetry: A Practical Guide, Springer (2007), Germany, ISBN: 9783662036372, 236p.
- [165] DX Li, Q Zhong, MZ Yu, X Wang, Large-scale particle tracking velocimetry with multi-channel CCD cameras, International Journal of Sediment Research. 28 (2013) 103–110. doi:10.1016/S1001-6279(13)60022-0.
- [166] S. Fu, P.H. Biwole, C. Mathis, Particle Tracking Velocimetry for indoor airflow field: A review, Building and Environment. 87 (2015) 34–44. doi:10.1016/j.buildenv.2015.01.014.
- [167] N. Kasagi, K. Nishino, Probing turbulence with three-dimensional particle-tracking velocimetry, Experimental Thermal and Fluid Science. 4 (1991) 601–612. doi:10.1016/0894-1777(91)90039-T.
- [168] C.P. Gendrich, M.M. Koochesfahani, D.G. Nocera, Molecular tagging velocimetry and other novel applications of a new phosphorescent supramolecule, Exp Fluids. 23 (1997) 361–372. doi:10.1007/s003480050123.
- [169] A. Cenedese, G. Doglia, G.P. Romano, G. De Michele, G. Tanzini, LDA and PIV velocity measurements in free jets, Experimental Thermal and Fluid Science. 9 (1994) 125–134. doi:10.1016/0894-1777(94)90105-8.
- [170] Drain, Leslie-E, The laser Doppler techniques (1980), Wiley, Chichester, ISBN: 0-471-27627-8, 241p.
- [171] J. Kilander, A. Rasmuson, Energy dissipation and macro instabilities in a stirred square tank investigated using an LE PIV approach and LDA measurements, Chemical Engineering Science. 60 (2005) 6844–6856. doi:10.1016/j.ces.2005.02.076.
- [172] H. Takagi, S. Shimada, T. Miwa, S. Kudo, R. Sanders, K. Matsuuchi, Unsteady hydrodynamic forces acting on a hand and its flow field during sculling motion, Human Movement Science. 38 IS - (2014) 133–142.
- [173] H. Takagi, M. Nakashima, T. Ozaki, K. Matsuuchi, Unsteady hydrodynamic forces acting on a robotic arm and its flow field: Application to the crawl stroke, Journal of Biomechanics. 47 (2014) 1401–1408. doi:10.1016/j.jbiomech.2014.01.046.
- [174] J. Günther, D. Hobbs, C. Albasi, C. Lafforgue, A. Cockx, P. Schmitz, Modeling the effect of packing density on filtration performances in hollow fiber microfiltration module: A spatial study of cake growth, Journal of Membrane Science. 389 (2012) 126–136. doi:10.1016/j.memsci.2011.10.055.
- [175] L. Oxarango, P. Schmitz, M. Quintard, Laminar flow in channels with wall suction

Reference

- or injection: a new model to study multi-channel filtration systems, *Chemical Engineering Science*. 59 (2004) 1039–1051. doi:10.1016/j.ces.2003.10.027.
- [176] M. Linkès, P. Fede, J. Morchain, P. Schmitz, Numerical investigation of subgrid mixing effects on the calculation of biological reaction rates, *Chemical Engineering Science*. 116 (2014) 473–485. doi:10.1016/j.ces.2014.05.005.
- [177] R.L. David, *CRC Handbook of Chemistry and Physics* (2005), CRC Press, Internet Version 2005, ISBN-13: 978-0849304842, 2616p.
- [178] H. Scott Fogler, *Elements of chemical reaction engineering*, *Chemical Engineering Science*. 42 (1987) 2493. doi:10.1016/0009-2509(87)80130-6.
- [179] J. Villiermaux, *Génie de la réaction chimique: conception et fonctionnement des réacteurs* (1982), Lavoisier, Technique et Documentation, Paris, ISBN: 2852067595, 448p.
- [180] J.H. Ham, B. Platzer, Semi-Empirical Equations for the Residence Time Distributions in Disperse Systems – Part 1: Continuous Phase, *Chemical Engineering & Technology*. 27 (2004) 1172–1178. doi:10.1002/ceat.200407038.
- [181] D. Bošković, S. Loebbecke, G.A. Gross, J.M. Koehler, Residence Time Distribution Studies in Microfluidic Mixing Structures, *Chemical Engineering & Technology*. 34 (2011) 361–370. doi:10.1002/ceat.201000352.
- [182] J. Thereska. L'application des radiotraceur dans les unités industrielles : bilan et perspectives ». *Traceurs et Méthodes de Tracage. Recents Progres en Genie des Procèdes* (Ed. SFGP, Nancy, France) (1998), ISBN : 2-910239-37-7, 61 (12), 1-8.
- [183] L. Fillaudeau, *Chauffage des fluides agroalimentaires par effet Joule direct: conductivité électrique et expressions analytiques des profils de température* (2004), *Industries Alimentaires Et Agricoles*.
- [184] J.P. Leclerc, D. Schweich, A. Bernard, C. Detrez, DTS : un logiciel d'aide à l'élaboration de modèles d'écoulement dans les réacteurs, *Rev. Inst. Fr. Pét.* 50 (1995) 641–656.
- [185] S.T. Wereley, R.M. Lueptow, Inertial particle motion in a Taylor Couette rotating filter, *Physics of Fluids*. 11 (1999) 325. doi:10.1063/1.869882.
- [186] S.T. Wereley, A. Akonur, R.M. Lueptow, Particle–fluid velocities and fouling in rotating filtration of a suspension, *Journal of Membrane Science*. 209 (2002) 469–484. doi:10.1016/S0376-7388(02)00365-4.
- [187] M. Rudolph, T. Shinbrot, R.M. Lueptow, A model of mixing and transport in wavy Taylor-Couette flow, *Physica D: Nonlinear Phenomena*. 121 (1998) 163–174. doi:10.1016/S0167-2789(98)00149-3.
- [188] A. Figueredo Cardero, E. Chico, L. Castilho, R. de Andrade Medronho, Particle image velocimetry (PIV) study of rotating cylindrical filters for animal cell perfusion processes, *Biotechnology Progress*. 28 (2012) 1491–1498. doi:10.1002/btpr.1618.
- [189] T. Jiang, H. Zhang, F. Yang, D. Gao, H. Du, Relationships between mechanically induced hydrodynamics and membrane fouling in a novel rotating membrane bioreactor, *Desalination and Water Treatment*. 51 (2013) 2850–2861. doi:10.1080/19443994.2012.750794.
- [190] T. Jiang, H. Zhang, H. Qiang, F. Yang, X. Xu, H. Du, Start-up of the anammox process and membrane fouling analysis in a novel rotating membrane bioreactor,

Reference

- Desalination. 311 (2013) 46–53. doi:10.1016/j.desal.2012.10.031.
- [191] H. Zhang, J. Zhang, W. Jiang, F. Yang, H. Du, A new folded plate membrane module for hydrodynamic characteristics improvement and flux enhancement, *Separation and Purification Technology*. 154 IS - (2015) 36–43.
- [192] N. Dietrich, *Étude locale et expérimentale des Phénomènes interfaciaux* (2008), PhD thesis, INPL, Vandoeuvre-les-Nancy, 373p.
- [193] T. Jiang, H. Zhang, H. Qiang, F. Yang, X. Xu, H. Du, Start-up of the anammox process and membrane fouling analysis in a novel rotating membrane bioreactor, *Desalination*. 311 (2013) 46–53. doi:10.1016/j.desal.2012.10.031.
- [194] N. Liu, Q. Zhang, G.-L. Chin, E.-H. Ong, J. Lou, C.-W. Kang, et al., Experimental investigation of hydrodynamic behavior in a real membrane bio-reactor unit, *Journal of Membrane Science*. 353 (2010) 122–134. doi:10.1016/j.memsci.2010.02.042.
- [195] X. Mao, A.J. Jaworski, Application of particle image velocimetry measurement techniques to study turbulence characteristics of oscillatory flows around parallel-plate structures in thermoacoustic devices, *Meas. Sci. Technol.* 21 (2010) 035403–17. doi:10.1088/0957-0233/21/3/035403.
- [196] B.S. Hyun, R. Balachandar, K. Yu, V.C. Patel, Assessment of PIV to measure mean velocity and turbulence in open-channel flow, *Exp Fluids*. 35 (2003) 262–267. doi:10.1007/s00348-003-0652-7.
- [197] J. Moreau, A. Liné, Proper orthogonal decomposition for the study of hydrodynamics in a mixing tank, *AIChE Journal*. 52 (2006) 2651–2655. doi:10.1002/aic.10854.
- [198] Z. Doulgerakis, Large scale vortex and strain dynamics in mixing vessels and implications for macro-mixing enhancement (2010), PhD thesis, King’s College, University of London, UK.
- [199] Z. Doulgerakis, M. Yianneskis, A. Ducci, On the Manifestation and nature of macroinstabilities in stirred vessels, *AIChE Journal*. 57 (2011) 2941–2954. doi:10.1002/aic.12519.
- [200] A. Liné, Eigenvalue spectrum versus energy density spectrum in a mixing tank, *Chemical Engineering Research and Design*. 108 (2016) 13–22. doi:10.1016/j.cherd.2015.10.023.
- [201] A. Liné, J.C. Gabelle, J. Morchain, D. Anne-Archard, F. Augier, On POD analysis of PIV measurements applied to mixing in a stirred vessel with a shear thinning fluid, *Chemical Engineering Research and Design*. 91 (2013) 2073–2083.
- [202] L. Sirovich, Turbulence and the dynamics of coherent structures. I. Coherent structures, *Quarterly of Applied Mathematics*. (1987).
- [203] B. Knight, L. Sirovich, Kolmogorov inertial range for inhomogeneous turbulent flows, *Phys. Rev. Lett.* 65 (1990) 1356–1359. doi:10.1103/PhysRevLett.65.1356.
- [204] T. Arimitsu, N. Arimitsu, PDF of velocity fluctuation in turbulence by a statistics based on generalized entropy, *Physica a: Statistical Mechanics and Its Applications*. 305 (2002) 218–226. doi:10.1016/S0378-4371(01)00665-3.
- [205] W.T.M. Verkley, P. Lynch, W.T.M. Verkley, P. Lynch, Energy and Enstrophy Spectra of Geostrophic Turbulent Flows Derived from a Maximum Entropy Principle, website: [Http://Dx.Doi.org/10.1175/2009JAS2889.1](http://Dx.Doi.org/10.1175/2009JAS2889.1). 66 (2009) 2216–2236. doi:10.1175/2009JAS2889.1.
- [206] J.D. Stenson, Investigating the mechanical properties of yeast cells (2008), PhD

Reference

- thesis, Department of Chemical Engineering, University of Birmingham, UK, 253p.
- [207] S. Stolberg, K.E. McCloskey, Can shear stress direct stem cell fate? *Biotechnology Progress*. 25 (2009) 10–19. doi:10.1002/btpr.124.
- [208] Valentin Jossen, Ralf Pörtner, Stephan C. Kaiser, Matthias Kraume, Dieter Eibl and Regine Eibl, Mass Production of Mesenchymal Stem Cells — Impact of Bioreactor Design and Flow Conditions on Proliferation and Differentiation, in: *Cells and Biomaterials in Regenerative Medicine*, InTech, 2014. doi:10.5772/59385.
- [209] R. Eibl, D. Eibl, R. Pörtner, G. Catapano, P. Czermak, *Cell and Tissue Reaction Engineering (2009)*, Springer, Berlin, Heidelberg. ISBN: 978-3-540-68175-5, 363p.
- [210] Bruce J Berne; Robert Pecora, *Dynamic light scattering : with applications to chemistry, biology, and physics (2000)*, Wiley, New York, ISBN: 9780486320243, 376p.
- [211] S. Bhattacharjee, DLS and zeta potential – What they are and what they are not? *Journal of Controlled Release*. 235 (2016) 337–351. doi:10.1016/j.jconrel.2016.06.017.
- [212] Lawrence K Wang; J H Tay; V Ivanov; Y -T Hung, *Environmental Biotechnology (2010)*, Spinger, ISBN: 9781603271400, 988p.
- [213] R.M. Walsh, P.A. Martin, Growth of *saccharomyces cerevisiae* and *saccharomyces uvarum* in a temperature gradient incubator, *Journal of the Institute of Brewing*. 83 (1977) 169–172. doi:10.1002/j.2050-0416.1977.tb06813.x.
- [214] A. Ducci, Z. Doulgerakis, M. Yianneskis, Decomposition of Flow Structures in Stirred Reactors and Implications for Mixing Enhancement, *Ind. Eng. Chem. Res*. 47 (2008) 3664–3676. doi:10.1021/ie070905m.
- [215] J.C. Gabelle, J. Morchain, D. Anne-Archard, F. Augier, A. Liné, Experimental determination of the shear rate in a stirred tank with a non-newtonian fluid: Carbopol, *AIChE Journal*. 59 (2013) 2251–2266. doi:10.1002/aic.13973.
- [216] B. Van Bergen, *The effect of mechanical shear on brewing yeast (2001)*, National Library of Canada, Ottawa, ISBN: 0612753506, 184p.
- [217] W. Ying, F. Yang, A. Bick, G. Oron, M. Herzberg, Extracellular Polymeric Substances (EPS) in a Hybrid Growth Membrane Bioreactor (HG-MBR): Viscoelastic and Adherence Characteristics, *Environ. Sci. Technol*. 44 (2010) 8636–8643. doi:10.1021/es102309y.
- [218] L.-L. Wang, L.-F. Wang, X.-M. Ren, X.-D. Ye, W.-W. Li, S.-J. Yuan, et al., pH Dependence of Structure and Surface Properties of Microbial EPS, *Environ. Sci. Technol*. 46 (2012) 737–744. doi:10.1021/es203540w.

Annexes

Annexes

Table.A 1 Specification of the existing industrial DF filters

Technology			Manufacturer	Model	Geometry	
Membrane movement	Mechanical movement	Shape of membrane			Membrane/ disk diameter (mm)	Filtration area (m ²)
Mobile membrane	Rotating	Disk	Spintek, Huntington Beach, CA, USA	Spintek ST II	Module Spintek ST II 25: 25 disks, maximum filtration area 2,3m ² , d=0,34m	500(cm ²)-2.3
			ANDRITZ KMPT (Vierkirchen, Germany), membrane supplier: KERAFOL	DCF (Dynamic membrane filtration)	1-do 374 mm / di 91 mm surface 0,20 m ²	0,03-32, (typical 8/10/16/32m ² in total)
					2-do 152 mm / di 25,5 mm surface 360 cm ²	
					3-do 312 mm / di 91 mm surface 0,14 m ²	
			Diva Envitec Pvt. Ltd., India	MSDF (modular spin disk filtration)	312mm, thickness 6mm, membrane surface 0.14m ² , diameter can be up to 500 mm +	25 m ² / per vessel
			Fraunhofer IGB, Germany, membrane supplier: KERAFOL	Rotating disk filter	/	/
			Westfalia Separator, Aalen, Germany	MSD (Multi Shafts disks)	312	80
			Mio Vigneto Products (Automatic Filter System)	Rocket M7	35 disk	7
				Rocket M7+7	70 disk	14
			Hitachi, Japan	AQUA UFO		100
		Novoflow (Oberndorf, Germany)	SSDF (Single Shaft Disk Filter) -1-312	312/374	1	
			SSDF-2-312	312/374	2	
			CRD 0.1 lab /0.5 lab (Compact rotating disk filters)	152	0.1/0.5	
		SpinTek, Los Alamitos, CA	High shear rotary membrane system (HSR-MS)	267 mm outer diameter (OD), 25.5 mm inner diameter (ID)	Usable membrane 0.08	
		HUBER (Berching, Germany), Vacuum Rotation Membrane VRM@ Bioreactor	VRM 20	Rotating plate: approx. 2.3 m	900	
			VRM 30	Rotating plate: approx.3.2 m	3840	
		Rectangular arms	Gurpreet Engineering Works, Kanpur, UP (India)	SBM (Spinning basket membrane)	4 membranes (or more)	Each of dimension 65 × 145 mm ² with an effective area of 55 × 130 mm ²
	Helical	Dalian University of Technology		Two pieces of the filter sheets (length × width × thickness at 300 mm × 30 mm × 2 mm)	Total area 0.018	
	Cylinder	Hemascience, Santa Ana, CA, USA	Plasmacell filter	26.8	58(cm ²)	
		Suker AG, Winterthur, Switzerland	Biodruck-filter (BDF-01)		0,04	
Vibrating	Disk	New Logic, CA, USA	VSEP series L	270 od, 9.4 id	503 cm ²	
		Pall Corp., USA, VMF (Vibrating Membrane Filtration)	VMF-PALLsep PS 50	600	3-37 depends on installed area	
			VMF-PALLsep PS 10	270	0,1-1 depends on installed area	
			VMF-PALLsep PS 400	610	40	

Annexes

		Rectangular sheet	Chemical and Biochemical Engineering Department, Western University, London, Ontario, Canada		68 × 89	68 × 89		
		Hollow fiber	CAPEC, Department of Chemical Engineering, Technical University of Denmark	HF membrane filter	120 (long)	Module 1:256 cm ² Module 2: 488 cm ²		
UNESCO Centre for Membrane Science & Technology, The University of New South Wales, Sydney, Australia			40 (long)					
Zhejiang University of Technology	Pendulum type oscillation (PTO)			Effective membrane area of 0.2 m ²				
Stationary membrane	Rotating	Disk membrane+ mixer	Pall Corp., USA, DMF (dynamic membrane filter)	DMF LAB6 system	6 inches (15.24cm)	0,0137 m ² /mb		
			University of Technology of Compiegne	Rotating disk module (RDM)	RDM-1,154 mm housing,150 mm disk			
					RDM-2,154 mm housing,145 mm disk			
			Bokela GmbH, Karlsruhe, Germany	DYNO	137-850	0.13-12		
			Metso-Paper, Finland (ex- Raisio-Flootek, Finland ex- ABB Flootek, Sweden)	Optifilter CR (Cross Rotational) Filter, CR 200/1	200	0,027m ² /mb		
				CR250/2	250	0.045m ² /mb (0,18m ²)		
				CR500/5	500	0,175m ² /mb (1,75m ²)		
				CR550 / 15 to 30	550	7.5-15		
				CR500/100(CROT)	500	0,20m ² /mb(20m ²)		
				CR 1000/ 26 to 60	1000	0,67m ² /mb (35-84m ²)		
				CR 1000/10	1000	0,675m ² /mb(13,5m ²)		
			CR 1010/70 to 100	1000+	0,7m ² /mb (98-140m ²)			
			Grundfos BioBooster (Bjerringbro, Denmark)	Rotating cross-flow (RCF) MBR	312	0.12		
			RVF Filtration, Paris, France	Rotating and Vibrating Filtration System (RVF)	Dimension in mm: length 1850, width 1460, height 1730			
				RVF5-FD-C				
				RVF5-E-C	Dimension in mm: length 1850, width 1460, height 1450			
				RVF5-U-C	Dimension in mm: length 1600, width 1250, height 1650			
				RVF4-L-C	Dimension in mm: length 1350, width 550, height 1100			
				RVF-Lab scale in Lisbp	142	Total: 0.048 each membrane: 0.012		
			FMX (Anti-Fouling Membrane Filtration System), BKT water&energy	Standard class (FMX-S100)		95		
Economic class (FMX-E)		40						
	Controlled shear filtration (CSF)	90	51.5 cm ²					
	Miltenyi Biotec	Life 18 disk separator						

Table.A 2 Operating conditions of PIV (all experiments)

		Laminar (Breox)	Turbulent (Water)
Trigger	Horizontal	<p>A: $\mu=0.13$ Pa.s 8 slices (6 gap+2) $N= 2, 10$ Hz, $Q_f= 50, 100$ and 150 L/h</p> <p>B: $\mu=0.8$ Pa.s 8 slices (6 gap+2) $N=2, 10$ Hz, $Q_f= 25, 50$ L/h</p> <p>C: $\mu=0.8$ Pa.s 3 slices (gap) $N=0, 2, 10$ Hz, $Q_f= 50$ L/h (Additional tests with permeat flow) (Additional tests with 5, 15, 20 Hz)</p>	<p>$\mu=1$ mPa.s 8 slices (6 gap+2) $N= 10$ Hz, $Q_f= 50, 100$ and 150 L/h</p>
	Vertical	<p>$\mu=0.8$ Pa.s 4 slices (R=30, 45, 65 mm and radial vertical plane) $N= 0, 2, 10$ Hz, $Q_f= 50$ L/h</p>	<p>$\mu=1$ mPa.s 4 slices $N= 0, 2, 10, 25, 50$ Hz, $Q_f= 100$ L/h</p>
No Trigger	Horizontal	<p>$\mu=0.8$ Pa.s 3 slices (gap) $N= 0, 2, 10$ Hz, $Q_f= 50$ L/h (Additional tests with permeat flow) (Additional tests with 15, 20 Hz)</p>	<p>$\mu=1$ mPa.s 3 slices (gap) $N= 0, 2, 10, 25, 50$ Hz, $Q_f= 100$ L/h</p>
	Vertical	<p>$\mu=0.8$ Pa.s 4 slices (R=30, 45, 65 mm and radial vertical plane) $N= 0, 2, 10$ Hz, $Q_f= 50$ L/h</p>	<p>$\mu=1$ mPa.s 4 slices $N= 0, 2, 10, 25, 50$ Hz, $Q_f= 100$ L/h</p>

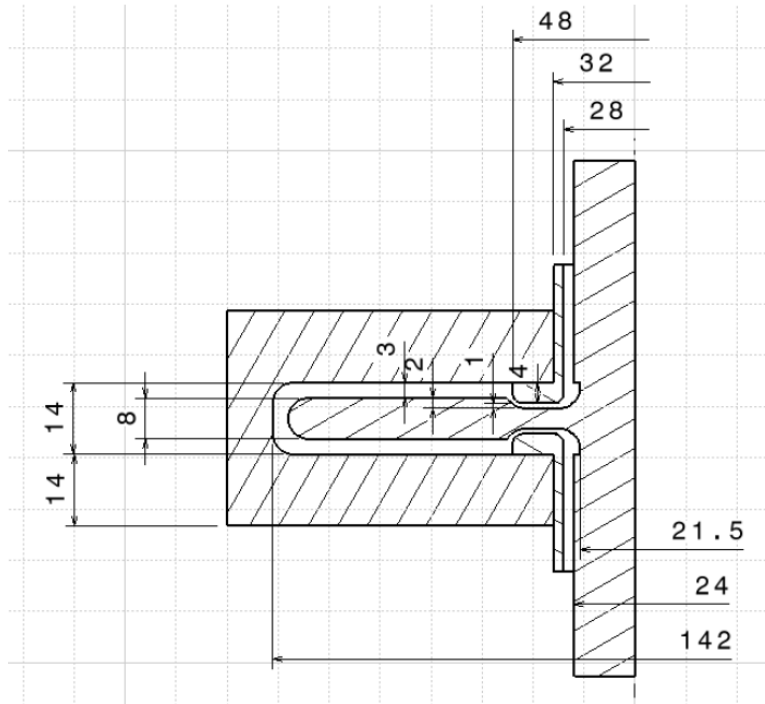


Fig.A 3 Technical design of the filtration cell (Unit: mm)

Supplementary information on fluid properties:

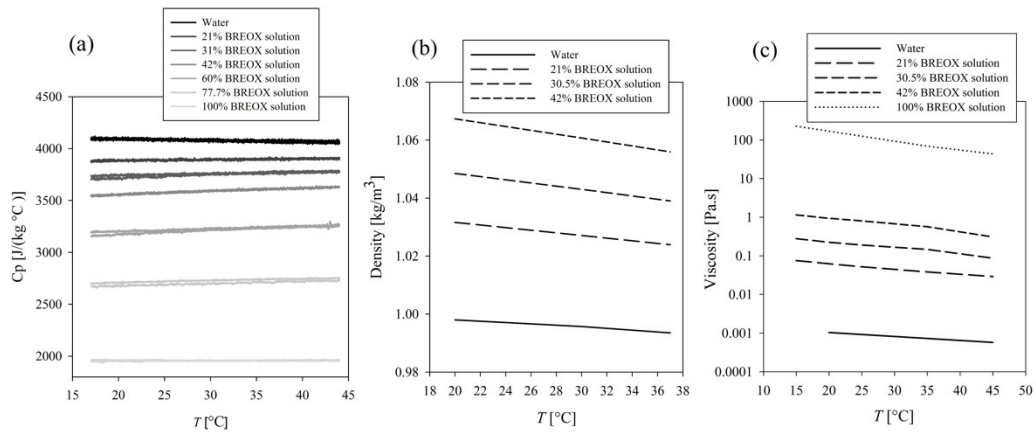


Fig.A 4 Heat capacity, density and viscosity of BREOX solution as a function of temperature (15 to 45°C) and max concentration (0 to 100%w/w)

Supplementary information of PIV experiments with trigger (laminar flow):

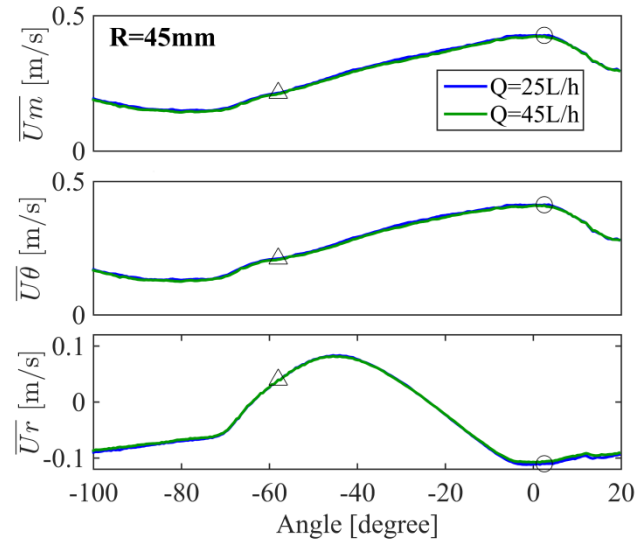


Fig.A 5 Comparison of velocity components with two flowrates Operating conditions: $Q_f= 25$ and 45 L/h, $N=2$ Hz; $\mu=0.81$ Pa·s and $T=20^\circ\text{C}$. Measurement position: $R=45$ mm, $z=2.25$ mm

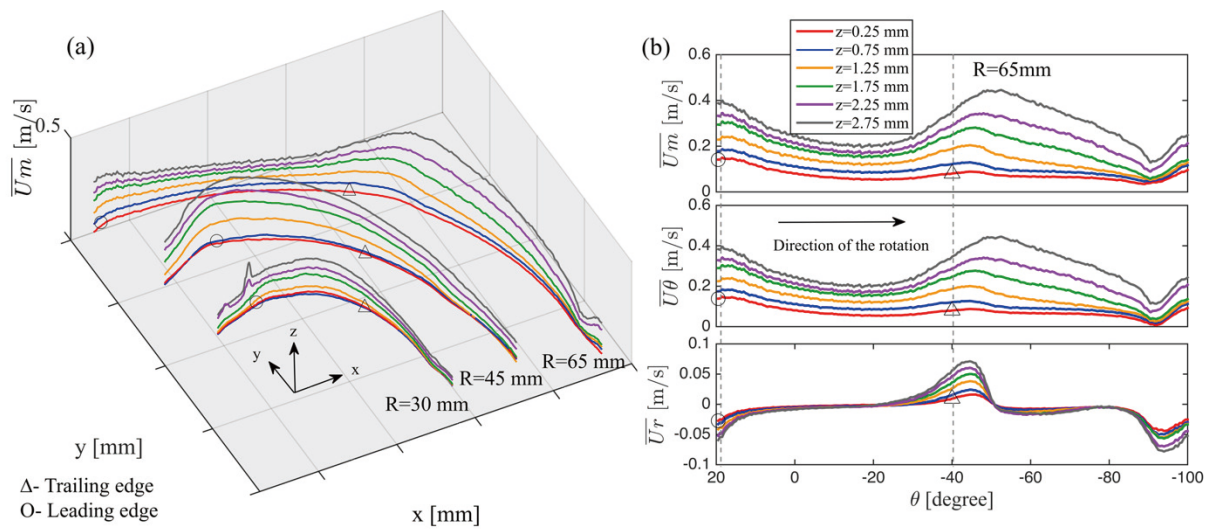


Fig.A 6 Evolution of mean velocity profiles \overline{U}_m and their radial and angular components \overline{U}_θ \overline{U}_r as a function of angular position for 6 horizontal planes (z_1 to z_6) within the membrane-impeller gap. (a): IDW mean velocity at $R= 30, 45$ and 65 mm; (b): mean, radial and angular velocity profiles, $\overline{U}_m, \overline{U}_\theta$ and \overline{U}_r , at $R=65$ mm. Operating conditions: $Q_f= 45$ L/h, $N=2$ Hz; $\mu=0.81$ Pa·s and $T=20^\circ\text{C}$. Symbols: O, leading edge and Δ , trailing edge of blade

Annexes

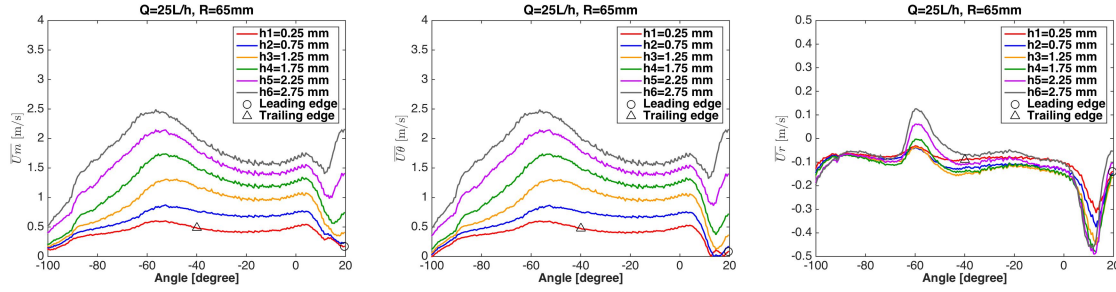


Fig.A 7 Evolution of mean velocity profiles \overline{U}_m and their radial and angular components \overline{U}_θ \overline{U}_r as a function of angular position for 6 horizontal planes (z_1 to z_6) within the membrane-impeller gap at $R=65$ mm. (a) \overline{U}_m , (b) \overline{U}_θ and (c) \overline{U}_r . Operating conditions: $Q_f= 25$ L/h, $N=10$ Hz; $\mu=0.81$ Pa·s and $T=20^\circ\text{C}$. Symbols: \circ , leading edge and \triangle , trailing edge of blade

Supplementary information of PIV experiments with trigger (turbulent flow):

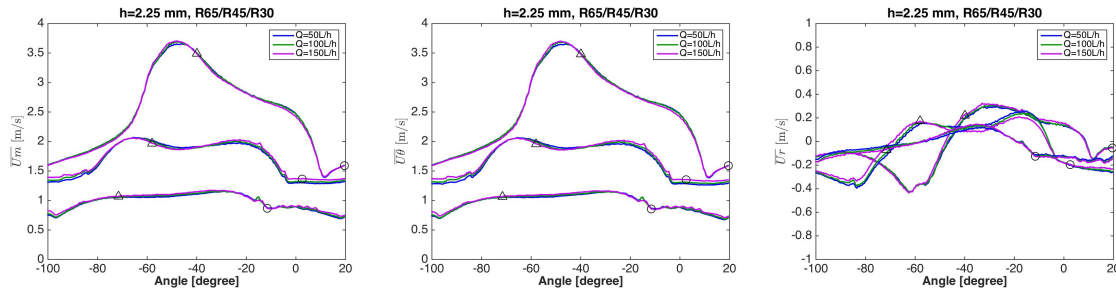


Fig.A 8 Evolution of mean velocity profiles \overline{U}_m and their radial and angular components \overline{U}_θ \overline{U}_r as a function of angular position for 3 flowrate ($z=2.25$ mm) within the membrane-impeller gap. (a) \overline{U}_m , (b) \overline{U}_θ and (c) \overline{U}_r . Operating conditions: $Q_f= 50, 100$ and 150 L/h, $N=10$ Hz; water, $\mu=1$ mPa·s and $T=20^\circ\text{C}$. Symbols: \circ , leading edge and \triangle , trailing edge of blade.

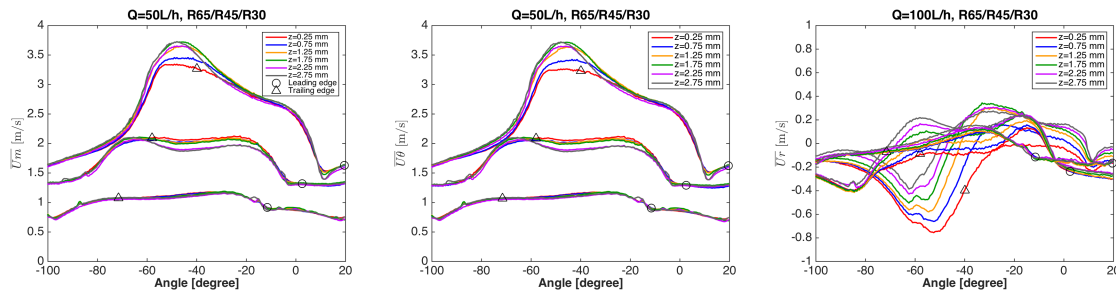


Fig.A 9 Evolution of mean velocity profiles \overline{U}_m and their radial and angular components \overline{U}_θ \overline{U}_r as a function of angular position for 3 flowrate (z_1 - z_6) within the membrane-impeller gap. (a) \overline{U}_m , (b) \overline{U}_θ and (c) \overline{U}_r . Operating conditions: $Q_f= 50, \text{ and } 150$ L/h, $N=10$ Hz; water, $\mu=1$ mPa·s and $T=20^\circ\text{C}$. Symbols: \circ , leading edge and \triangle , trailing edge of blade

Supplementary information of PIV experiments without trigger

Portrait of phase between coefficients of mode 2 versus given mode in *laminar flow*:

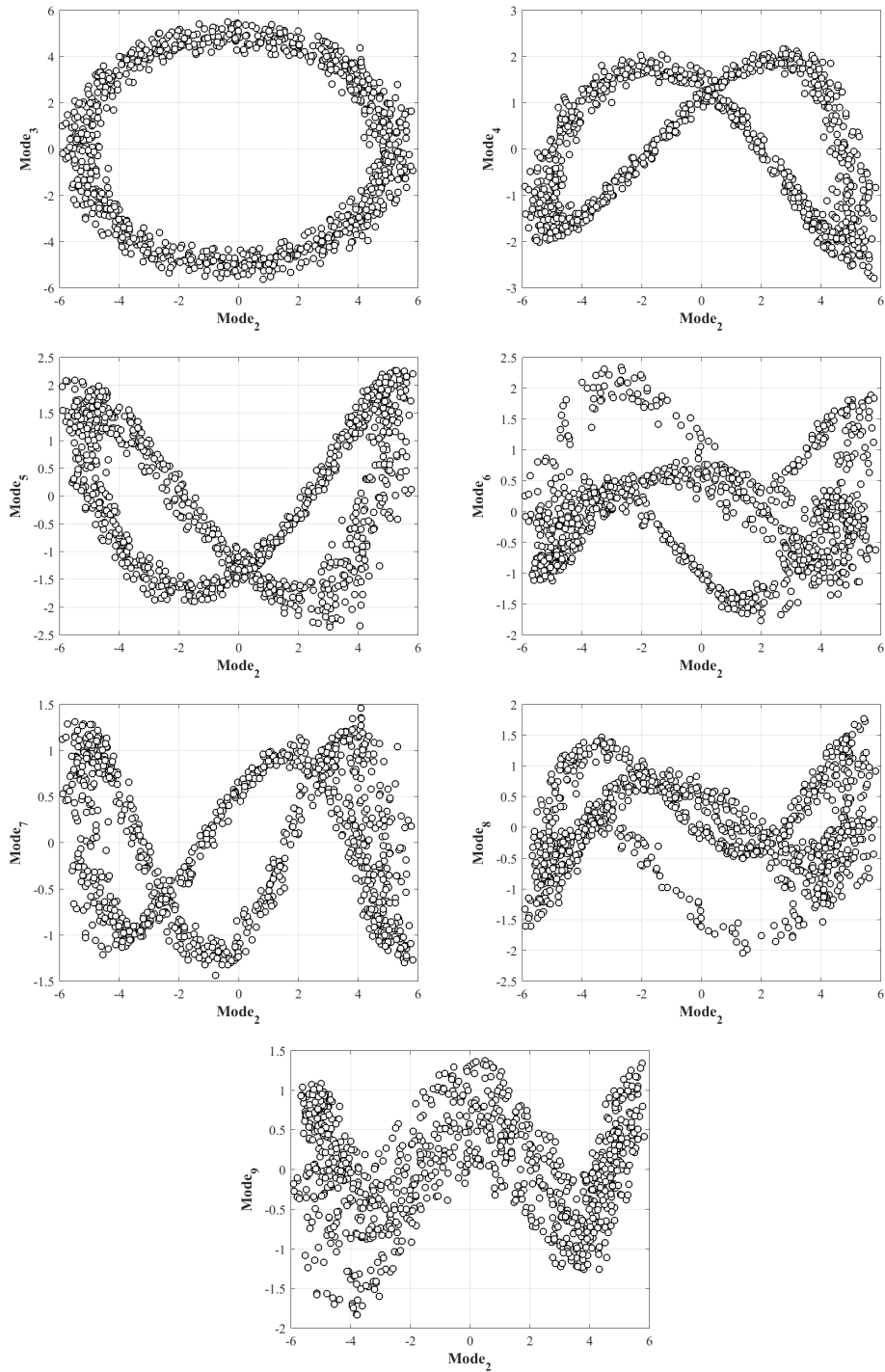


Fig.A 10 Portrait of phase between coefficients of mode 2 and the given modes. Operating conditions: horizontal measurement at plane $z_2=1.5$ mm, $Q_f= 50$ L/h, $N=2$ Hz, $Re_{mixing}=42$; BREOX solution, $\mu=0.85$ Pa·s and $T=20^\circ\text{C}$, data acquisition rate 7 Hz, 1000 pairs of images

Annexes

Portrait of phase between coefficients of mode 3 versus given mode in *laminar flow*:

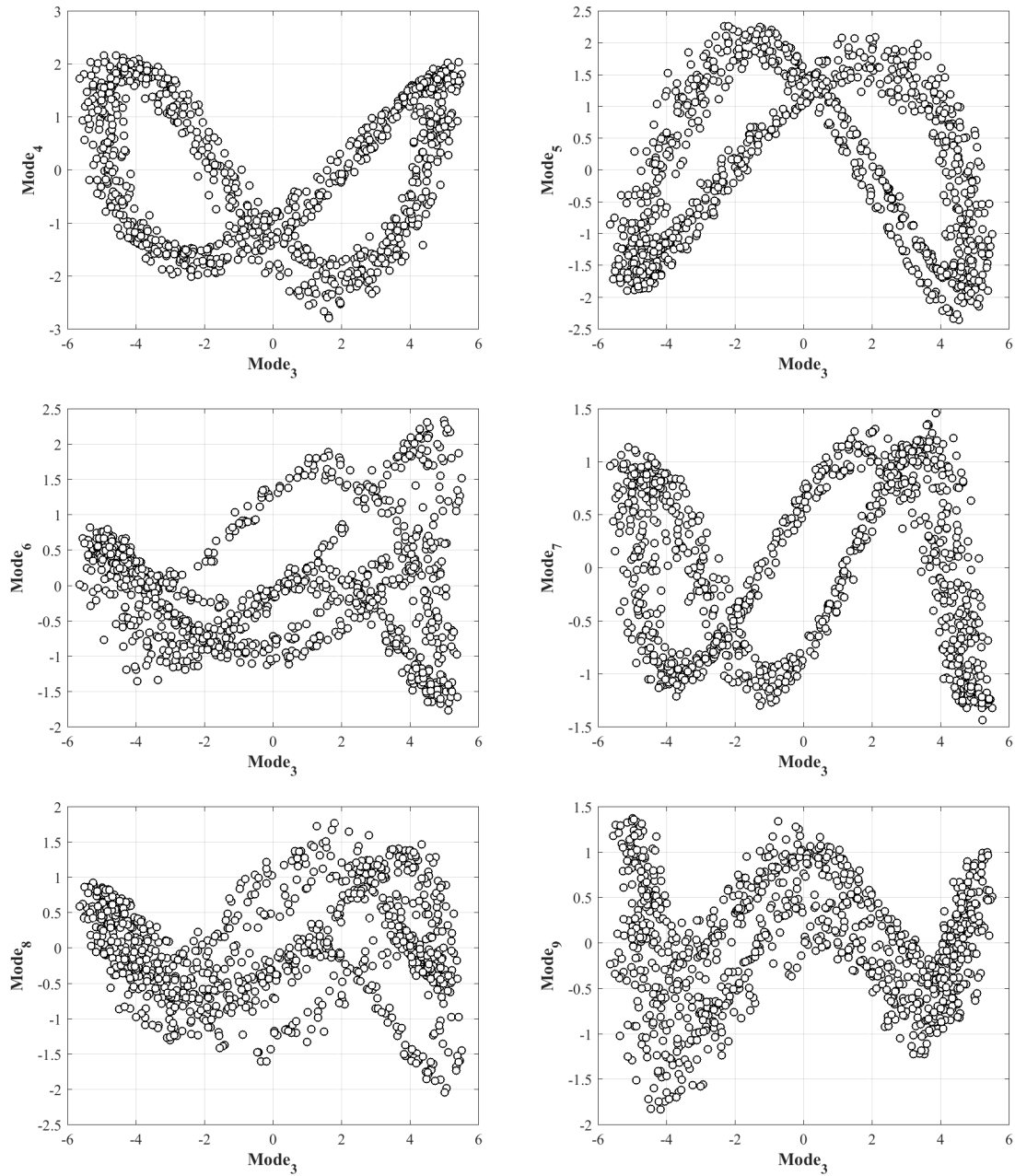


Fig.A 11 Portrait of phase between coefficients of mode 3 and the given modes. Operating conditions: horizontal measurement at plane $z_2=1.5$ mm, $Q_f=50$ L/h, $N=2$ Hz, $Re_{mixing}=42$; BREOX solution, $\mu=0.85$ Pa·s and $T=20^\circ\text{C}$, data acquisition rate 7 Hz, 1000 pairs of images

Portrait of phase between coefficients of mode 4 versus given mode in laminar flow:

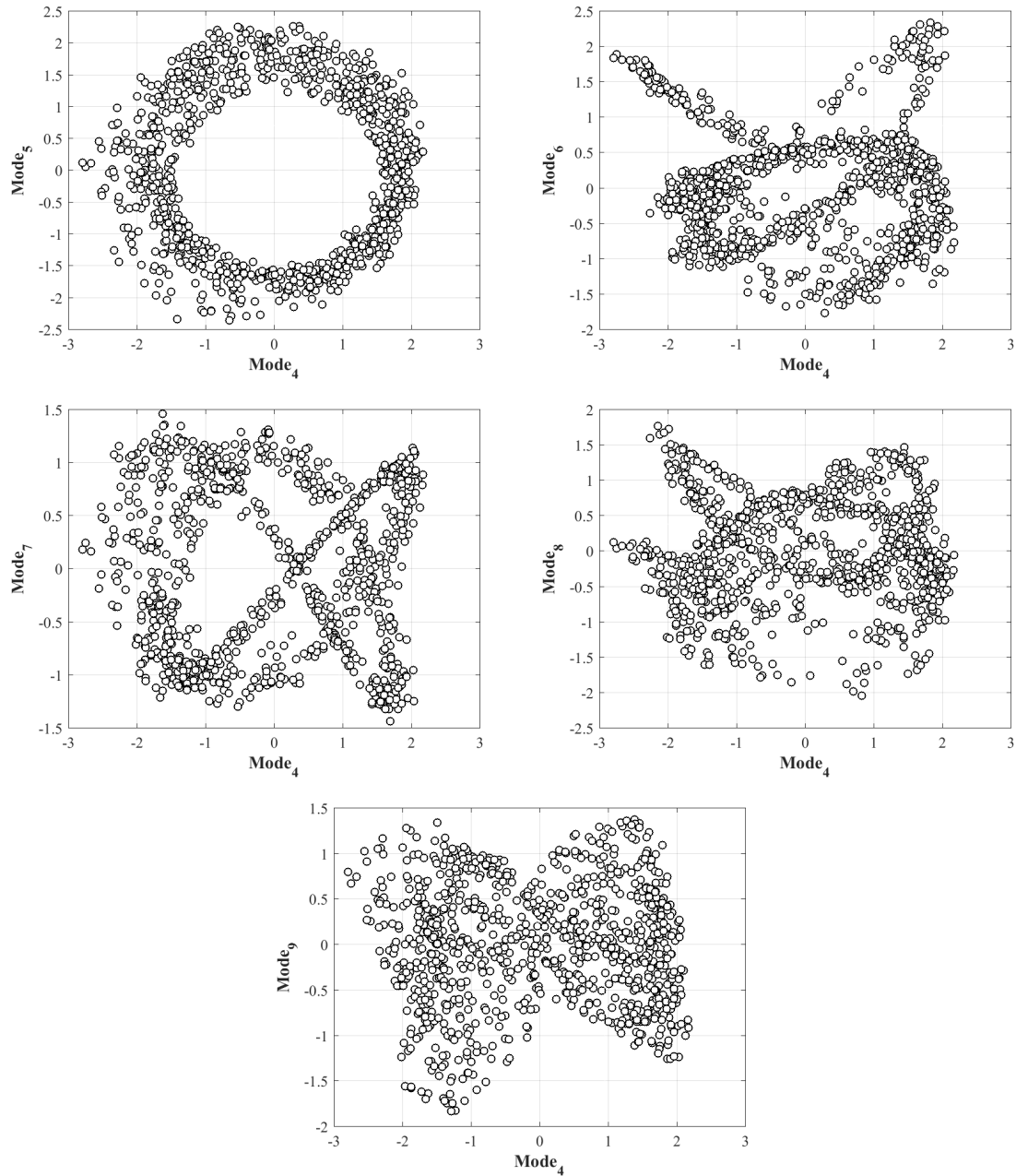


Fig.A 12 Portrait of phase between coefficients of mode 4 and the given modes. Operating conditions: horizontal measurement at plane $z_2=1.5$ mm, $Q_f= 50$ L/h, $N=2$ Hz, $Re_{mixing}=42$; BREOX solution, $\mu=0.85$ Pa·s and $T=20^\circ\text{C}$, data acquisition rate 7 Hz, 1000 pairs of images

Portrait of phase between coefficients of mode 5/6 versus given mode in laminar flow:

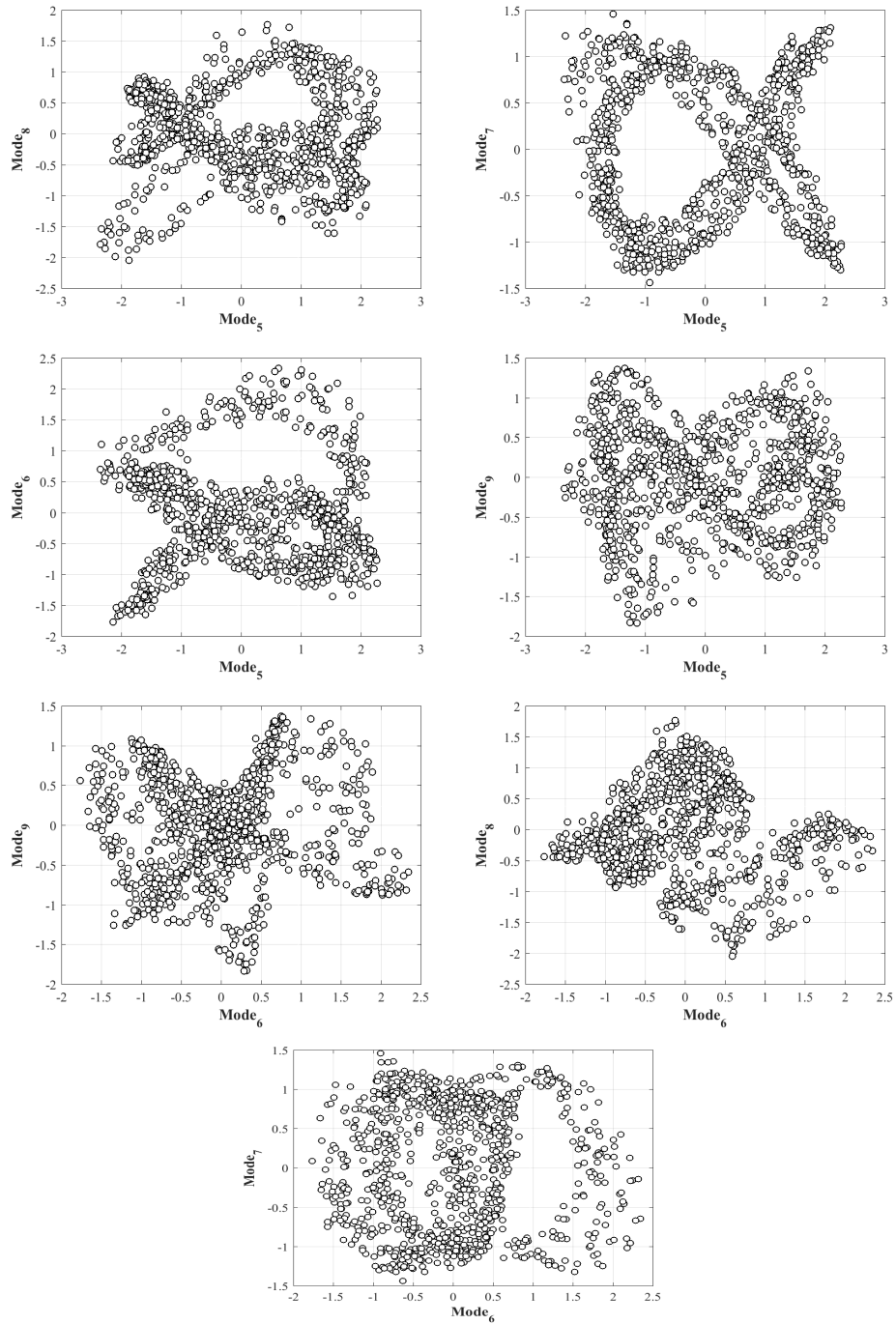


Fig.A 13 Portrait of phase between coefficients of the given modes. Operating conditions: horizontal measurement at plane $z_2=1.5$ mm, $Q_f= 50$ L/h, $N=2$ Hz, $Re_{mixing}=42$; BREOX solution, $\mu=0.85$ Pa·s and $T=20^\circ\text{C}$, data acquisition rate 7 Hz, 1000 pairs of images

Annexes

Reconstructed velocity field based on related organized motion in laminar flow:

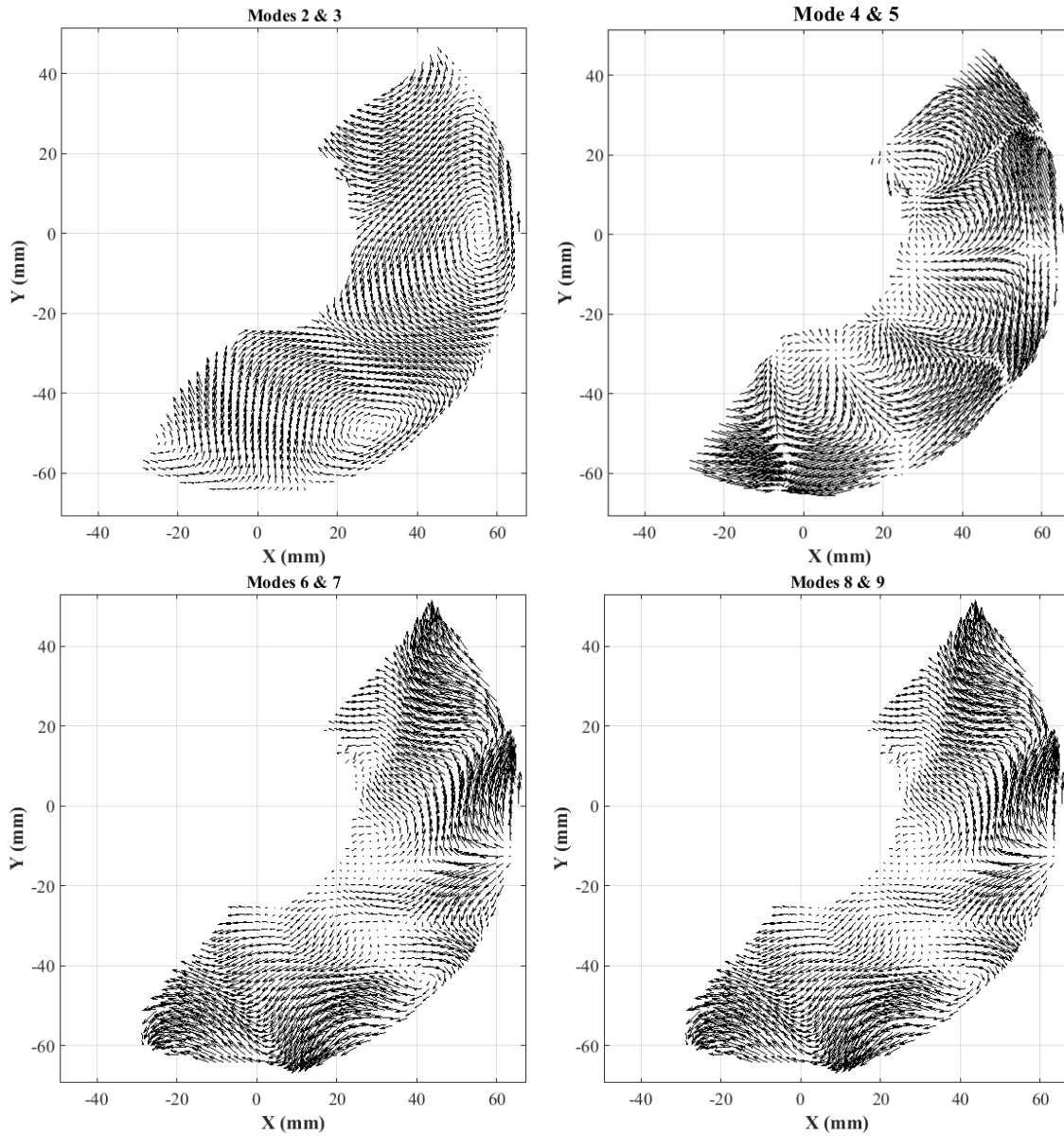


Fig.A 14 Reconstructed velocity field based on the related organized motions. Operating conditions of the raw data: horizontal measurement at plane $z_2=1.5$ mm, $Q_f= 50$ L/h, $N=2$ Hz, $Re_{mixing}=42$; BREOX solution, $\mu=0.85$ Pa·s and $T=20^\circ\text{C}$, data acquisition rate 7 Hz, 1000 pairs of images

Annexes

Portrait of phase between coefficients of mode 2 versus given mode in turbulent flow:

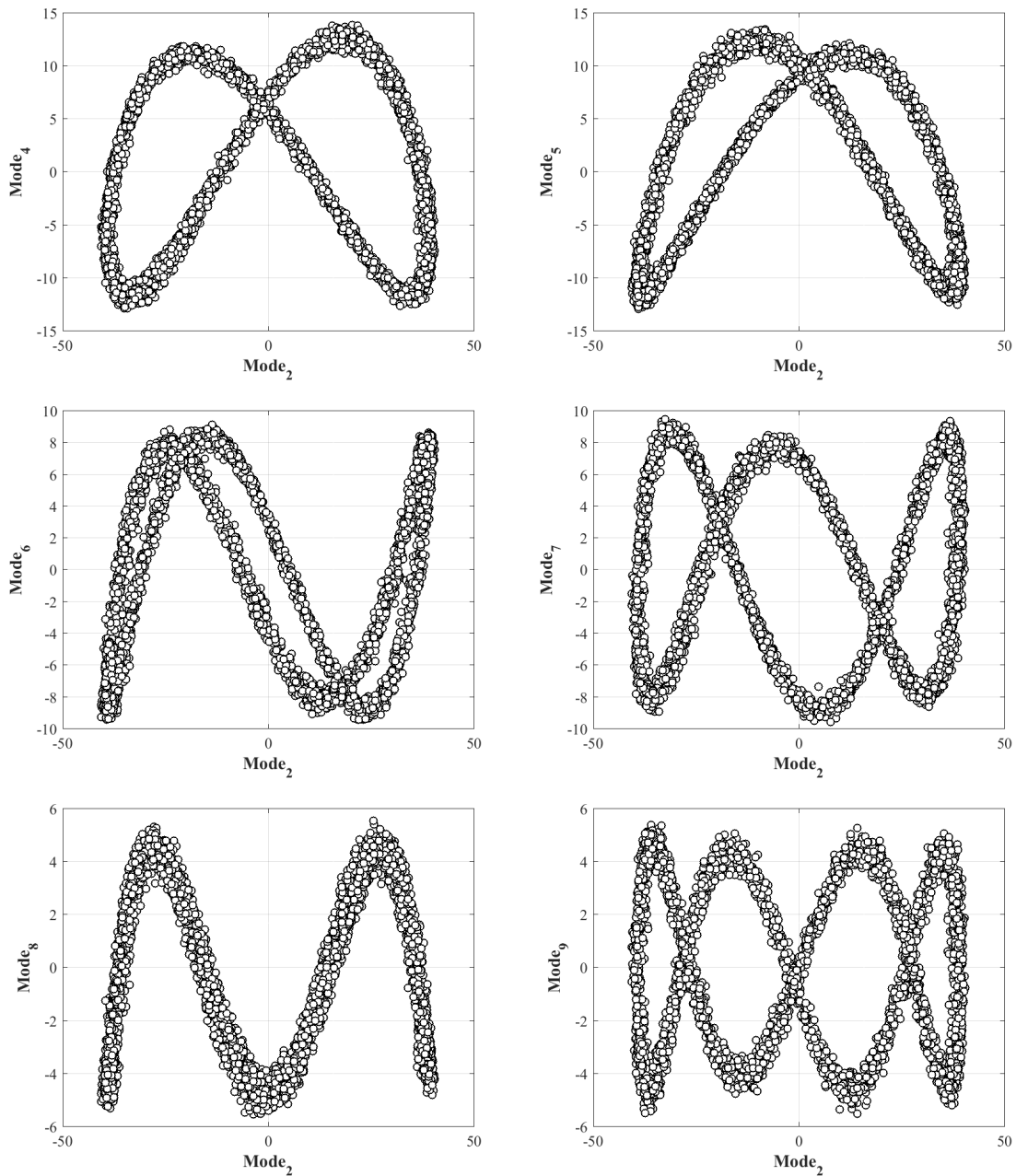


Fig.A 15 Portrait of phase between coefficients of given mode. Operating conditions: horizontal measurement plane $z_2=1.5$ mm, $Q_f=100$ L/h, $N=10$ Hz; water, $\mu=1$ mPa·s and $T=20^\circ\text{C}$, data acquisition rate 7 Hz, 3778 pairs of images

Annexes

Portrait of phase between coefficients of mode 3 versus given mode in turbulent flow:

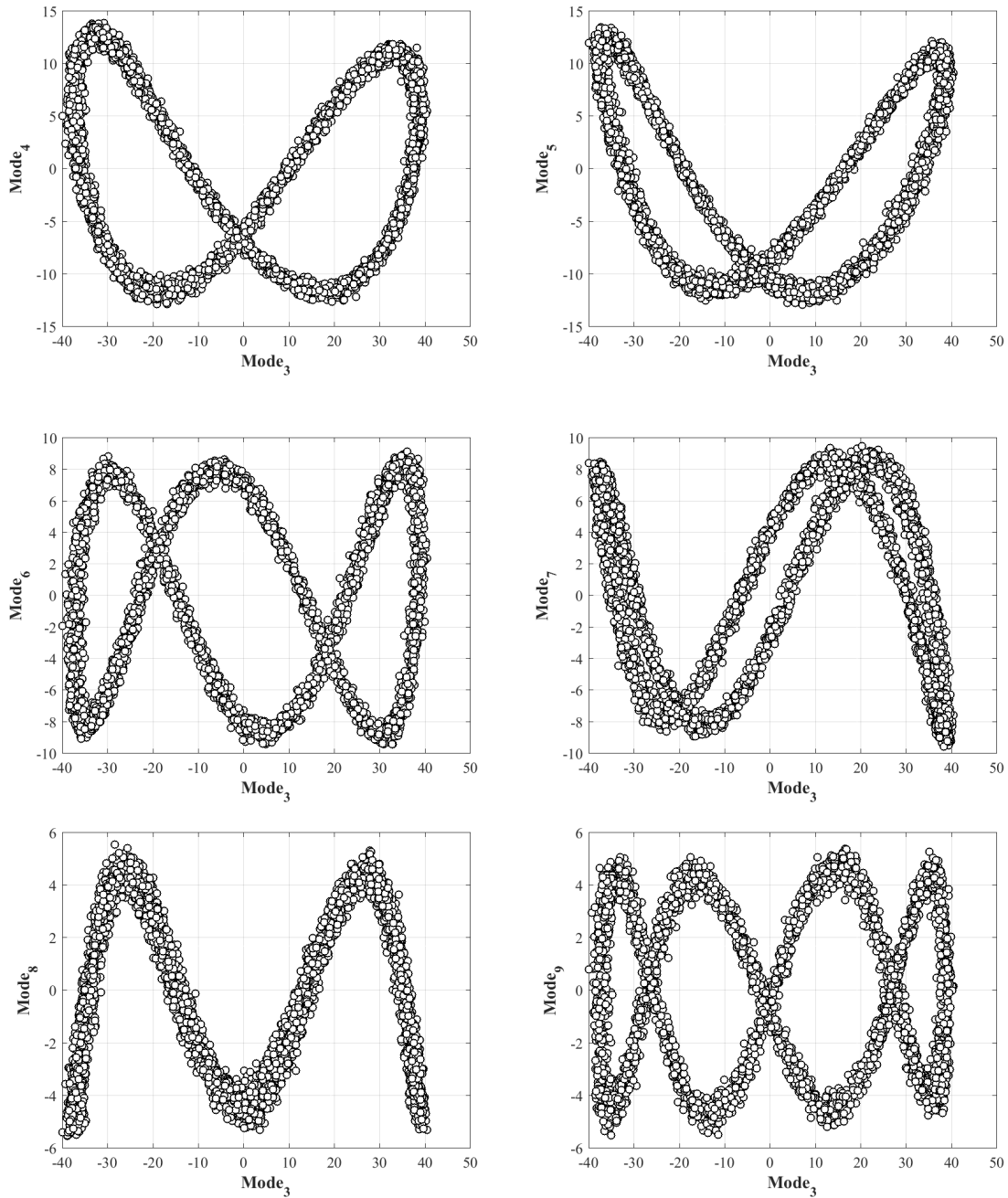


Fig.A 16 Portrait of phase between coefficients of given mode. Operating conditions: horizontal measurement plane $z_2=1.5$ mm, $Q_f=100$ L/h, $N=10$ Hz; water, $\mu=1$ mPa·s and $T=20^\circ\text{C}$, data acquisition rate 7 Hz, 3778 pairs of images

Annexes

Portrait of phase between coefficients of mode 4 versus given mode in turbulent flow:

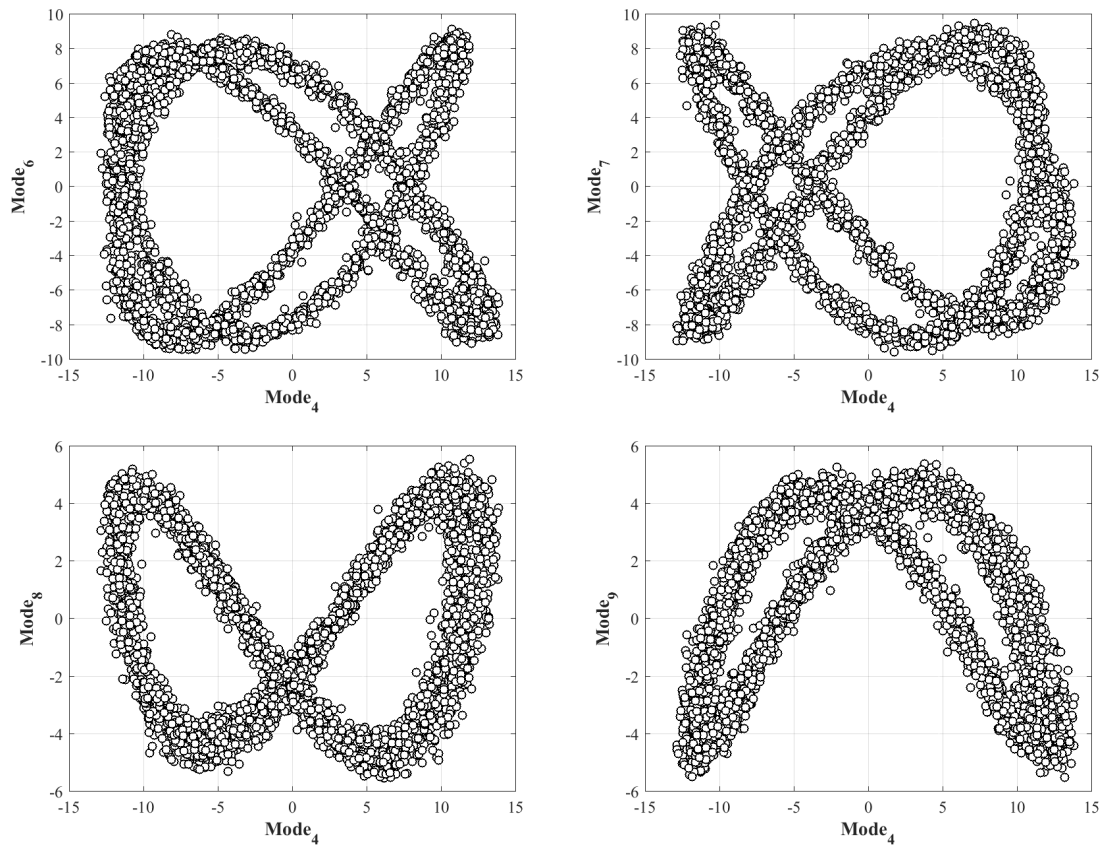


Fig.A 17 Portrait of phase between coefficients of given mode. Operating conditions: horizontal measurement plane $z_2=1.5$ mm, $Q_f=100$ L/h, $N=10$ Hz; water, $\mu=1$ mPa·s and $T=20^\circ\text{C}$, data acquisition rate 7 Hz, 3778 pairs of images

Portrait of phase between coefficients of mode 5/6 versus given mode in turbulent flow:

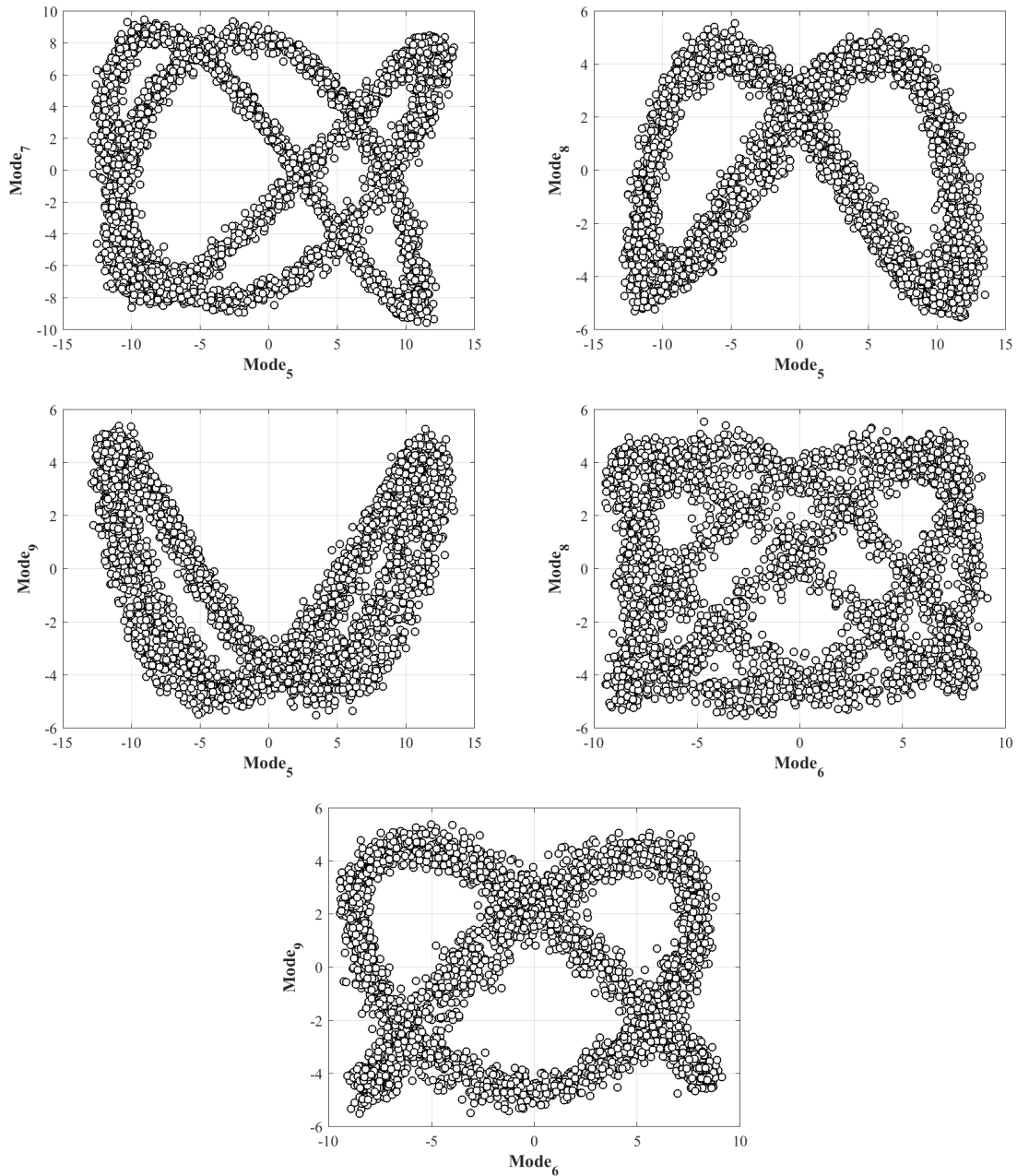


Fig.A 18 Portrait of phase between coefficients of given mode. Operating conditions: horizontal measurement plane $z_2=1.5$ mm, $Q_f=100$ L/h, $N=10$ Hz; water, $\mu=1$ mPa·s and $T=20^\circ\text{C}$, data acquisition rate 7 Hz, 3778 pairs of images

Annexes

Reconstructed velocity field based on related organized motion in turbulent flow:

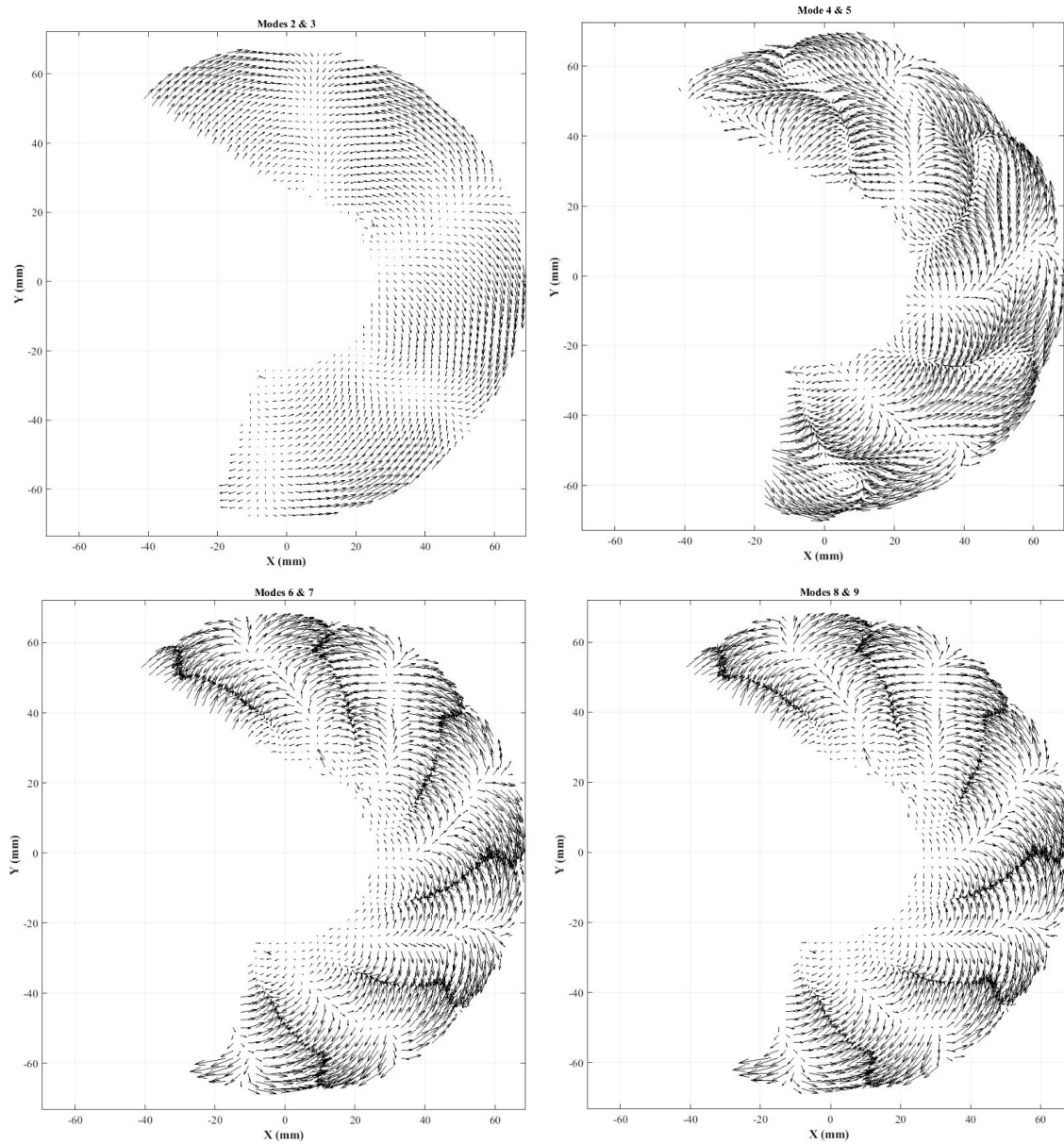


Fig.A 19 Reconstructed velocity field based on the related organized motions. Operating conditions of the raw data: horizontal measurement plane $z_2=1.5$ mm, $Q_f= 100$ L/h, $N=10$ Hz; water, $\mu=1$ mPa·s and $T=20^\circ\text{C}$, data acquisition rate 7 Hz, 3778 pairs of images

Extended Abstract

This PhD thesis focuses on the understanding and the control of dynamic interactions between physical and biological mechanisms considering an alternative membrane separation into industrial bioprocess. It aims to carry scientific knowledge related to the control of bioreaction considering complex hydrodynamics and retention-permeation locks specific to membrane separation.

A dynamic filtration technology, called rotating and vibrating filtration (RVF), was investigated in this study. It uses disc-shaped flat sheet membranes in the vicinity of the rotating bodies. These rotating bodies as well as the pulsating blows generate highly dynamic vortex movements of filtered liquid being in contact with the membrane surface resulting in high values of shear rates thus preventing any particles or molecules to accumulate on the surface of the membrane or to enter inside the pores. This work is motivated by several scientific and technical locks related to RVF module, which are: (1) to characterize and to quantify velocity fields, locally and instantaneously, (2) shear stresses at membrane surface linked to the operating conditions and the rheological evolution of the fluid.

Scientific questions:

Research was dedicated to a better understanding of the complex hydrodynamics within RVF module into bioprocess context. Several scientific questions were identified (mentioned in *Chapter I*):

- How global performances (power consumption, friction curve, heat dissipation, Residence Time Distribution) can be characterized and interpreted?
- How long will a cell suffer in such stressful environment?
- What will be the magnitude of this mechanical stress?
- Does it damage microbial cell population?
- What is the local flow pattern in the filtration cell? And how does it organize and structure in the filtration cell?
- Is it possible to identify local and instantaneous velocity and shear stress?
- Are experimental measurements and simulations consistent at global and local scales?

Résumé Étendu

Structure of this thesis:

To answer these questions, this thesis focuses on four major parts as the follows:

(1) Literature review: in the recent decades, many efforts and a great number of studies have been done to develop novel DF modules in lab and pilot scale. Reviewing the existing DF modules, they can be mainly classified by mobile and stationary membrane as well as rotating (disk, disk-like membrane, impeller, arms etc.) and vibrating (or oscillating) system.

(2) Global approach. investigation of Residence Time Distribution (RTD) and thermal balance has been carried out and compared to the previous global study (power consumption and friction curves).

(3) Local approach. As a major part in this PhD work, Particle Image Velocimetry (PIV) was carried out and compared to CFD simulation. PIV preliminary study was conducted with a trigger strategy to access through angle-resolved measurements to an averaged velocity field. Further study was performed with a non-trigger strategy and applied to POD analysis in order to identify the coherent structure of the flow by decomposing the mean contribution, the organized and turbulent fluctuations.

(4) Bioprocess application. In this part, an exploratory work to characterize the effect of Dynamic Filtration on prokaryote cell population (*Escherichia coli*) was carried out by quantifying cell integrity or damage as a function of time and rotation speed during filtration process in turbulent regime.

Main results:

To this end, experiments and numerical simulations have been performed to investigate the hydrodynamics at global and local scales under laminar and turbulent regimes with Newtonian fluids under biotic and abiotic conditions, result shows that:

(1) Thermal balance (heat dissipation) is highly correlated to mixing power (power consumption curve). The temperature increased dramatically at high rotation speed, especially in laminar flow (ex. +11°C under operating conditions $Q_f=25$ L/h and $N=25$ Hz). In turbulent flow, with $Q_f=50$ L/h and $N=50$ Hz, temperature increased up to 9°C. Considering a temperature increase limited to 4°C (compatible with cell culture), restricted operating conditions (minimum

Résumé Étendu

flowrate and maximum mixing rate) can be estimated from thermal balance and power consumption curve.

(3) In RTD study, results indicated that in laminar flow, mean residence time t_s remained constant at a given Q_f , whatever N was. Effective volume V_I was almost constant, slightly affected by flowrate, with a mean value at 1.3 L (87% out of the RVF total volume). In turbulent regime, t_s increased linearly as a function of N at a given Q_f . The effective volume V_I was only mixing rate dependent, whereas flowrate had no effect. The effective volume ranged from 1.1 up to 1.6 L (74 up to 100% out of the RVF total volume). Combining with the CFD simulations in laminar regime, it indicated that a short-cut and dead-zone might exist in the RVF module. Modeling of RTD by PFR+(J) CSTR model (effective volume V_I and $J=2.5\pm 0.6$) enabled to access to the mean residence time and its distribution for cells in a stressful environment.

(4) In the PIV experiments with optical trigger, results in laminar regime showed that velocity fields and their related profiles were well organized at different horizontal slices. A typical parabolic profile was observed and simulated in the vertical measurements, and shear stress field was established by CFD. In turbulent regime, velocities were highly uniform (bulk), and exhibited an almost linear profile along vertical direction.

(5) In PIV experiments without the optical trigger and applying POD analysis, important local parameters including velocity, shear stress (wall shear stress, mean viscous shear, fluctuating shear) and torque were investigated. It enabled to decompose the instantaneous velocity into mean flow (mode 1) and the fluctuations (including organized and turbulent contributions):

- In laminar regime (ex. $N=2$ Hz), the main contribution for the total torque was due to the upper and lower wall (40 % each), the lateral (external) wall contributing for 20%. Contribution of each mode to the total kinetic was discussed. Mode 1 represented the mean contribution (90% of the total kinetic energy). Organized motion was based on modes 2 to 5 (7-8% of the total kinetic energy), and the related RMS wall shear stress were shown to be quite important and up to 45% of the mean wall shear stress.
- In turbulent regime (ex. $N=10$ Hz), the lateral (external) wall shear stress with value 250 Pa contributed 90% of the total torque. Mode 1 represented the mean contribution (95% of the total kinetic energy). POD analysis showed that the organized

Résumé Étendu

fluctuations were based on the modes 2-9 (4.4-5.5% of the total kinetic energy), and their coherent structure were remarkably organized.

(6) Observation with prokaryote cell suspensions (*E.coli*) indicated that cells were damaged and disrupted under extrem conditions, $N=50$ Hz and $t=5$ h. Moreover, at $N=50$ Hz, clusters and agregates with disrupted cell were observed. This was not observed with prokaryote cells in food bioprocessing (brewing and wine making). Consequently, cell damage induced by mechanical stress needs to be further explored in the light of local and global hydrodynamics.

Highlight of this thesis:

These actions and related discoveries combined multi-scale and multidisciplinary approaches, which gave more information on the impact of DF on bioprocess, such as:

- thermal and mechanical effect on microbial cells;
- diagnosing the functioning of global flow behaviors, in order to apply better operating conditions, leading to optimize industrial processes, as well as the DF design;
- introducing the flow pattern and coherent structures, as well as giving support to better understand the mechanism of fouling removal by examining the local parameters including local velocity fields/profiles, local shear stress, fluctuations (organized motion and turbulence)

Perspectives:

Interactions between biological matrices and Dynamic Filtration must be deeply studied to intensify bioprocesses. Realizing the lack of knowledge on complex and evolving culture media (FCV, cell growth, bio-production), and (ii) intensification of microbial cultures under high cell density conditions (cellular activity and viability), future works related to dynamic filtration may be focused on:

- (8) the scientific and technical bottlenecks related to retention / permeation issues (catalytic biomass and physico-chemical components) associated with complex biological matrices;
- (9) interactions between matrices and membrane materials (nature, porosity and cut-off threshold);

Résumé Étendu

(10)the impact of the DF on the performances of prokaryote and eukaryote strains (biological activity, viability, cell lysis, etc.).

Scientific investigations may also include further works into hydrodynamics:

(11)other local techniques can be applied to investigate local parameters such as temperature to analyze local thermal effects coupled with internal age distribution;

(12)Electrochemical methods may be applied to quantify the instantaneous and local wall shear stress at membrane surface.

(13)experiments can be carried out with non-Newtonian fluids to explore shear thinning/thickening and/or visco-plastic behaviors in laminar and turbulent regimes;

(14)CFD simulations with more complex conditions (transitional and turbulent regimes with Newtonian and Non-Newtonian fluids) need to be explored and validated to design DF modules.

Résumé Étendu

Résumé Étendu

Cette thèse porte sur la compréhension et le contrôle des interactions dynamiques entre les mécanismes physiques et biologiques en considérant une séparation membranaire alternative dans les bioprocédés industriels. Il vise à apporter des connaissances scientifiques liées au contrôle de la bioréaction en considérant l'hydrodynamique complexe et le verrou rétention-perméation spécifiques à la séparation membranaire.

Une technologie de filtration dynamique, appelée filtration rotative et vibrante (RVF), a été étudiée dans cette étude. Il utilise des membranes planes en forme de disque au voisinage des corps rotatifs. Ces corps rotatifs génèrent des mouvements tourbillonnaires du liquide filtré en contact avec la surface de la membrane, ce qui entraîne des valeurs de cisaillement élevées empêchant ou limitant ainsi le colmatage surfacique et interne de la membrane par des particules ou des molécules. Ce travail est motivé par plusieurs verrous scientifiques et techniques liés au module RVF qui sont: (1) de caractériser et de quantifier localement et instantanément les champs de vitesse (2) d'évaluer les contraintes de cisaillement à la surface de la membrane en lien avec les conditions opératoires et l'évolution rhéologique du fluide et (iii) d'en évaluer l'impact sur une population microbienne.

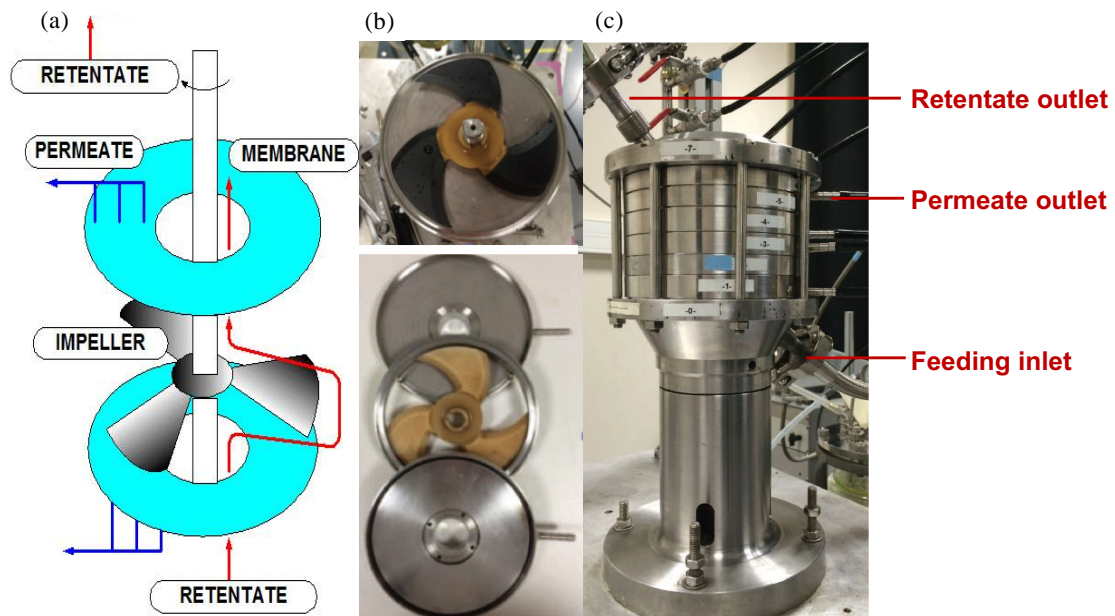


Fig. Ab. 1. Scheme and illustration of filtration cell and of RVF module

Questions scientifiques :

Plusieurs questions scientifiques ont été identifiées (mentionnées au chapitre I):

- Comment les performances globales (consommation d'énergie, courbe de frottement, dissipation thermique, distribution du temps de séjour) peuvent-elles être caractérisées et interprétées?
- Combien de temps une cellule va-t-elle souffrir dans un environnement aussi stressant?
- Quelle sera l'ampleur de ce stress mécanique?
- Est-ce que cela endommage la population de cellules microbiennes?
- Quel est le profil d'écoulement local dans la cellule de filtration? Comment s'organise-t-il et se structure-t-il?
- Est-il possible d'identifier la vitesse locale et instantanée et la contrainte de cisaillement?
- Les mesures expérimentales et les simulations sont-elles cohérentes aux échelles globale et locale?

Structure de cette thèse:

Pour répondre à ces questions, cette thèse se divise en trois parties principales :

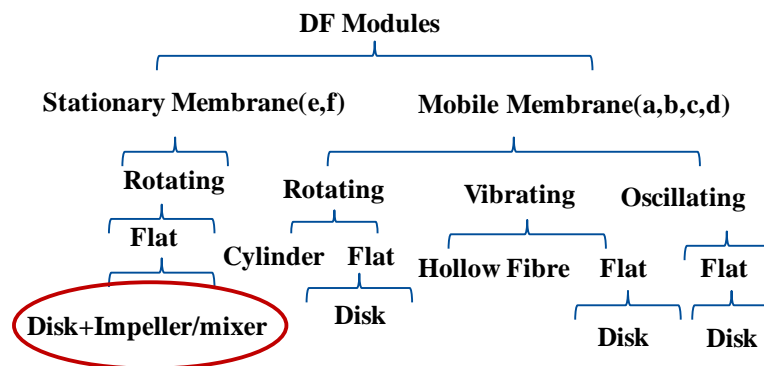


Fig. Ab. 2: Classification of DF modules according to the membrane motion (identification of RVF module)

(1) Revue de la littérature: au cours des dernières décennies, de nombreux efforts et un grand nombre d'études ont été réalisés pour développer de nouveaux modules de DF aux échelles laboratoire et pilote. En examinant les modules DF existants, ils peuvent être principalement

Résumé Étendu

classés selon les membranes (mobile et fixe) et le mouvement généré par rotation (disque, membrane en forme de disque, turbine, bras etc.) et/ou vibration (ou oscillation).

(2) Approche globale : des études de la distribution du temps de séjour, DTS (Residence time distribution, RTD) et du bilan énergétique (puissance mécanique dissipée et bilan thermique) ont été réalisées et comparées à une approche globale précédemment conduite (courbes de consommation de puissance et de frottement).

(3) Approche locale : en tant qu'élément majeur de ce travail de thèse, la vélocimétrie par imagerie de particules (PIV) a été réalisée et comparée à la simulation numérique des écoulements, CFD (Computational Fluid Dynamic). L'étude PIV préliminaire a été menée avec un tachymètre (synchronisation des positions et des prises de vue) pour accéder à un champ de vitesse moyen pour une position angulaire définie. Une étude complémentaire a été réalisée sans synchronisation pour déterminer les composantes orthogonales propres, POD (Proper Orthogonal Decomposition) de l'écoulement. L'analyse POD a permis d'identifier les structures cohérentes de l'écoulement en identifiant la contribution moyenne, les fluctuations organisées et turbulentes.

(4) Application de bioprocédés : en dernier lieu, un travail exploratoire visant à caractériser l'effet de la filtration dynamique sur la population de cellules procaryotes (*Escherichia coli*) a été réalisé en quantifiant l'intégrité ou la lyse mécanique des cellules en fonction du temps et de la vitesse de rotation en régime turbulent.

Résultats principaux:

Des expériences et des simulations numériques ont été réalisées pour étudier l'hydrodynamique aux échelles globale et locale sous des régimes laminaires et turbulents avec des fluides newtoniens dans des conditions biotiques et abiotiques, nos résultats montrent:

(1) Le bilan thermique (dissipation thermique par frottement) est fortement corrélé à la puissance de mélange (courbe de consommation d'énergie). La température a augmenté considérablement pour les vitesses de rotation élevées, en particulier en régime laminaire et aux faibles débits (ex : $\Delta T \geq + 11^\circ\text{C}$ pour $Q_f = 25 \text{ L/h}$ et $N = 25 \text{ Hz}$ avec une viscosité, $\mu = 0.35 \text{ Pa.s}$). En écoulement turbulent, les mêmes variations sont notables et pour $Q_f = 50 \text{ L/h}$ et $N = 50 \text{ Hz}$, la température augmente jusqu'à 9°C . En considérant une augmentation de température limitée à 4°C afin de prendre en compte la thermodependance de l'activité microbienne, les conditions de

Résumé Étendu

fonctionnement restreintes (débit minimum, vitesse d'agitation maximum) sont identifiées à partir du bilan énergétique (puissance mécanique dissipée et bilan thermique)..

(2) Dans l'étude de la DTS, les résultats ont montré que en régime laminaire, le temps de séjour moyen, t_s reste constant pour un débit donné, Q_f , quelque soit la vitesse de rotation, N . Le volume effectif, V_I reste quasi constant ($V_I=1,3$ L équivalent à 87% du volume total) avec une légère augmentation avec le débit. En régime turbulent, t_s augmente linéairement en fonction de N pour un débit donné, Q_f . Le volume effectif, V_I ne dépend alors que du nombre de Reynolds d'agitation et varie de 1,1 à 1,6 L (soit de 74 à 100% du volume total). En régime laminaire, les simulations numériques des écoulements ont indiqué l'existence d'une zone morte. Enfin, la modélisation de la DTS par un modèle associant un réacteur piston et J réacteur parfaitement agité (volume effectif V_I et $J = 2,5 \pm 0,6$) a permis de décrire le temps de séjour moyen et la distribution associée. La DTS d'une population microbienne subissant un environnement stressant peut ainsi être prédite et discutée.

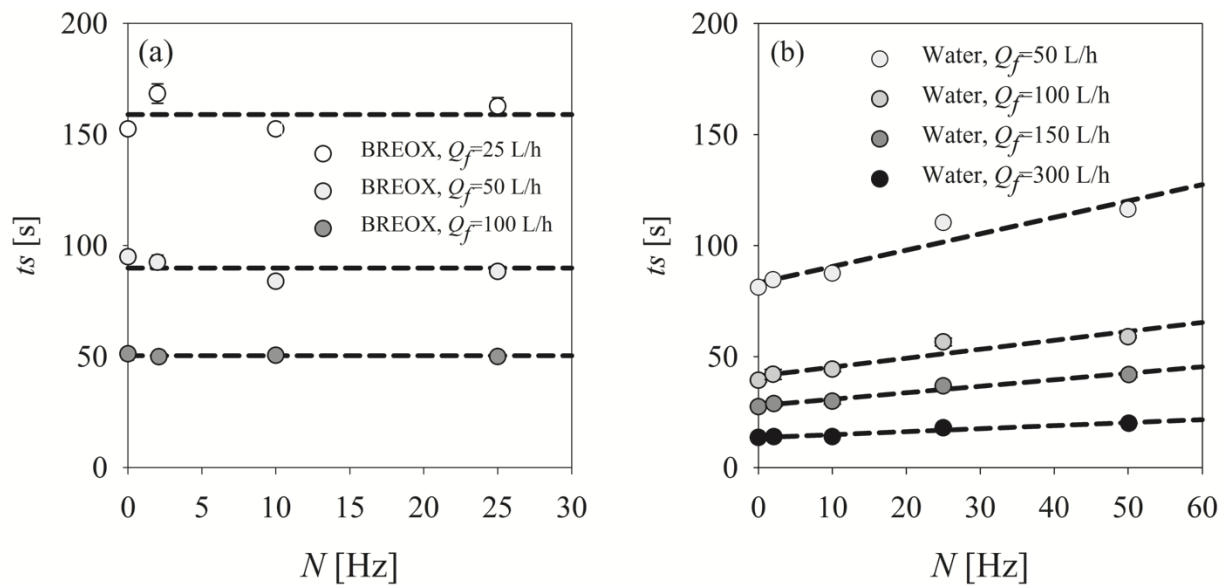


Fig. Ab. 3: Mean residence time t_s as a function of rotation speed N for (a) laminar flow regime, operating condition: BREOX solution $\mu=0.35$ Pa·s, $Q_f=25, 50, 100$ L/h, $N=0, 2, 10, 25$ Hz; and for (b) turbulent flow regime, operating condition: water, $Q_f=50, 100, 150, 300$ L/h, $N=0, 2, 10, 25, 50$ Hz

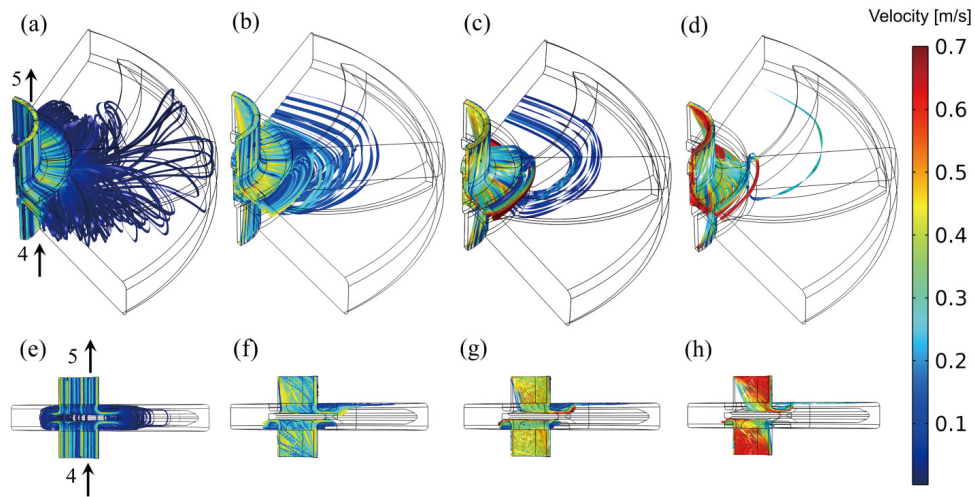


Fig. Ab. 4: Illustration of streamlines in the filtration cell issued from CFD simulation in 3D (a, b, c, d) and 2D (e, f, g, h) view with rotation frequency $N=0$ Hz (a, e), $N=2$ Hz (b, f), $N=5$ Hz (c, g), $N=10$ Hz (d, h). Direction of the streamline: from cross-section 4 to 5; Operating conditions:

*$Q_f= 45$ L/h; $\mu=0.85$ Pa·s and $T=20^\circ\text{C}$. * Notice each figure has 500 streamlines*

(3) Dans les expériences PIV (avec synchronisation entre prise de vue et position angulaire), différents plans (z) ont été étudiés en régime laminaire. Les résultats obtenus ont montré que les champs de vitesse horizontaux et leurs profils associés étaient bien organisés. Un profil parabolique typique a été observé et simulé dans les mesures verticales. De même le champ de contrainte de cisaillement a pu être établi par CFD. En régime turbulent, les vitesses étaient très uniformes (cœur) et présentaient un profil presque linéaire le long de la direction verticale à proximité des parois.

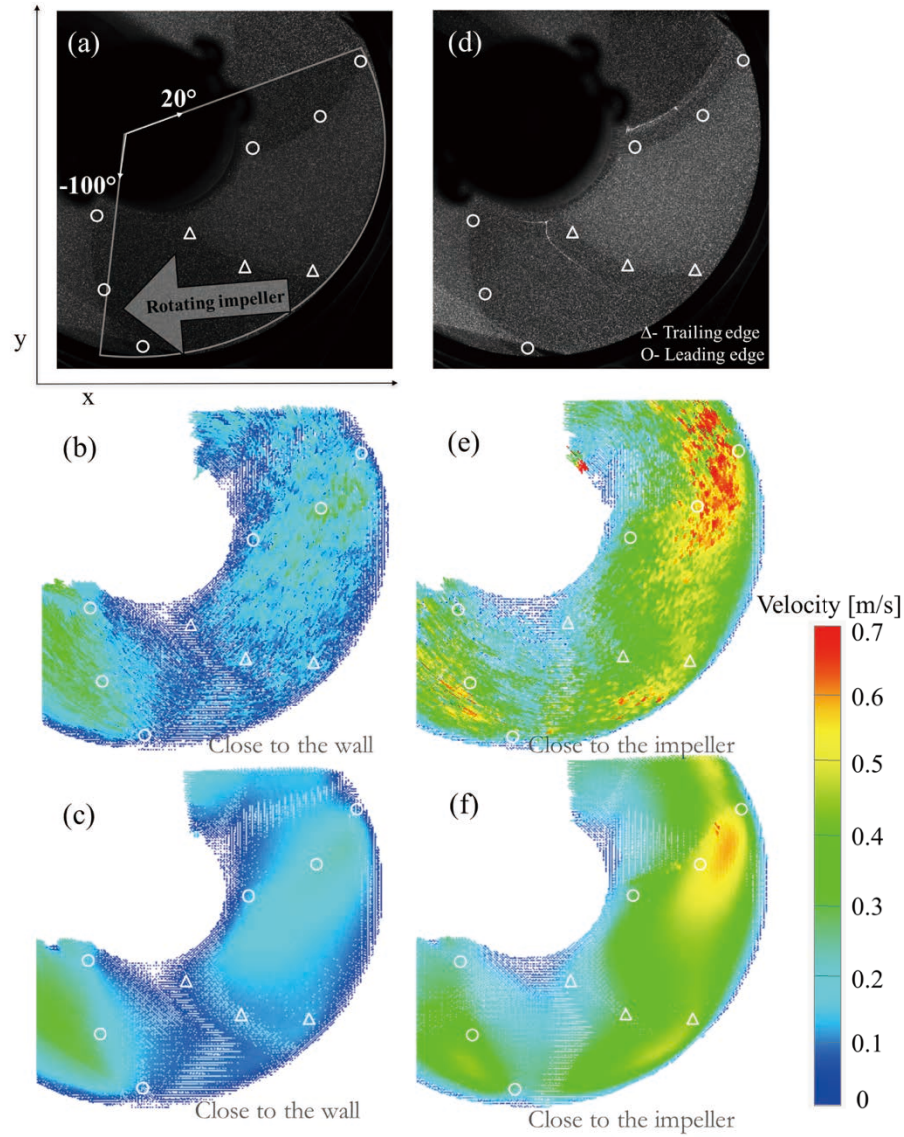


Fig. Ab. 5: Illustration of PIV raw images in horizontal measurement (a, d), instantaneous velocity fields (b, e, issued from single image pair) and time-averaged velocity fields (c, f, averaged of 1000 image pairs) in the RVF module. Slice positions: z_1 close to the wall (a, b and c) and z_6 close to the impeller (d, e and f); Operating conditions: $Q_f= 45 \text{ L/h}$, $N=2 \text{ Hz}$; $\mu=0.85 \text{ Pa}\cdot\text{s}$ and $T=20^\circ\text{C}$. Symbols: O, leading edge and Δ, trailing edge of blade

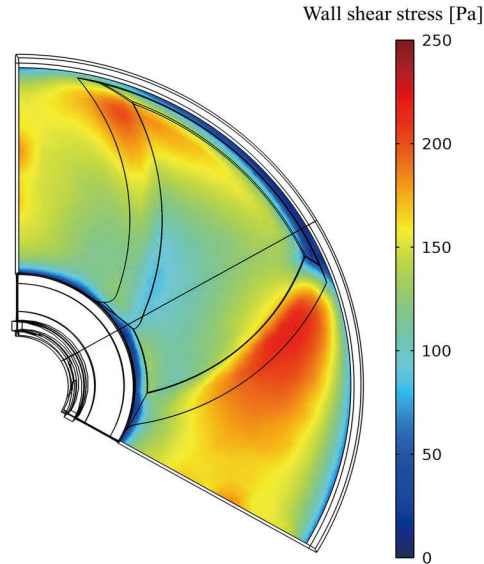


Fig. Ab. 6: Field of wall shear stress ($z=0$ and 14 mm) calculated from CFD simulations. Operating conditions: $Q_f=45$ L/h, $N=2$ Hz; $\mu=0.85$ Pa·s and $T=20^\circ\text{C}$. (Notice: $z=0$ and 14 mm is at the surface of the walls where membranes are mounted)

(4) Dans les expériences PIV (sans synchronisation), des paramètres locaux importants incluant la vitesse, la contrainte de cisaillement (contrainte de cisaillement de la paroi, cisaillement visqueux moyen, cisaillement fluctuant) et le couple ont été étudiés. Ils ont permis de décomposer la vitesse instantanée en un débit moyen (mode 1) et les fluctuations associées (y compris les contributions organisées et turbulentes):

- En régime laminaire (ex: $N = 2$ Hz), les contributions principales pour le couple était due aux parois supérieure et inférieure (40% chacune), la paroi latérale (entretoise externe) ne contribuait que pour 20%. La contribution de chaque mode à l'énergie cinétique totale a été discutée. Le mode 1 représentait la contribution moyenne (90% de l'énergie cinétique totale). Le mouvement organisé était basé sur les modes 2 à 5 (7-8% ale), et la déviation moyenne absolue de la contrainte de cisaillement à la paroi était très importante et atteignait jusqu'à 45% de la valeur moyenne de la contrainte de cisaillement à la paroi.

- En régime turbulent (ex: $N = 10$ Hz), la contrainte de cisaillement à la paroi latérale (externe) a atteint 250 Pa et contribue à 90% du couple l. L'impact des parois supérieure et inférieure est devenu alors quasiment négligeable. Le mode 1 représentait la

Résumé Étendu

contribution moyenne (95% de l'énergie cinétique totale). L'analyse POD a montré que les fluctuations organisées étaient basées sur les modes 2-9 (4,4-5,5% de l'énergie cinétique totale), et que leur structure cohérente était remarquablement organisée.

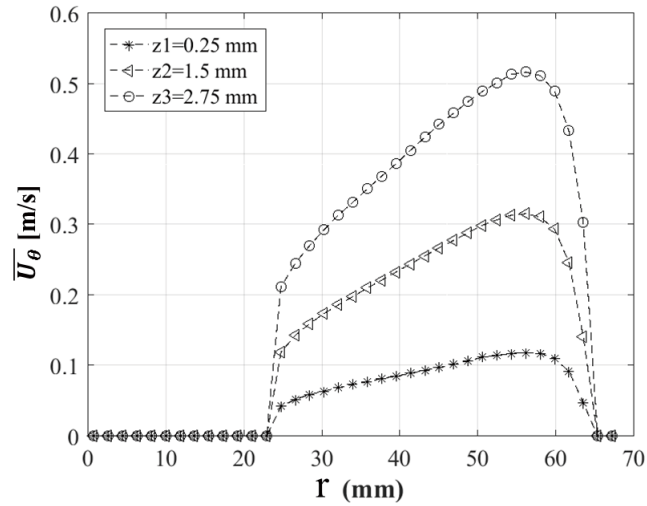


Fig. Ab. 7: Radial profiles of tangential mean velocities at 3 planes, $z=0.25$, 1.5 and 2.75 mm (distance from the upper wall). Operating conditions: horizontal measurements at $Q_f=50$ L/h, $N=2$ Hz; BREOX solution, $\mu=0.85$ Pa·s, Remixing=42, and $T=20^\circ\text{C}$

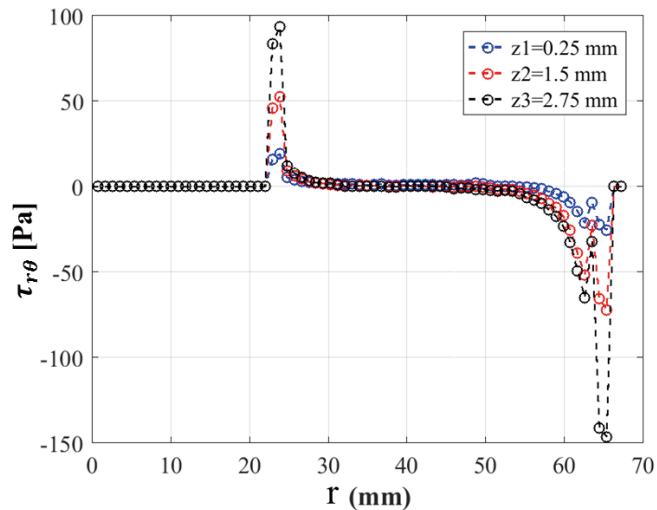


Fig. Ab. 8: Radial profiles of viscous mean shear at 3 planes, $z=0.25$, 1.5, and 2.75 mm (distance from the upper wall). Operating conditions: horizontal measurements at $Q_f=50$ L/h, $N=2$ Hz; BREOX solution, $\mu=0.85$ Pa·s, Remixing=42, and $T=20^\circ\text{C}$

Résumé Étendu

(6) Les observations des suspensions de cellules procaryotes (*E. coli*) ont indiqué que les cellules ont été endommagées et/ou détruites dans des conditions extrêmes, $N = 50$ Hz et $t = 5$ h. De plus, à $N = 50$ Hz, des amas et agrégats avec des cellules rompues ont été observés. Ceci n'a pas été observé avec les cellules eucaryotes dans les bioprocédés alimentaires (mout de fermentation issus de brassage et vinification). Par conséquent, les dommages cellulaires induits par les contraintes mécaniques doivent être explorés plus avant à la lumière de l'hydrodynamique locale et globale qui a été caractérisée.

Principaux résultats de cette thèse:

Ces actions et les découvertes associées ont reposées sur des approches multi-échelles et multi-disciplinaires et ont fourni un éclairage nouveau sur l'impact et l'utilisation de la filtration dynamique (module RVF) dans les bioprocédés, tels que:

- effets thermique et mécanique sur les cellules microbiennes;
- caractérisation du comportement hydrodynamique, afin d'appliquer de meilleures conditions opératoires d'optimiser les bioprocédés industriels et de concevoir des modules de DF;
- détermination des patrons d'écoulement et des structures cohérentes, ainsi qu'une meilleure compréhension des mécanismes de limitation de l'encrassement en connaissant les paramètres hydrodynamiques locaux (champs / profils de vitesse, contrainte de cisaillement, fluctuations organisées et turbulente)

Perspectives:

Les interactions entre les matrices biologiques et la filtration dynamique doivent être étudiées pour intensifier les bioprocédés. Constatant le manque de connaissances sur les milieux de culture complexes et évolutifs (FCV, croissance cellulaire, bioproduction) et (ii) l'intensification des cultures microbiennes sous haute densité cellulaire (activité cellulaire, viabilité), les travaux futurs liés à la filtration dynamique se focaliseront sur:

(1) les verrous scientifiques et techniques liés aux problèmes de rétention / perméation (biomasse catalytique, composants physico-chimiques) associés à des matrices biologiques complexes;

Résumé Étendu

(2) les interactions entre les matrices et les matériaux membranaires (nature, porosité et seuil de coupure);

(3) l'impact de la DF sur les performances des souches procaryotes et eucaryotes (activité biologique, viabilité, lyse cellulaire, etc.).

Les investigations scientifiques peuvent également inclure d'autres travaux en lien avec l'hydrodynamique:

(4) d'autres techniques locales peuvent être appliquées pour étudier les paramètres locaux tels que la température pour analyser les effets thermiques couplés à la distribution d'âge interne;

(5) des méthodes électrochimiques peuvent être appliquées pour quantifier la contrainte de cisaillement instantanée et locale à la surface de la membrane.

(6) des expériences peuvent être réalisées avec des fluides non-newtoniens pour explorer les comportements rheofluidifiant, rheoépaississant et/ou visco-plastique (seuil d'écoulement) dans les régimes laminaire et turbulent;

(7) Les simulations numériques pourront prendre en considération des conditions plus complexes (régimes transitoire et turbulent avec des fluides newtonien et non-newtonien) et être validées pour concevoir des modules de DF.

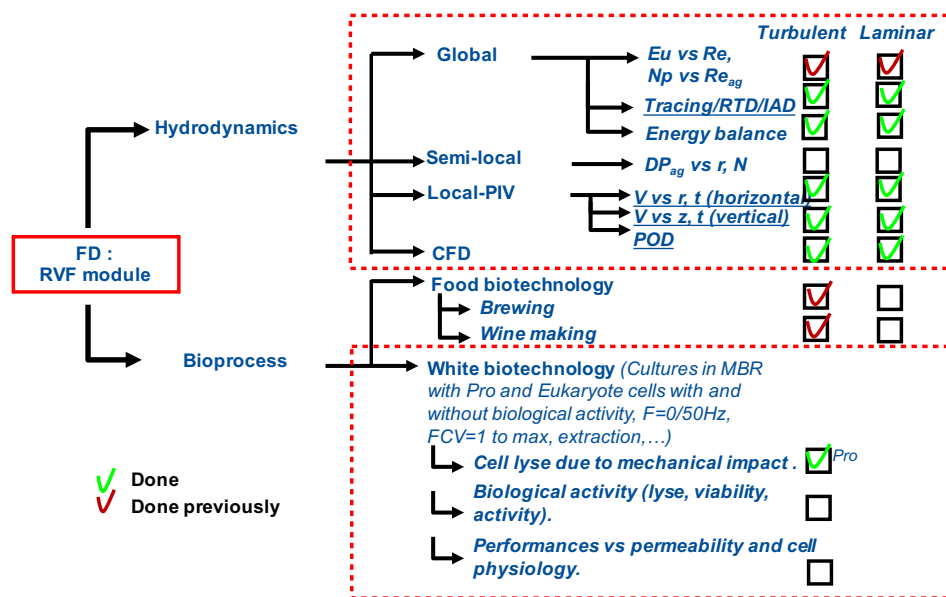


Fig. Ab. 9: Overview of scientific strategy and obtained results with RVF module

